EFFECT OF OUTFLOW ORIENTATION AND MULTIPLE JETS ORIFICE PLATE CONFIGURATIONS ON HEAT TRANSFER IN A RECTANGULAR DUCT

By

MOHAMMED KHALEEL AHMED

A Thesis presented to the

DEANSHIP OF GRADUATE STUDIES

KING FAHD UNIVERSITY OF PETROLEUM & MINERALS

DHAHRAN, SAUDI ARABIA

In Partial Fulfillment of the
Requirements for the Degree of

MASTER OF SCIENCE

In

MECHANICAL ENGINEERING
MARCH 2005

KING FAHD UNIVERSITY OF PETROLEUM & MINERALS
DHAHRAN 31261, SAUDI ARABIA

DEANSHIP OF GRADUATE STUDIES

This thesis, written by **MOHAMMED KHALEEL AHMED** under the direction of his Thesis Advisor and approved by his Thesis Committee, has been presented to and accepted by the Dean of Graduate Studies, in partial fulfillment of the requirements for the degree of **MASTER OF SCIENCE IN MECHANICAL ENGINEERING.**

Thesis Committee

_____
Dr. Luai Al-Hadhrami (Advisor)

_____
Prof. Syed M. Zubair (Member)

_____
Prof. Mohammed A. Habib (Member)

_____
Dr. Faleh Al-Sulaiman
Department Chairman

_____
Dr. Mohammed A. Al-Ohali
Dean of Graduate Studies

_____
Date

Dedicated to My Beloved Parents, Sister & Brother

ACKNOWLEDGEMENTS

In the name of Allah, the Most Gracious and the Most Merciful

All praise and thanks are due to Almighty **Allah**, *subhanahu Wa Ta'ala*, for bestowing me with health, knowledge, opportunity, courage and patience to complete this work. Thereafter, acknowledgement is due to King Fahd University of Petroleum and Minerals for my admittance, and to its learned faculty members for imparting quality learning and knowledge with their valuable support and able guidance.

My deep appreciation and heartfelt gratitude goes to my thesis advisor Dr. Luai Al-Hadhrami for his constant endeavor, guidance and the numerous moments of attention he devoted throughout the course of this research work. His valuable suggestions made this work interesting and knowledgeable to me. I would also acknowledge Dr. Luai Al-Hadhrami for his cooperation in providing the Heat Transfer Lab facility.

I am deeply indebted and grateful to my thesis committee members Dr. Syed M. Zubair and Dr. M. A. Habib for their extensive guidance, continuous support, constructive and positive criticism and thought-provoking contribution in my research work. It was surely an honor and an exceptional learning experience to work with them. Acknowledgements are also due to Lab engineers Mr. Saeed Al-Baba and Mr. Mohandes Karam for their help and support during experiments.

I am also thankful to department chairman Dr. Faleh Al-Sulaiman for providing me a favorable environment where I was able to utilize my skills.

Acknowledgement is due to all my senior colleagues at the university who were always there to help me in my work. Special thanks are due to my friends Obaid, Kaleem, Mazhar, Khaja, Qaiyum, Khaliq, Imran, Sami, Basha, Shafeeq, Shujath, Omer, Awes, Saad, Bilal, Sanaullah and all others who have provided wonderful company and good memories that will last a life time. Thanks are also due to my flat mates, they made my stay at KFUPM memorable.

Family support plays a vital role in the success of an individual. I am thankful to my parents, brother and sister for their constant prayers, encouragement and inspiration. Also I am grateful to all my relatives for their support, encouragement and prayers.

TABLE OF CONTENTS

LIST OF TABLES ..... **x**

LIST OF FIGURES ..... **xi**

THESIS ABSTRACT (ENGLISH) ..... **xvii**

THESIS ABSTRACT (ARABIC) ..... **xviii**

NOMENCLATURE ..... **xix**

CHAPTER 1 ..... **1**

INTRODUCTION **1**

1.1 General Introduction **1**

1.1.1 Types of Cooling 3

1.1.2 Overview of a Turbine Blade 4

1.2 Jet Impingement **6**

1.2.1 Literature review 9

1.2.1.1 Effect of nozzle-to-plate distance 18

1.2.1.2 Effect of cross-flow 18

1.3 Motivation to investigate **21**

1.4 Objective of the present study **22**

CHAPTER 2 ..... **24**

EXPERIMENTAL SETUP AND PROCEDURE **24**

2.1 General set-up and Apparatus **24**

2.1.1 Construction details 27

2.1.2 Test section 28

2.1.3 Outflow orientation 31

2.1.4 Orifice plates 33

2.1.5 Instrumentation and Data Acquisition 35

2.2 Data Reduction **40**

2.2.1 Reynolds number calculations 40

2.2.2 Nusselt number calculations 40

2.3 Procedure 43

CHAPTER 3 45

UNCERTAINITY ANALYSIS 45

3.1 Introduction 45

3.2 Measurement Errors 46

3.3 Uncertainty Evaluation Procedure 49

3.3.1 Uncertainty in Nusselt number 50

3.3.2 Uncertainty in Jet Reynolds number 52

3.4 EES Program 53

3.5 Sample Uncertainty Calculations 56

3.5.1 Orifice Plate – 1 56

3.5.2 Orifice Plate – 2 57

3.5.3 Orifice Plate – 3 58

3.5.4 Orifice Plate – 4 59

3.5.5 Uncertainty in jet Reynolds numbers 60

CHAPTER 4 62

ORIFICE PLATE - 1 62

4.1 Effect of feeding channel aspect ratio on local Nusselt number 64

4.2 Effect of jet Reynolds number on local Nusselt number 70

4.3 Effect of outflow orientation on local Nusselt number 77

4.4 Effect of jet-to-plate distance on local Nusselt number 83

4.5 Averaged Nusselt Number 89

4.5.1 Effect of feeding channel aspect ratio 89

4.5.2 Effect of outflow orientation 90

4.5.3 Correlations of averaged Nusselt number 94

CHAPTER 5 97

ORIFICE PLATE – 1 & 2 97

5.1 Effect of feeding channel aspect ratio on local Nusselt number 98

5.2 Effect of jet Reynolds number on local Nusselt number 105

5.3 Effect of outflow orientation on local Nusselt number 113

5.4 Averaged Nusselt number 119

5.4.1 Effect of feeding channel aspect ratio 119

5.4.2 Effect of outflow orientation 120

5.4.3 Correlations of averaged Nusselt number 123

CHAPTER 6 126

ORIFICE PLATE - 2 126

6.1 Effect of feeding channel aspect ratio on local Nusselt number 126

6.2 Effect of jet Reynolds number on local Nusselt number 133

6.3 Effect of outflow orientation on local Nusselt number 140

6.4 Effect of Jet-to-plate distance on local Nusselt number 146

6.5 Average Nusselt Number 152

6.5.1 Effect of feeding channel aspect ratio 152

6.5.2 Effect of outflow orientation 153

6.5.3 Correlations of Averaged Nusselt number 156

CHAPTER 7 159

ORIFICE PLATE - 3 159

7.1 Effect of feeding channel aspect ratio on local Nusselt number 159

7.2 Effect of jet Reynolds number on local Nusselt number 166

7.3 Effect of outflow orientation on local Nusselt number 173

7.4 Effect of jet-to-plate distance on local Nusselt number 179

7.5 Average Nusselt Number 185

7.5.1 Effect of feeding channel aspect ratio 185

7.5.2 Effect of outflow orientation 186
7.5.3 Correlations of averaged Nusselt number 189
CHAPTER 8 192
ORIFICE PLATE - 4 192
8.1 Effect of feeding channel aspect ratio on local Nusselt number 194
8.2 Effect of jet Reynolds number on local Nusselt number 200
8.3 Effect of outflow orientation on local Nusselt number 207
8.4 Effect of jet-to-plate distance on local Nusselt number 213
8.5 Average Nusselt Number 219
8.5.1 Effect of feeding channel aspect ratio 219
8.5.2 Effect of outflow orientation 220
8.4.3 Correlations of averaged Nusselt number 225
CHAPTER 9 228
CONCLUSIONS 228
8.1 Orifice plate – 1 228
8.2 Orifice plate 1 & 2 229
8.3 Orifice plate – 2 230
8.4 Orifice plate – 3 231
8.5 Orifice plate – 4 232
APPENDIX A 234
SAMPLE CALCUATIONS OF LOCAL NUSSELT NUMBER 234
BIBLIOGRAPHY 236

LIST OF TABLES

Table 2.1 Instrumentation and software used for Data acquisition..... 37

Table 3.1 Sample Uncertainty calculations of Nusselt number for minimum value 56

Table 3.2 Sample Uncertainty calculations of Nusselt number for maximum value..... 56

Table 3.3 Sample Uncertainty calculations of Nusselt number for minimum value 57

Table 3.4 Sample Uncertainty calculations of Nusselt number for maximum value..... 57

Table 3.5 Sample Uncertainty calculations of Nusselt number for minimum value 58

Table 3.6 Sample Uncertainty calculations of Nusselt number for maximum value..... 58

Table 3.7 Sample Uncertainty calculations of Nusselt number for minimum value 59

Table 3.8 Sample Uncertainty calculations of Nusselt number for maximum value..... 59

Table 3.9 Sample Uncertainty calculations of Jet Reynolds number for $\mathrm{Re}_j = 9300$ 60

Table 3.10 Sample Uncertainty calculations of Jet Reynolds number for $\mathrm{Re}_j = 14400$ 60

Table 3.11 Sample Uncertainty calculations of Jet Reynolds number for $\mathrm{Re}_j = 18800$ 60

Table 3.12 The derived parameters used to find the uncertainty. 61

LIST OF FIGURES

Figure 1.1 Schematic of a Gas turbine (Fred Thomas [46]) 2
Figure 1.2 A typical turbine blade cooling arrangement 5
Figure 1.3 Schematic of impingement cooling arrangement in a first-stage turbine inlet guide vane. 7
Figure 1.4 Three commonly used nozzle arrangements for impinging jet arrays..... 11
Figure 1.5 Definitions of the cross-flow schemes investigated by Obot and Trabold [37] ... 12
Figure 2.1 Schematic of the test section. 26
Figure 2.2 Three-dimensional view of the test section for case 1..... 30
Figure 2.3 Illustration of three exit outflow orientations. 32
Figure 2.4 Orifice plate orientations considered in this study 34
Figure 2.5 Illustration of thermocouples mounted in a groove at the back of a copper plate.36
Figure 2.6 Photograph of the program being used..... 39
Figure 3.1, Distribution of errors upon repeated measurements (Figliola, R.S. [47]) 48
Figure 4.1 Effect of feeding channel aspect ratio $2.5 \le H/d \le 4.5$ on local Nusselt number distribution for case – 1 and jet-to-plate distance $S/d = 3$. 67
Figure 4.2 Effect of feeding channel aspect ratio $2.5 \le H/d \le 4.5$ on local Nusselt number distribution for case – 2 and jet-to-plate distance $S/d = 3$. 68
Figure 4.3 Effect of feeding channel aspect ratio $2.5 \le H/d \le 4.5$ on local Nusselt number distribution for case – 3 and jet-to-plate distance $S/d = 3$. 69
Figure 4.4 Effect of jet Reynolds number and feeding channel aspect ratio $2.5 \le H/d \le 4.5$ on local Nusselt number distribution for $S/d = 3$ and case – 1. 73
Figure 4.5 Effect of jet Reynolds number and feeding channel aspect ratio $2.5 \le H/d \le 4.5$ on local Nusselt number distribution for $S/d = 3$ and case – 2. 74
Figure 4.6 Effect of jet Reynolds number and feeding channel aspect ratio $2.5 \le H/d \le 4.5$ on local Nusselt number distribution for $S/d = 3$ and case – 3. 76
Figure 4.7 Effect of outflow orientation and feeding channel aspect ratio $2.5 \le H/d \le 4.5$ on local Nusselt number distribution for $S/d = 3$ and $\mathrm{Re}_j = 5000$. 78

Figure 4.8 Effect of outflow orientation and feeding channel aspect ratio $2.5 \le H/d \le 4.5$ on local Nusselt number distribution for $S/d = 3$ and $\mathrm{Re}_j = 7500$ 81

Figure 4.9 Effect of outflow orientation and feeding channel aspect ratio $2.5 \le H/d \le 4.5$ on local Nusselt number distribution for $S/d = 3$ and $\mathrm{Re}_j = 10000$ 82

Figure 4.10 Effect of jet-to-plate distance and feeding channel aspect ratio $2.5 \le H/d \le 4.5$ on local Nusselt number distribution for $\mathrm{Re}_j = 10000$ and case – 1. 85

Figure 4.11 Effect of jet-to-plate distance and feeding channel aspect ratio $2.5 \le H/d \le 4.5$ on local Nusselt number distribution for $\mathrm{Re}_j = 10000$ and case – 2. 86

Figure 4.12 Effect of jet-to-plate distance and feeding channel aspect ratio $2.5 \le H/d \le 4.5$ on local Nusselt number distribution for $\mathrm{Re}_j = 10000$ and case – 3. 88

Figure 4.13 Effect of feeding channel aspect ratio $2.5 \le H/d \le 4.5$ and jet-to-plate distances on averaged Nusselt number for different outflow orientation. 92

Figure 4.14 Effect of outflow orientation and feeding channel aspect ratio on averaged Nusselt number for different jet-to-plate distances $(2 \le S/d \le 4)$ 93

Figure 4.15 Averaged Nusselt number comparisons with the existing correlations..... 96

Figure 5.1 Effect of feeding channel aspect ratio $2.5\,cm \le H/d \le 4.5\,cm$ on local Nusselt number distribution for case – 1 and $S = 3\,cm$. (Filled symbol: $d = 1\,cm$ and Unfilled symbol: $d = 0.5\,cm$) 102

Figure 5.2 Effect of feeding channel aspect ratio $2.5\,cm \le H/d \le 4.5\,cm$ on local Nusselt number distribution for case – 2 and $S = 3\,cm$. (Filled symbol: $d = 1\,cm$ and Unfilled symbol: $d = 0.5\,cm$) 103

Figure 5.3 Effect of feeding channel aspect ratio $2.5\,cm \le H/d \le 4.5\,cm$ on local Nusselt number distribution for case – 3 and $S = 3\,cm$. (Filled symbol: $d = 1\,cm$ and Unfilled symbol: $d = 0.5\,cm$) 104

Figure 5.4 Effect of jet Reynolds number and feeding channel aspect ratio $2.5\,cm \le H/d \le 4.5\,cm$ on local Nusselt number distribution for case – 1 and $S = 3\ cm$. (Filled symbol: $d = 1\,cm$ and Unfilled symbol: $d = 0.5\,cm$) 108

Figure 5.5 Effect of jet Reynolds number and feeding channel aspect ratio $2.5cm \le H/d \le 4.5cm$ on local Nusselt number distribution for case – 2 and $S = 3\ cm$. (Filled symbol: $d = 1cm$ and Unfilled symbol: $d = 0.5cm$) 109

Figure 5.6 Effect of jet Reynolds number and feeding channel aspect ratio $2.5cm \le H/d \le 4.5cm$ on local Nusselt number distribution for case – 3 and $S = 3cm$.(Filled symbol: $d = 1cm$ and Unfilled symbol: $d = 0.5cm$)..... 112

Figure 5.7 Effect of outflow orientation and feeding channel aspect ratio $2.5cm \le H/d \le 4.5cm$ on local Nusselt number distribution for $\mathrm{Re}_j = 5000$ and $S = 3cm$. (Filled symbol: $d = 1cm$ and Unfilled symbol: $d = 0.5cm$)..... 114

Figure 5.8 Effect of outflow orientation and feeding channel aspect ratio $2.5cm \le H/d \le 4.5cm$ on local Nusselt number distribution for $\mathrm{Re}_j = 7500$ and $S = 3cm$. (Filled symbol: $d = 1cm$ and Unfilled symbol: $d = 0.5cm$)..... 117

Figure 5.9 Effect of outflow orientation and feeding channel aspect ratio $2.5cm \le H/d \le 4.5cm$ on local Nusselt number distribution for $\mathrm{Re}_j = 10000$ and $S = 3cm$. (Filled symbol: $d = 1cm$ and Unfilled symbol: $d = 0.5cm$)..... 118

Figure 5.10 Effect of outflow orientation on averaged Nusselt number for different feeding channel aspect ratios $2.5cm \le H/d \le 4.5cm$ and $S = 3cm$. (Filled symbol: $d = 1cm$ and Unfilled symbol: $d = 0.5cm$) 121

Figure 5.11 Effect of feeding channel aspect ratio $2.5cm \le H/d \le 4.5cm$ on the averaged Nusselt number for different outflow orientations and $S = 3cm$. (Filled symbol: $d = 1cm$ and Unfilled symbol: $d = 0.5cm$) 122

Figure 5.12 Averaged Nusselt number comparisons with the existing correlations..... 125

Figure 6.1 Effect of feeding channel aspect ratio $5 \le H/d \le 9$ on local Nusselt number distribution for case – 1 and jet-to-plate distance $S/d = 6$. 130

Figure 6.2 Effect of feeding channel aspect ratio $5 \le H/d \le 9$ on local Nusselt number distribution for case – 2 and jet-to-plate distance $S/d = 6$. 131

Figure 6.3 Effect of feeding channel aspect ratio $5 \le H/d \le 9$ on local Nusselt number distribution for case – 3 and jet-to-plate distance $S/d = 6$ 132
Figure 6.4 Effect of jet Reynolds number and feeding channel aspect ratio $5 \le H/d \le 9$ on local Nusselt number distribution for $S/d = 6$ and case – 1. 136
Figure 6.5 Effect of jet Reynolds number and feeding channel aspect ratio $5 \le H/d \le 9$ on local Nusselt number distribution for $S/d = 6$ and case – 2.. 137
Figure 6.6 Effect of jet Reynolds number and feeding channel aspect ratio $5 \le H/d \le 9$ on local Nusselt number distribution for $S/d = 6$ and case – 3. 139
Figure 6.7 Effect of outflow orientation and feeding channel aspect ratio $5 \le H/d \le 9$ on local Nusselt number distribution for $S/d = 6$ and $\mathrm{Re}_j = 9300$ 141
Figure 6.8 Effect of outflow orientation and feeding channel aspect ratio $5 \le H/d \le 9$ on local Nusselt number distribution for $S/d = 6$ and $\mathrm{Re}_j = 14400$ 144
Figure 6.9 Effect of outflow orientation and feeding channel aspect ratio $5 \le H/d \le 9$ on local Nusselt number distribution for $S/d = 6$ and $\mathrm{Re}_j = 18800$ 145
Figure 6.10 Effect of jet-to-plate distance and feeding channel aspect ratio $5 \le H/d \le 9$ on local Nusselt number distribution for $\mathrm{Re}_j = 18800$ and case – 1. 148
Figure 6.11 Effect of jet-to-plate distance and feeding channel aspect ratio $5 \le H/d \le 9$ on local Nusselt number distribution for $\mathrm{Re}_j = 18800$ and case – 2. 149
Figure 6.12 Effect of jet-to-plate distance and feeding channel aspect ratio $5 \le H/d \le 9$ on local Nusselt number distribution for $\mathrm{Re}_j = 18800$ and case – 3. 151
Figure 6.13 Effect of feeding channel aspect ratio $(5 \le H/d \le 9)$ and jet-to-plate distances on averaged Nusselt number for different outflow orientation..... 154
Figure 6.14 Effect of outflow orientation and feeding channel aspect ratio on averaged Nusselt number for different jet-to-plate distances $(4 \le S/d \le 8)$ 155
Figure 6.15 Averaged Nusselt number comparisons with the existing correlations..... 158
Figure 7.1 Effect of feeding channel aspect ratio $5 \le H/d \le 9$ on local Nusselt number distribution for case – 1 and jet-to-plate distance $S/d = 6$ 163

Figure 7.2 Effect of feeding channel aspect ratio $5 \le H/d \le 9$ on local Nusselt number distribution for case – 2 and jet-to-plate distance $S/d = 6$. 164
Figure 7.3 Effect of feeding channel aspect ratio $5 \le H/d \le 9$ on local Nusselt number distribution for case – 3 and jet-to-plate distance $S/d = 6$. 165
Figure 7.4 Effect of jet Reynolds number on local Nusselt number distribution for $S/d = 6$ and case – 1. 169
Figure 7.5 Effect of jet Reynolds number on local Nusselt number distribution for $S/d = 6$ and case – 2. 170
Figure 7.6 Effect of jet Reynolds number on local Nusselt number distribution for $S/d = 6$ and case – 3. 172
Figure 7.7 Effect of outflow orientation on local Nusselt number distribution for $S/d = 6$ and $\mathrm{Re}_j = 9300$ 174
Figure 7.8 Effect of outflow orientation on local Nusselt number distribution for $S/d = 6$ and $\mathrm{Re}_j = 14400$. 177
Figure 7.9 Effect of outflow orientation on local Nusselt number distribution for $S/d = 6$ and $\mathrm{Re}_j = 18800$. 178
Figure 7.10 Effect of jet-to-plate distance on local Nusselt number distribution for $\mathrm{Re}_j = 18800$ and case – 1. 181
Figure 7.11 Effect of jet-to-plate distance on local Nusselt number distribution for $\mathrm{Re}_j = 18800$ and case – 2. 182
Figure 7.12 Effect of jet-to-plate distance on local Nusselt number distribution for $\mathrm{Re}_j = 18800$ and case – 3. 184
Figure 7.13 Effect of feeding channel aspect ratio $(5 \le H/d \le 9)$ and jet-to-plate distances on averaged Nusselt number for different outflow orientation. 187
Figure 7.14 Effect of outflow orientation and feeding channel aspect ratio on averaged Nusselt number for different jet-to-plate distances $(4 \le S/d \le 8)$. 188
Figure 7.15 Averaged Nusselt number comparisons with the existing correlations. 191

Figure 8.1 Effect of feeding channel aspect ratio $5 \le H/d \le 9$ on local Nusselt number distribution for case – 1 and jet-to-plate distance $S/d = 4$. 197
Figure 8.2 Effect of feeding channel aspect ratio $5 \le H/d \le 9$ on local Nusselt number distribution for case – 2 and jet-to-plate distance $S/d = 4$. 198
Figure 8.3 Effect of feeding channel aspect ratio $5 \le H/d \le 9$ on local Nusselt number distribution for case – 3 and jet-to-plate distance $S/d = 4$. 199
Figure 8.4 Effect of jet Reynolds number and feeding channel aspect ratio $5 \le H/d \le 9$ on local Nusselt number distribution for $S/d = 4$ and case – 1. 203
Figure 8.5 Effect of jet Reynolds number and feeding channel aspect ratio $5 \le H/d \le 9$ on local Nusselt number distribution for $S/d = 4$ and case – 2. 204
Figure 8.6 Effect of jet Reynolds number and feeding channel aspect ratio $5 \le H/d \le 9$ on local Nusselt number distribution for $S/d = 4$ and case – 3. 206
Figure 8.7 Effect of outflow orientation and feeding channel aspect ratio $5 \le H/d \le 9$ on local Nusselt number distribution for $S/d = 4$ and $\mathrm{Re}_j = 9300$. 208
Figure 8.8 Effect of outflow orientation and feeding channel aspect ratio $5 \le H/d \le 9$ on local Nusselt number distribution for $S/d = 4$ and $\mathrm{Re}_j = 14400$. 211
Figure 8.9 Effect of outflow orientation and feeding channel aspect ratio $5 \le H/d \le 9$ on local Nusselt number distribution for $S/d = 4$ and $\mathrm{Re}_j = 18800$. 212
Figure 8.10 Effect of jet-to-plate distance and feeding channel aspect ratio $5 \le H/d \le 9$ on local Nusselt number distribution for $\mathrm{Re}_j = 18800$ and case – 1. 215
Figure 8.11 Effect of jet-to-plate distance and feeding channel aspect ratio $5 \le H/d \le 9$ on local Nusselt number distribution for $\mathrm{Re}_j = 18800$ and case – 2. 216
Figure 8.12 Effect of jet-to-plate distance and feeding channel aspect ratio $5 \le H/d \le 9$ on local Nusselt number distribution for $\mathrm{Re}_j = 18800$ and case – 3. 218
Figure 8.13 Effect of feeding channel aspect ratio $(5 \le H/d \le 9)$ and jet-to-plate distances on averaged Nusselt number for different outflow orientation. 223
Figure 8.15 Averaged Nusselt number comparisons with the existing correlations..... 227

THESIS ABSTRACT

NAME: **MOHAMMED KHALEEL AHMED**

TITLE: **EFFECT OF OUTFLOW ORIENTATION AND MULTIPLE JETS ORIFICE PLATE CONFIGURATIONS ON HEAT TRANSFER IN A RECTANGULAR DUCT**

MAJOR: **MECHANICAL ENGINEERING**

DATE: **MARCH, 2005**

Experimental investigation is carried out to study the heat transfer characteristics in a rectangular duct cooled by an array of impinging jets. Air ejected from an array of orifice jets is aimed at the heated target surface and exits from the radial outlets. The effect of outflow orientation, feeding channel aspect ratios $5 \le H/d \le 9$ *and jet to target plate distance* $4 \le S/d \le 8$ *is investigated with a single array of equally spaced orifice jets. The effect of jet Reynolds number is also studied with the range for orifice plate 1 and 2 being* $5000 \le \mathrm{Re}_j \le 10000$ *and for orifice plates 2, 3 and 4 being* $9300 \le \mathrm{Re}_j \le 18800$. *The effect of orifice jet diameter on the heat transfer distribution is also studied with* $d = 0.5$ *and* $1cm$.

Results indicate that the outflow orientation causing crossflow effect significantly affects the Nusselt number distributions on the target surface. Local Nusselt number increases with an increase in jet Reynolds number over the entire impingement surface. Nusselt number is also significantly affected by the feeding channel aspect ratio H/d *the jet-to-plate spacing* S/d. *The feeding channel aspect ratio* H/d *which gives the maximum heat transfer is obtained for all the orifice plates. Similarly the jet-to-plate distance* S/d *which gives maximum heat transfer compared to the other jet-to-plate distances is also found for all the orifice plates studied individually. The highest Nusselt numbers are obtained for the outflow orientation where the flow exits in both the directions. Correlations were developed for averaged Nusselt number as a function of jet Reynolds number for all the orifice plates.*

MASTER OF SCIENCE DEGREE

KING FAHD UNIVERSITY OF PETROLEUM & MINERALS

Dhahran, Saudi Arabia

MARCH, 2005

ملخص الرسالة

الاســـــــــم: محمد خليل احمد
عنوان الرسالة: تأثير توجيه السريان وفتحات النفث المتعدده على انتقال الحراره فى مجرى مستطيل
التخصـــــص: الهندسة الميكانيكيه
تاريخ التخـرج: مارس 2005 م

يهدف هذا البحث الى دراسه خصائص انتقال الحراره داخل انبوب مستطيل المقطع يبرد بواسطه مصفوفه من المنافث المماسيه وذلك عن طريق التجارب العمليه. فالهواء الخارج من الفوهه يتم توجيهه على السطح الساخن ثم يخرج فى الاتجاه القطرى. تم دراسه تأثير توجيه المنفث والنسب البعديه للمجرى $5 \le H/d \le 9$ وايضا نسبه بعد المنفث عن السطح $4 \le S/d \le 8$ مع مصفوفه احاديه من المنافث ذات مسافات متساويه فيما بينها. كما تم دراسه تأثير رقم رينولد للسطح 1 و 2 فى حدود $5000 \le \mathrm{Re}_j \le 10000$ وللاسطح 2و 3 و 4 فى حدود $9300 \le \mathrm{Re}_j \le 18800$. وتأثير قطر الفوهه على توزيع انتقال الحراره تم دراسته ايضا لقطرين 0.5 و 1 سنتيميتر.

وقد اوضحت النتائج ان توجيه السريان يسبب حدوث سريان متقاطع يوثر بشكل كبير على توزيع قيمه رقم ناسلت على السطح. تزداد قيم رقم ناسلت مع زياده قيمه رقم رينولد للمنفث على طول سطح التبريد. وكذلك يتأثر قيمه رقم ناسلت تأثرا ملحوظا مع قيم النسبه البعديه للمجرى ونسبه مسافه الفوهه من السطح. تم الحصول على قيم النسب البعديه التى تعطى اعلى انتقال حراره على كل الاسطح وبالمثل تم الحصول على قيمه نسبه بعد المنفث عن السطح التى تعطى اعلى انتقال حراره على كل الاسطح. اكبر قيم لرقم ناسلت تم الحصول عليه لموضع السريان الذى يجعل السريان يخرج فى كلا الجهتين. تم تطوير علاقات رياضيه تعطى قيم رقم ناسلت المتوسطه كداله فى رقم رينولد للمنفث لجميع الاسطح.

درجة الماجستير
جامعة الملك فهد للبترول والمعادن
الظهران- المملكة العربية السعودية
مارس 2005 م

NOMENCLATURE

$A_{cp,i}$	Area of the copper plate [m^2]
d	Diameter of the orifice jet [m]
h_i	Local convective heat transfer co-efficient [W/m^2K]
H	Width of the feeding channel [m]
I	Current supplied to heater [Amp]
k_{air}	Thermal conductivity of air [W/m.K]
k_{wood}	Thermal conductivity of wood [W/m.K]
l	Length of the copper plate [m]
Nu	Local Nusselt number
Nu_{avg}	Average Nusselt number
Nu_s	Smooth tube average Nusselt number
$q^{"}$	Heat flux from the heater [W/m]
$Q_{cp,i}$	Heat input for each copper plate [W]
$Q_{actual,i}$	Actual heat released from target surface [W]
$Q_{cond,i}$	Heat lost due to conduction [W]
$Q_{rad,i}$	Heat lost due to radiation [W]
$Q_{total,i}$	Total heat input [W]
Re_j	Jet Reynolds number
R	Resistance of the heater [Ohms]
S	Jet-to-plate distance [m]
t	Thickness of wood block behind the heater [m]
T_{in}	Inlet temperature [ºC]
$T_{s,i}$	Surface temperature [ºC]
T_{surr}	Temperature of the surroundings [ºC]
T_w	Wood block temperature [ºC]
i	Index number for copper plate
U	Uncertainty

V	Voltage supplied to the heater
V_{avg}	Average velocity of all jets
w	Width of the copper plate
$\forall$	Volume flow rate
X	Distance in the x-direction

Subscript

cp	Copper plate
i	Index number for each copper plate
j	Jet
w	Wood

Greek

ε	Emissivity
σ	Stefan- Boltzman constant

CHAPTER 1

INTRODUCTION

1.1 General Introduction

Modern gas turbines operate at high temperatures (on the order of $1400^{o}C$) to achieve high thermal efficiency. The continuing trend toward higher inlet temperatures in gas turbine engine development has resulted in increasing heat loads to turbine components. The development of new materials as well as cooling schemes has seen the rapid growth of the turbine inlet temperature (firing temperature) leading to high turbine efficiencies. Operating gas turbines under such severe conditions causes high thermal stresses in the blade structure, oxidation, creep rupture and in extreme cases melting which results in reduced blade operation life. In general turbine blades, in order to withstand the higher inlet temperature of the turbines must either be made from similar materials or have superior cooling designs or both. No suitable material is presently available that can withstand the high level of thermal stress in a hot operating environment of turbines. Therefore, standard metal blades with special cooling techniques are used. Sophisticated external and internal cooling techniques for turbine blades are needed to prevent the blades from burning away. In a typical gas turbine, the blades are cooled with air from the air compressor.

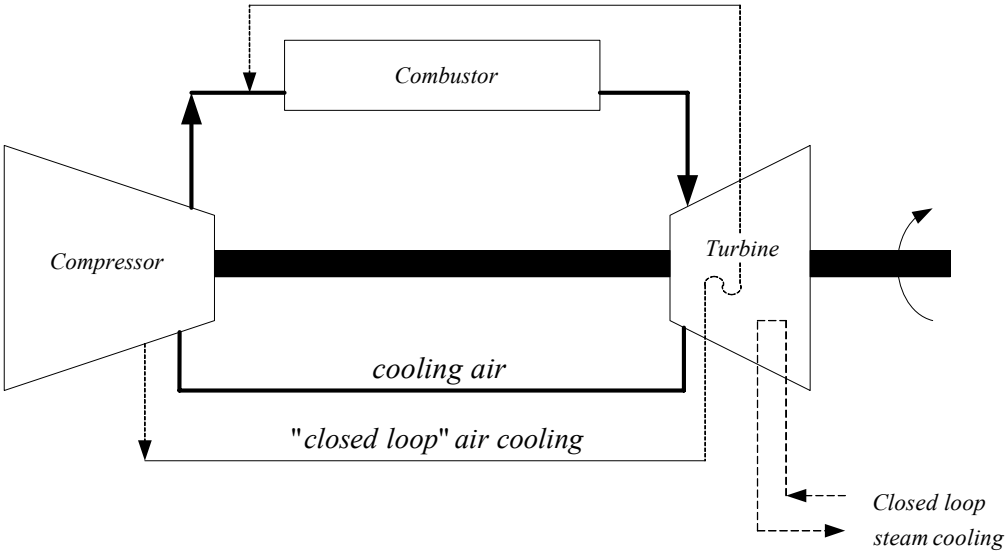

Figure 1.1 Schematic of a Gas turbine (Fred Thomas [46])

Recent advanced industrial gas turbines have been designed with so-called closed-loop blade cooling shown in figure 1.1, in which air, or even steam, are used for blade cooling and then routed to the combustor, in the case of air-cooled blades, or to a steam turbine, in the case of steam-cooled blades. In the case of cooling the cool air is bled from the compressor and is directed to the stator, the rotor, and other parts of the turbine rotor and casing to provide adequate cooling. The effect of coolant depends on the aerodynamics depends on the type of cooling involved, the mainstream temperature, the location and direction of coolant injection, and the amount of coolant being used. A number of these factors are being studied experimentally and numerically in the past few decades.

1.1.1 Types of Cooling

In high temperature gas turbines cooling systems need to be designed for turbine blades, vanes, end walls, shroud, and other components to meet metal temperature limits. Different types of air-cooling techniques are being employed in the past and are being used today. Major advances have been made in incorporating cooling in aircraft bas turbines. The air-cooling technique can be classified as follows

1. External cooling (For external stream temperature $> 1600\ ^{o}K$)
    a. Local film cooling
    b. Full-coverage film cooling
    c. Transpiration cooling
2. Internal cooling (For external stream temperatures of $1300 - 1600\ ^{o}K$)
    a. Convection cooling
    b. Impingement cooling

c. Internally air-cooled thermal barrier

1.1.2 Overview of a Turbine Blade

A typical turbine blade cooling arrangement is shown in figure 1.2. Non-uniform heat loads are generated along the blade surface when hot gases impinge on the blade. The coolant ($650^{o}C$) for the blades is air extracted from the compressor of the engine. Coolant passages of different geometry are constructed inside the blade. Jet impingement, convection, and pin fin cooling are widely used to remove excess heat loads from the blades as discussed above. Roughness elements such as ribs are widely used to augment heat transfer inside the coolant passages. Jet impingement cooling is widely used to augment the heat transfer inside the coolant passages. Jet impingement cooling is widely used from the leading edge to the mid-chord region of the blade, convection cooling is used in the mid-chord section, and pin fin cooling is used in the trailing edge region of the blade. Film cooling minimizes the heat from entering the blade surface. This is achieved by bleeding air from the coolant passages and ejecting the coolant into the mainstream flow. Air extracted from the compressor to cool turbine blades is expensive and ejection of coolant into the mainstream flow results in mixing pressure losses. Therefore, it is important to optimize the use of coolant and also efficiency design cooling schemes to reduce the thermal stresses in the blade structure and increase the overall efficiency of the gas turbine engine.

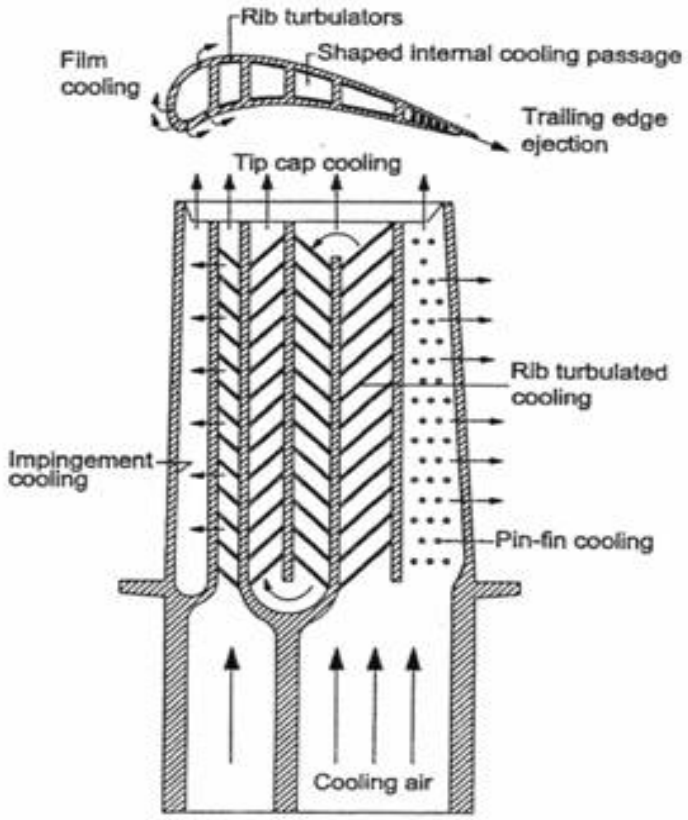

Figure 1.2 A typical turbine blade cooling arrangement

1.2 Jet Impingement

Impingement heat transfer is considered as a promising heat transfer enhancement technique. Jet impingement cooling systems have been used in advanced gas turbine engines, which operate at a high temperature $1300-1500^{o}C$ to improve thermal efficiency, and power output. Among all convection heat transfer enhancement methods, it provides significantly high local heat transfer coefficient. At the surface where a large amount of heat is to be removed /addition, this technique can be employed directly through very simple design involving a plenum chamber and orifices. The cooling air is blasted on the inner surface of the airfoil by high-velocity air jets, permitting an increased amount of heat to be transferred to the cooling air from the metal surface. For instance, in gas turbine cooling, jet impingement heat transfer is suitable for the leading edge of a rotor airfoil, where the thermal load is highest and a thicker cross-section enables accommodation of a coolant plenum and impingement holes. This cooling method can be restricted to desired sections of the airfoil to maintain even temperatures over the entire surface. For instance, the leading edge of the blade needs to be cooled more than the mid-chord section or trailing edge, so the gas is impinged. A major shortcoming of the convection cooling method is that this method does not always cool effectively the leading edge of the blade. This problem can, however, be improved by applying impingement cooling at the leading edge as show in figure 1.3. 'Impingement' means 'collision' that the coolant flow collides into the target surface and guarantees a thin stagnant boundary layer at the stagnant core for cold coolant contacting the hot surface without damping. Jet impingement cooling (or heating as well) is a very effective

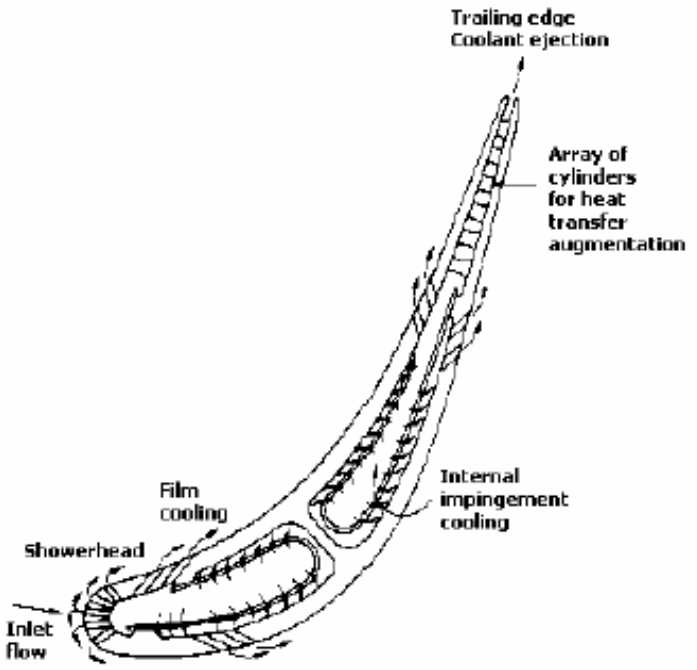

Figure 1.3 Schematic of impingement cooling arrangement in a first-stage turbine inlet guide vane.

heat transfer mechanism. The main reason is that jet impingement flow forms a very thin boundary layer.

In jet impingement technique the cooling air is forced radially through a center core of the blade, then turned perpendicular to the radial direction, and passed through a series of holes so that it impinges on the inside of the blade. This method is very effective locally and is well studied for the leading edge where the outside surface of the blade is approached by the impinging very hot gas.

This technique is also employed in turbine guide vanes (stators). Other applications for jet impingement could be combustor chamber wall, steam generators, ion thrusters, tempering of glass, electronic devices cooling and paper drying, etc.

Figure 1.3 illustrates how jet impingement cooling is employed in a vane airfoil. This is a typical jet impingement configuration for gas turbine vanes that consists with two chambers separated by a perforated wall. One chamber is pressurized with coolant air. Through the perforated wall, the opposite wall of the other chamber experiences impingement heat transfer effect. Typically, more than one heat transfer enhancement methods are used in the airfoils to protect it from being over-heated.

1.2.1 Literature review

This section presents an overview of the current knowledge of the flow and heat transfer of multiple impinging jet arrays. The hydrodynamics of multiple jet heat transfer are discussed in this section. The dependencies of the Nusselt number on geometrical parameters and the Reynolds number are discussed on the basis of non-dimensional correlations. Next, a short literature survey is presented on the category of rib roughened surfaces and the jet impingement mechanism.

The flow from impinging jets in an array has the same three flow regions as single impinging jets. However, there are some basic differences in the fluid mechanics of single and multiple jets. Two types of interactions that do not occur in single jets may influence the individual jets that make up a multi-jet system. First, there is possible interference between adjacent jets prior to their impingement on the surface. The likelihood of such interference effects is enhanced when the jets are closely spaced and when the distance between the nozzle and the impingement plate (nozzle-to-plate distance) is relatively large. Second, there is an interaction due to collision of wall jets associated with the adjacent impinged jets. These collisions are expected to be of increased importance when the jets are closely spaced, the nozzle-to-plate distance is small, and the jet velocity is high (Viskanta [43]).

Finally, the spatial arrangement of the nozzles in the array has an influence on the flow characteristics of multiple impinging jets. There are numerous possible spatial

arrangements of the nozzles in an array. Figure 1.4 shows the three most common arrangements for round nozzle arrays. The number of nearest neighbors of each nozzle and the impinged area per nozzle differ per arrangement. Therefore, the arrangement of the nozzles determines the way the jets interact with each other.

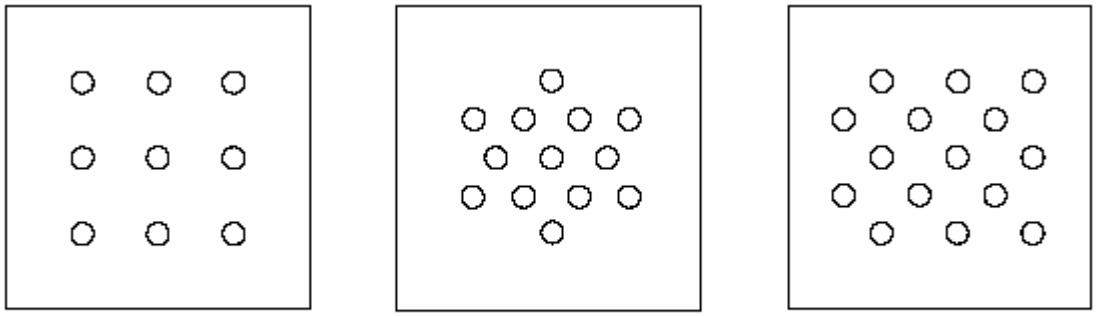

Figure 1.4 Three commonly used nozzle arrangements for impinging jet arrays.

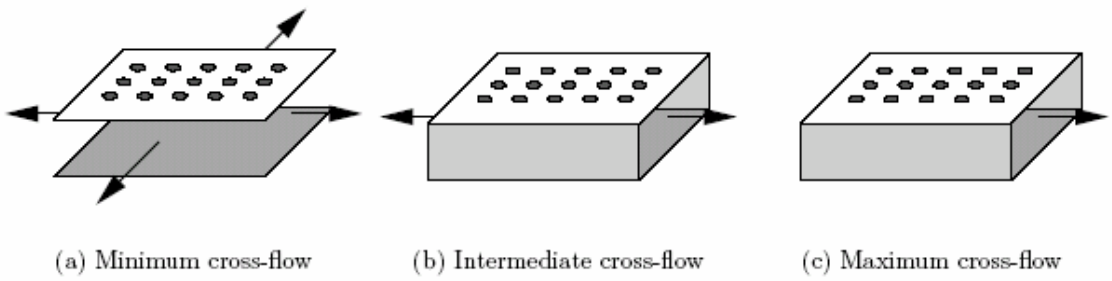

Figure 1.5 Definitions of the cross-flow schemes investigated by Obot and Trabold [37]

Many researchers have contributed their efforts towards better understanding of Impingement cooling. Studies on impingement heat transfer enhancement technique focused on single jet impingement and then expanded to impingement jet arrays. The cross-flow is another important parameter that affects jet impingement heat transfer performance. Cross-flow is the spent jet flow upstream of the local jet and reinforced by the local jet flow after its impingement. Strong cross-flow is a non-desirable factor in impingement heat transfers, because cross flow tends to push the impinging airflow downstream and dilutes the impinging jet intensity. However, for cross flow velocity less than 10% of the jet average velocity, the surface heat transfer is enhanced. For any impingement jet array situations, cross flow is inevitable. Some studies have shown how cross flow affects heat transfer. These studies presented correlations that account for regular arrays of impingement jet holes with low to moderate cross flow effect. Both correlations show monotonous decreases in Nusselt number with stronger cross flow.

Chupp et al [6] evaluated the heat transfer coefficient for impingement cooling on the leading edge of the turbine blade. They developed dimensionless empirical correlation, which predicts heat transfer for impingement cooling with cross flow, with fixed geometry and location and with the only variation of Reynolds number.

Metzger et al [36] studied the heat transfer characteristics for inline and staggered arrays of circular jets with crossflow of spent air. They had the same mass flow rate through each jet used for cooling. Heat transfer characteristics were presented based on the jet hole

diameter. Nusselt numbers are presented as a function of four geometric parameters; channel height (z/d), chordwise and spanwise hole spacing (x/d and y/d) and the hole pattern. For $1 \leq z/d \leq 3$, Nusselt numbers increase with channel height, for the same Reynolds number, for upstream and for downstream the reverse is true. They suggest that the effect on Nusselt number is more pronounced for the spanwise hole spacing. Nusselt numbers reach a minimum as far upstream as the second or third row of holes after which the values increase continuously. This possibility is significant since the implication of several prior studies of similar prior studies of similar flow configurations is that increasing the crossflow always tends to degrade the heat transfer performance.

Florschuetz et al, [13-14] performed experimental and theoretical investigations for stream wise distributions of jet and cross flow velocities and measured the heat transfer characteristics for inline and staggered arrays of circular jets impingement with initial cross flow. Their results show that the initial cross flow lowers the impinging heat transfer performance. As the initial cross flow rate increases, convective heat transfer will be more dominated by the cross flow. They presented the characteristics periodic variations as a function of geometric parameters, including the effect of hole pattern. They also presented correlations for both inline and staggered hole patterns with cross flow.

Bunker and Metzger [35] conducted an experimental study to evaluate the heat transfer coefficient in the leading edge region of a turbine blade with out film extraction. The various parameters covered in their study are jet Reynolds number, jet spacing and jet

travel distance. The conclusions given by them are the heat transfer increase is by decreasing the leading edge sharpness and by less jet travel distance, further conclusions are, the less jet spacing induces high span wise heat transfer coefficient.

Goldstein and Behbahani [16] measured the heat transfer to an impinging air jet with and without cross flow of air. The heat transfer co-efficient measurements were made for a circular jet with a jet to plate spacing of 6 and 12 diameters in the presence of crossflow of 8.5m/s and 16.5m/s. The results specify that, at large jet-to-plate spacing the cross flow diminish the peak heat transfer coefficient; at a smaller spacing cross flow increases the peak heat transfer coefficient.

Huber and Viskanta [22] studied the effect of axisymmetric air jet arrays with spent air exits located between the jets. The conclusions made by them are the decrease in jet spacing causes less jet interference before impingement and the heat transfer coefficients are same for single and array type jets. To maintain a uniform heat transfer over the entire surface covered by a jet array the spent air exits are mandatory.

Huber and Viskanta [23] studied the heat transfer from the target plate perimeter and center jet impingement in a confined impinging array of axisymmetric air jets. The results of their study were the wall jets for the perimeter orifices have high rates of heat transfer where as the centre jets having a resistance from the surrounding orifices do not have comparatively

high heat transfer. The difference between the heat transfer rates for the centre and perimeter jets were resulted to be less than 12 %.

Huang et al [21] experimentally investigated the detailed heat transfer coefficient distributions under an array of impinging inline jets under three different cross flow directions using the transient liquid crystal technique. They had 12 rows of 4 circular holes on the orifice plate and the distance between the jet orifice plate and the impingement target surface was set to three times the diameter of the jet hole. They studied the Nusselt number distribution for Reynolds numbers 4800, 9550, 12800 and 18300. The results discussed by them are, when the spent flow has an opposite direction to incoming flow, Nusselt number peak occurs at leading section of the heat transfer target wall. When spent flow has the same direction as the incoming flow, the Nusselt number at the trailing part will be slightly higher than the leading part, but with an overall performance of 40% lower. One more important conclusion given by them is when both directions are allowed for spent air removal; Nusselt number is uniformly high, and this case is said to be the best case. They have successfully correlated the overall average Nusselt number with Reynolds number.

Hollworth and Dagan [20] conducted experiments on geometry by removing spent airflow right after impinging in order to reduce the cross flow. They drilled holes on the target plate at the same position with impingement jet holes and the positions in between. The tests conducted by them for both inline arrangements and for staggered arrangements, the latter always yielded higher average heat transfer. They reported 20-30% higher heat transfer rate compared with side venting case. Ekkad [12] also studied a jet impingement

plate with holes to reduce cross-flow effect. They saw that the presence of holes on target surface increases overall heat transfer

1.2.1.1 Effect of nozzle-to-plate distance

It appears that multiple jet arrays with low values of H/D produce high area-averaged heat transfer coefficients. Metzger et al. [35] found a maximum average Nusselt number at $H/D = 1.0$, for values of the pitch between 1.67 and 6.67. Huber and Viskanta [23] explain that the major degradation of the heat transfer coefficient for the jets in an array is due to adjacent jet interactions, which occur before impingement. These interactions increase the decay of the jet velocity and the entrainment of surrounding air (see also Kataoka [29]). At smaller separation distances, adjacent jet interactions are strongly reduced due to the smaller distance for the interactions to occur.

Gardon and Cobonpue [15] have found a correlation of the form

$$Nu_{avg} = 0.993\ \mathrm{Re}^{0.625}\ (H/D)^{-0.625}\ (S/D)^{-0.375} \qquad \ldots (2.4)$$

Where Nu_{avg} is the area averaged Nusselt number. The H/D dependence is strong, due to the interaction between adjacent jets.

1.2.1.2 Effect of cross-flow

Obot and Trabold [37] have investigated the influence of cross-flow on multiple impinging jet heat transfer. Three cross-flow schemes, named minimum, intermediate, and maximum cross-flow, were investigated. The definition of these schemes is shown in figure

1.5. Obot and Trabold [37] found that cross-flow lowers heat transfer coefficients, because spent fluid from upstream jets in an array can sweep away the downstream jets and delay impingement. Additionally, they found that the magnitude of this effect increases with increasing nozzle-to-plate distance. The parameters α_1, α_2, and α_3 in the non-dimensional correlation

$$Nu_{avg} = \alpha_1 \, \mathrm{Re}^{0.8} \, (H/D)^{\alpha_2} \, (S/D)^{\alpha_3} \qquad \ldots (2.6)$$

are dependent on the cross-flow scheme used. The values of α_3 could be stated as 0.815, 0.676, and 0.595 for minimum, intermediate, and maximum cross-flow, respectively. The value of α_2 depends on the pitch and the cross-flow scheme used. The exponent is more negative for strong cross-flow and small values of the pitch. Matsumoto et al. [34] investigated heat transfer from an impinging jet array with the same cross-flow schemes. Their results agree well with the theory of Obot and Trabold [37].

Hwang et al [25] experimentally investigated the effect of outflow orientation on heat transfer and pressure drop characteristics in a triangular duct cooled by array of tangential jets using the transient liquid crystal technique. Three different outflow orientations were studied similar to Huang et al [21]. They used higher range of Reynolds numbers, $12600 \leq Re \leq 42000$ for this study. For the outflow orientations of the spent air flowing in the same direction of incoming flow and in the opposite direction of incoming flow, jet flow rate increases with the axial distance and the high jet flow rate near the downstream end is

induced by the significant crossflow of low static pressure. They describe that the case for the outflow in both directions has a uniform jet flow rate because of the less crossflow. They suggest that among all the three cases, the case with the outflow in both directions has moderate pressure loss. They developed empirical correlation for Nusselt number in terms of Reynolds number for three different outflow orientations for the first time.

Hwang et al [26] carried out an experimental investigation on the jet spacing effect on the Impingement heat transfer in a triangular duct with a tangential jet array using the transient liquid crystal technique. Their test section and outflow orientations are similar to that of Hwang et al [25]. They studied the effect of jet Reynolds number ($3000 \leq Re \leq 12600$) and jet spacing ($1.5 \leq s/d \leq 6.0$). They stated that with the same jet velocity, decreasing the jet spacing increases the local heat transfer coefficient and for the same flow rate, reducing the jet spacing reduces the heat transfer enhancement near the leading-edge apex. They also stated that as the Reynolds number is increased the heat transfer on both the walls of the triangular duct increases.

Pramanick et al [39] carried the detailed numerical analysis on flow predictions in a two-pass channel connected by one or two holes on the divider walls with heat transfer enhancement by impingement and swirl. They replaced the conventional design with 180° U-bend by the divider plate with series of straight and angled circular holes. Two configurations studied by them had one and two rows of 12 holes equally spaced axially. The analysis was presented for Reynolds number equal to 25000. The enhanced cooling as said by them was

obtained by the combination of impingement and cross-flow induced swirl. They also described that the production if impingement inside such channels with additional swirl generation provides high velocity air to contact the hot surfaces of the channels and removes heat more effectively than traditional rib turbulator channel.

1.3 Motivation to investigate

Many researchers, so far, have studied internal forced convection cooling of a gas turbine rotor blade. They focused mainly on the effects of Reynolds number and the internal geometry of the heat transfer surface and pressure drop in the uniformly heated square and rectangular channels. Moreover concentration of many researchers was on the rectangular channel separated by an orifice plate with number of arrays of jets to cool the leading edge region of a gas turbine blade. All the studies showed that there is good amount of heat transfer with this kind of an arrangement. However, with the advancement of gas turbine technology, it became necessary to focus on the regions exposed to the most severe thermal conditions, leading and trailing edge regions as shown in figure 1.2 in the Introduction chapter. In particular, the leading edge region, due to the exposure to high temperatures and a thicker cross-section of this portion of the blade can suitably accommodate for impingement cooling. Jet impingement mechanism is commonly used to cool the leading edge region. Apart from impingement, crossflow is also of great significance in this process of cooling. The outflow openings cause different types of crossflow, which leads to the heat transfer enhancement. Normally in the previous studies, a multiple array of jets were used for cooling process, using this kind of arrangement of multiple arrays causes a huge amount of pressure drop across the impingement orifice plate. The heat transfer characteristics were presented

with this kind of an orifice plate arrangement. To accomplish/attain the least pressure drop across the orifice plate, which leads to an increase in the velocity and thus the heat transfer, an orifice plate with a single array of equally spaced jets was used. This orifice plate is being used to study the jet impingement heat transfer characteristics on a heated target surface with the crossflow generated by different outflow orientations.

The ability to numerically predict the effects of crossflow on the flow field and heat transfer, either in stationary or a rotating frame is limited. Therefore many experimental investigations have been conducted in order to determine those configurations which produce the optimum results in terms of both heat transfer and pressure drop.

1.4 Objective of the present study

In the present experimental work for the first time, the effect of feeding channel width on the heated target surface is being investigated with the combined effect of three different outflow orientations and the impingement channel width. In the present study we have studied the heat transfer characteristics of the heated target surface using the single array of impinging jets. Three different orifice plate configurations are being studied namely centerline, staggered and tangential arrangement.

The purpose of the present work is to study the effect of the outflow orientation and feeding channel width on the heat transfer characteristics of the impingement heated target surface using a single array of equally spaced jets on a orifice plate in a rectangular duct. Moreover, the effects of jet-to-plate spacing $4 \le S/d \le 8$ and the feeding channel width $5 \le H/d \le 9$ on the heat transfer characteristics are also studied. Three different outflow orientations are being studied to get different crossflow effects i.e., the exit flow

Case - 1 (Coincident with the entry flow),

Case - 2 (Opposing to the entry flow),

Case - 3 (Passes out in both the directions).

Tests were conducted with two orifice plates having jet size of diameter 0.5 and 1 cm. The heat transfer characteristics are being studied by varying the jet Reynolds number in the following range of $5000 \le \mathrm{Re}_j \le 10000$ for orifice plate 1 and 2 and $9300 \le \mathrm{Re}_j \le 18800$ for orifice plate 2, 3 and 4 by applying the constant heat flux to the target surface.

CHAPTER 2

EXPERIMENTAL SETUP AND PROCEDURE

The experimental apparatus and methods followed are described in detail in the section below. The turbine blade-cooling channel was modeled by a rectangular channel with two channels separated by an orifice plate consisting of an array of equally spaced orifice jets to cause a jet-impingement setup.

2.1 General set-up and Apparatus

The schematic of the experimental facility is depicted in figure 2.1. The test rig used to study the heat transfer characteristics was manufactured using Plexi-glass. The test section consists of two channels, impingement channel (10) and the feeding channel (9). Air enters the test section in the feeding channel and is directed onto the heated copper plates in the impingement channel to study the heat transfer characteristics. The target plates made of copper were heated using a constant flux heater, which was controlled by a variable resistance transformer. The other side of the heater was insulated to get the heat transferred only in one direction i.e. onto copper plates. The mass flow rate of the compressed air (1) entering the test section was passed through a settling chamber (2) and was controlled with the help of valves (3) and the pressure regulators (5). The pressure drop across pressure regulators was measured using the pressure gauges (4).

Gas flow meters (7) were used to measure the mass flow rate entering the test rig, which were protected by the air filters (6) of 50μ capacities. The average surface temperature of each of the copper plates was determined from the readings of two T-type thermocouples installed in the grooves drilled at the back surface of the plates to within 1 mm of the surface; the analog signals generated by these temperature sensors were transmitted to the signal-conditioning unit (12), where they were selectively processed (the following operations were performed on the signals generated by the thermocouples: linearization, cold junction compensation, amplification). The resulting analog signals were converted into digital signals by a DAQ card installed on the motherboard of a personal computer and recorded with an application developed in Lab VIEW.

The supply pressure was regulated by a pressure gauge fixed after the settling chamber at the entrance. The entrance pressure and mass flow rate to the test section was regulated by a pressure reducer valve mounted after the first pressure gauge, the second pressure gauge was used to measure the inlet pressure supply to the test section. There upon air was passed through a set of air filters of 50μ capacities to make sure complete dry air passes to the test section. The airflow rate was measured using the mass flow rate-measuring device fixed after the air filters.

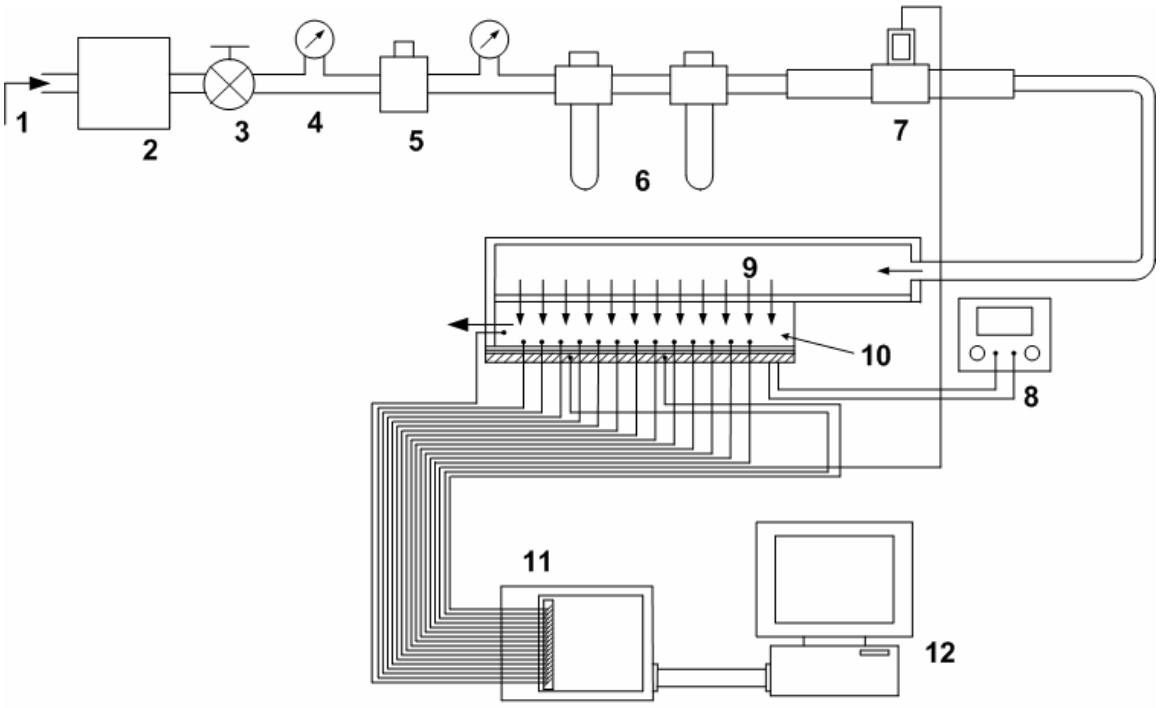

1. Compressed air supply
2. Settling chamber
3. Valve
4. Pressure gauges
5. Pressure reducer valve
6. Air filters
7. Digital Mass flow rate meter
8. AC power transformer
9. Feeding channel
10. Impingement channel
11. Data acquisition system
12. Monitoring personal computer

Figure 2.1 Schematic of the test section.

2.1.1 Construction details

Plexiglas was used in the construction of the test section and orifice plate 1cm in size throughout. Plexiglas is a good choice of material for the following reasons.

1. It is very smooth, reducing anomalous flow behavior, thereby reducing the number of variables affecting the analysis.
2. It is easier to machine. Metal would be smoother and would hold better accuracy in sizing, but was conductive.
3. It is very easy to glue acrylic parts together.
4. It gives transparent, facilitating observation and various measurements.

The length of the test section is 106.54 cm. The width of the feeding channel is considered as H, and the width of the impingement channel is taken as S. The jet plate geometry was chosen with reference to the previous studies. As discussed above copper plates were glued upon the heater, which was glued to the wood material to get one dimensional heat transfer from the heater. Two T-type thermocouples were fixed inside the wooden plate upon which the copper plates were glued, on the other side, to measure the heat being lost by conduction from the copper plates. The top and bottom plates of the test section, made from Plexi-glass, were fastened to the wooden bars with the help of nuts and bolts. To avoid the leakage from this joint, between the wooden plate and the Plexi-glass sheet, proper care was taken by using a rubber insulation of thickness 3 mm. This insulation provided good bonding, without glue, between the wood and the Plexiglas material to avoid

the leakage of the air supply in the test section. A provision to move the copper plates' assembly was given in the top and bottom faceplates by providing grooves to adjust the assembly to an appropriate distance as desired.

The feeding channel aspect ratio was controlled by placing plates made of Plexiglas. Three plates of thickness 1 cm each were used to control the aspect ratio of the feeding channel. Plates were used as per the size requirements of the feeding channel. These plates were fastened to the other wooden piece of the test section, with the help of nuts and bolts. The leaks from the feeding channel were also controlled in the same manner as discussed above in the impingement channel. The plates used to control the aspect ratio of the feeding channel were short in size compared to the length of the test section, so as to have less disturbance of the incoming air.

A leak test was then performed. This consisted of letting airflow at or above maximum pressure, and squirting soapy water onto all areas where air leaks might occur. Even a small leak could produce a noticeable soap bubble. After the model dried, the leaks were sealed by applying silicone. This process was repeated until no leaks were found (usually after the second leak test).

2.1.2 Test section

Figure 2.2 shows the three-dimensional sketch of the test section. The test section as mentioned above consists of two channels, impingement channel and the feeding channel. It consists of two compartments joined by the orifice plate, which has a single array of equally spaced jets. The jet orifice plate thickness is taken equal to the jet diameter. There are 13

circular jets drilled on the orifice plate. The jet-to-jet spacing is twice the jet-hole diameter, measure between the centers of the two consecutive jets. The length of the test section is 106.54 cm. The width of the feeding channel is considered as H, and the width of the impingement channel is taken as S. The jet plate geometry was chosen with reference to the previous studies. The test section is made of Plexiglas material. The impingement target surface constitutes a series of copper plates, each with 4.1 × 4.2 cm in size, arranged in accordance with the orifice jets, such that the impingement jet hits the geometric center of the copper plate. The copper plates are separated from each other by 1 mm distance to avoid the relative heat conduction between each other, thus dividing the target surface into segments. The thickness of the copper plate is 0.5 cm.

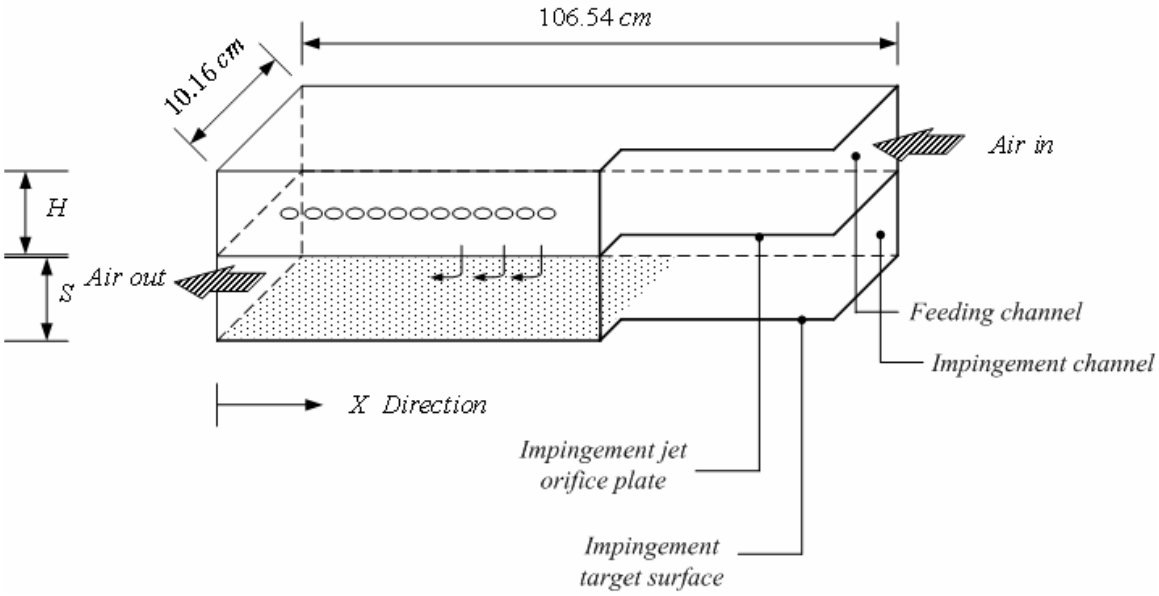

Figure 2.2 Three-dimensional view of the test section for case 1.

2.1.3 Outflow orientation

Figure 2.3 shows the schematic of the three different exit outflow orientations, which are obtained by changing the discharge openings. The upper chamber is called as the Feeding channel and the lower chamber in which the jets impinge on the target surface is the impingement channel. The flow develops in the open area provided in the feeding channel before entering the jets. The exit of jets in three different outflow orientations from the impingement channel creates different crossflow effects. The three different outflow orientations are represented with case numbers as shown in the figure 2.3.

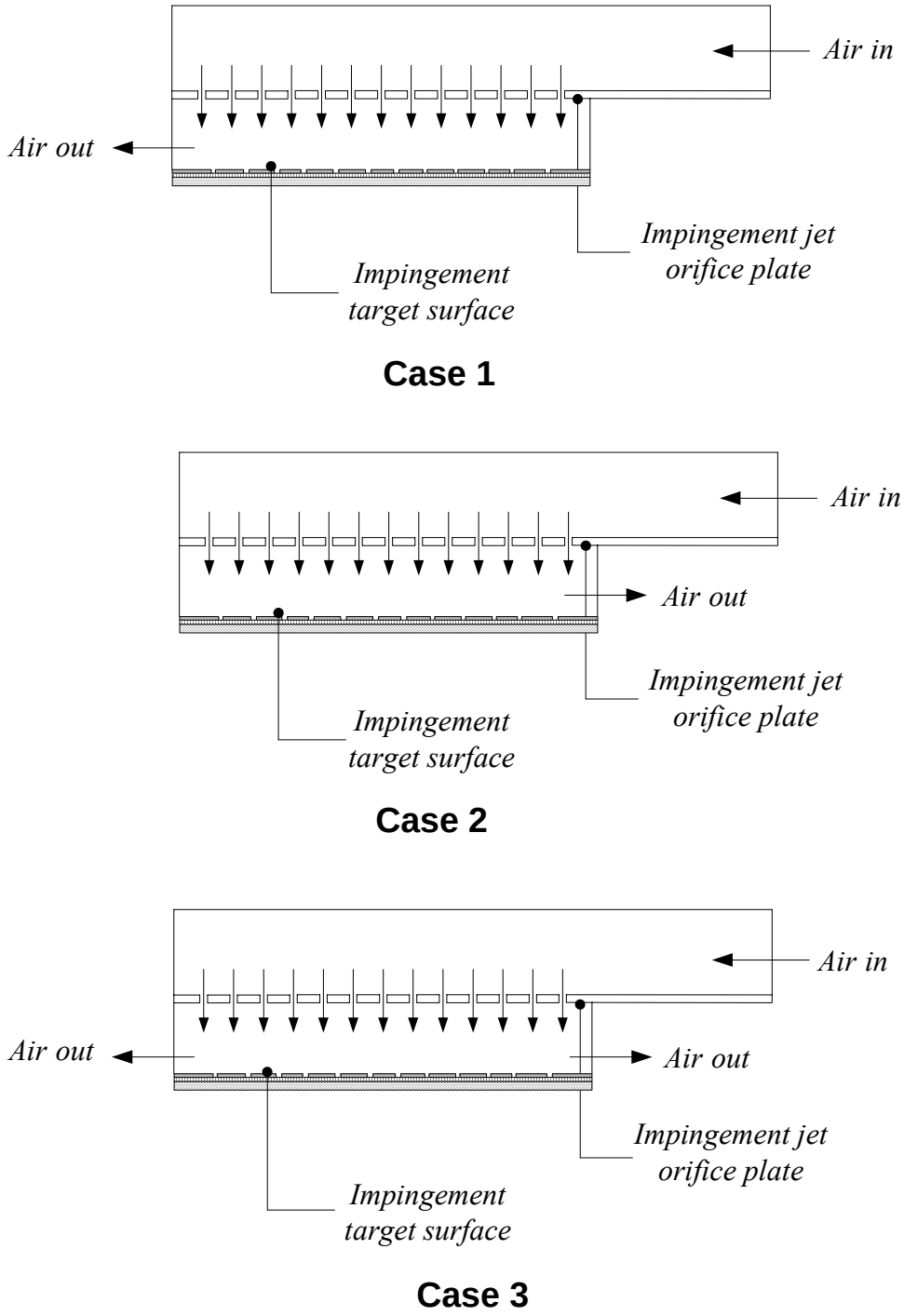

Figure 2.3 Illustration of three exit outflow orientations.

2.1.4 Orifice plates

Four different orifice plate geometries were taken in the present study. As shown in the figure 2.4, one plate was taken with orifice jets of diameter 1 cm and the other three plates were manufactured with the orifice jet size of 0.5 cm. The orifice plates were also manufactured from the Plexiglas material. Each plate has 13 holes of similar diameter of jets equally spaced. The distance between the two consecutive orifice plates is 2 times the orifice jet diameter for orifice jet of size $d = 1cm$ whereas it is 4 times the orifice jet diameter for orifice jet of size $d = 0.5cm$. Similarly the thickness of orifice plates is equal to the diameter of the jet for orifice jet of size $d = 1cm$, whereas it is equal to twice the diameter of the orifice jet for orifice jet diameter of size $d = 0.5cm$.

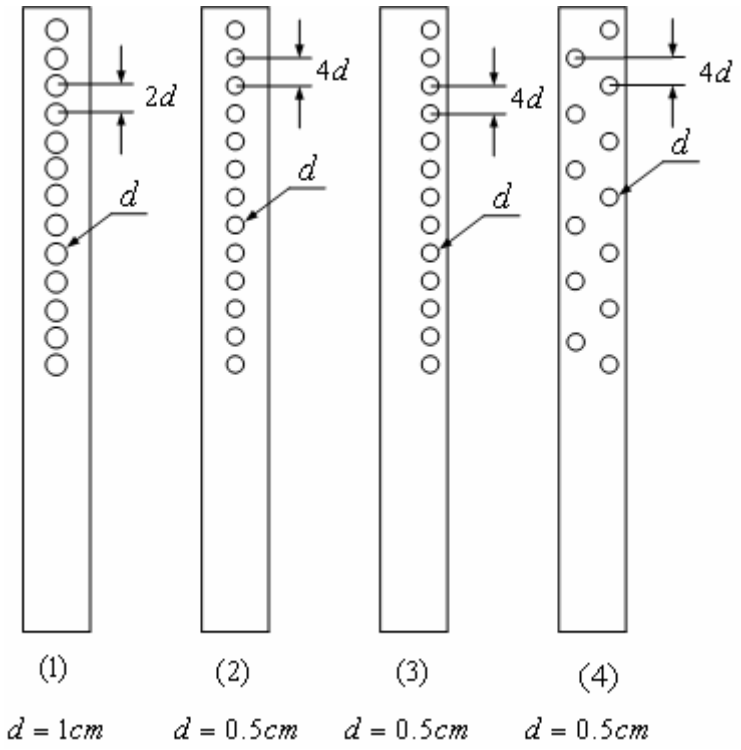

Figure 2.4 Orifice plate orientations considered in this study

2.1.5 Instrumentation and Data Acquisition

Instruments used in the current experimental investigation are being listed in table 2.1. The temperature of the copper plates was measured using the T-type thermocouples. The thermocouples beads were in contact with the copper plate in a groove prepared at the back. Temperature of each plate was monitored with two thermocouples mounted at the back. Thus the temperature of the plate was taken as the average of the two readings. Figure 2.5 shows the arrangement of the thermocouples mounted at the back of the copper plates. They are fixed in a groove of 2.5 mm thick, care was taken that the thermocouple bead touches the copper plate and is not left in air in the groove. The thermocouple was fixed to the copper plate with the help of epoxy glue.

The thermocouple wires were 0.01” in diameter and were covered with 0.006” thick Teflon insulation. All the 13 plates were fixed with same T-type thermocouples mounted at the back in a groove. The other end of the thermocouples were connected to the terminal block that allowed the transmission of data to the Data acquisition system.

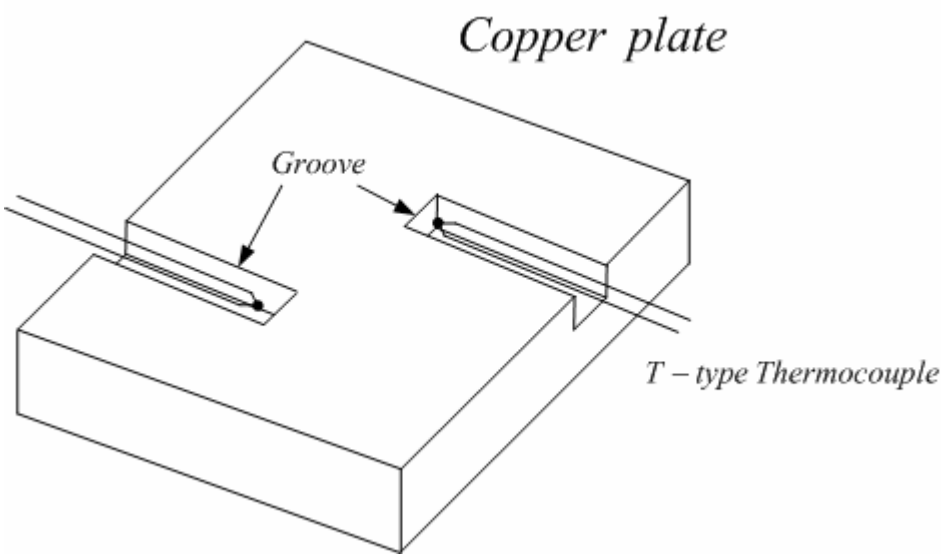

Figure 2.5 Illustration of thermocouples mounted in a groove at the back of a copper plate.

Table 2.1 Instrumentation and software used for Data acquisition

	Characteristics	**Manufacturer**
FMA – 1600 mass flow meter	Accuracy: +1%	Omega
SCXI - 1000 chassis	-	National Instruments
SCXI - 1380 high accuracy isothermal terminal block	Accuracy: +0.5%	National Instruments
SCXI - 1100 32-channel isolated analog input module	Offset error +1.5mV/gain, gain error: +0.03%	National Instruments
Lab VIEW 7.0	-	National Instruments
SAI - T thermocouples	Accuracy: 0.3%	Omega

The data signals from the thermocouples were sent to a National Instruments SCXI (Signal Conditioning eXtensions for Instrumentation) signal-conditioning module. The conditioned signals were sent to a data-acquisition (DAQ) card mounted in a Dell Personal computer. The signals were read into the computer using the National Instruments LabVIEW (Laboratory Virtual Instruments Engineering Workbench) instrument and analysis software. A T-type virtual instrument (VI) feature in LabVIEW was used to convert the voltage signals to pressures and flows.

A program written using the LabVIEW software enabled continuous readout of the experimental data. The data was displayed on the computer screen in a virtual instrument format configured especially for the experiment. This program records the data continuously with the specified interval of time. Figure 2.6 shows the LabVIEW program that is being used in the current study. The user could write the data continuously from the virtual instrument to a log file upon a command. Flow levels were set manually using a digital flow meter in combination with a control valve and were monitored by the LabVIEW program. Current supply to the heater fixed at the back of the copper plates, used to heat at constant heat flux, was controlled by the user through a AC power transformer (variable resistance transformer) and displayed along with the other data. The resistance of the heater was measured with the multi-purpose meter manufactured by Omega^{R}. Mass flow rate of the air coming into the test section was measured using the Digital mass flow meters manufactured by Omega^{R}. The instrument was already calibrated by the manufacturer, but to make sure the calibration is correct the instrument was recalibrated.

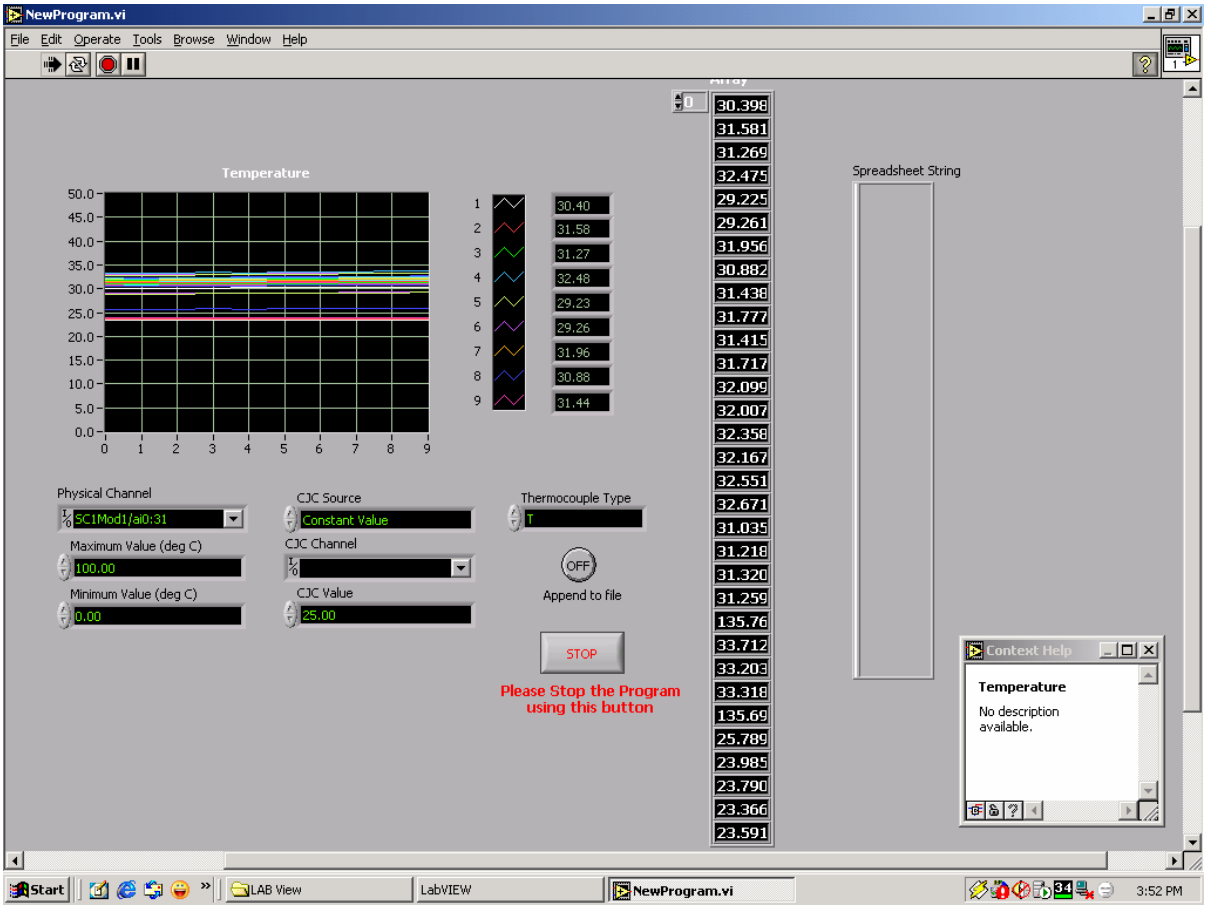

Figure 2.6 Photograph of the program being used

2.2 Data Reduction

2.2.1 Reynolds number calculations

Average velocity of all the orifice jets is calculated using the following expression with total area taken as the summation of areas of all the 13 jets on the orifice plate

$$V_{avg} = \frac{\forall}{A_{tot}} = \frac{\forall}{\sum_{i=1}^{13} A_i} = \frac{\forall}{\sum_{i=1}^{13} \frac{\pi}{4} d^2} \tag{2.1}$$

Where A_i – Area of the jet

$\forall$ – Volume flow rate of the fluid entering the test section.

The Jet Reynolds number is calculated using the formula

$$\mathrm{Re}_j = \frac{\rho V_{avg} d}{\mu} \tag{2.2}$$

The data reduction equation for the jet Reynolds number is taken as:

$$\mathrm{Re} = \frac{\rho V_{avg} d}{\mu} = \frac{\rho d}{\mu} \frac{\forall}{13 \times \frac{\pi}{4} d^2} \tag{2.3}$$

2.2.2 Nusselt number calculations

The area of each plate is calculated by:

$$A_{cp} = l \times w \tag{2.4}$$

The total area of all the 13 plates is calculated using the expression:

$$A_{cp,total} = A_{cp,1} + A_{cp,2} + ... + A_{cp,13} \tag{2.5}$$

The total power input to all the copper plates was computed using the voltage and current the former being measured across the heater.

$$Q_{total} = \frac{V^2}{R} = VI \tag{2.6}$$

The heat flux supplied to each copper plate is calculated using

$$q^{"} = \frac{Q_{total}}{A_{total}} \tag{2.7}$$

The heater gives the constant heat flux for each copper plate. The heat supplied to each copper plate from the heater is calculated using the following procedure

$$Q_i = q^{"} \times A_{cp,i} \tag{2.8}$$

Where, i - the index number for each copper plate.

The heat lost by conduction through the wood and to the surrounding by radiation is depicted in figure 4 and is estimated using the following equations for each plate.

$$Q_{cond,i} = k_{wood}\ A_{cp,i}\ \frac{(T_{s,i} - T_w)}{t} \tag{2.9}$$

$$Q_{rad,i} = \varepsilon \sigma A_{cp,i}\ (T_{s,i}^4 - T_{surr}^4) \tag{2.10}$$

The actual heat supplied to each copper plate is found by deducting the losses from the total heat supplied to the heater.

$$Q_{actual,i} = Q_{cp,i} - (Q_{cond,i} + Q_{rad,i}) \tag{2.11}$$

The local convective heat transfer coefficient for each of the copper plate is calculated using

$$h_i = \frac{Q_{actual,i}}{A_{cp,i}(T_{s,i} - T_{in})} \tag{2.12}$$

The average temperature of the heated target surface $T_{s,i}$ is obtained as the average of the readings of the two thermocouples fixed in each copper plate. To calculate h, T_{in} was considered instead of the bulk temperature or the reference temperature. Based on the literature available, Obot and Trabold [37] discussed that the heat transfer coefficients do not exceed 10% with the adiabatic wall or the reference temperature T_R to replace the inlet temperature T_{in} in heat transfer coefficient equation above. In principle, T_R should be the average recovery temperature measured at the target surface at actual crossflow temperature, but it is difficult to measure in practical experiment. Therefore, in the present paper, the inlet temperature of the air is used as the reference temperature. It is measured at the test section inlet, where the air first enters the feeding channel.

The data reduction equation for the convective heat transfer coefficient is considered along with the heat losses by conduction and radiation.

$$h_i = \frac{Q_{actual,i}}{A_{cp,i}\,(T_{s,i} - T_{in})} = \frac{Q_i - (Q_{cond,i} + Q_{rad,i})}{A_{cp,1}\,(T_{s,i} - T_{in})} = \frac{\dfrac{V^2}{R\,A_{total}} - \dfrac{k_w}{t}(T_{s,i} - T_{in}) - \varepsilon\sigma(T_{s,i}^4 - T_{in}^4)}{(T_{s,i} - T_{in})} \tag{2.13}$$

The non-dimensional heat transfer coefficient on the impingement target surface is represented by Nusselt number as, with the hydraulic diameter is taken as the diameter of the orifice jet.

$$Nu_i = \frac{h_i\, d}{k_{air}} \tag{2.14}$$

The data reduction equation for the Nusselt number is considered along with the heat losses by conduction and radiation.

$$Nu_i = \frac{d}{k_{air}} \left(\frac{\frac{V^2}{R\, A_{total}} - \frac{k_w}{t}(T_{s,i} - T_{in}) - \varepsilon\sigma(T_{s,i}^4 - T_{in}^4)}{(T_{s,i} - T_{in})} \right) \tag{2.15}$$

2.3 Procedure

Tests were carried out using all the orifice plates. For orifice plate 1 and 2 the tests were carried out with the jet Reynolds number ranging between $(5000 \le \mathrm{Re}_j \le 10000)$ and for orifice plates 2, 3 and 4 the jet Reynolds number were ranged between $(9300 \le \mathrm{Re}_j \le 18800)$ for a constant heat flux power input. The procedure followed during the experiment is as follows. Initially the mass flow rate was adjusted to the required value for the experiment to be conducted and the air is blown continuously into the test section. Heat was supplied to the copper plates with electric resistive constant flux heaters (manufactured by Omega^R) from backside to provide uniform heat flux. The temperature of the copper plates was measured by two thermocouples mounted in a groove of 2.5 mm on the back of the copper plates. Thus the temperature of a particular plate is taken as the average of the reading of two thermocouples. One thermocouple is respectively fixed at the inlet and two at the outlet to monitor the flow temperature. The temperatures of the copper plates,

pressure, temperature of the air at the inlet, the mass flow rate of the air were continuously monitored. After the temperature of the copper plates reaches the steady state condition, all the data was collected with Lab VIEW program. The Nusselt number was then calculated based upon the collected data. The same procedure was repeated for the three outflow orientations described in figure 3, with all the jet-to-plate distances $(4 \le S/d \le 8)$ and feeding channel aspect ratio $(5 \le H/d \le 9)$.

CHAPTER 3

UNCERTAINITY ANALYSIS

3.1 Introduction

An uncertainty analysis provides a powerful design tool for evaluating different measurement systems and methods and for reporting measured data. It is a principal tool used during the development of a test plan. In this chapter, a systematic approach to identifying and quantifying errors that is used during the design, execution, and interpretation of tests is presented.

As we know from our past knowledge that the measurement is the process of assigning a value to a physical variable. The error in the measurement is simply the difference between the true value of the variable and the value assigned by our measurement. However, in any instrument, the true value is not known. Thus instead of the actual error, we estimate the probable error in the measurement, called the uncertainty. Decreasing in the range of the uncertainty means a more accurate result. It defines the interval about the measured value within which we suspect the true value must fall. It is the process of identifying and quantifying errors that is called uncertainty analysis.

3.2 Measurement Errors

Although no general discussion of errors can be complete in listing the elements contributing to error in a particular measurement. In the discussion below errors are grouped into two very general categories (Figliola, R.S. [47])

1. Bias error
2. Precision error.

In general, the classification of an error element as containing bias error, precision error, or both can be simplified by considering the methods used to quantify the error. Treat an error as a precision error if it can be statistically estimated in some manner; otherwise treat the error as a bias error. If we consider the repeated measurement of a variable under conditions that are expected to produce the same value of the measured variable. The relationship between the true value and the measured data set, containing both bias and precision errors, is illustrated in figure 3.1.

The total error in a single measurement is the sum of the bias and the precision errors in that measurement. The total error contained in a set of measurements obtained under seemingly fixed conditions can be described by an average bias error and a statistical estimate of the precision errors in the measurements. Within a sample of many measurements:

i. The bias errors will shift the sample mean away from the true mean of the measured variable by a fixed amount.

ii. The precision errors bring about a normal distribution of measured values about the sample mean.

Because accuracy deals with the difference between the true value and the measured value, an accurate measurement has both small bias and precision errors.

The best estimate of the true value sought in a measurement is provided by its sample mean value and the uncertainty (P%) in that value:

$$x' = \bar{x} \pm u_x \quad (P\%) \tag{3.1}$$

Uncertainty is the method used to quantify the u_x term.

The following *assumptions* are implicit in an uncertainty analysis:

1. The test objectives are known.
2. The measurement itself is a clearly defined process in which all known calibration corrections for basis error have already been applied.
3. Data are obtained under fixed operating conditions.

It is expected that the user of the equipment have some experiences with the system components.

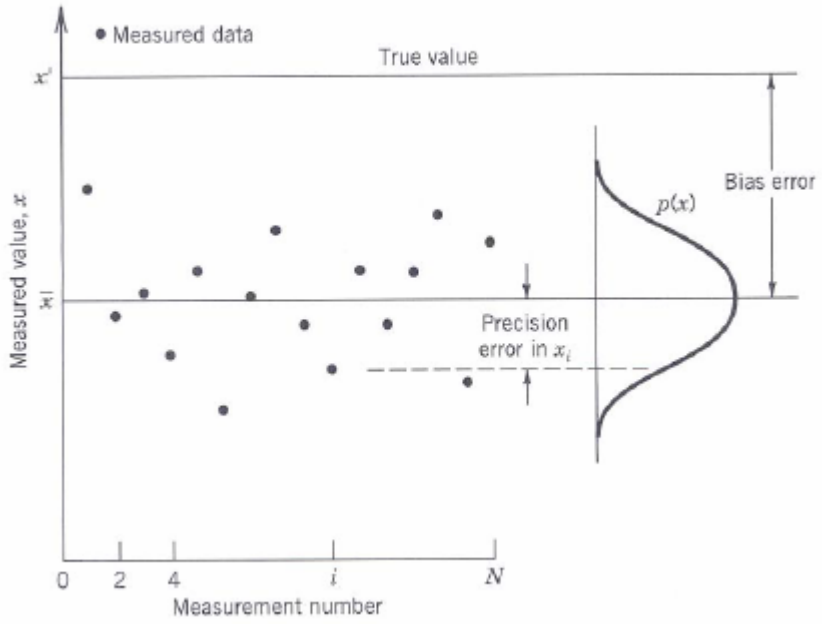

Figure 3.1, Distribution of errors upon repeated measurements (Figliola, R.S. [47])

3.3 Uncertainty Evaluation Procedure

Uncertainty analysis equations used in the current experimental work are taken from Coleman and Steele [7], which includes the precision, bias, and the resultant uncertainty. It is stated by the authors that the bias errors are often neglected in books and articles on error analysis or uncertainty analysis by a simple assumption that "*all bias errors have been eliminated by calibration*". Therefore we consider the precision uncertainty only to calculate the amount of uncertainty in the current experimental investigation.

The method for performing the uncertainty analysis used in the present experimental investigation is taken from Taylor B.N. [45] The theory for the current uncertainty analysis is summarized in detail in the following discussion.

In many cases a dependent variable y is not measured directly, but is determined from N other quantities $x_1, x_2, x_3, ..., x_N$ through a functional relation f

$$y = f(x_1, x_2, x_3, ..., x_N) \tag{3.2}$$

Included among the quantities x_i are corrections, as well as quantities that take into account other sources of variability, such as different observers, instruments samples, laboratories, and times at which observations are made. The corrections that significantly affect the measurement result are applied to compensate for each recognized systematic effect. The correction may be either positive, negative, or zero.

The combined standard uncertainty of the measurement result y, designated by $u_c(y)$ and taken to represent the estimated standard deviation of the result, is the positive square root of the estimated variance $u_c^2(y)$ obtained from

$$u_c^2(y) = \sum_{i=1}^{N} \left(\frac{\partial f}{\partial x_i} \right)^2 u^2(x_i) \tag{3.3}$$

It is of important note that the uncertainty equation is based on the first order Taylor series approximation of $y = f(x_1, x_2, x_3, ..., x_N)$ and is conveniently referred to as the *law of propagation of uncertainty*. The partial derivatives $\partial f / \partial x_i$ (often referred to as *sensitivity coefficients*) evaluated at $u(x_i)$ which may be defined as the standard uncertainty associated with the input estimate x_i.

3.3.1 Uncertainty in Nusselt number

The data reduction equation for the Nusselt number is considered along with the heat losses by conduction and radiation.

$$Nu_i = \frac{d}{k_{air}} \left(\frac{\dfrac{V^2}{R\,A_{total}} - \dfrac{k_w}{t}(T_{s,i} - T_{in}) - \varepsilon\sigma(T_{s,i}^4 - T_{in}^4)}{(T_{s,i} - T_{in})} \right) \tag{3.4}$$

Taking into consideration only the measured values, which have significant uncertainty, the convective heat transfer coefficient is a function of:

$$Nu_i = f(V, R, T_{s,i}, T_{in}, T_w, T_{surr}, A_{cp,i}, k_w, \varepsilon, A_{total}, k_{air}, d) \tag{3.5}$$

Thermal conductivity of wood, temperature of wood, temperature of the surroundings and emissivity are not considered as the experiment is carried out in a controlled environment and they contribute very less in the Nusselt number calculation. Temperature of the wood has a very less effect on the uncertainty of heat transfer coefficient due to the large thickness of the wood and also due to the insulation material attached to the wooden block. Temperature of the surroundings also has a very less effect on the uncertainty as the work is carried out in a controlled environment and the temperature of the surroundings is maintained within a desired limit.

Thus the data reduction equation (3.5) reduces to the following simplified form

$$Nu_i = f(V, R, T_{s,i}, T_{in}, A_{total}, d) \tag{3.6}$$

The standard uncertainty in the Nusselt number neglecting the covariance is calculated using

$$\begin{aligned}\left(U_{c,Nu_i}\right)^2 = &\left(\frac{\partial Nu_i}{\partial V}u_V\right)^2 + \left(\frac{\partial Nu_i}{\partial R}u_R\right)^2 + \left(\frac{\partial Nu_i}{\partial T_{s,i}}u_{T_{s,i}}\right)^2 + \left(\frac{\partial Nu_i}{\partial T_{in}}u_{T_{in}}\right)^2 \\ &+ \left(\frac{\partial Nu_i}{\partial A_{total}}u_{A_{total}}\right)^2 + \left(\frac{\partial Nu_i}{\partial d}u_d\right)^2\end{aligned} \tag{3.7}$$

Uncertainty propagation for the dependent variable in terms of the measured values is calculated using the EES software. The measured variables x_1, x_2 etc have a random variability that is referred to as its uncertainty, this uncertainty is displayed as $a \pm u_x$. The

input to EES for calculating the uncertainty of a dependent variable is the magnitude of the measured variable and the uncertainty in each measured variable.

3.3.2 Uncertainty in Jet Reynolds number

The data reduction equation for the jet Reynolds number is taken as:

$$\mathrm{Re} = \frac{\rho V_{avg}\, d}{\mu} = \frac{\rho\, d}{\mu} \frac{\forall}{13 \times \frac{\pi}{4} d^2} \tag{3.8}$$

Taking into consideration only the measured values, which have significant uncertainty, the jet Reynolds number is a function of

$$\mathrm{Re} = f(\forall, d) \tag{3.9}$$

Density of air and the dynamic viscosity of air is not included in the measured variables since it has negligible error in the computation of the uncertainty in jet Reynolds number.

$$\left(U_{c,\mathrm{Re}_j}\right)^2 = \left(\frac{\partial \mathrm{Re}_j}{\partial \forall} u_{\forall}\right)^2 + \left(\frac{\partial \mathrm{Re}_j}{\partial d} u_d\right)^2 \tag{3.10}$$

Uncertainty propagation for the dependent variable in terms of the measured values is calculated using the EES software. The measured variables x_1, x_2 etc have a random variability that is referred to as its uncertainty, this uncertainty is displayed as $a \pm u_x$. The input to EES for calculating the uncertainty of a dependent variable is the magnitude of the measured variable and the uncertainty in each measured variable. The Uncertainty results obtained using EES displays the partial derivative of the calculated variable with respect to

each measured variable and the percentage of the total uncertainty in the calculated variable resulting from the uncertainty in each measured variable.

Note: The percentage is calculated as the ratio of the square of the product of the partial derivative and uncertainty in the calculated variable.

3.4 EES Program

```
{Program to Calculate the Uncertainty in  Nusselt number for a Tabular column}
T_s = 63.18 "[C]"
R = 60.05
V = 77.69 "[V]"
T_in = 21 "[C]"
A_tot = 0.02386 "[m^2]"
d = 0.005 "[m]"

k_air = 0.0257 "[W/m K]"
k_w = 0.087 "[W/m K]"

T_surr = 21 "[C]"

ep = 0.8
sig = 5.67e-8

A_cp = 0.00168 "[m^2]"
t = 0.03 "[m]"
T_w = 30.097035 "[C]"
 Vol = 458.77"[m/s]"
ro = 1.225"[kg/s]"
mu = 1.835*10e-5
A_tot1 = 10.2101*10e-4 "[m^2]"
D_h = 0.01"[m]"

Q_tot = (V^2/R)
e_tot = Q_tot/A_tot
Q_1 = e_tot*A_cp

Q_cond1 = ((k_w/t)*A_cp*(T_s – T_w))
Q_rad1 = (ep*sig*A_cp*(T_s^4 – T_surr^4))

Q_actual1 = Q_1 – Q_cond1 – Q_rad1
h = (Q_actual1)/(A_cp*(T_s – T_in))
Nu = ((h*d)/k_air)
```

```
V_avg = (Vol*1.6667*10e-5)/A_tot1
Re = (ro*V_avg*d)/mu



{Program to Calculate the Uncertainty in  Nusselt number for a single value}
T_s = 62.09489 "[C]"
R = 60.05
V = 77.69
T_in = 21 "[C]"
A_tot = 0.02386 "[m^2]"
d = 0.005 "[m]"

k_air = 0.0257 "[W/m C]"
k_w = 0.087 "[W/m C]"

T_surr = 21 "[C]"

ep = 0.8
sig = 5.67e-8

A_cp = 0.00168 "[m^2]"
t = 0.03 "[m]"
T_w = 30.097035 "[C]"

Vol = 458.77"[m/s]"
ro = 1.225"[kg/s]"
mu = 1.835*10e-5
A_tot1 = 10.2101*10e-4 "[m^2]"
D_h = 0.01"[m]"

Q_tot = (V^2/R)
e_tot = Q_tot/A_tot
Q_1 = e_tot*A_cp

Q_cond1 = ((k_w/t)*A_cp*(T_s – T_w))
Q_rad1 = (ep*sig*A_cp*(T_s^4 – T_surr^4))

Q_actual1 = Q_1 – Q_cond1 – Q_rad1
h = (Q_actual1)/(A_cp*(T_s – T_in))
Nu = ((h*d)/k_air)
```

{Program to Calculate the Uncertainty in Reynolds number for a Tabular column}

ro = 1.225"[kg/s]"
mu = 1.835*10e-6
A_tot1 = 2.5545*10e-4 "[m^2]"

V_avg = (Vol*1.6667*10e-5)/A_tot1
Re = (ro*V_avg*d)/mu

{Program to Calculate the Uncertainty in Reynolds number for a single value}
Vol = 458
d = 0.01 "[m]"
ro = 1.225"[kg/s]"
mu = 1.835*10e-6
A_tot1 = 2.5545*10e-4 "[m^2]"

V_avg = (Vol*1.6667*10e-5)/A_tot1
Re = (ro*V_avg*d)/mu

3.5 Sample Uncertainty Calculations

3.5.1 Orifice Plate – 1

Table 3.1 Sample Uncertainty calculations of Nusselt number for minimum value

Variable ± Uncertainty	Partial Derivative	% of Uncertainty
Nu = 12.14 ± 0.5964		
A_{cp} = 0.02386 ± 0.0001 *(m^2)*	$\partial Nu/\partial A_{cp}$ = -529.6	0.79 %
d = 0.01 ± 0.0001 *(m)*	$\partial Nu/\partial d$ = 2429	16.59 %
R = 60.05 ± 1 *(Ω)*	$\partial Nu/\partial R$ = -0.2104	12.45 %
T_{in} = 21 ± 2 *(^oC)*	$\partial Nu/\partial T_{in}$ = 0.1873	39.44 %
T_{in} = 85.85 ± 0.3 *(^oC)*	$\partial Nu/\partial T_s$ = -0.1963	0.98 %
V = 77.66 ± 1 *(^oC)*	$\partial Nu/\partial V$ = 0.3253	29.76 %

Table 3.2 Sample Uncertainty calculations of Nusselt number for maximum value

Variable ± Uncertainty	Partial Derivative	% of Uncertainty
Nu = 36.03 ± 3.5		
A_{cp} = 0.02386 ± 0.0001 *(m^2)*	$\partial Nu/\partial A_{cp}$ = -1524	0.19 %
d = 0.01 ± 0.0001 *(m)*	$\partial Nu/\partial d$ = 7206	4.24 %
R = 60.05 ± 1 *(Ω)*	$\partial Nu/\partial R$ = -0.6056	2.99 %
T_{in} = 21 ± 2 *(^oC)*	$\partial Nu/\partial T_{in}$ = 1.599	83.48 %
T_{in} = 43.54 ± 0.3 *(^oC)*	$\partial Nu/\partial T_s$ = -1.624	1.94 %
V = 77.66 ± 1 *(^oC)*	$\partial Nu/\partial V$ = 0.9362	7.16 %

3.5.2 Orifice Plate – 2

Table 3.3 Sample Uncertainty calculations of Nusselt number for minimum value

Variable ± Uncertainty	Partial Derivative	% of Uncertainty
Nu = 20.58 ± 1.316		
A_{cp} = 0.02386 ± 0.0001 *(m^2)*	$\partial Nu/\partial A_{cp}$ = -880.7	0.45 %
d = 0.005 ± 0.0001 *(m)*	$\partial Nu/\partial d$ = 4115	9.78 %
R = 60.05 ± 1 *(Ω)*	$\partial Nu/\partial R$ = -0.3499	7.07 %
T_{in} = 21 ± 2 *(^oC)*	$\partial Nu/\partial T_{in}$ = 0.5276	64.28 %
T_{in} = 60± 0.3 *(^oC)*	$\partial Nu/\partial T_s$ = -0.5422	1.53 %
V = 77.66 ± 1 *(^oC)*	$\partial Nu/\partial V$ = 0.5409	16.89 %

Table 3.4 Sample Uncertainty calculations of Nusselt number for maximum value

Variable ± Uncertainty	Partial Derivative	% of Uncertainty
Nu = 53.93 ± 7.48		
A_{cp} = 0.02386 ± 0.0001 *(m^2)*	$\partial Nu/\partial A_{cp}$ = -2270	0.09 %
d = 0.005 ± 0.0001 *(m)*	$\partial Nu/\partial d$ = 10787	2.08 %
R = 60.05 ± 1 *(Ω)*	$\partial Nu/\partial R$ = -0.9019	1.45 %
T_{in} = 21 ± 2 *(^oC)*	$\partial Nu/\partial T_{in}$ = 3.564	90.81 %
T_{in} = 36.13 ± 0.3 *(^oC)*	$\partial Nu/\partial T_s$ = -3.602	2.09 %
V = 77.66 ± 1 *(^oC)*	$\partial Nu/\partial V$ = 1.394	3.47 %

3.5.3 Orifice Plate – 3

Table 3.5 Sample Uncertainty calculations of Nusselt number for minimum value

Variable ± Uncertainty	Partial Derivative	% of Uncertainty
Nu = 16.1 ± 0.8946		
A_{cp} = 0.02386 ± 0.0001 *(m^2)*	$\partial Nu/\partial A_{cp}$ = -694.3	0.60 %
d = 0.005 ± 0.0001 *(m)*	$\partial Nu/\partial d$ = 3220	12.96 %
R = 60.05 ± 1 *(Ω)*	$\partial Nu/\partial R$ = -0.2759	9.51 %
T_{in} = 21 ± 2 *(^oC)*	$\partial Nu/\partial T_{in}$ = 0.3254	52.93 %
T_{in} = 70.47± 0.3 *(^oC)*	$\partial Nu/\partial T_s$ = -0.3371	1.28 %
V = 77.66 ± 1 *(^oC)*	$\partial Nu/\partial V$ = 0.4264	22.72 %

Table 3.6 Sample Uncertainty calculations of Nusselt number for maximum value

Variable ± Uncertainty	Partial Derivative	% of Uncertainty
Nu = 48.02 ± 5.992		
A_{cp} = 0.02386 ± 0.0001 *(m^2)*	$\partial Nu/\partial A_{cp}$ = -2024	0.11 %
d = 0.005 ± 0.0001 *(m)*	$\partial Nu/\partial d$ = 9604	2.57 %
R = 60.05 ± 1 *(Ω)*	$\partial Nu/\partial R$ = -0.804	1.80 %
T_{in} = 21 ± 2 *(^oC)*	$\partial Nu/\partial T_{in}$ = 2.829	89.16 %
T_{in} = 37.97 ± 0.3 *(^oC)*	$\partial Nu/\partial T_s$ = -2.862	2.05 %
V = 77.66 ± 1 *(^oC)*	$\partial Nu/\partial V$ = 1.243	4.3 %

3.5.4 Orifice Plate – 4

Table 3.7 Sample Uncertainty calculations of Nusselt number for minimum value

Variable ± Uncertainty	Partial Derivative	% of Uncertainty
Nu = 17.19 ± 0.9885		
A_{cp} = 0.02386 ± 0.0001 *(m^2)*	$\partial Nu/\partial A_{cp}$ = -739.5	0.56 %
d = 0.005 ± 0.0001 *(m)*	$\partial Nu/\partial d$ = 3437	12.09 %
R = 60.05 ± 1 *(Ω)*	$\partial Nu/\partial R$ = -0.2938	8.84 %
T_{in} = 21 ± 2 *(^oC)*	$\partial Nu/\partial T_{in}$ = 0.37	56.05 %
T_{in} = 67.45± 0.3 *(^oC)*	$\partial Nu/\partial T_s$ = -0.3824	1.35 %
V = 77.66 ± 1 *(^oC)*	$\partial Nu/\partial V$ = 0.4542	21.12 %

Table 3.8 Sample Uncertainty calculations of Nusselt number for maximum value

Variable ± Uncertainty	Partial Derivative	% of Uncertainty
Nu = 30.98 ± 2.659		
A_{cp} = 0.02386 ± 0.0001 *(m^2)*	$\partial Nu/\partial A_{cp}$ = -1314	0.24 %
d = 0.005 ± 0.0001 *(m)*	$\partial Nu/\partial d$ = 6195	5.43 %
R = 60.05 ± 1 *(Ω)*	$\partial Nu/\partial R$ = -0.522	3.85 %
T_{in} = 21 ± 2 *(^oC)*	$\partial Nu/\partial T_{in}$ = 1.185	79.41 %
T_{in} = 47.15 ± 0.3 *(^oC)*	$\partial Nu/\partial T_s$ = -1.206	1.85 %
V = 77.66 ± 1 *(^oC)*	$\partial Nu/\partial V$ = 0.8069	9.21 %

3.5.5 Uncertainty in jet Reynolds numbers

Table 3.9 Sample Uncertainty calculations of Jet Reynolds number for $\mathrm{Re}_j = 9300$

Variable ± Uncertainty	Partial Derivative	% of Uncertainty
Re = 9300 ± 185.907		
$\forall$ = 458.8 ± 0.1 *(lit/sec)*	$\partial \mathrm{Re}/\partial \forall$ = 43.56	0.05 %
d = 0.01 ± 0.0001 *(m)*	$\partial \mathrm{Re}/\partial d$ = 1.995E+06	99.95 %

Table 3.10 Sample Uncertainty calculations of Jet Reynolds number for $\mathrm{Re}_j = 14400$

Variable ± Uncertainty	Partial Derivative	% of Uncertainty
Re = 14400 ± 287.86		
$\forall$ = 688.55 ± 0.1 *(lit/sec)*	$\partial \mathrm{Re}/\partial \forall$ = 21.78	0.05 %
d = 0.01 ± 0.0001 *(m)*	$\partial \mathrm{Re}/\partial d$ = 997441	99.95 %

Table 3.11 Sample Uncertainty calculations of Jet Reynolds number for $\mathrm{Re}_j = 18800$

Variable ± Uncertainty	Partial Derivative	% of Uncertainty
Re = 18800 ± 375.84		
$\forall$ = 688.55 ± 0.1 *(lit/sec)*	$\partial \mathrm{Re}/\partial \forall$ = 17.95	0.06 %
d = 0.01 ± 0.0001 *(m)*	$\partial \mathrm{Re}/\partial d$ = 1.6988E+06	99.94 %

Table 3.12 The derived parameters used to find the uncertainty.

Parameter	Resultant Derivatives
$\frac{\partial Nu}{\partial V}$	$\frac{d(2V)}{R k_{air} A_{cp} (T_s - T_{in})}$
$\frac{\partial Nu}{\partial R}$	$-\frac{d(V^2)}{R^2 k_{air} A_{cp} (T_s - T_{in})}$
$\frac{\partial Nu}{\partial T_s}$	$\frac{d\left(-\frac{k_w}{t} - 4\varepsilon\sigma T_s^3\right)}{k_{air} A_{cp} (T_s - T_{in})} - \frac{d\left(VI - \frac{k_w}{t}(T_s - T_w) - \varepsilon\sigma(T_s^4 - T_{surr}^4)\right)}{k_{air} A_{cp} (T_s - T_{in})^2}$
$\frac{\partial Nu}{\partial T_{in}}$	$\frac{d\left(VI - \frac{k_w}{t}(T_s - T_w) - \varepsilon\sigma(T_s^4 - T_{surr}^4)\right)}{k_{air} A_{cp} (T_s - T_{in})^2}$
$\frac{\partial Nu}{\partial A_{cp}}$	$-\frac{d\left(VI - \frac{k_w}{t}(T_s - T_w) - \varepsilon\sigma(T_s^4 - T_{surr}^4)\right)}{k_{air} A_{cp}^2 (T_s - T_{in})}$
$\frac{\partial \mathrm{Re}_j}{\partial \forall}$	$\frac{\rho}{\mu d}$
$\frac{\partial \mathrm{Re}}{\partial d}$	$-\frac{\rho \forall}{\mu d^2}$

CHAPTER 4

ORIFICE PLATE - 1

Jet impingement heat transfer is dependent on several flow and geometrical parameters. The jet impingement Nusselt number is presented as a functional form of,

$$Nu_i = \left(\frac{h_i\, d}{k_{air}}\right) = f\left[\mathrm{Re}_j,\ \left(X/d, S/d, H/d\right), outflow\ orientation\right] \qquad (4.1)$$

Where, Re_j is the flow parameter, distance along the target surface X/d, and feeding channel aspect ratio H/d are the geometric parameters. The flow exit direction is an important parameter having a significant effect on impingement heat transfer. The jet inlet condition is the direction in which the flow enters the impingement channel.

Figure 2.3 shows three outflow orientations where air comes into the feeding channel and leaves through jets made in the orifice jet plate to impinge on the heated target surface located in the impingement channel. For all the three cases air enters the feeding channel at $X/d = 57.15$. For case 1, air exits the impingement channel at low X/d $(X/d = 0)$ and therefore the crossflow develops towards the exit. This case is typical of that seen by Flourshеutz et al [14]. For case 2, the flow exits the impingement channel at $X/d = 57.15$ and as the flow moves forward from low X/d crossflow develops at low X/d and increases towards large X/d $(X/d = 57.15)$. For case 3, the flow exits the impingement

channel at both the directions i.e., at $X/d = 0$ *and* 57.15 and the crossflow develops towards both the ends of the test section.

Tests were carried out for three different outflow orientations with Reynolds number ranging between $5000 \le \mathrm{Re}_j \le 10000$ by varying the feeding channel aspect ratio (H/d). Three different values of the feeding channel aspect ratio $2.5 \le H/d \le 4.5$ were considered while carrying out the experiments.

Flow orientation affects the flow inside the impingement channel and leads into different heat transfer characteristics. As air impinges on the target surface, crossflow starts developing and grows continuously towards the exit resulting into thicker boundary layer, which suppresses the jet impingement effect. In addition, crossflow causes distortion to the jet impingement in which the jet is no longer impinging normally on the target surface.

All the results presented in this paper are for $0 \le X/d \le 57.15$ over the entire span of the target plates. Where X is defined from the opposite end of the feeding channel of the test section as shown in figure 2.2. All the results presented below are being extracted using the orifice plate with centerline jets of diameter 1cm.

The local Nusselt number distribution for all the three outflow orientations by varying the jet-to-plate distance is presented in detail, as a function of non-dimensional location X/d on the target surface for jet Reynolds number and the feeding channel aspect ratio H/d in the forthcoming discussion.

4.1 Effect of feeding channel aspect ratio on local Nusselt number

Figure 4.1 – 4.3, gives a detail insight into the local Nusselt number distribution presenting the effect of feeding channel aspect ratio $2.5 \le H/d \le 4.5$ on the heat transfer from the target surface. All the outflow orientations are discussed.

Figure 4.1 shows effect of feeding channel aspect ratio on the local Nusselt number distribution over the entire length of the target surface for case – 1, where the flow exits at low X/d $(X/d = 0)$. The crossflow develops from large X/d to low X/d as the air exits at low X/d. The heat transferred from the target surface decreases with an increase in feeding channel aspect ratio from H/d = 2.5 to 4.5 for all the feeding channel aspect ratios studied. Over the entire length of the target surface, the feeding channel aspect ratio $H/d = 2.5$ gives the maximum heat transfer for all the jet Reynolds numbers $5000 \le \mathrm{Re}_j \le 10000$ studied. This is primarily due to the increase in the strength of the jets with an decrease in the feeding channel ratios. Observing the effect of the feeding channel aspect ratio on the local Nusselt number distribution for all the jet Reynolds numbers studied, $H/d = 2.5$ gives the maximum heat transfer among all the feeding channel aspect ratios studied. $H/d = 2.5$ gives a margnial increase in the local Nusselt number compared to $H/d = 3.5$, whereas $H/d = 2.5$ gives a maximum of 4% increase in local Nusselt number is observed compared to $H/d = 4.5$ for all the jet Reynolds numbers studied. With an increase in the feeding channel aspect ratio the difference in the magnitude of the local Nusselt number also increases for an increase in the jet Reynolds number. Among all the Reynolds numbers studied, $\mathrm{Re}_j = 10000$ gives the maximum heat transfer. The local Nusselt number distribution is more sensitive for higher values of jet Reynolds number compared to

the low values. As discussed earlier in figure 6, a peak of local Nusselt number at $X/d = 40.2$ is observed this is due to the flow entering the impingement channel at large X/d, where the effect of crossflow is minimal. At $15.6 \le X/d \le 36.1$ crossflow dominates the impingement of jets and a linearly decreasing distribution of local Nusselt number is observed towards the exit for all the feeding channel aspect ratios studied.

Figure 4.2 shows the effect of the feeding channel aspect ratio on the local Nusselt number distribution for case – 2. For case – 2, the flow exits at low X/d $(X/d = 0)$, causing crossflow development towards the exit. The magnitude of local Nusselt number observed for case – 2 is less compared to the values of case – 1. $H/d = 2.5$ gives the maximum heat transfer over the entire length of the target surface for all the jet Reynolds numbers studied. For all the jet Reynolds numbers studied, $H/d = 2.5$ gives a marginal increase in heat transfer from the entire length of the target surface compared to $H/d = 3.5$ whereas $H/d = 2.5$ gives a maximum of 4.5% increase in heat transfer compared to $H/d = 4.5$. It is also observed that the magnitude of the local Nusselt number increases with an increase in the jet Reynolds number for all the feeding channel aspect ratios studied. The variation in the local Nusselt number is more sensitive with respect to a change in feeding channel aspect ratio at high jet Reynolds number whereas it is less sensitive at low jet Reynolds numbers. At $40.2 \le X/d \le 57.15$ the magnitude of local Nusselt number decreases from $X/d = 40.2$ to $X/d = 57.15$, this is due to the obstruction caused by the crossflow to the impinging jets.

Figure 4.3 shows the effect of feeding channel aspect ratio on the local Nusselt number distribution for case – 3. For case – 3 air exits at $X/d = 0$ and $X/d = 57.15$, where

the crossflow has a predominant effect over the heat transfer characteristics. It is observed that at $0 \le X/d \le 15$ and $40.2 \le X/d \le 57.15$ the local Nusselt number decreases towards exit, this may be due to the crossflow at the exit and thus reduces the strength of the impinging jets and the heat transferred from the target surface. The magnitude of local Nusselt number at $15.6 \le X/d \le 36.1$ is high compared to the other X/d locations this may be due to the strong impingement of jets. For an increase in feeding channel aspect ratio a corresponding increase in local Nusselt number is observed. $H/d = 2.5$ gives the maximum values of feeding channel aspect ratio for all the jet Reynolds numbers studied. Considering the effect of feeding channel aspect ratio for all jet Reynolds numbers on heat transfer characteristics in detail, $H/d = 2.5$ gives the highest heat transfer similar to case – 1 and case – 2. $H/d = 2.5$ gives a marginal increase in heat transfer compared to $H/d = 3.5$, further $H/d = 2.5$ gives a maximum of 3% more heat transfer is observed compared to $H/d = 4.5$. Similar to case – 1 and case – 2, with respect to the effect of feeding channel aspect ratio on local Nusselt number characteristics it is observed that the local Nusselt number is sensitive to a change in feeding channel aspect ratio at high jet Reynolds numbers.

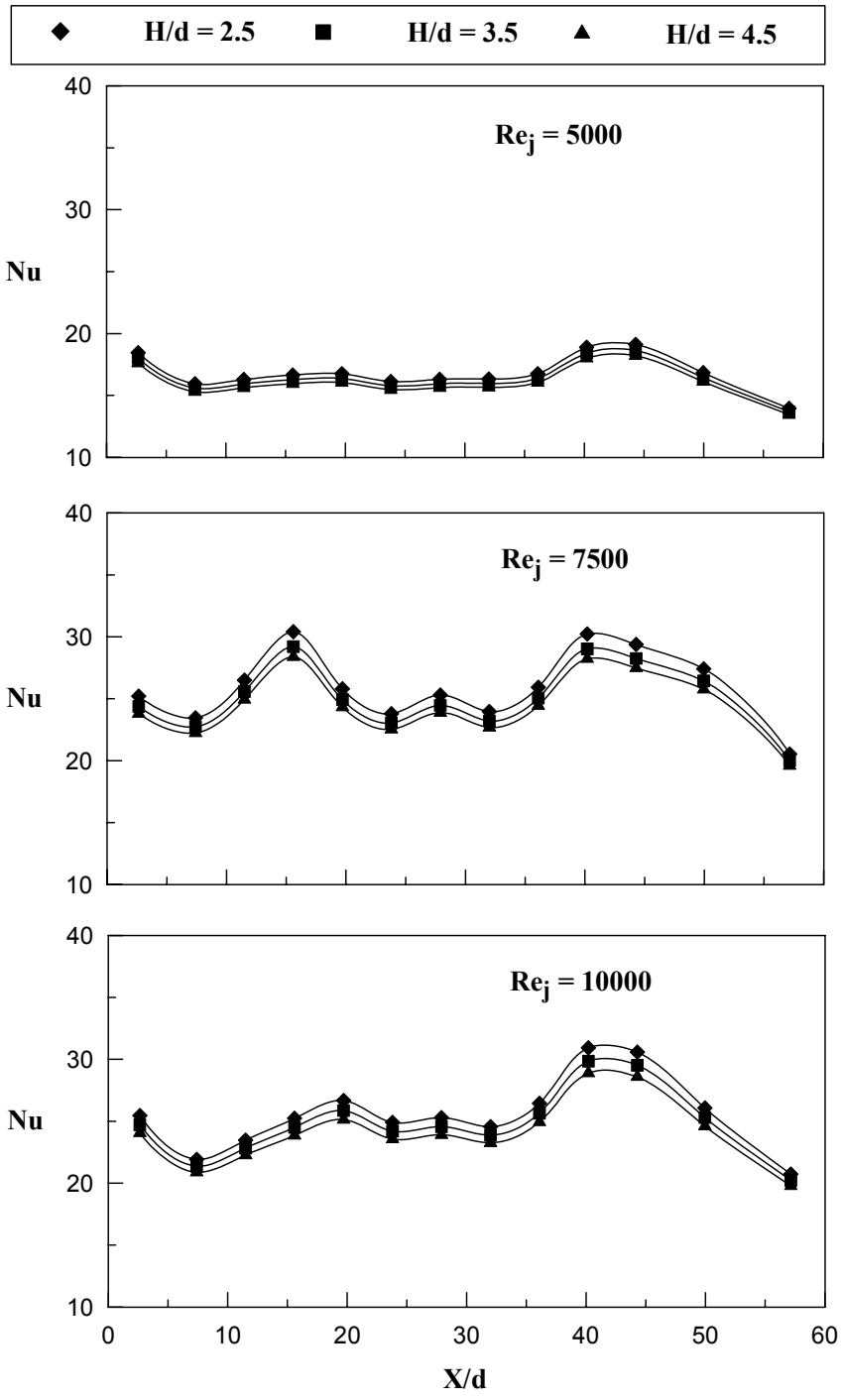

Figure 4.1 Effect of feeding channel aspect ratio $2.5 \le H/d \le 4.5$ on local Nusselt number distribution for case – 1 and jet-to-plate distance $S/d = 3$.

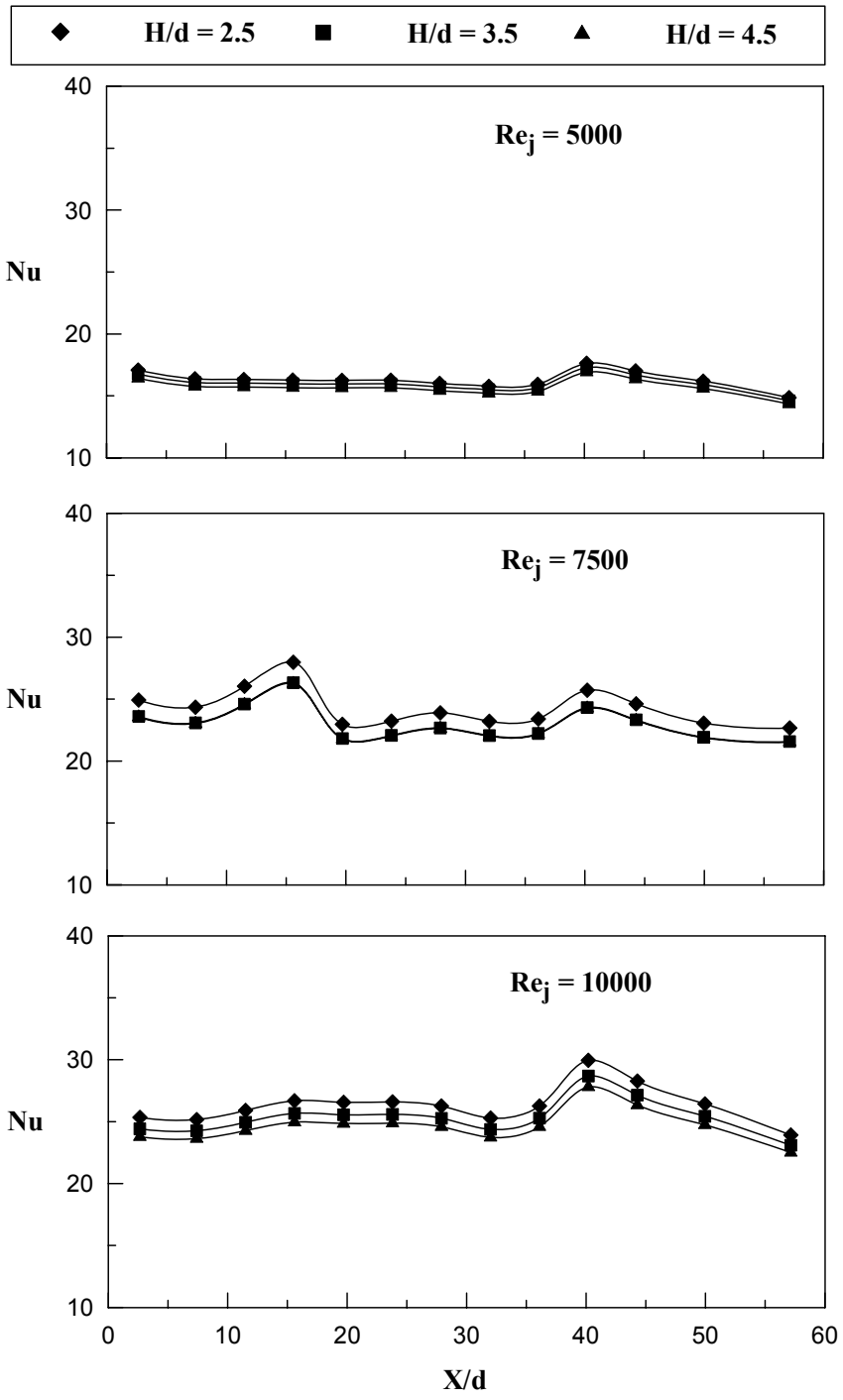

Figure 4.2 Effect of feeding channel aspect ratio $2.5 \le H/d \le 4.5$ on local Nusselt number distribution for case – 2 and jet-to-plate distance $S/d = 3$.

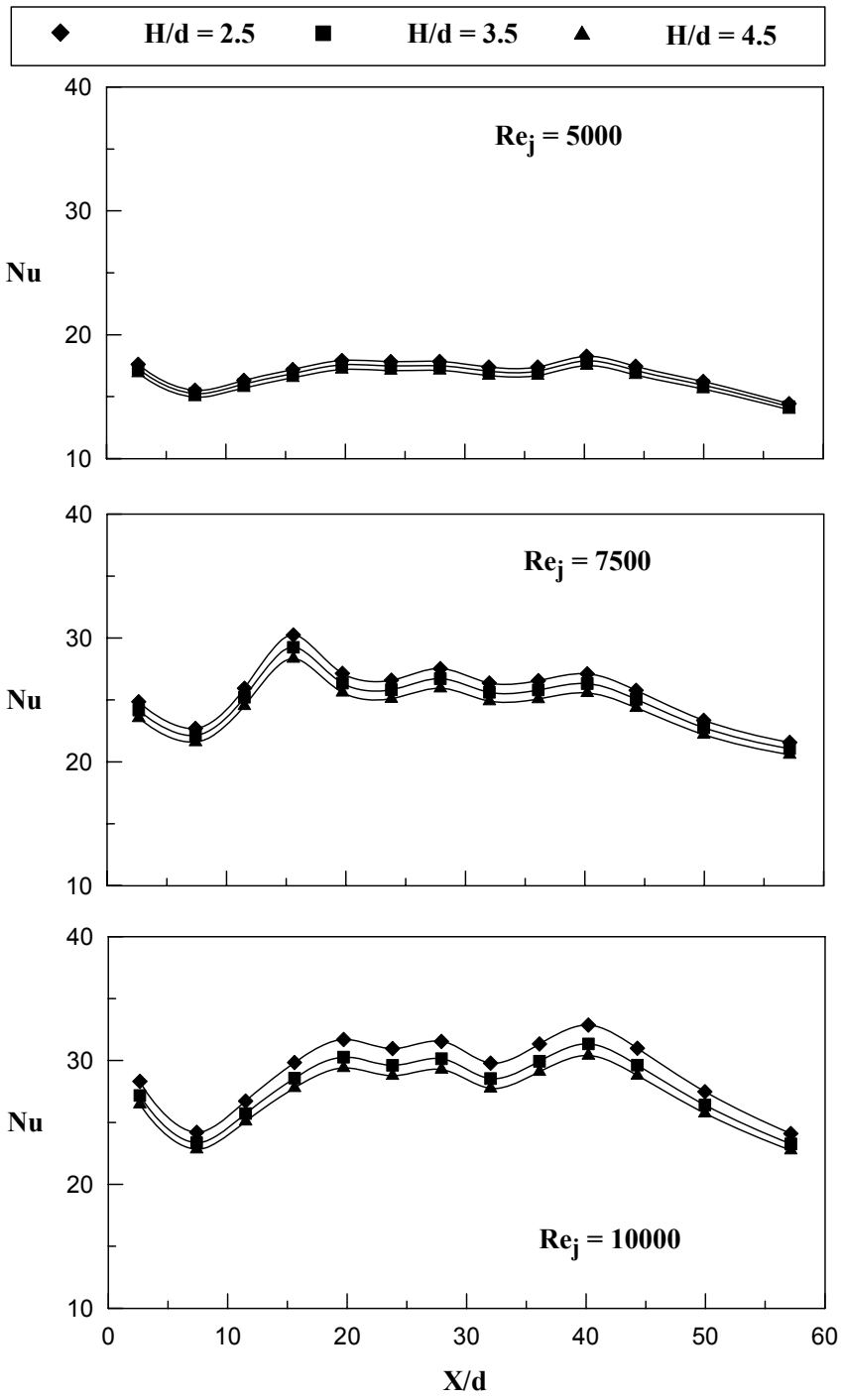

Figure 4.3 Effect of feeding channel aspect ratio $2.5 \le H/d \le 4.5$ on local Nusselt number distribution for case – 3 and jet-to-plate distance $S/d = 3$.

4.2 Effect of jet Reynolds number on local Nusselt number

Figure 4.4 - 4.6 shows the local Nusselt number distribution for different jet Reynolds numbers $5000 \le \mathrm{Re}_j \le 10000$, expressing the effect of the feeding channel aspect ratio on the heat transfer from the heated target surface.

Figure 4.4 shows the local Nusselt number distribution plotted for case – 1, which gives a detailed insight into the effect of the feeding channel aspect ratio. Three different values of the feeding channel aspect ratios are considered in this part of the study $2.5 \le H/d \le 4.5$. The results are presented for three jet Reynolds numbers $5000 \le \mathrm{Re}_j \le 10000$. It is observed that for an increase in the jet Reynolds number there is a corresponding increase in the magnitude of local Nusselt number. For case – 1, the flow exits the impingement channel at low X/d $(X/d = 0)$. A peak of local Nusselt number is observed at $X/d = 40.2$, this may be due to the strong impingement of jets as the air enters the impingement channel at large X/d where the effect of crossflow is minimal resulting into thinner boundary layer. Among all the feeding channel aspect ratios examined, $H/d = 2.5$ gives the maximum heat transfer for all the jet-to-plate distances studied. $H/d = 2.5$ gives a maximum of 5% increase in the local Nusselt number from the target surface compared to $H/d = 3.5$, whereas it gives a maximum of 7.6% more heat transfer compared to $H/d = 4.5$. At $15.6 \le X/d \le 36.1$ uniformly decreasing heat transfer is observed along the target surface for all the feeding channel aspect ratios studied, this is due to the crossflow of the air which reduces the strength of the impinging jets. A considerable increase in the Nusselt number is observed at large X/d $(X/d = 57.15)$ for $\mathrm{Re}_j = 10000$,

whereas for $\mathrm{Re}_j = 5000$ and $\mathrm{Re}_j = 7500$ a uniform behavior of local Nusselt number is observed this is due to the strong impingement at high velocities thus reducing the boundary layer thickness which leads to high heat transfer.

Figure 4.5 shows the local Nusselt number distribution for case – 2 plotted for different jet Reynolds numbers $5000 \le \mathrm{Re}_j \le 10000$ by varying the feeding channel aspect ratios $2.5 \le H/d \le 4.5$. For case – 2 air exits the impingement channel at $X/d = 57.15$ opposite to the entry flow, this leads to the development of more crossflow towards large X/d ($X/d = 57.15$). Similar to the case – 1 an increase in jet Reynolds number leads to a corresponding increase in local Nusselt number for all the H/d values studied. At large X/d ($X/d = 57.15$), the flow exits at this location causing greater amount of crossflow obstructing the impingement of jets at this location, thus less magnitude of local Nusselt number is observed. A uniform distribution of local Nusselt number is observed along the entire length of the heated target surface except a peak of local Nusselt number at $X/d = 40.2$ which may due to the strong impingement of jets at that location. Although similar behavior of local Nusselt number is observed for $H/d = 2.5$ and $H/d = 3.5$, but $H/d = 2.5$ gives a marginal increase in local Nusselt number over the entire target surface compared to $H/d = 3.5$, whereas a maximum of 5.2% more heat transfer is observed over the entire target surface is observed compared to $H/d = 4.5$. The variation in the magnitude of local Nusselt number is considerable for a change in jet Reynolds number from $\mathrm{Re}_j = 5000$ to $\mathrm{Re}_j = 7500$ for all the feeding channel aspect ratios studied, this is reflected from the similar behavior of local Nusselt number. Whereas a marginal increase in the magnitude of the local Nusselt number is observed for an increase of jet Reynolds number

from $\mathrm{Re}_j = 7500$ to $\mathrm{Re}_j = 10000$. At $40.2 \le X/d \le 57.15$, a decrease in local Nusselt number is observed from $X/d = 40.2$ towards the exit at $X/d = 57.15$, this may be due to the development of crossflow towards the exit, which obstructs the impingement of jets and thickens the boundary layer. This behavior of local Nusselt number is observed for all the H/d values studied.

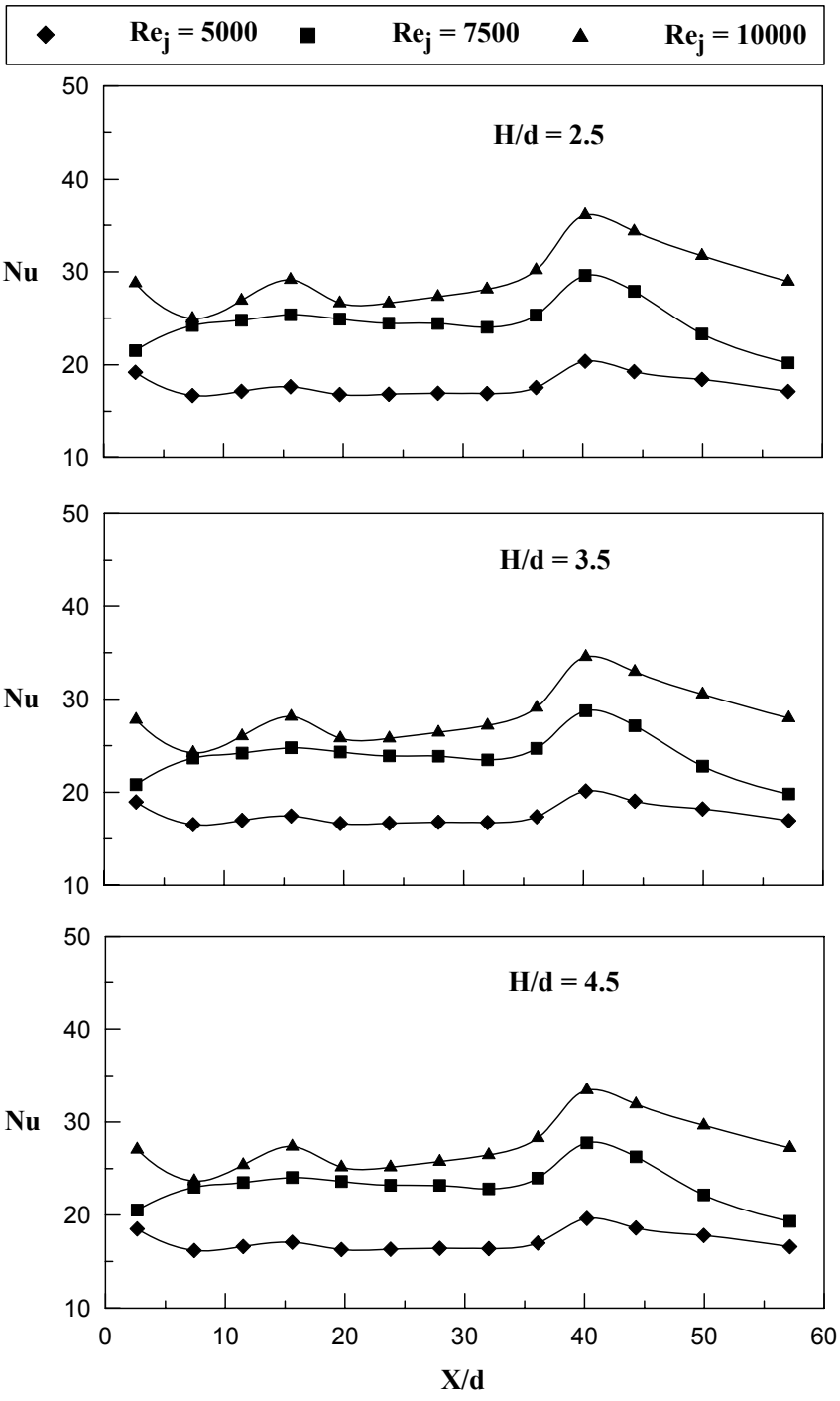

Figure 4.4 Effect of jet Reynolds number and feeding channel aspect ratio $2.5 \le H/d \le 4.5$ on local Nusselt number distribution for $S/d = 3$ and case – 1.

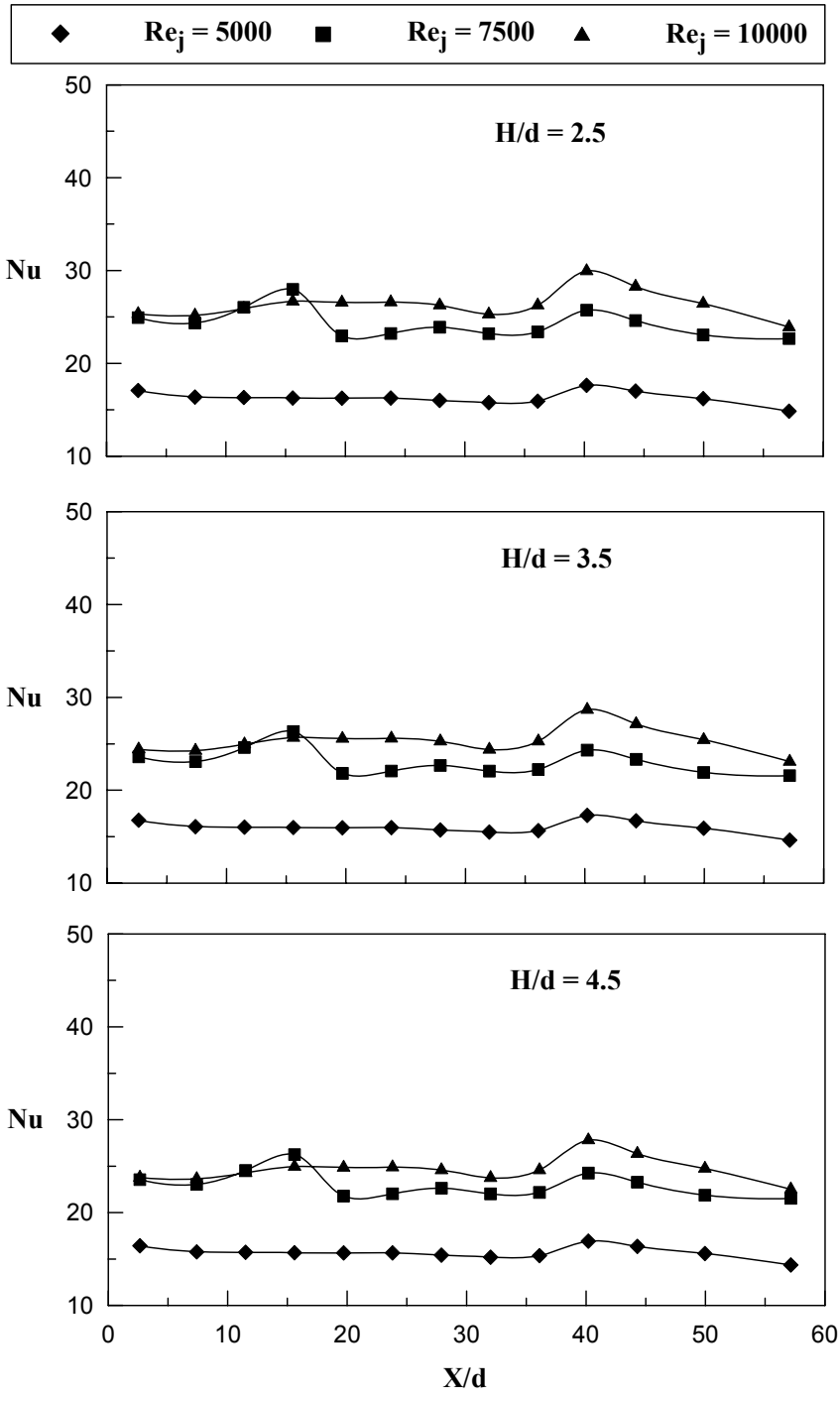

Figure 4.5 Effect of jet Reynolds number and feeding channel aspect ratio $2.5 \le H/d \le 4.5$ on local Nusselt number distribution for $S/d = 3$ and case – 2.

Figure 4.6 presents the local Nusselt number distribution for case – 3 where the air exits from both the directions at low X/d $(X/d = 0)$ and large X/d $(X/d = 57.15)$. It is observed that the crossflow develops at both the exit directions, which reduces the heat transferred from the target surfaces. Similar to case – 1 and case – 2, $H/d = 2.5$ has the maximum heat transfer from the entire length of the target surface. $H/d = 2.5$ gives minimum increase in heat transfer compared to $H/d = 3.5$, whereas $H/d = 2.5$ gives a maximum of 4.98% more heat transfer compared to $H/d = 4.5$. The magnitude of local Nusselt number between $15.6 \le X/d \le 36.1$ and $40.2 \le X/d \le 57.15$ is almost similar for all the feeding channel aspect ratios H/d studied for case – 3, whereas for case – 1 and case – 2 completely different distribution of local Nusselt number is observed. Similar to case – 1 and case – 2 the increase in the magnitude of the local Nusselt number for an increase in jet Reynolds number from $\mathrm{Re}_j = 5000$ to $\mathrm{Re}_j = 7500$ is more compared to the increase from $\mathrm{Re}_j = 7500$ to $\mathrm{Re}_j = 10000$.

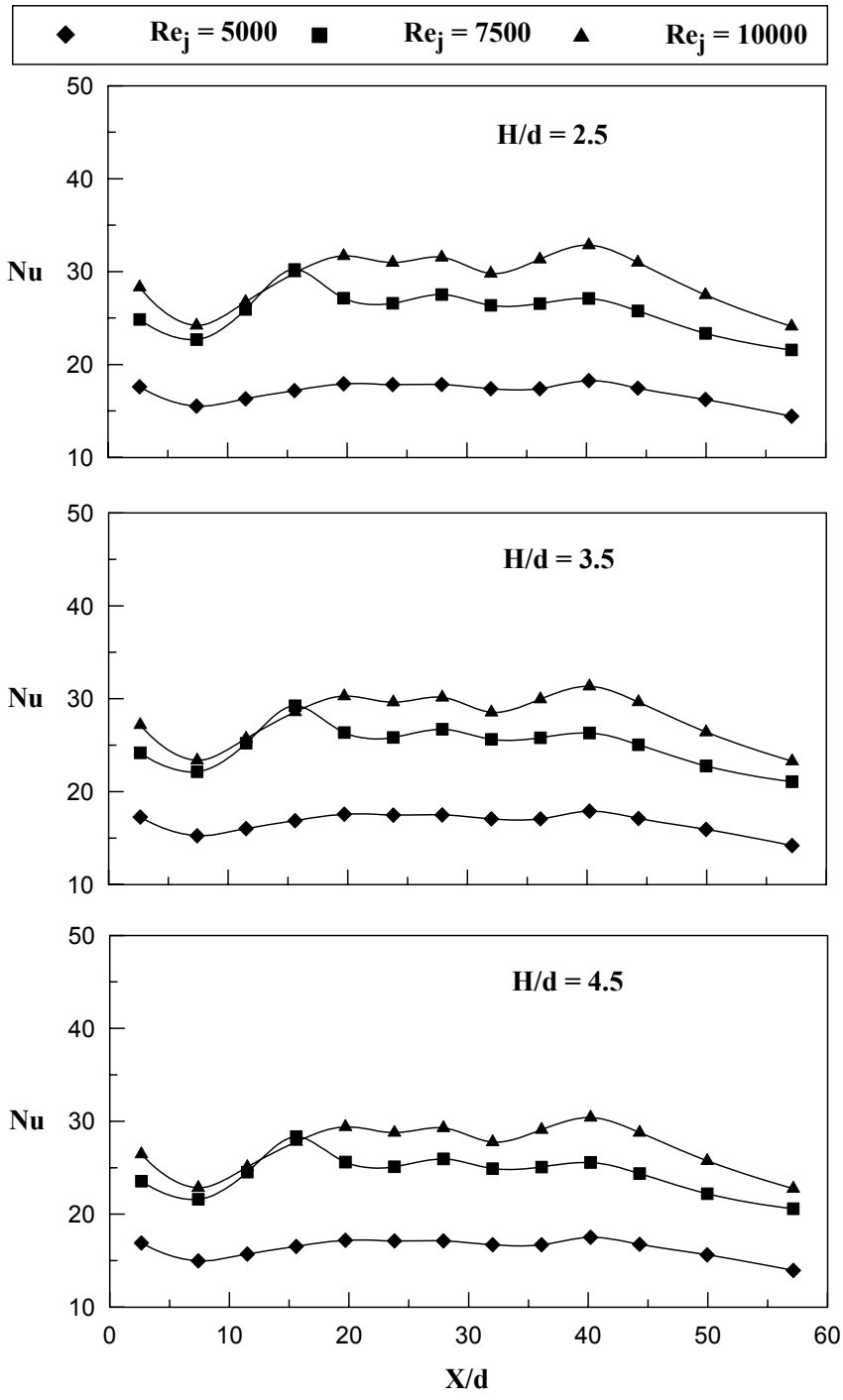

Figure 4.6 Effect of jet Reynolds number and feeding channel aspect ratio $2.5 \le H/d \le 4.5$ on local Nusselt number distribution for $S/d = 3$ and case – 3.

4.3 Effect of outflow orientation on local Nusselt number

Figure 4.7 – 4.9 shows the effect of the outflow orientation on the local Nusselt number distribution for different feeding channel aspect ratio $2.5 \le H/d \le 4.5$. All the jet Reynolds numbers studied $5000 \le \mathrm{Re}_j \le 10000$ are discussed individually.

Figure 4.7 presents the effect of the outflow orientation on the local Nusselt number distribution plotted for different feeding channel aspect ratios $2.5 \le H/d \le 4.5$ for $\mathrm{Re}_j = 5000$. Among all the H/d values studied very low variation of local Nusselt number is observed with respect to outflow orientation at low X/d $(0 \le X/d \le 16.1)$. It is observed that case – 3 has maximum heat transfer at $15.6 \le X/d \le 36.1$ this is due to the strong impingement in this region as the flow exits in both the directions. At $40.2 \le X/d \le 57.15$ case – 1 has the highest heat transfer due to the closed end and due to the less crossflow effect resulting in stronger impingement reducing the boundary layer thickness followed by case – 2 and case – 3 respectively. Case – 2 has the least values of local Nusselt number over the entire length of the target surface for all the feeding channel aspect ratios studied. This may be due to air exits in the opposite direction to the air coming in which in-turn causes heavy crossflow and thus less values of local Nusselt number. Similar to the cases studied before for the effect of feeding channel aspect ratio, $H/d = 2.5$ has the maximum heat transfer over the entire length of the target surface.

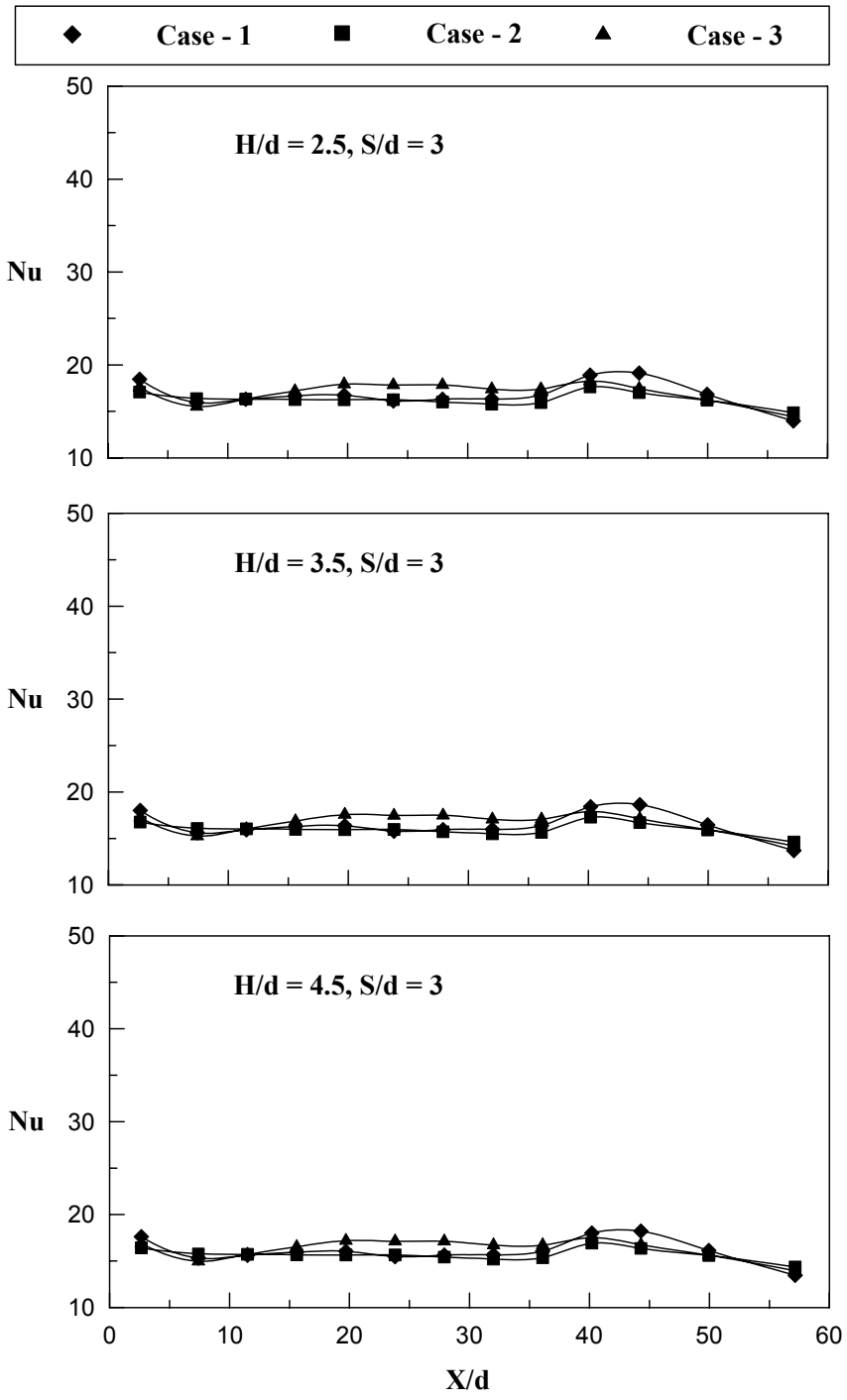

Figure 4.7 Effect of outflow orientation and feeding channel aspect ratio $2.5 \le H/d \le 4.5$ on local Nusselt number distribution for $S/d = 3$ and $\mathrm{Re}_j = 5000$.

Figure 4.8 presents the effect of the outflow orientation on the local Nusselt number distribution plotted for different feeding channel aspect ratios $2.5 \le H/d \le 4.5$ for $\mathrm{Re}_j = 7500$. It is observed that as the jet Reynolds number increases from 5000 to 7500 a maximum of 15% increase in local Nusselt number is observed. Similar to the local Nusselt number distribution for $\mathrm{Re}_j = 5000$, case – 3 has maximum heat transfer at $15.6 \le X/d \le 36.1$ due to the strong impingement of jets, whereas case – 1 and case – 2 gives less values of local Nusselt number due to the increase in the amount of the crossflow. At $40.2 \le X/d \le 57.15$ less variation in local Nusselt number is found as compared to Nusselt number distribution for $\mathrm{Re}_j = 5000$, whereas the behavior of local Nusselt number for case – 2 and case – 3 is almost similar as in both the cases air exits at large X/d ($X/d = 57.15$) and for case – 3 air also exits at low X/d ($X/d = 0$). Similar to $\mathrm{Re}_j = 5000$, case – 1 has the highest magnitude of local Nusselt number at $40.2 \le X/d \le 57.15$ and case – 2 has the least magnitude of local Nusselt number over the entire length of the target surface for all the feeding channel aspect ratios studied. It is also observed that the feeding channel aspect ratio $H/d = 2.5$ gives the maximum values of the local Nusselt numbers compared to the other H/d values.

Figure 4.9 presents the effect of the outflow orientation on the local Nusselt number distribution plotted for different feeding channel aspect ratios $2.5 \le H/d \le 4.5$ for $\mathrm{Re}_j = 10000$. It is observed that, for $\mathrm{Re}_j = 10000$, a variation in the magnitude of local Nusselt number values is observed over the entire length of the target surface for all the outflow orientations studied compared to the other two jet Reynolds numbers, $\mathrm{Re}_j = 5000$

and $\mathrm{Re}_j = 7500$ studied previously. Moreover as the H/d values increases from 2.5 to 4.5 a corresponding increase in the magnitude of local Nusselt number is observed. Maximum heat transfer is observed for $H/d = 2.5$ similar to $\mathrm{Re}_j = 5000$ *and* 7500 where $H/d = 2.5$ gives the maximum values of local Nusselt number. Similar to the other two jet Reynolds number studied, at $15.6 \le X/d \le 36.1$, case – 3 has the highest magnitude of the local Nusselt number compared to case – 1 and case – 2, whereas at $40.2 \le X/d \le 57.15$ case – 1 has the highest heat transfer due to the stronger impingement of jets decreasing the boundary layer thickness as the jets enters the impingement channel at this location thus having minimum crossflow effect. The variation in magnitude of the local Nusselt number observed at $40.2 \le X/d \le 57.15$ for $\mathrm{Re}_j = 10000$ is very high compared to the variation in the other two jet Reynolds numbers $\mathrm{Re}_j = 5000$ and $\mathrm{Re}_j = 7500$. The reason may be due to the increase in the strength of the jets with an increase in the jet velocity which causes the variation in the local Nusselt number to be less sensitive with respect to the outflow orientation.

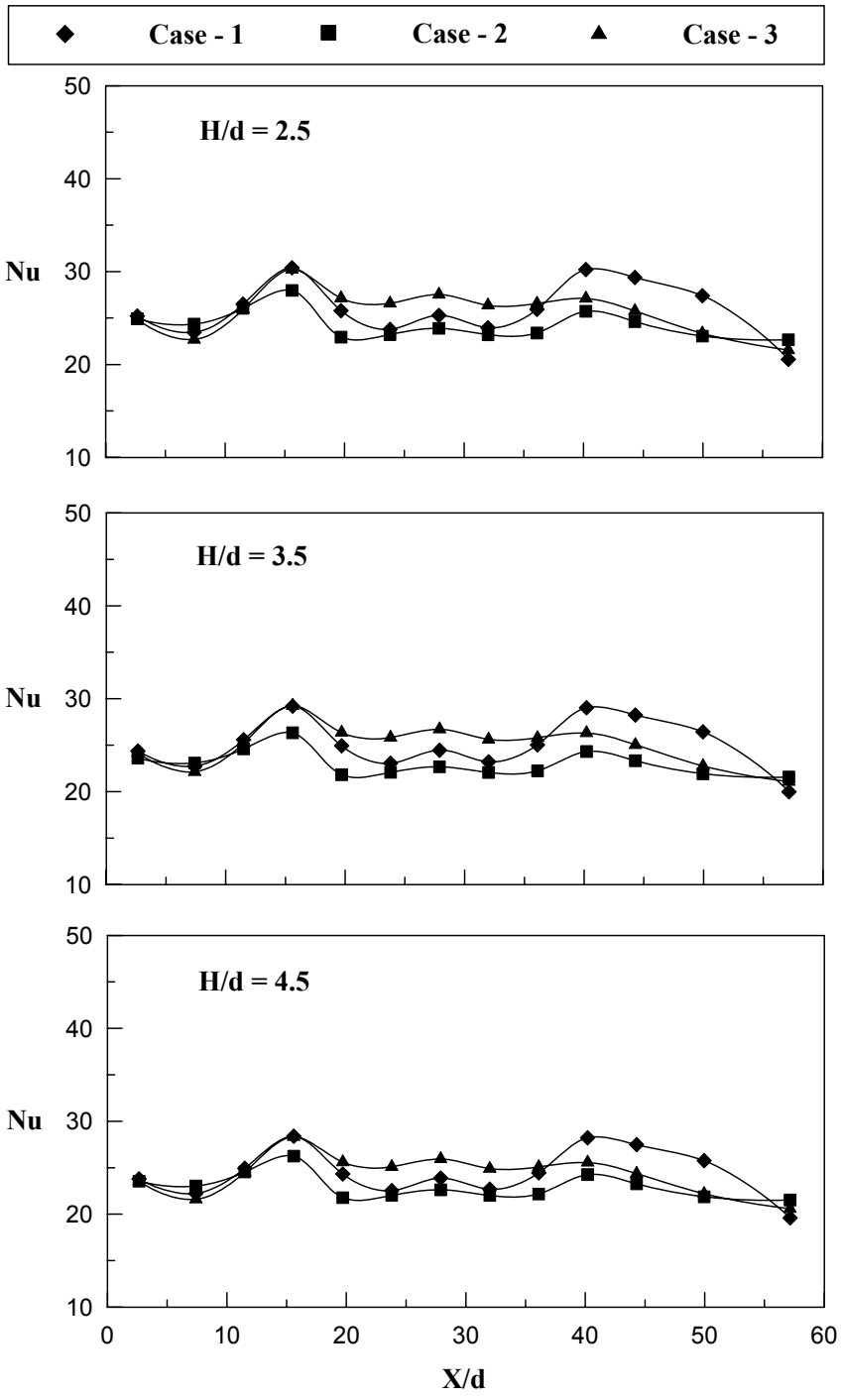

Figure 4.8 Effect of outflow orientation and feeding channel aspect ratio $2.5 \le H/d \le 4.5$ on local Nusselt number distribution for $S/d = 3$ and $\mathrm{Re}_j = 7500$.

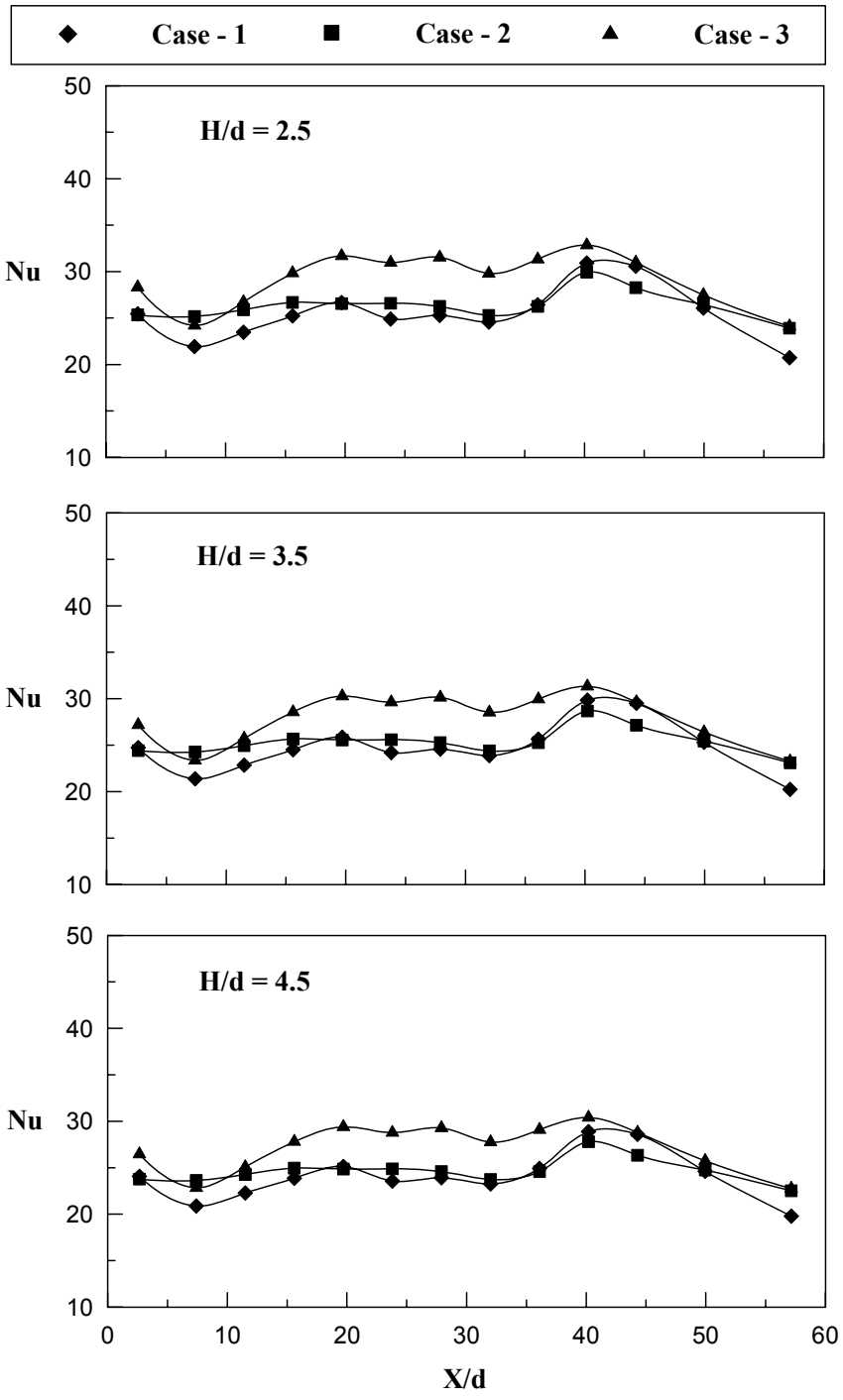

Figure 4.9 Effect of outflow orientation and feeding channel aspect ratio $2.5 \le H/d \le 4.5$ on local Nusselt number distribution for $S/d = 3$ and $\mathrm{Re}_j = 10000$.

4.4 Effect of jet-to-plate distance on local Nusselt number

Figure 4.10 – 4.12, gives a detail insight into the effect of the feeding channel aspect ratio $2.5 \le H/d \le 4.5$ on the local Nusselt number distribution for different jet-to-plate distances $(2 \le S/d \le 4)$ with $\mathrm{Re}_j = 10000$ for all the outflow orientations on the heat transfer from the target surface. Jet Reynolds number $\mathrm{Re}_j = 10000$ is selected as this gives the maximum heat transfer among all the jet Reynolds numbers studied.

Figure 4.10 shows the local Nusselt number distribution over the entire length of the target surface for case – 1, where the flow exits at low X/d $(X/d = 0)$. The crossflow develops from large X/d $(X/d = 57.15)$ to low X/d $(X/d = 0)$ therefore a corresponding decrease in the heat transfer is observed from larger X/d to low X/d. The above phenomenon is observed for all the H/d values $2.5 \le H/d \le 4.5$. The heat transfer from the target surface decreases with an increase in jet-to-plate distance from $S/d = 4$ to 8, this behavior is observed for all the feeding channel aspect ratios studied. Over the entire length of the target surface, the jet-to-plate distance $S/d = 2$ gives the maximum heat transfer and $S/d = 4$ gives the least heat transfer among all the S/d values and for all the feeding channel aspect ratios studied. Observing the effect of the feeding channel aspect ratio on the local Nusselt number distribution, $H/d = 2.5$ gives the maximum heat transfer for the cases studied. $H/d = 2.5$ gives a maximum of 6% increase in local Nusselt number compared to $H/d = 3.5$, whereas a maximum of 11.8% more heat transfer is observed compared to $H/d = 4.5$. It is also observed that the magnitude of local Nusselt number at $40.2 \le X/d \le 57.15$ is more compared to that at $15.6 \le X/d \le 36.1$, this is due to the strong impingement of the jets and less crossflow effect as the flow first enters the impingement

channel at this location. At $15.6 \le X/d \le 36.1$ crossflow dominates the impingement of jets and leads to lesser magnitude of the local Nusselt number.

Figure 4.11 shows the effect of the jet-to-plate distance on the local Nusselt number distribution for case – 2 comparing different feeding channel aspect ratios $2.5 \le H/d \le 4.5$ for $\mathrm{Re}_j = 10000$. For case – 2 the flow exits at low X/d $(X/d = 0)$, which shows the development of crossflow towards low X/d. Similar to case – 1, $S/d = 2$ has the maximum heat transfer from the entire length of the target surface for all the H/d values examined $2.5 \le H/d \le 4.5$. Among all the feeding channel aspect ratios studied, $H/d = 2.5$ gives the maximum amount of heat transfer from the entire target surface. Although the Nusselt number distribution for $H/d = 3.5$ *and* 4.5 is similar $H/d = 2.5$ has a marginal increase in heat transfer from the target surface compared to $H/d = 3.5$ whereas a maximum of 9.1% increase in heat transfer is observed compared to $H/d = 4.5$. It is observed that the local Nusselt number distribution for $H/d = 9$ is less sensitive for a change in the jet-to-plate distance as the magnitude of local Nusselt number is similar with a very less difference in magnitude. For the feeding channel aspect ratios $H/d = 2.5$ and $H/d = 3.5$, the change in jet-to-plate distance has considerable variation on the local Nusselt number distribution compared to $H/d = 4.5$. The maximum variation in the magnitude of the local Nusselt number for $H/d = 3.5$ *and* 4.5 with respect to the jet-to-plate distance is 5%.

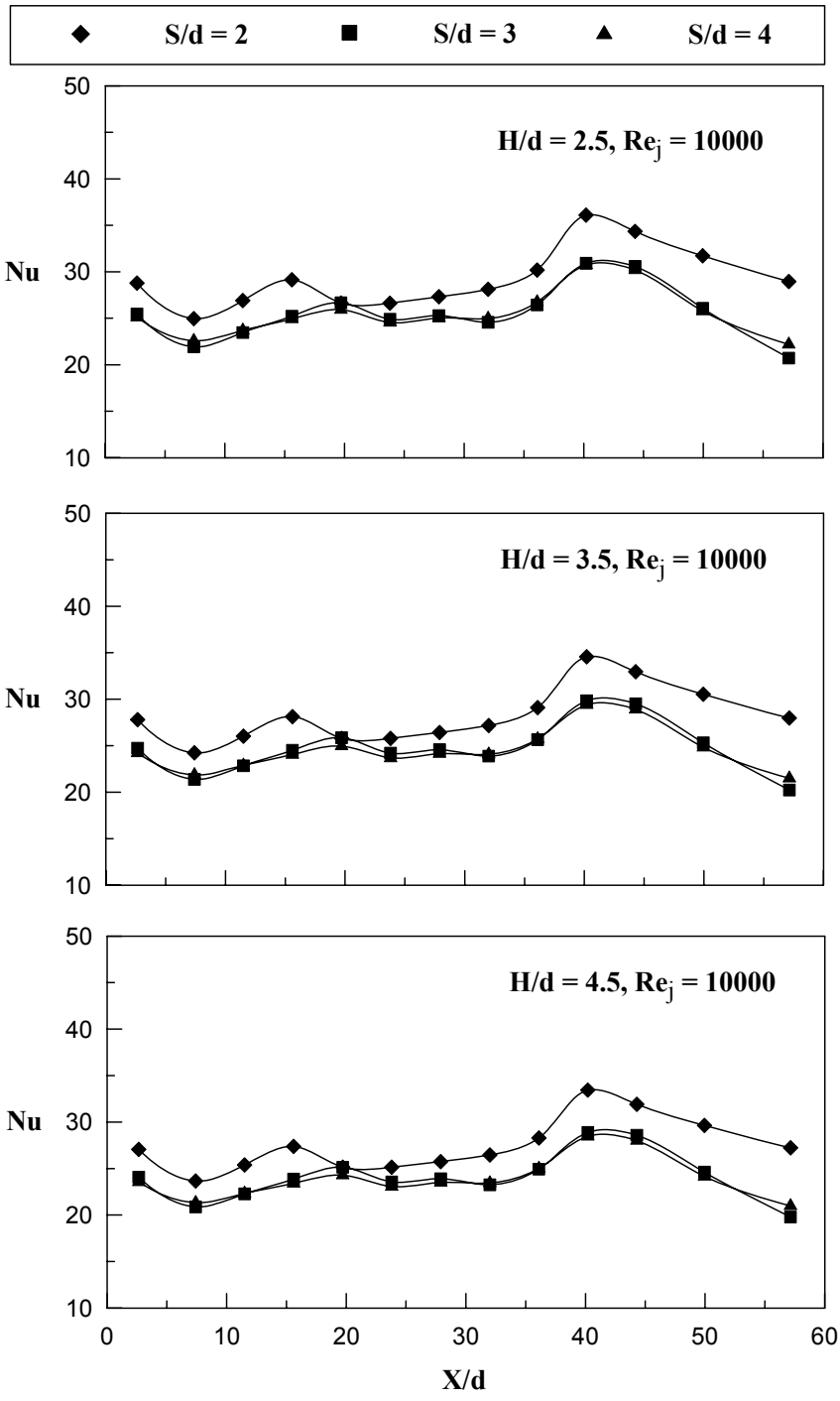

Figure 4.10 Effect of jet-to-plate distance and feeding channel aspect ratio $2.5 \le H/d \le 4.5$ on local Nusselt number distribution for $\mathrm{Re}_j = 10000$ and case – 1.

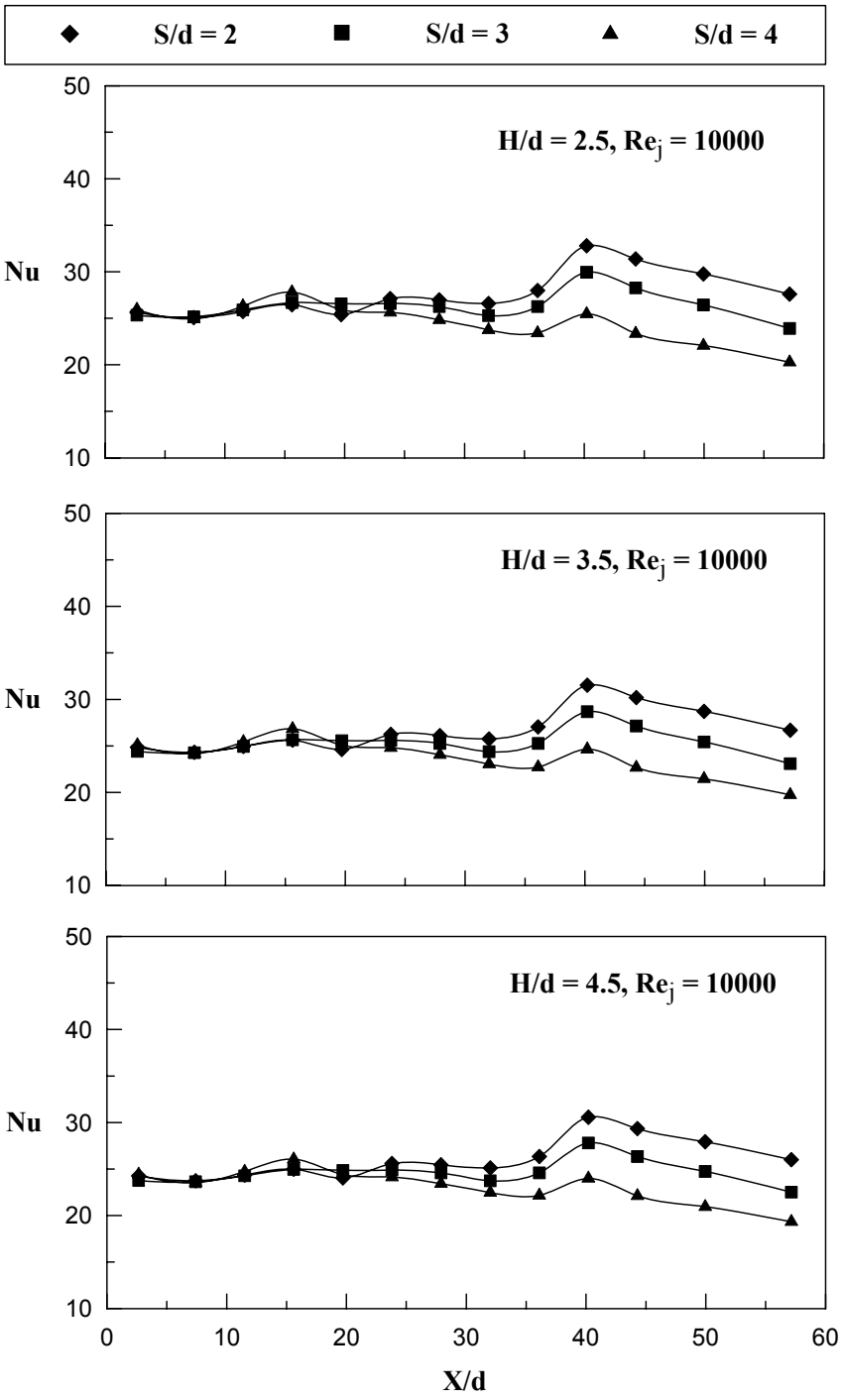

Figure 4.11 Effect of jet-to-plate distance and feeding channel aspect ratio $2.5 \le H/d \le 4.5$ on local Nusselt number distribution for $\mathrm{Re}_j = 10000$ and case – 2.

Figure 4.12 shows the effect of the jet-to-plate distance on the local Nusselt number distribution for case – 3 comparing different feeding channel aspect ratios $2.5 \le H/d \le 4.5$ for $\mathrm{Re}_j = 10000$. For case – 3 air exits at $X/d = 0$ and $(X/d = 57.15)$, where the crossflow has a predominant effect over the heat transfer characteristics. It is observed that at $40.2 \le X/d \le 57.15$ the local Nusselt number decreases towards exit i.e. at large X/d $(X/d = 57.15)$ for all the H/d values examined $2.5 \le H/d \le 4.5$. The heat transfer at $15.6 \le X/d \le 36.1$ has less magnitude of local Nusselt number this may be due to the effect of the crossflow dominating the strength of the impinging jets. For an increase in jet-to-plate distance a corresponding decrease in local Nusselt number is observed. Investigating the effect of feeding channel aspect ratio, $H/d = 2.5$ gives the highest heat transfer similar to case – 1 and case – 2. $H/d = 4.5$ gives very less values of local Nusselt number compared to $H/d = 2.5$, further a maximum of 11% more heat transfer is observed compared to $H/d = 3.5$. Among all the jet-to-plate distances investigated $S/d = 2$ gives the maximum heat transfer over the entire length of the target surface, this is due to the strong impingement of the jets, with less travel distance, which thins the boundary layer resulting in high values of local Nusselt number. Whereas $S/d = 4$ gives the minimum values of the local Nusselt number over the entire length of the target surface similar to the other two outflow orientations discussed earlier.

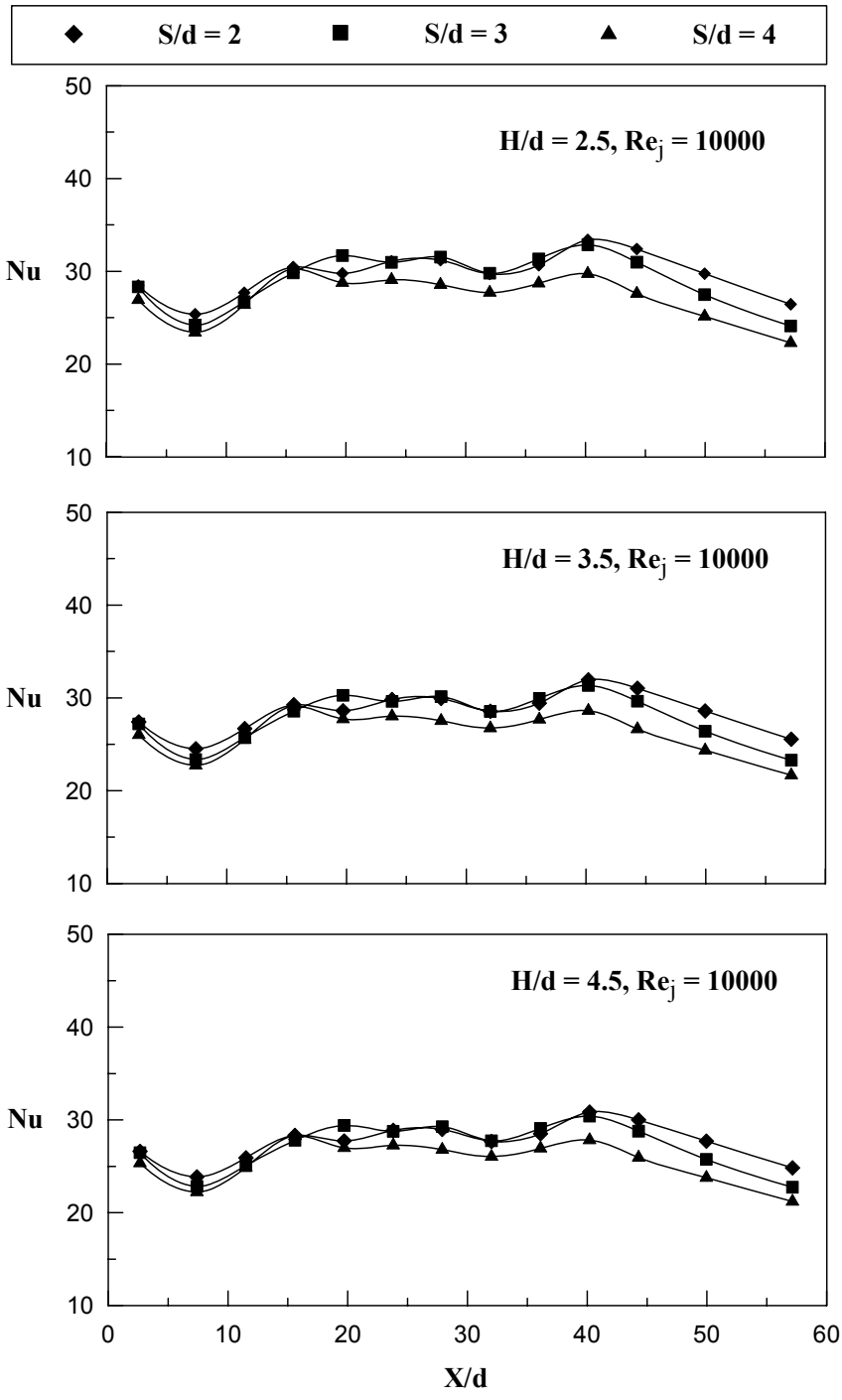

Figure 4.12 Effect of jet-to-plate distance and feeding channel aspect ratio $2.5 \le H/d \le 4.5$ on local Nusselt number distribution for $\mathrm{Re}_j = 10000$ and case – 3.

4.5 Averaged Nusselt Number

Figures 4.13 – 4.14 shows the averaged Nusselt number Nu_{avg} as a function of jet Reynolds number Re_j, considering all the outflow orientations, the feeding channel aspect ratio $2.5 \le H/d \le 4.5$. The value of Nu_{avg} is an average of the detailed results on the entire target plate surface. The detailed results from the present study are averaged over the entire target plate to produce a single averaged Nusselt number.

4.5.1 Effect of feeding channel aspect ratio

Figure 4.13 shows the effect of the feeding channel aspect ratio $2.5 \le H/d \le 4.5$ for averaged Nusselt number as a function of the jet Reynolds number for all the outflow orientations studied. The averaged Nusselt number increases linearly with an increase in the jet Reynolds number. It is also observed that as the feeding channel aspect ratio H/d increases from 2.5 to 3.5 there is a corresponding decrease in the magnitude of the averaged Nusselt number and with an increase of H/d from 3.5 to 4.5 there is a corresponding decrease in the magnitude of averaged Nusselt number, indicating decrease in the strength of the impinging jets with an increase in the feeding channel aspect ratios. For $\mathrm{Re}_j = 10000$, the difference in the magnitude of the average Nusselt number is quite large compared to the other two jet Reynolds numbers studied. The jet Reynolds number $\mathrm{Re}_j = 5000$, is less sensitive to the jet-to-plate distance as there is no much variation observed from the magnitude of the averaged Nusselt number. Large variation in the averaged Nusselt number is observed at less value of the feeding channel aspect ratios $H/d = 2.5$ and $H/d = 3.5$,

whereas the feeding channel aspect ratio $H/d = 4.5$ is less sensitive. Case – 1 and case – 3 have the maximum values of averaged Nusselt number compared to case – 2 as the flow exit in opposite direction compared to the flow entry, which causes crossflow obstructing the impingement of jets.

4.5.2 Effect of outflow orientation

Figure 4.14 shows the averaged Nusselt number distribution as a function of jet Reynolds number. The effect of feeding channel aspect ratio $2.5 \le H/d \le 4.5$ is shown in detail. It is observed that as the feeding channel aspect ratio is increased from 2.5 to 3.5 there is a corresponding decrease in the values of averaged Nusselt numbers, whereas a further decrease in the feeding channel aspect ratio from 3.5 to 4.5 leads to a further decrease in the averaged Nusselt number this may be due to the disturbance caused to the impinging jet with an increase in the crossflow at high feeding channel aspect ratios. This implies that $H/d = 2.5$ gives the maximum values of heat transfer among all the feeding channel aspect ratios studied. Among all the outflow orientations studied, case – 3, the case where the flow exits in both the directions $X/d = 0$ and $X/d = 57.15$ has the high amount of heat transferred from the target surface, where as case – 2 has the least amount of heat transferred from the target surface for all the feeding channel aspect ratios examined, this may be because of the flow exit in opposite direction as to that of the entry in the impingement channel. Case – 2 has the least amount of heat transferred from the target surface, this may also be due to the obstruction caused to the flow of jets at large X/d due to the crossflow of the air at the exit of the impingement channel.

The feeding channel aspect ratio $H/d = 4.5$ gives a very less variation in the averaged Nusselt number with respect to the outflow orientations at all the jet Reynolds numbers, where as for $H/d = 2.5$ *and* 3.5 a considerable variation in the magnitude of averaged Nusselt number is observed. The jet Reynolds number $\mathrm{Re}_j = 5000$, is less sensitive to the outflow orientation as there in no much variation observed in the magnitude of the averaged Nusselt number at this location.

Among all the feeding channel aspect ratios studied $H/d = 2.5$ gives the highest values of averaged Nusselt number indicating high heat transfer from the target surface for all the jet-to-plate distances studied, whereas $H/d = 4.5$ gives the least amount of heat transfer. The feeding channel aspect ratio $H/d = 4.5$ gives the less values of averaged Nusselt number compared to $H/d = 3.5$ because of the disturbance caused to the boundary layer due to crossflow, which becomes more severe at very less H/d values, a maximum difference of 4% is observed in the magnitude of the averaged Nusselt number.

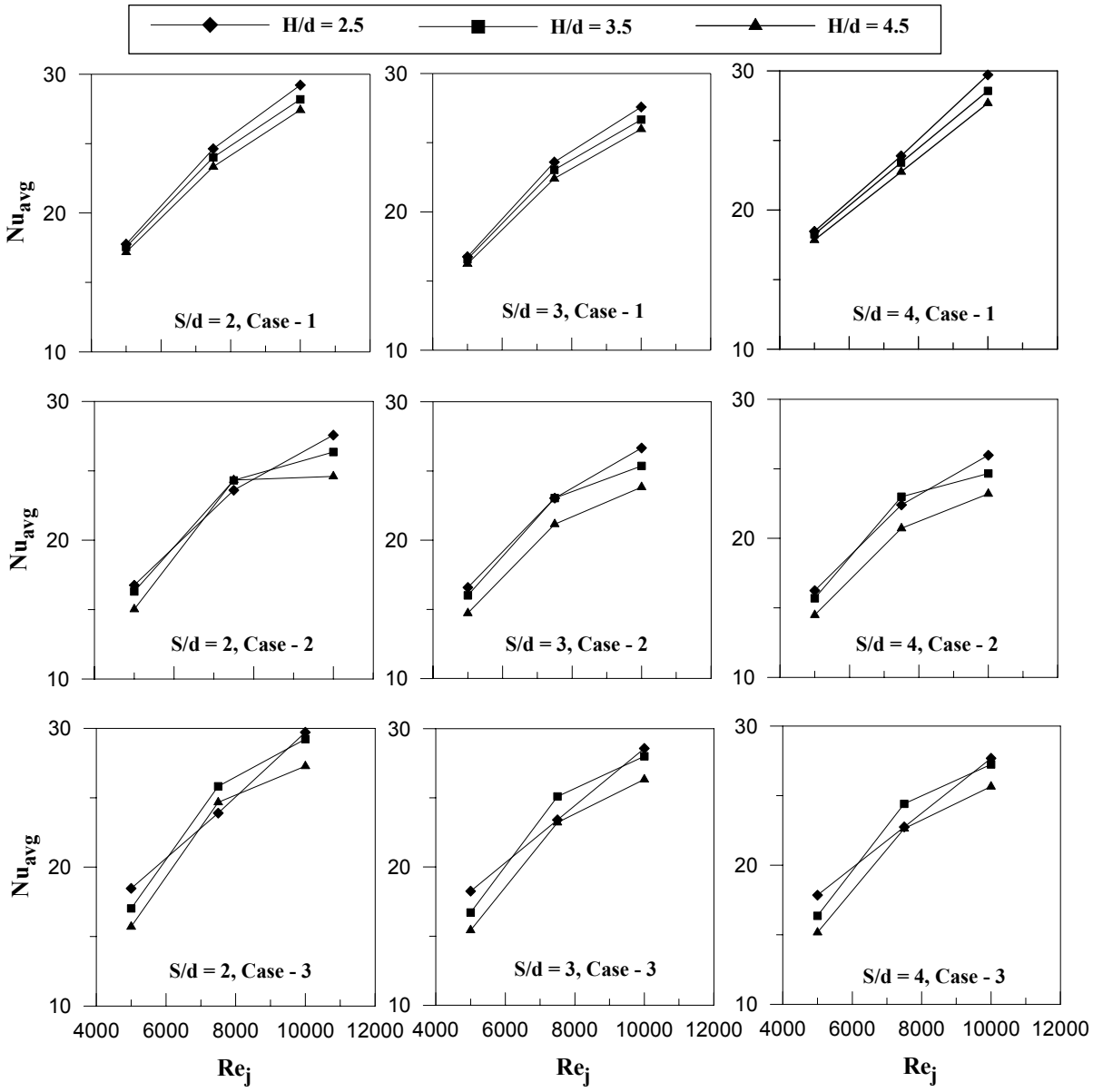

Figure 4.13 Effect of feeding channel aspect ratio $2.5 \le H/d \le 4.5$ and jet-to-plate distances on averaged Nusselt number for different outflow orientation.

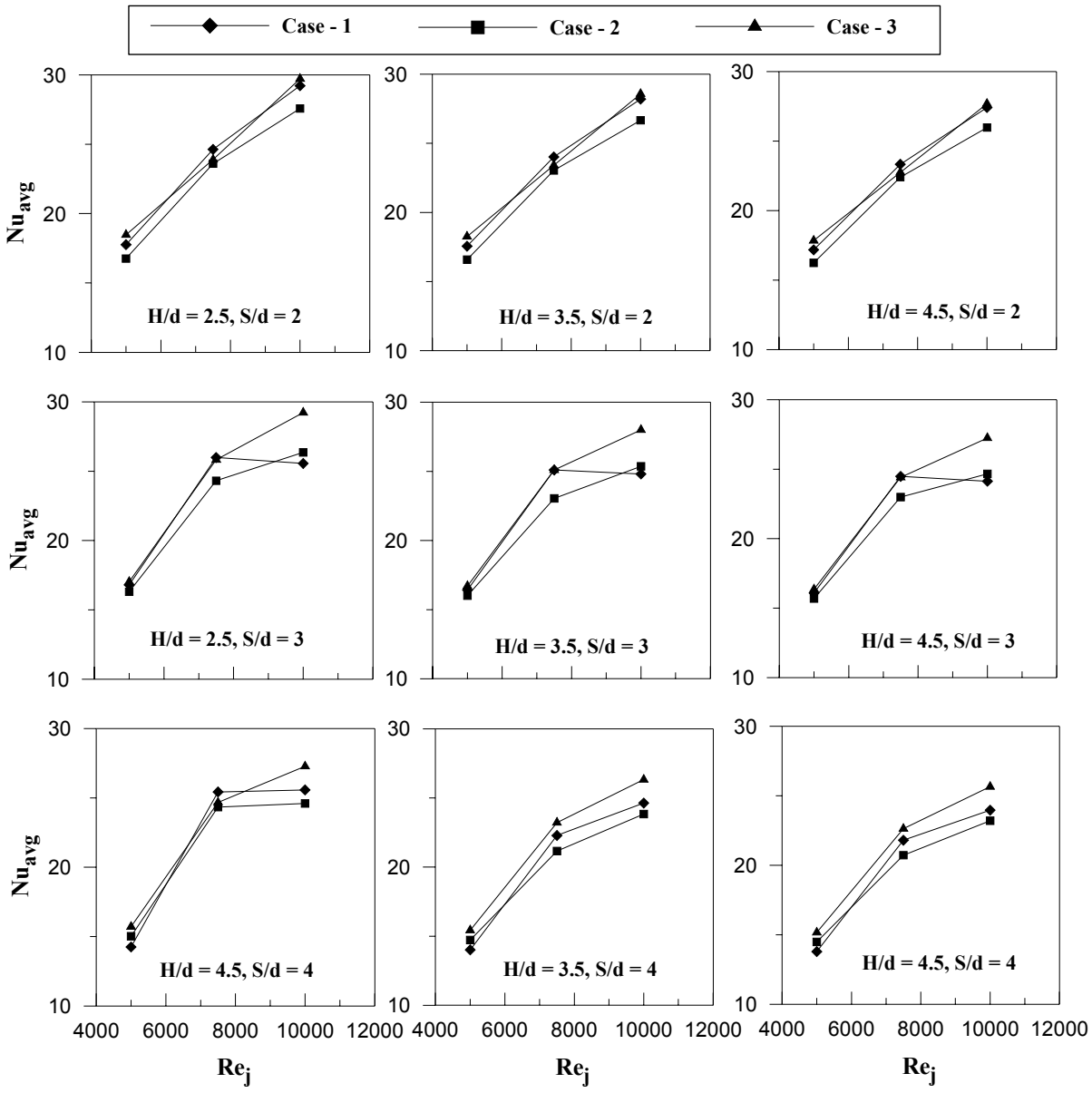

Figure 4.14 Effect of outflow orientation and feeding channel aspect ratio on averaged Nusselt number for different jet-to-plate distances $(2 \le S/d \le 4)$.

4.5.3 Correlations of averaged Nusselt number

The results for three different outflow orientations are correlated for the jet Reynolds number Re_j and the normalized jet-to-plate distance S/d dependence as

$$Nu_{avg} = A(\mathrm{Re}_j)^B (S/d)^C (H/d)^D \qquad (4.2)$$

The present results are correlated for all outflow orientations individually for jet Reynolds number Re_j dependence as shown in Figure 4.15. Previous studies in the field of jet impingement have involved in developing correlations for the averaged Nusselt number as a function of the jet Reynolds number by considering many parameters. Correlations by Huang et al [21], Kercher and Tabakoff [30] and Florscheutz et al [14] are compared to the averaged Nusselt number in the present investigation. Huang et al [21] studied the outflow orientations similar to ones used in the present study. They presented results for the outflow orientation 1 and 2 correlating for Reynolds number dependence as $Nu = 0.035\,\mathrm{Re}^{0.76}$, whereas for outflow orientation 3 which has the highest magnitude of heat transferred from the target surface is correlated as $Nu = 0.082\,\mathrm{Re}^{0.727}$. Kercher and Tabakoff [30] also studied the effect of crossflow and it is similar to the case – 1 in the present study. They varied the jet hole diameter, the hole spacing x, y and the jet to target plate distance. Based on all of these geometrical parameters, they proposed a correlation of the form $Nu = \phi_1 \phi_2\,\mathrm{Re}^m (z/d)^{0.91}\,\mathrm{Pr}^{1/3}$, where ϕ_1 and ϕ_2 are constants based on X/d and Y/d, respectively. Florschuetz et al [14] presented the correlations with different coefficients of

inline and staggered rows. The correlation for jet impingement with minimum crossflow is given as $Nu = 0.363(X/d)^{-0.554}(Y/d)^{-0.422}(Z/d)^{0.068}\,\mathrm{Re}_j^{-0.554}\,\mathrm{Pr}^{1/3}$.

The detailed values of the local Nusselt number are averaged over the entire length of the target surface to obtain an single averaged Nusselt number. The averaged Nusselt numbers for each outflow orientation are plotted against the jet Reynolds number. The present results are correlated for the jet Reynolds number dependence as $Nu_{avg} = 0.0407\,(\mathrm{Re}_j)^{0.757}(S/d)^{0.611}(H/d)^{1.795}$ for case 1 and 2. The correlations for Huang et al [21] for case 1 and 2 are in good comparison with the present study. Kercher and Tabakoff [30] presented the results for the outflow orientation – 1 and the results of the present study are in good comparison with the existing correlation. The case with maximum heat transfer from the target surface, outflow orientation – 3, is correlated for the jet Reynolds number dependence as $Nu_{avg} = 0.0387\,(\mathrm{Re}_j)^{0.694}(S/d)^{0.243}(H/d)^{2.183}$. The correlation used from Florschuetz et al [14] is for the case with minimum crossflow. Huang et al [21] also presented a separate correlation for the case with high heat transfer, this case in their study had the less crossflow effect. The results from the present study for case – 3 are lower than the existing correlations, which includes the crossflow effect. The correlation for case – 3 in the present study is in good agreement with the correlation presented by Florschuetz et al [14] and Huang et al [21]. Thus it is evident from the above discussion that the crossflow effect is more dominant on outflow orientation 1 and 2 compared to outflow orientation – 3.

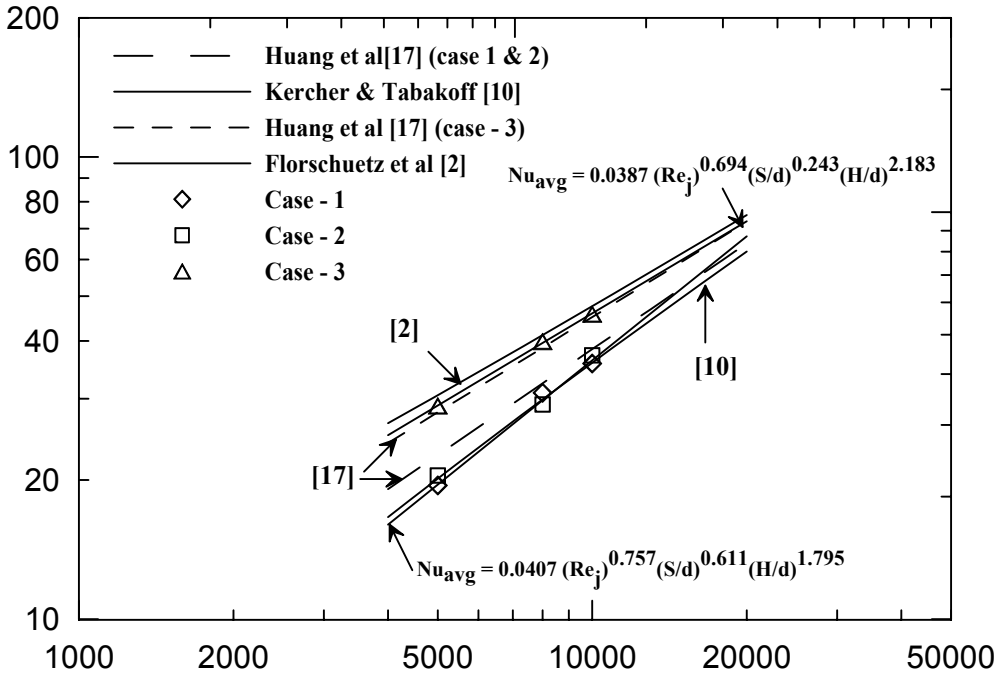

Figure 4.15 Averaged Nusselt number comparisons with the existing correlations

CHAPTER 5

ORIFICE PLATE – 1 & 2

Jet impingement heat transfer is dependent on several flow and geometrical parameters. The jet impingement Nusselt number is presented as a functional form of,

$$Nu_i = \left(\frac{h_i \;\; d}{k_{air}} \right) = f\left[\mathrm{Re}_j,\ (X, H),\ \ outflow \;\; orientation, orifice \;\; jet \;\; size \right] \qquad (5.1)$$

Where, Re_j is the flow parameter, jet spacing to the Hydraulic diameter (considered as the width of the feeding channel) ratio X and jet-to-plate distance S are the geometric parameters. The flow exit direction, orifice jet diameter and the jet-to-plate distance are also important parameters having a significant effect on impingement heat transfer.

Figure 2.3 shows three cases where air comes into the feeding channel and leaves through jets made in the orifice jet plate to impinge on the heated target surface located in the impingement channel. For all the three cases air enters the feeding channel at $X = 57.15\,cm$. For case 1, air exits the impingement channel at low X $(X = 0\,cm)$ and therefore the crossflow develops towards the exit. This case is typical of that seen by [2]Flournsheutz et al. For case 2, the flow exits the impingement channel at $X = 57.15\,cm$ and as the flow moves forward from low X crossflow develops at low X and increases towards large X ($X = 57.15\,cm$). For case 3, flow exits the impingement channel at both the directions i.e., at $X = 0 \; and \; 57.15\,cm$ and the crossflow develops towards both the ends of the test section.

Tests were carried out for three different outflow orientations with Reynolds number ranging between $5000 \le \mathrm{Re}_j \le 10000$ and with two-orifice jet diameters $d = 0.5\ and\ 1\,cm$ respectively by varying the feeding channel width H. Three different values of jet-to-plate distances $(2.5cm \le H \le 4.5cm)$ were considered while carrying out the experiments.

Outflow orientation affects the flow inside the impingement channel and leads into different heat transfer characteristics. As air impinges on the target surface, crossflow starts developing and grows continuously towards the exit resulting into thicker boundary layer, which suppresses the jet impingement effect. In addition, crossflow causes distortion to the jet impingement in which the jet is no longer impinging normally on the target surface.

All the results presented in this paper are for $2.65cm \le X \le 57.15cm$ over the entire span of the target plates. Where X is defined from the opposite end of the feeding channel of the test section as shown in figure 2.2. All the results discussed in the sections followed are being extracted using the orifice plates with jet diameters 0.5 and 1 cm respectively.

The local Nusselt number distribution for all the three outflow orientations by varying the jet-to-plate distance is presented in detail, as a function of non-dimensional location X on the target surface for jet Reynolds number Re_j and jet-to-plate distance S in the forthcoming discussion.

5.1 Effect of feeding channel aspect ratio on local Nusselt number

Figure 5.1 – 5.3, gives a detail insight into the local Nusselt number distribution presenting the effect of feeding channel width $(2.5cm \le H \le 4.5cm)$ on the heat transfer from the target surface. All the outflow orientations are discussed.

Figure 5.1 shows effect of feeding channel width and two orifice jet sizes $d = 0.5\ and\ 1\,cm$ on the local Nusselt number distribution over the entire length of the target surface for case – 1, where the flow exits at low X $(X = 0\,cm)$. The crossflow develops from large X to low X as the air exits at low X. The heat transferred from the target surface decreases with an increase in feeding channel width from $H = 2.5\,cm$ to $H = 4.5\,cm$ for all the feeding channel widths for both the orifice jet sizes. Over the entire length of the target surface, the feeding channel width $H = 2.5\,cm$ gives the maximum heat transfer for all the jet Reynolds numbers $\left(5000 \le \mathrm{Re}_j \le 10000\right)$ studied. This is primarily due to the increase in the strength of the jets at low feeding channel widths. Observing the effect of the feeding channel width on the local Nusselt number distribution for all the jet Reynolds numbers studied, $H = 2.5\,cm$ gives the maximum heat transfer among all the feeding channel widths studied. The difference in the magnitude of the local Nusselt number for all the feeding channel widths studied is very less for all the jet Reynolds number studied. This is observed from the marginal difference in magnitude for orifice jet size $d = 1\,cm$, whereas the increase in the magnitude of the local Nusselt number from $H = 3.5\,cm$ to $H = 2.5\,cm$ is high at low jet Reynolds numbers for orifice jet size $d = 0.5\,cm$ Among all the jet Reynolds numbers studied, $\mathrm{Re}_j = 10000$ gives the maximum heat transfer. As discussed earlier in figure 6, a peak of local Nusselt number at $X = 40.02\,cm$ is observed this is due to the flow entering the impingement channel at large X/d, where the effect of crossflow is minimal. At $15.6\,cm \le X \le 36.1\,cm$ crossflow dominates the impingement of jets and a linearly decreasing distribution of local Nusselt number is observed towards the exit.

Figure 5.2 shows the effect of the feeding channel width and two orifice jet sizes $d = 0.5\ and\ 1\,cm$ on the local Nusselt number distribution for case – 2. For case – 2 the flow exits at low X $(X = 0\,cm)$, causing crossflow development towards the exit. The magnitude of local Nusselt number observed for the case – 2 is less compared to case – 1. $H = 2.5\,cm$ gives the maximum heat transfer over the entire length of the target surface for both the orifice jet sizes and all the jet Reynolds numbers studied. For all the jet Reynolds numbers studied, $H = 2.5\,cm$ gives a marginal increase in heat transfer from the target surface compared to $H = 3.5\,cm$ whereas $H = 2.5\,cm$ gives a maximum of 4% increase in heat transfer is observed compared to $H = 4.5\,cm$, for orifice jet size $d = 1\,cm$. Whereas for $d = 0.5\,cm$, a considerable increase in local Nusselt number is observed for an decrease in feeding channel width from $H = 3.5\,cm$ to $H = 2.5\,cm$. It is also observed that the magnitude of the local Nusselt number increases with an increase in the jet Reynolds number for all the feeding channel widths studied. The variation in the local Nusselt number is more sensitive with respect to a change in feeding channel width at high jet Reynolds number whereas it is less sensitive at low jet Reynolds numbers. At $40.02\,cm \le X \le 57.15\,cm$ the magnitude of local Nusselt number decreases from $X = 40.02\,cm$ to $X = 57.15\,cm$, this is due to the obstruction caused by the crossflow to the impinging jets.

Figure 5.3 shows the effect of feeding channel width and two orifice jet sizes $d = 0.5\ and\ 1cm$ on the local Nusselt number distribution for case – 3 . For case – 3 air exits at $(X = 0\,cm)$ and $(X = 57.15\,cm)$, where the crossflow has a predominant effect over the heat transfer characteristics. For both the orifice jet sizes studied, it is observed that at $0\,cm \le X \le 15.6\,cm$ and $40.02\,cm \le X \le 57.15\,cm$ the

local Nusselt number decreases towards exit, this may be due to the crossflow at the exit that reduces the strength of the impinging jets and the heat transferred from the target surface. The magnitude of local Nusselt number at $15.6\,cm \le X \le 36.1\,cm$ is high compared to the other X/d locations this may be due to the strong impingement of jets. For an increase in feeding channel width a corresponding decrease in local Nusselt number is observed. $H = 2.5\,cm$ gives the maximum values of local Nusselt numbers for all the jet Reynolds numbers and both the orifice jet sizes studied. Considering the effect of feeding channel width for all jet Reynolds numbers on heat transfer characteristics in detail, $H = 2.5\,cm$ gives the highest heat transfer similar to case – 1 and case – 2. For $d = 1cm$, the increase in magnitude of Nusselt number for an increase in the feeding channel ratio is marginal. Whereas for $d = 0.5\,cm$, $H = 2.5cm$ gives a marginal increase in heat transfer compared to $H = 3.5\,cm$, further $H = 2.5\,cm$ gives a maximum of 5% more heat transfer compared to $H = 4.5\,cm$. The distribution of the local Nusselt number for $d = 0.5\,cm$ is uniform over the entire length of the target surfaces as studied in the previous cases. Similar to case – 1 and case – 2, with respect to the effect of feeding channel width on local Nusselt number characteristics it is observed that the local Nusselt number is sensitive to a change in feeding channel width at high jet Reynolds numbers.

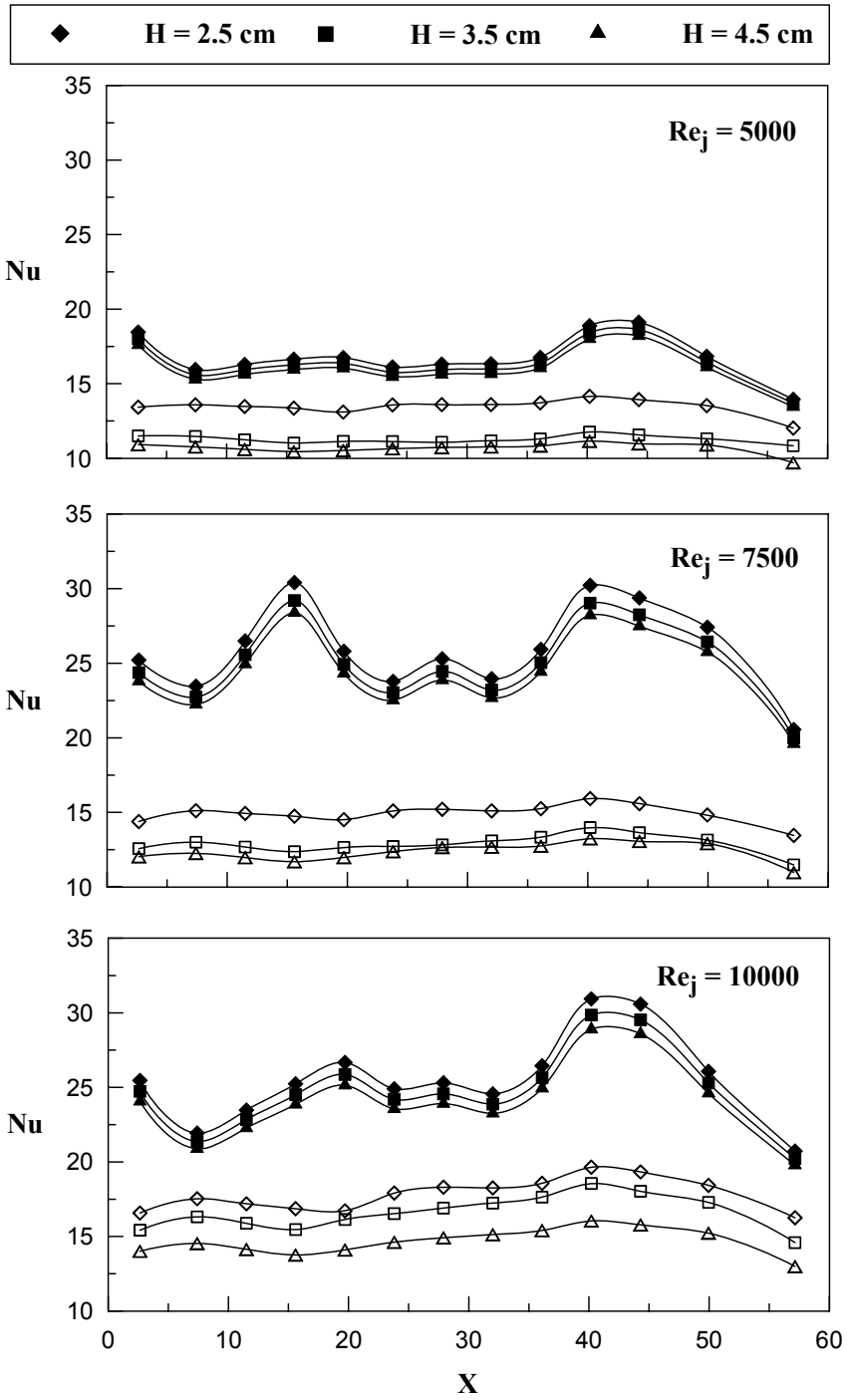

Figure 5.1 Effect of feeding channel aspect ratio $2.5\,cm \le H/d \le 4.5\,cm$ on local Nusselt number distribution for case – 1 and $S = 3\,cm$. (Filled symbol: $d = 1\,cm$ and Unfilled symbol: $d = 0.5\,cm$)

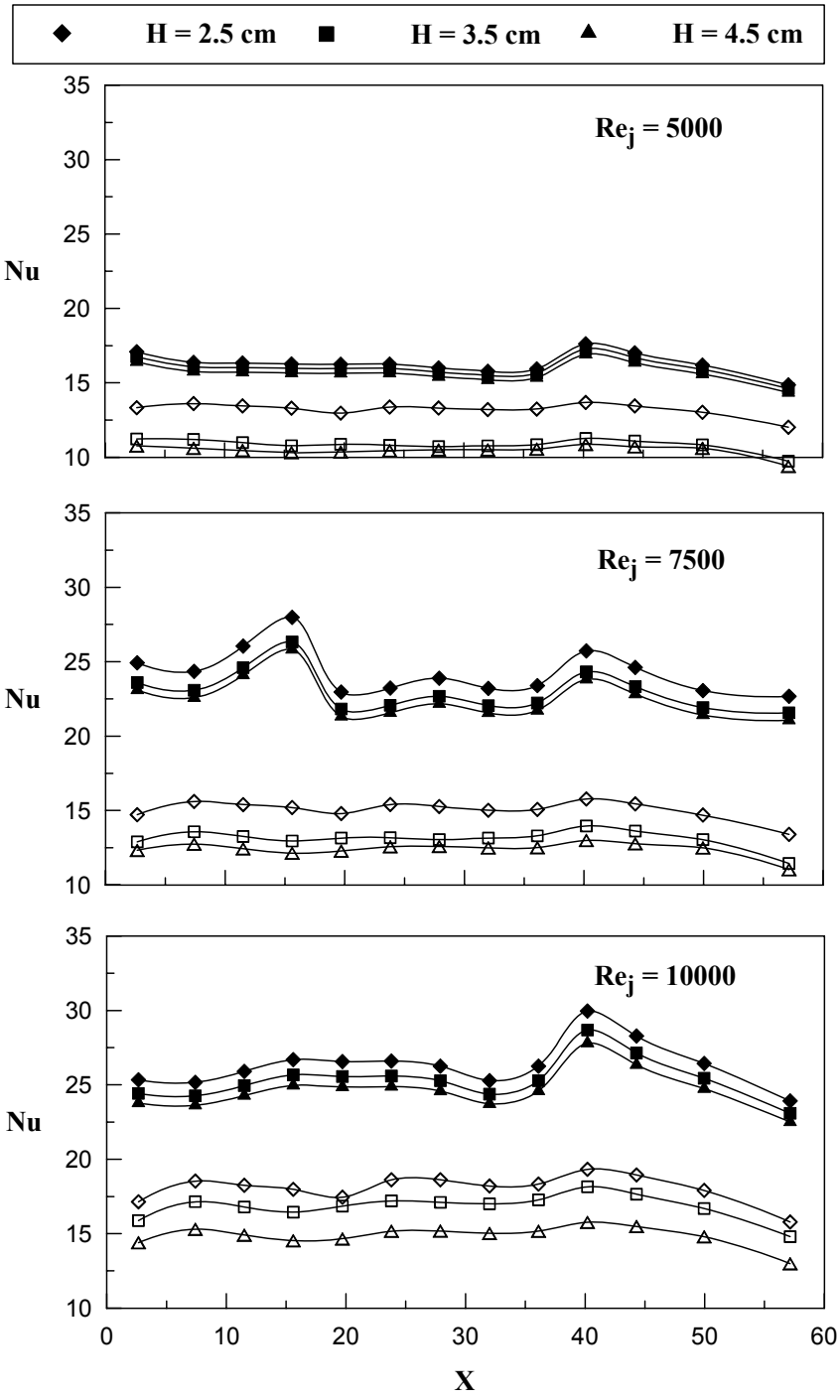

Figure 5.2 Effect of feeding channel aspect ratio $2.5\,cm \le H/d \le 4.5\,cm$ on local Nusselt number distribution for case – 2 and $S = 3\,cm$. (Filled symbol: $d = 1\,cm$ and Unfilled symbol: $d = 0.5\,cm$)

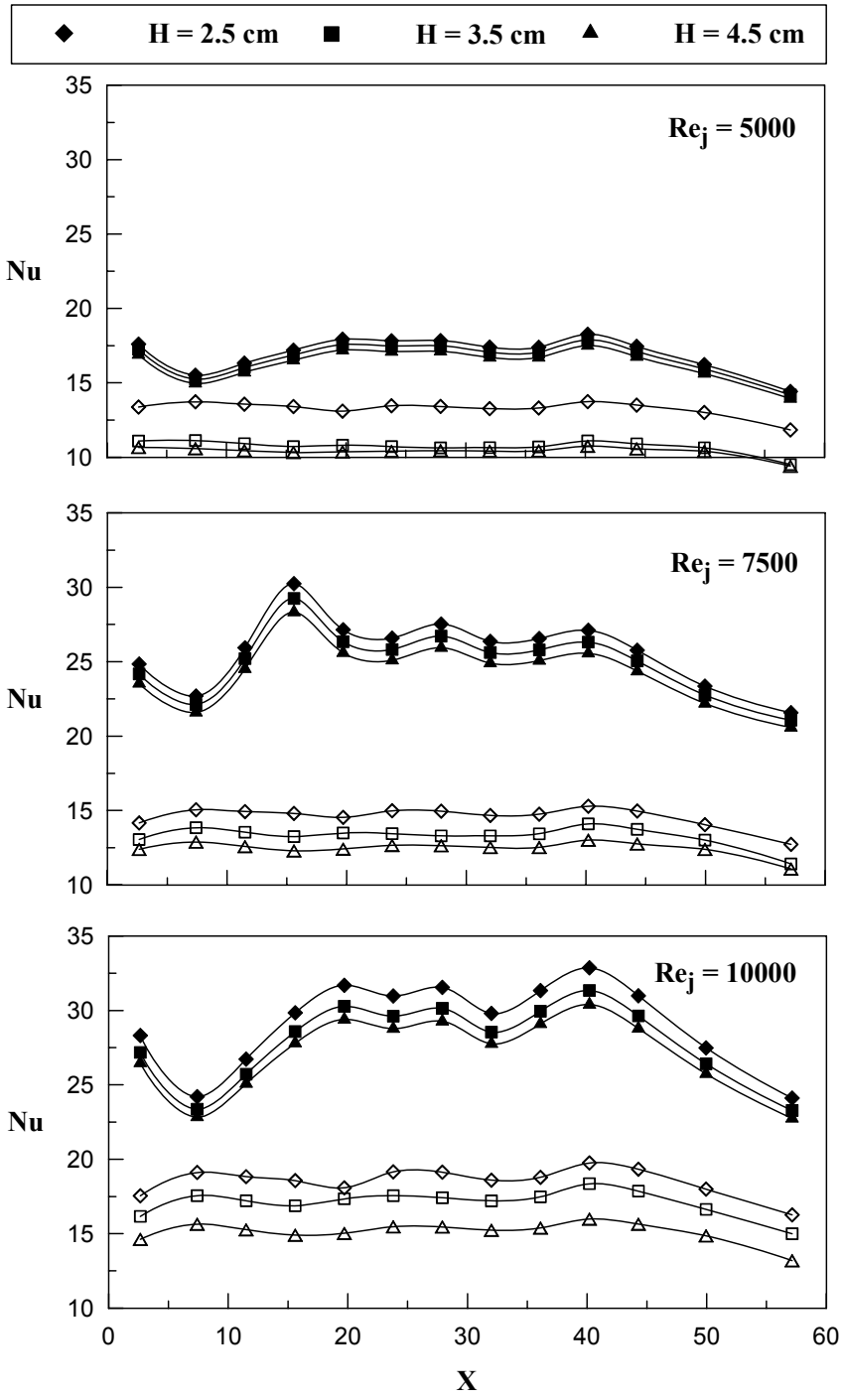

Figure 5.3 Effect of feeding channel aspect ratio $2.5\,cm \le H/d \le 4.5\,cm$ on local Nusselt number distribution for case – 3 and $S = 3\,cm$. (Filled symbol: $d = 1\,cm$ and Unfilled symbol: $d = 0.5\,cm$)

5.2 Effect of jet Reynolds number on local Nusselt number

Figure 5.4 – 5.6, gives a detail insight into the local Nusselt number distribution presenting the effect of jet Reynolds number $\left(5000 \le \mathrm{Re}_j \le 10000\right)$ on the heat transfer from the target surface. All the outflow orientations are discussed.

Figure 5.4 shows the local Nusselt number distribution plotted for case – 1, which gives a detailed insight into the effect of the feeding channel width. Three different values of the feeding channel width and two orifice jet sizes $d = 0.5 \; and \; 1\,cm$ are considered in this part of the study $\left(2.5cm \le H \le 4.5cm\right)$. The results are presented for three jet Reynolds numbers $\left(5000 \le \mathrm{Re}_j \le 10000\right)$. The distribution of the local Nusselt number is uniform across the entire length of the target surface for orifice jet size $d = 0.5\,cm$. It is observed that for an increase in the jet Reynolds number there is a corresponding increase in the magnitude of local Nusselt number. Highest values of local Nusselt number are observed for $\mathrm{Re}_j = 10000$ compared to the other two jet Reynolds numbers. Increasing the jet Reynolds number from $\mathrm{Re}_j = 5000$ to $\mathrm{Re}_j = 7500$ gives a maximum of 11% increase in the local Nusselt number values whereas for an increase from $\mathrm{Re}_j = 7500$ to $\mathrm{Re}_j = 10000$ a marginal increase in the magnitude of local Nusselt number is observed indicating the increase in strength of jets with an increase in jet Reynolds number for orifice jet size $d = 1\,cm$. Whereas, for $d = 0.5\,cm$, 5% increase in the magnitude of Nusselt number is observed. For case – 1, the flow exits the impingement channel at low X $(X = 0\,cm)$. At large X $(X = 40.2\,cm)$ a peak of local Nusselt number is observed this may be due to strong impingement of the air jets and also because the effect of crossflow is minimal, which reduces the boundary layer thickness.

Among all the feeding channel widths examined $(2.5cm \le H \le 4.5cm)$, $H = 2.5cm$ gives the maximum values of local Nusselt number for all the jet-to-plate distances studied. $H = 2.5cm$ gives a marginal increase in the local Nusselt number from the target surface compared to $H = 3.5cm$, whereas 6% increase in local Nusselt number is observed compared to $H = 4.5cm$. At $15.6cm \le X \le 36.1cm$ a uniform decrease in magnitude of local Nusselt number is observed, for both the orifice jet sizes, along the target surface from $X = 36.1cm$ to $X = 0cm$ for all the feeding channel widths studied, this may be due to the crossflow of the air generated towards the exit.

Figure 5.5 shows the effect of feeding channel width and two orifice jet sizes $d = 0.5 \text{ and } 1cm$ on the local Nusselt number distribution for case – 2 as a function of jet Reynolds numbers $(5000 \le \mathrm{Re}_j \le 10000)$. For case – 2 air exits the impingement channel at $X = 57.15cm$, this leads to the development of crossflow towards the exit. Similar to the case – 1 an increase in jet Reynolds number leads to the corresponding increase in the local Nusselt number for all the feeding channel widths studied. The heat transfer observed from orifice jet size $d = 1cm$ is twice to that observed using $d = 0.5cm$. As observed in case – 1 the local Nusselt number distribution for $d = 0.5cm$ is uniform across the entire length of the target surface. The magnitude of local Nusselt number at $15.6cm \le X \le 36.1cm$ is more compared to the other X/d locations this may be due to the strong impingement of jets at this location. Although similar distribution of local Nusselt number is observed for $H = 2.5cm$ and $H = 3.5cm$, but $H = 4.5cm$ gives a marginal increase in heat transfer from the entire target surface compared to $H = 3.5cm$ and $H = 2.5cm$ gives a maximum of 7%

more heat transfer from the entire target surface compared to $H = 4.5\,cm$. The local Nusselt number is sensitive for a change in jet Reynolds number, this is observed from the difference in magnitude of local Nusselt number varying with respect to jet Reynolds number. For $d = 1\,cm$, $\mathrm{Re}_j = 10000$ gives the maximum values of local Nusselt number for all the feeding channel widths studied. Nusselt number distribution for $\mathrm{Re}_j = 5000$ and $\mathrm{Re}_j = 7500$ is close with a maximum difference in magnitude being 60%. At $40.02\,cm \le X \le 57.15\,cm$, a decrease in local Nusselt number is observed from $X = 40.02\,cm$ towards the exit at $X = 57.15\,cm$, this is due to the development of crossflow towards the exit, which obstructs the impingement of jets and thickens the boundary layer. For $d = 0.5\,cm$, a uniform increase in the local Nusselt number is observed for an increase in jet Reynolds number from $\mathrm{Re}_j = 5000$ to $\mathrm{Re}_j = 7500$ and to $\mathrm{Re}_j = 10000$. This behavior of local Nusselt number at large X/d is observed for all the feeding channel widths studied.

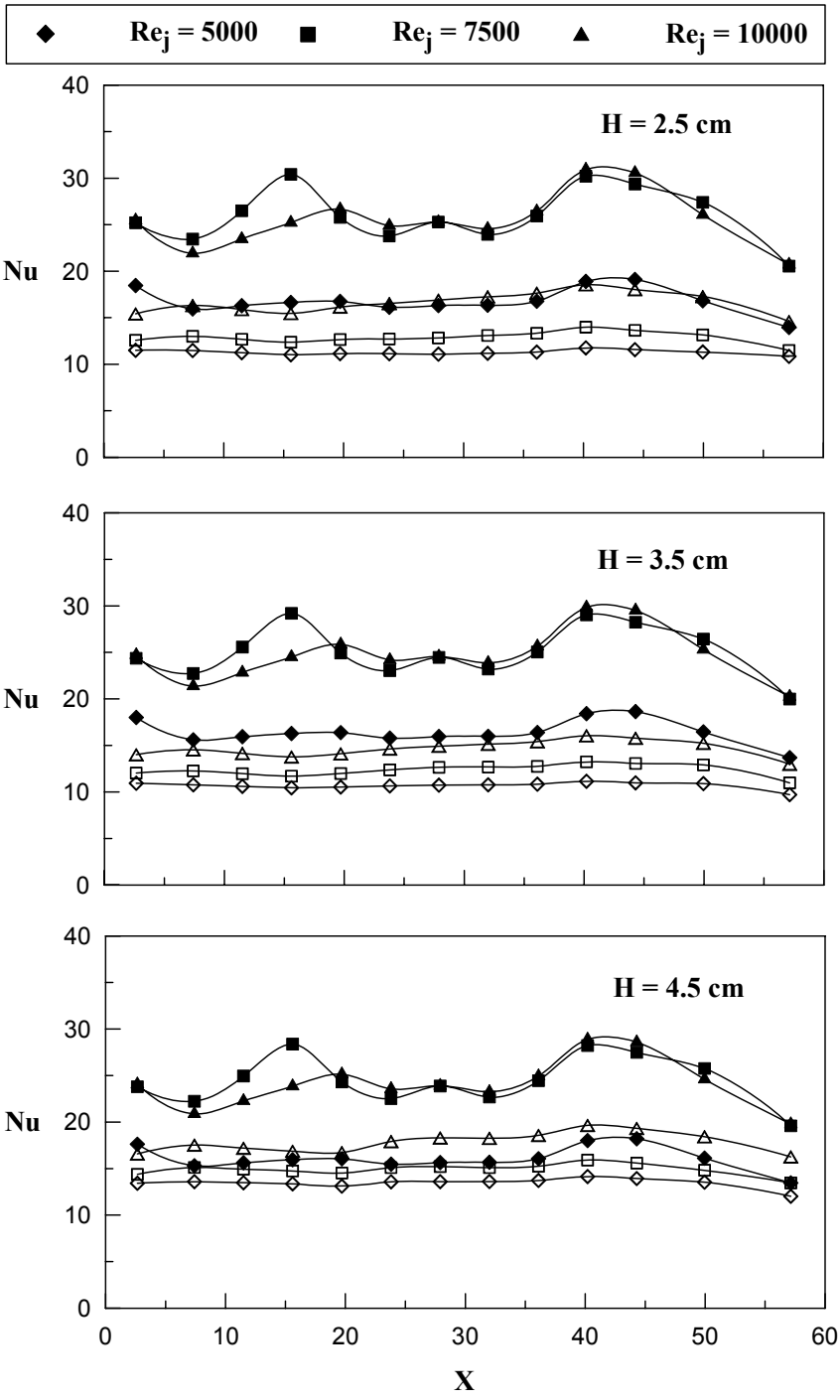

Figure 5.4 Effect of jet Reynolds number and feeding channel aspect ratio $2.5\,cm \le H/d \le 4.5\,cm$ on local Nusselt number distribution for case – 1 and $S = 3\ cm$.

(Filled symbol: $d = 1\,cm$ and Unfilled symbol: $d = 0.5\,cm$)

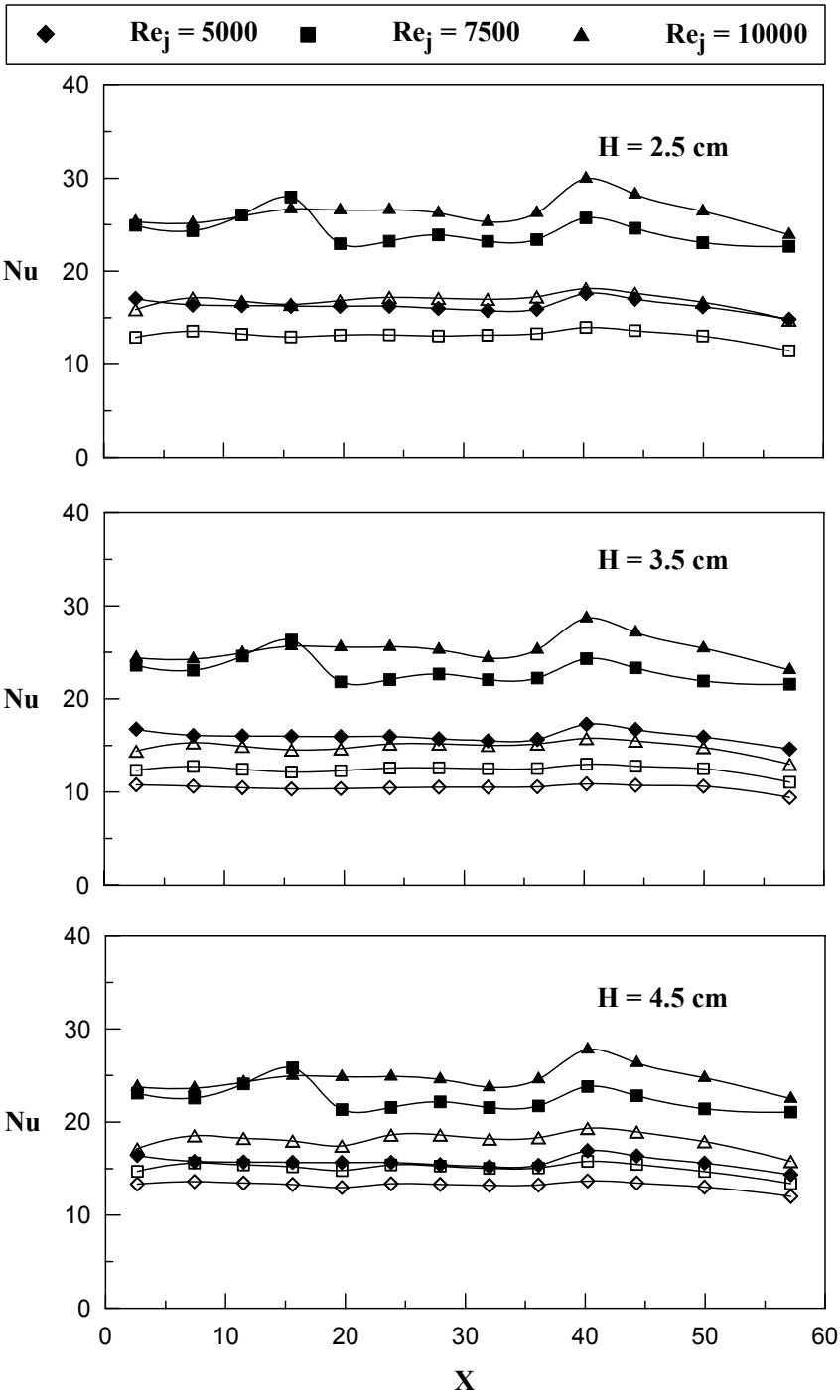

Figure 5.5 Effect of jet Reynolds number and feeding channel aspect ratio $2.5\,cm \le H/d \le 4.5\,cm$ on local Nusselt number distribution for case – 2 and $S = 3\ cm$.

(Filled symbol: $d = 1\,cm$ and Unfilled symbol: $d = 0.5\,cm$)

Figure 5.6 presents the effect of feeding channel width and two orifice jet sizes $d = 0.5\ and\ 1cm$ on local Nusselt number distribution for case – 3 where the air exits from both the directions at low X $(X = 0\,cm)$ and at large X $(X = 57.15\,cm)$. As observed in case – 1 and case – 2 the heat transfer observed from orifice jet size $d = 1cm$ is twice compared to the heat transfer observed from $d = 1\,cm$. It is observed that the crossflow develops at both the exit directions, which reduces the heat transferred from the target surfaces. Similar to heat transfer observed from case – 1 and case – 2, $H = 2.5\,cm$ has the maximum heat transfer for case – 3. $H = 2.5\,cm$ gives a maximum of 8.1% more heat transfer compared to $H = 3.5\,cm$ and $H = 2.5\,cm$ gives a maximum of 12.3% more heat transfer compared to $H = 4.5\,cm$, for both the orifice jet sizes studied. For $d = 1\,cm$, the magnitude of local Nusselt number at $15.6\,cm \le X \le 36.1\,cm$ is more compared to the other X/d locations this is due to the strong impingement of jets at the centre of the target surface compared to the exit locations where the crossflow more less dominant over the impingement effect. Small peaks of local Nusselt number are observed at $X = 40.02\,cm$ and $X = 32\,cm$ which are the result of the stronger jet impingement. At $0\,cm \le X \le 15.6\,cm$ and $40.02\,cm \le X \le 57.15\,cm$ a linearly decreasing local Nusselt number distribution is observed towards the exit this is primarily due to the crossflow obstructing the impinging jets towards the exit of impingement channel. For $d = 0.5\,cm$, the distribution of local Nusselt number is uniform over the entire length of the target surface as observed in case – 1 and case – 2. The difference in the magnitude of local Nusselt number for an increase of jet Reynolds number from $\mathrm{Re}_j = 5000$ to $\mathrm{Re}_j = 7500$ is similar to the increase in magnitude from $\mathrm{Re}_j = 7500$

and $\mathrm{Re}_j = 10000$ for all the feeding channel widths studied. Similar to the outflow orientations 1 and 2, $\mathrm{Re}_j = 10000$ gives the maximum values of local Nusselt number compared to the other jet Reynolds numbers studied.

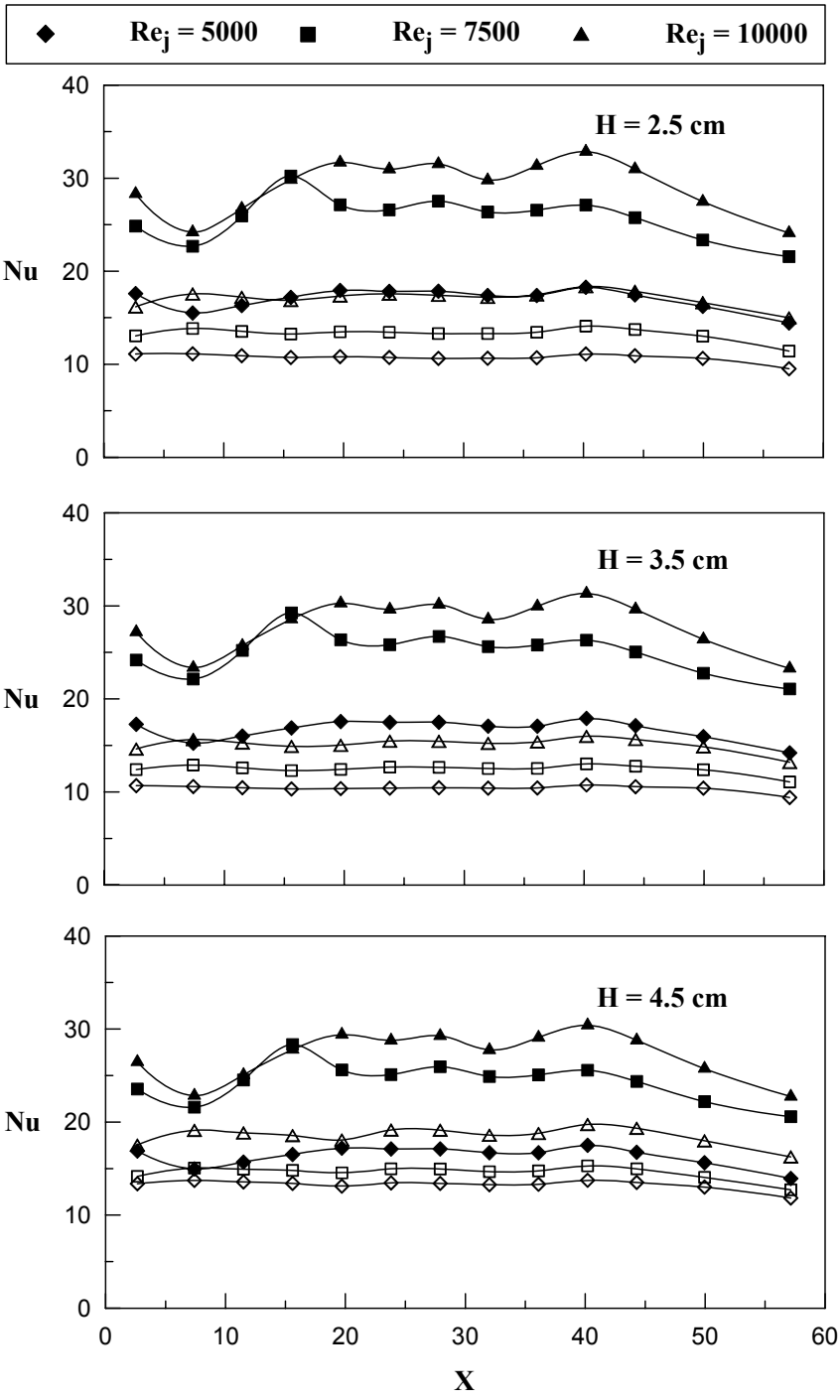

Figure 5.6 Effect of jet Reynolds number and feeding channel aspect ratio $2.5\,cm \le H/d \le 4.5\,cm$ on local Nusselt number distribution for case – 3 and $S = 3\,cm$.(Filled symbol: $d = 1\,cm$ and Unfilled symbol: $d = 0.5\,cm$)

5.3 Effect of outflow orientation on local Nusselt number

Figure 5.7 – 5.9 shows the effect of the outflow orientation for different feeding channel widths $(2.5cm \le H \le 4.5cm)$ and two orifice jet sizes $d = 0.5 \; and \; 1\,cm$ on local Nusselt number. All the jet Reynolds numbers studied $(5000 \le \mathrm{Re}_j \le 10000)$ are discussed individually.

Figure 5.7 represents the effect of the outflow orientation on the local Nusselt number distribution plotted for different feeding channel widths $(2.5cm \le H \le 4.5cm)$ and two orifice jet sizes $d = 0.5 \; and \; 1\,cm$ for $\mathrm{Re}_j = 5000$. Among all the feeding channel widths studied very less variation in the magnitude of local Nusselt number is observed with respect to outflow orientation at $15.6cm \le X \le 36.1cm$ for case – 2 and case – 3. Whereas, for case – 1 a linearly decreasing local Nusselt number distribution is observed from $X = 40.02cm$ to $X = 15.6cm$, this may be due to the crossflow getting intensified towards the exit, opposing and decreasing the strength of the impingement jets. At $40.02cm \le X \le 57.15cm$ for all the feeding channel widths studied, case – 1 has the highest heat transfer due to air entering the impingement channel at this location resulting in stronger impingement reducing the boundary layer thickness. At $15.6cm \le X \le 36.1cm$, case – 3 has the highest heat transfer from the target surface. Similar to the above discussions, $H = 2.5cm$ gives the maximum heat transfer over the entire length of the target surface. For $d = 0.5cm$, the variation in the magnitude of the local Nusselt number is very less with respect to the change in outflow orientation. It is also observed that case – 2 has the least magnitude of local Nusselt number over the entire length of the target surface for all the feeding channel widths studied.

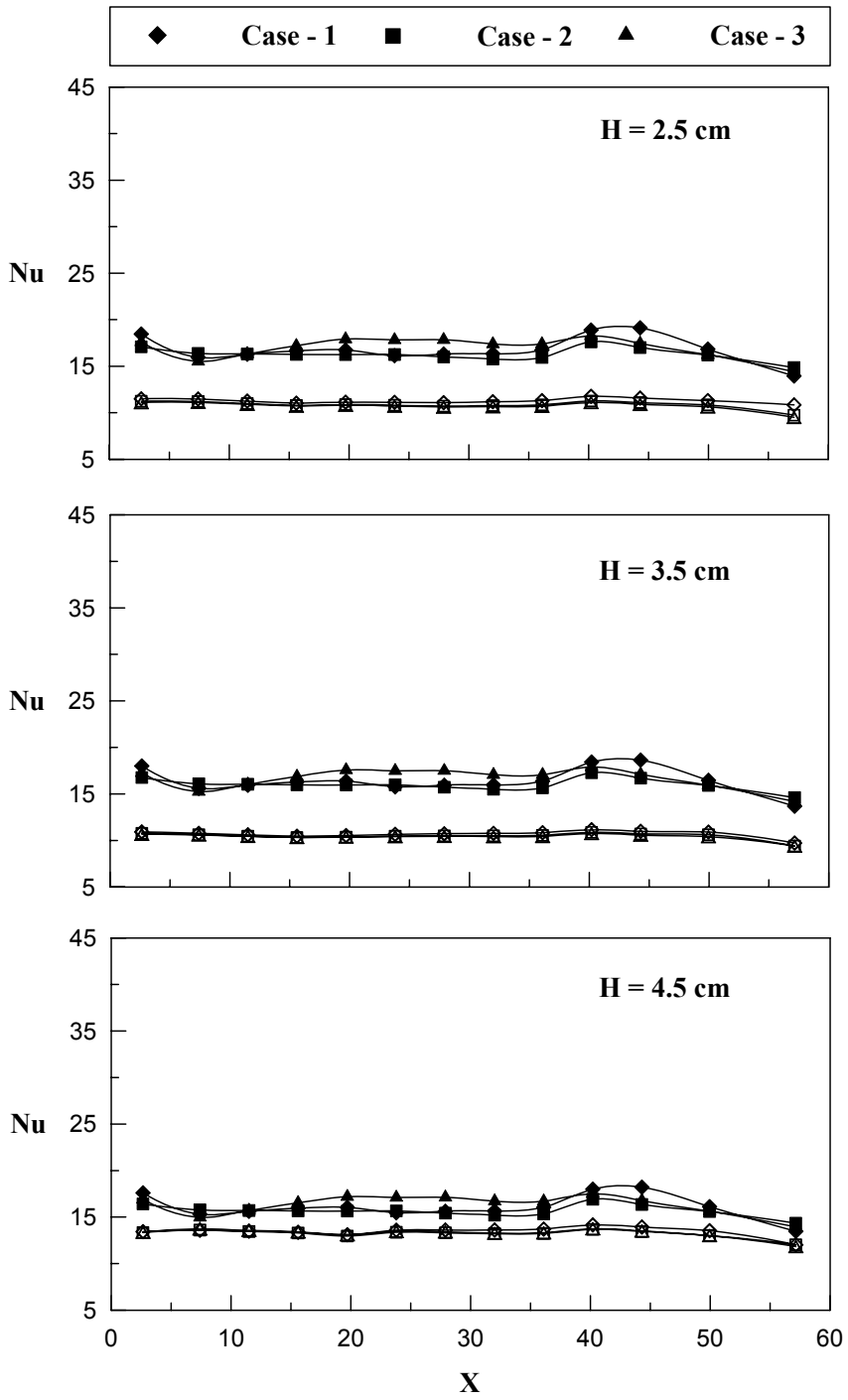

Figure 5.7 Effect of outflow orientation and feeding channel aspect ratio $2.5\,cm \le H/d \le 4.5\,cm$ on local Nusselt number distribution for $\mathrm{Re}_j = 5000$ and $S = 3\,cm$.

(Filled symbol: $d = 1\,cm$ and Unfilled symbol: $d = 0.5\,cm$)

Figure 5.8 shows the effect of feeding channel width and two orifice jet sizes $d = 0.5 \; and \; 1 \, cm$ on the local Nusselt number distribution for different outflow orientations studied and for $\mathrm{Re}_j = 7500$. It is observed that as the jet Reynolds number increases from 5000 to 7500 a maximum of 21% increase in the magnitude of local Nusselt number is found. Similar to $\mathrm{Re}_j = 5000$, case – 1 has maximum heat transfer at $40.02 \, cm \le X \le 57.15 \, cm$ due to the strong impingement of jets for both the orifice jet sizes studied. Whereas case – 2 has the least magnitude of local Nusselt number due to the obstruction to the impinging jets caused by the crossflow. The local Nusselt number distribution at $15.6 \, cm \le X \le 36.1 \, cm$ is uniform for case – 3 and case – 2 whereas a linearly decreasing local Nusselt number distribution is observed at $X = 12.5 \, cm$ towards $X = 0 \, cm$. At $15.6 \, cm \le X \le 36.1 \, cm$, case – 3 has the highest magnitude of local Nusselt number compared to the other two outflow orientations. Similar to $\mathrm{Re}_j = 5000$, $H = 2.5 \, cm$ has the highest magnitude of local Nusselt number compared to the other two feeding channel widths studied. For $d = 1 \, cm$, unlike $\mathrm{Re}_j = 5000$, where the variation in the magnitude of local Nusselt number is very less, for $\mathrm{Re}_j = 7500$ the variation with respect to outflow orientation is more comparatively for all the feeding channel widths studied. For $d = 0.5 cm$, the variation in the magnitude of the local Nusselt number with respect to the outflow orientation is very less comparatively.

Figure 5.9 shows the effect of feeding channel width and two orifice jet sizes $d = 0.5 \; and \; 1 \, cm$ on the local Nusselt number distribution for all the outflow orientations and

$\mathrm{Re}_j = 10000$. It is observed that as the jet Reynolds number increases from 7500 to 10000 a maximum of 26% increase in local Nusselt number is found similar to $\mathrm{Re}_j = 7500$. It is also observed that very less variation in local Nusselt number is observed at large X $40.02\,cm \le X \le 57.15\,cm$ compared to $\mathrm{Re}_j = 5000$ and $\mathrm{Re}_j = 7500$ for all the outflow orientations and the orifice jet sizes studied. Moreover as the H values increase from 2.5 to 4.5 a corresponding decrease in the magnitude of local Nusselt number is observed. Similar to the other two jet Reynolds number investigated, at $15.6\,cm \le X \le 36.1\,cm$, case – 3 and case – 2 have the uniform distribution of local Nusselt number whereas case – 1 has a linearly decreasing local Nusselt number from $X = 40.02\,cm$ to $X = 15.6\,cm$, the reason being explained previously. Maximum heat transfer is observed for $H = 2.5\,cm$ similar to $\mathrm{Re}_j = 5000$ and $\mathrm{Re}_j = 7500$ followed by $H = 3.5\,cm$ and $H = 4.5\,cm$.

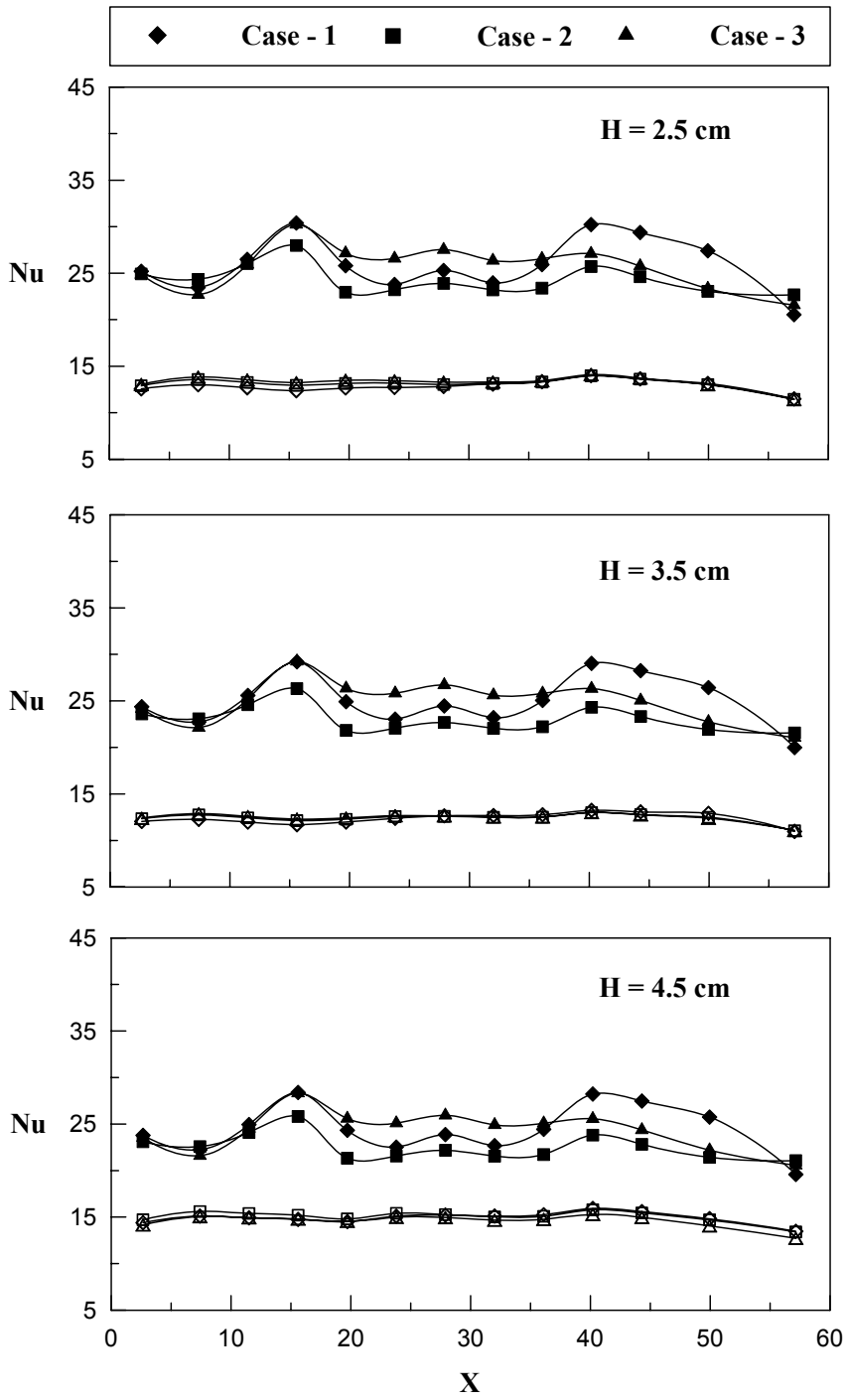

Figure 5.8 Effect of outflow orientation and feeding channel aspect ratio $2.5\,cm \le H/d \le 4.5\,cm$ on local Nusselt number distribution for $\mathrm{Re}_j = 7500$ and $S = 3\,cm$.

(Filled symbol: $d = 1\,cm$ and Unfilled symbol: $d = 0.5\,cm$)

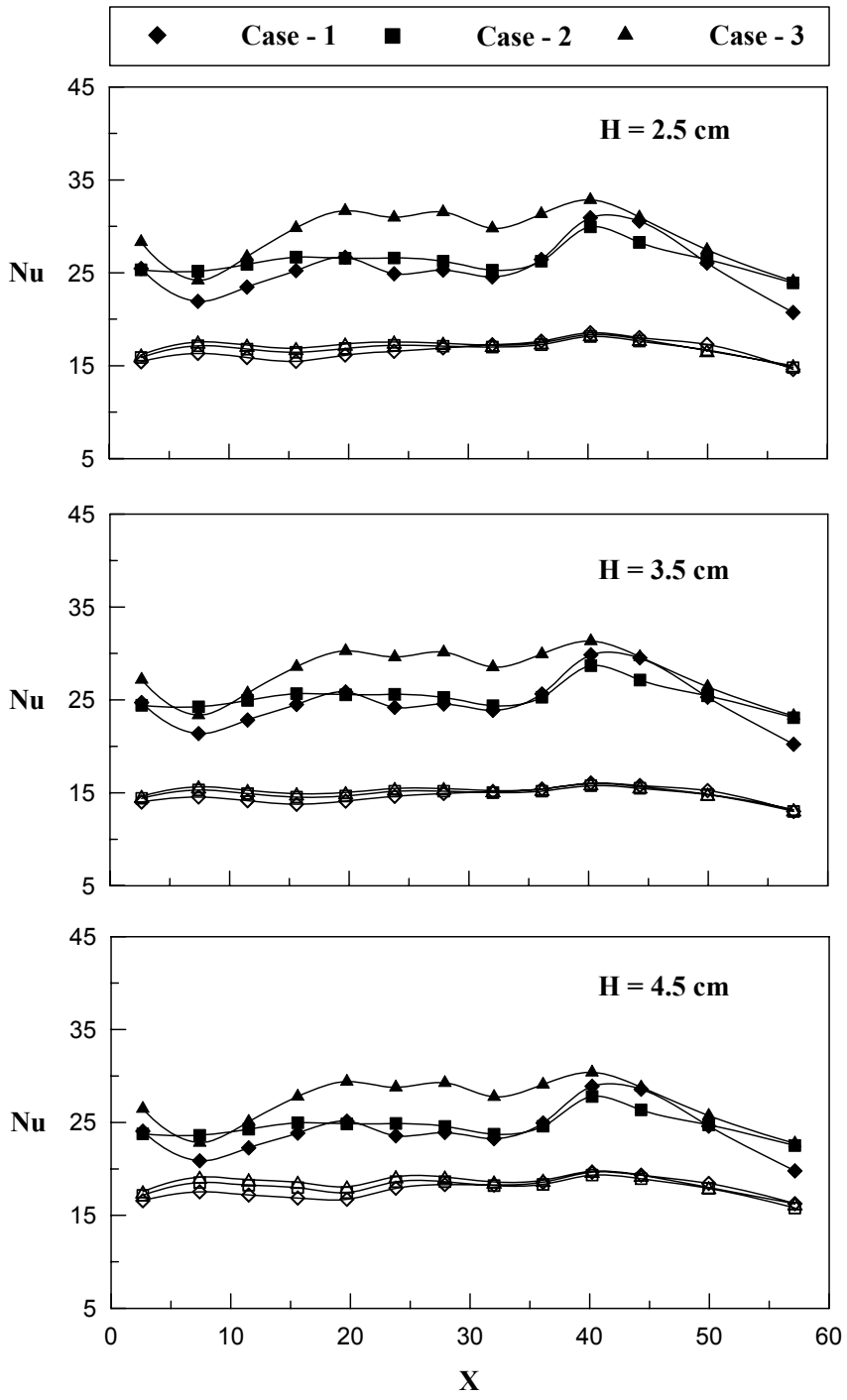

Figure 5.9 Effect of outflow orientation and feeding channel aspect ratio $2.5\,cm \le H/d \le 4.5\,cm$ on local Nusselt number distribution for $\mathrm{Re}_j = 10000$ and $S = 3\,cm$.

(Filled symbol: $d = 1\,cm$ and Unfilled symbol: $d = 0.5\,cm$)

5.4 Averaged Nusselt number

Figures 5.10 - 5.11 shows the average Nusselt number Nu_{avg} as a function of jet Reynolds number Re_j, plotted for all outflow orientations and the feeding channel aspect ratio $(2.5cm \le H \le 4.5cm)$. The value of Nu_{avg} is an average of the detailed results on the target surface.

5.4.1 Effect of feeding channel aspect ratio

Figure 5.10 shows the effect of the feeding channel width and two orifice jet sizes $d = 0.5 \; and \; 1\,cm$ on average Nusselt number for different outflow orientations. The averaged Nusselt number increases linearly with an increase in the jet Reynolds number. Among all the feeding channel widths studied $H = 2.5\,cm$ has the maximum values of the Nu_{avg} for orifice jet size $d = 1\,cm$, for all the outflow orientations, the reason being the strong impingement of jets with minimum effect of crossflow. Whereas for orifice jet size, $d = 0.5\,cm$, similar behavior of heat transfer distribution is observed for all the feeding channel widths, with $H = 2.5\,cm$ giving the highest heat transfer. The Nu_{avg} values decreases with an increase in the feeding channel width, this is primarily due to the increase in the crossflow effect which reduces the strength of the impingement jets. In detail, the averaged Nusselt number distribution for all the feeding channel widths is almost similar for all the outflow orientations studied for orifice jet size $d = 0.5\,cm$ and $d = 1\,cm$ with a difference in the magnitude of Nu_{avg}. The behavior of average Nusselt number is almost

similar with a maximum difference in magnitude equal to 11%. The difference in magnitude of average Nusselt number for $H = 2.5\,cm$ is very high compared to the other jet-to-plate distances studied for orifice jet size $d = 0.5\,cm$, whereas for $d = 1\,cm$, a uniform increase in the magnitude of average Nusselt number is observed for all the outflow orientations studied.

5.4.2 Effect of outflow orientation

Figure 5.11 shows the effect of outflow orientation and two orifice jet sizes $d = 0.5\ and\ 1\,cm$ on the average Nusselt number for different feeding channel widths studied $\left(2.5\,cm \le H \le 4.5\,cm\right)$. It is observed that the averaged Nusselt number increases linearly with an increase in the jet Reynolds number, as stated in the previous discussion. Case – 3 has the highest heat transfer from the target surface for all the jet-to-plate distances studied and for all the orifice jet sizes investigated, the only exception being the case – 1 having high values of the averaged Nusselt number for all the feeding channel widths at jet Reynolds number $\mathrm{Re}_j = 7500$. The reason for case – 3 giving the highest values of local Nusselt number is the less crossflow in the impingement channel compared to the other two outflow orientations where crossflow is dominant. Case – 2 has the lowest values of the average Nusselt number for all the jet-to-plate distances studied and for all the orifice jet sizes investigated, this may be due to the exit flow from the impingement channel being in the opposite direction of the inlet flow into the feeding channel.

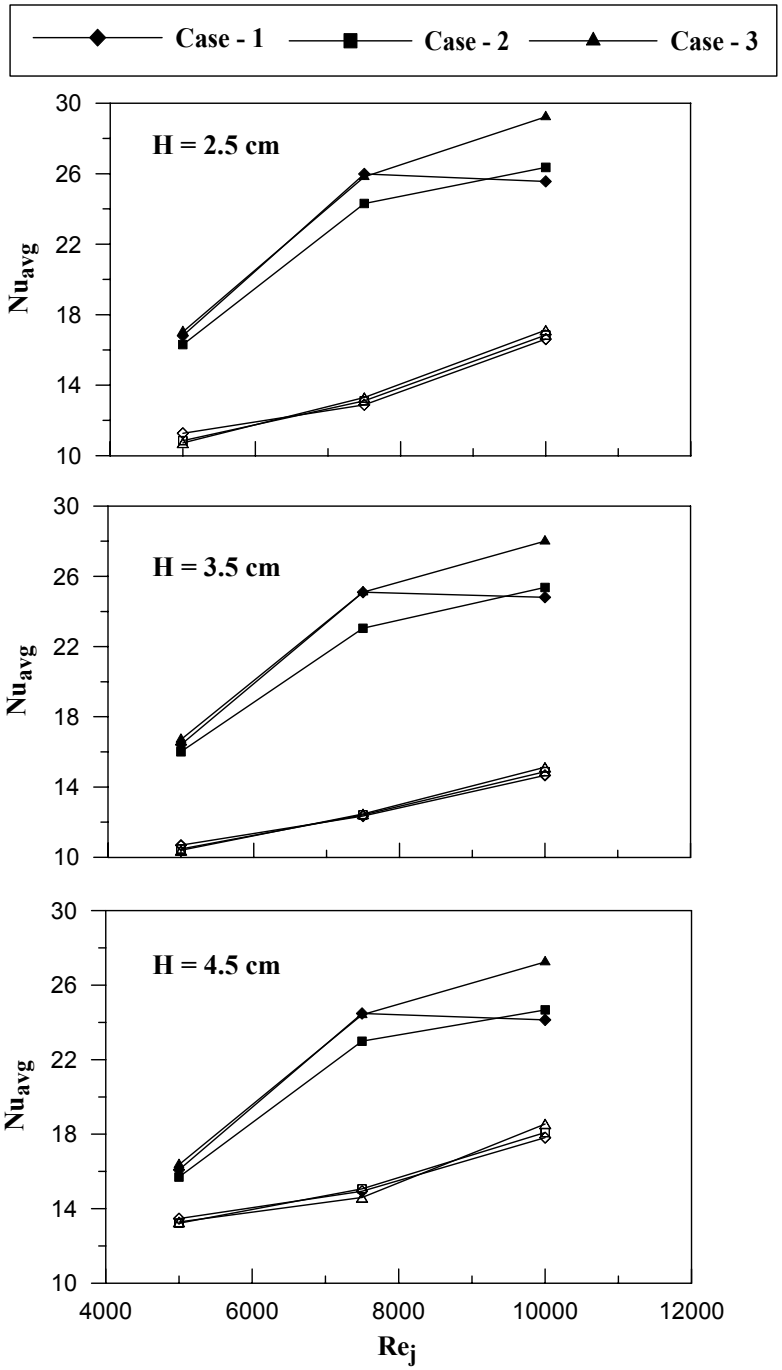

Figure 5.10 Effect of outflow orientation on averaged Nusselt number for different feeding channel aspect ratios $2.5cm \le H/d \le 4.5cm$ and $S = 3cm$. (Filled symbol: $d = 1cm$ and Unfilled symbol: $d = 0.5cm$)

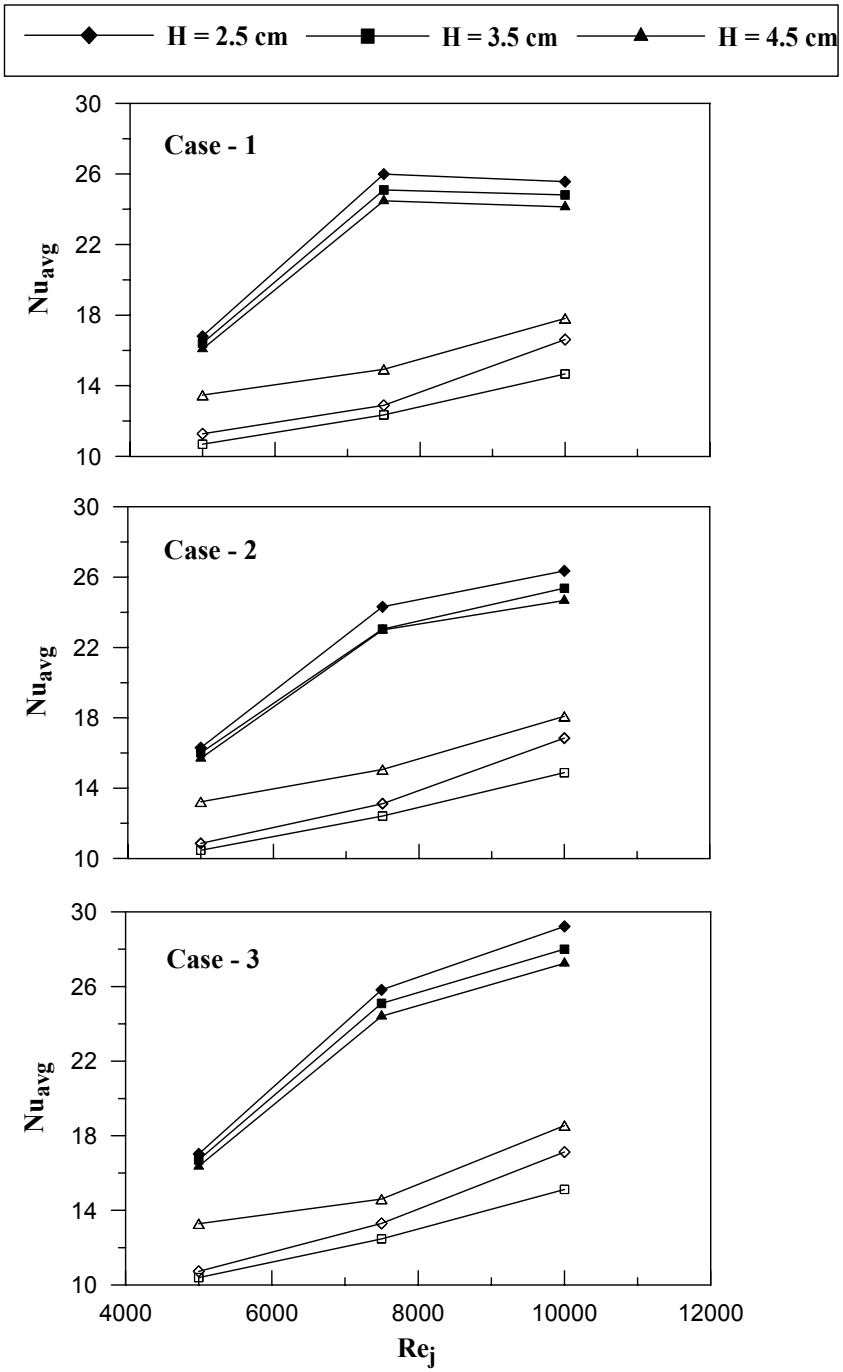

Figure 5.11 Effect of feeding channel aspect ratio $2.5cm \le H/d \le 4.5cm$ on the averaged Nusselt number for different outflow orientations and $S = 3cm$. (Filled symbol: $d = 1cm$ and Unfilled symbol: $d = 0.5cm$)

5.4.3 Correlations of averaged Nusselt number

The results for three different outflow orientations are correlated for the jet Reynolds number Re_j and the normalized jet-to-plate distance S/d dependence as

$$Nu_{avg} = A\,(\mathrm{Re}_j)^B \tag{5.2}$$

The present results are correlated for all outflow orientations individually for jet Reynolds number Re_j dependence. Previous studies in the field of jet impingement have involved in developing correlations for the averaged Nusselt number as a function of the jet Reynolds number by considering many parameters. Correlations by Huang et al [14], Kercher and Tabakoff [30] and Florscheutz et al [14] are compared to the averaged Nusselt number in the present investigation. Huang et al [21] studied the outflow orientations similar to ones used in the present study. They presented results for the outflow orientation 1 and 2 correlating for Reynolds number dependence as $Nu = 0.035\,\mathrm{Re}^{0.76}$, whereas for outflow orientation 3 which has the highest magnitude of heat transferred from the target surface is correlated as $Nu = 0.082\,\mathrm{Re}^{0.727}$. Kercher and Tabakoff [30] also studied the effect of crossflow and it is similar to the case – 1 in the present study. They varied the jet hole diameter, the hole spacing x, y and the jet to target plate distance. Based on all of these geometrical parameters, they proposed a correlation of the form $Nu = \phi_1\,\phi_2\,\mathrm{Re}^m\,(z/d)^{0.91}\,\mathrm{Pr}^{1/3}$, where ϕ_1 and ϕ_2 are constants based on X/d and Y/d, respectively. Florschuetz et al [14] presented the correlations with different coefficients of inline and staggered rows. The correlation for jet

impingement with minimum crossflow is given as $Nu = 0.363(X/d)^{-0.554}(Y/d)^{-0.422}(Z/d)^{0.068}\,\mathrm{Re}_j^{-0.554}\,\mathrm{Pr}^{1/3}$.

The detailed values of the local Nusselt number are averaged over the entire length of the target surface to obtain an single averaged Nusselt number. The averaged Nusselt numbers for each outflow orientation are plotted against the jet Reynolds number. The present results are correlated for the jet Reynolds number dependence as $Nu = 0.0098\,\mathrm{Re}^{0.8922}$ for case 1 and 2. The correlations for Huang et al [21] for case 1 and 2 are in good comparison with the present study. Kercher and Tabakoff [30] presented the results for the outflow orientation – 1 and the results of the present study are in good comparison with the existing correlation. The case with maximum heat transfer from the target surface, outflow orientation – 3, is correlated for the jet Reynolds number dependence as $Nu = 0.1033\,\mathrm{Re}^{0.6619}$. The correlation used from Florschuetz et al [14] is for the case with minimum crossflow. Huang et al [21] also presented a separate correlation for the case with high heat transfer, this case in their study had the less crossflow effect. The results from the present study for case – 3 are lower than the existing correlations, which includes the crossflow effect. The correlation for case – 3 in the present study is in good agreement with the correlation presented by Florschuetz et al [14] and Huang et al [21]. Thus it is evident from the above discussion that the crossflow effect is more dominant on outflow orientation 1 and 2 compared to outflow orientation – 3.

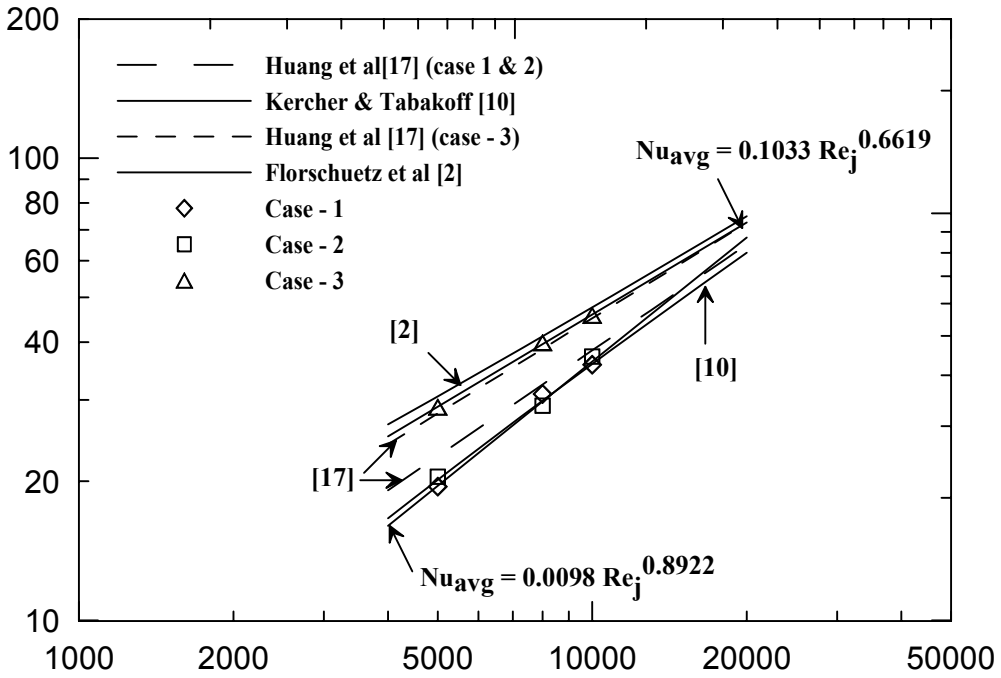

Figure 5.12 Averaged Nusselt number comparisons with the existing correlations

CHAPTER 6

ORIFICE PLATE - 2

In this chapter a detailed discussion on the results obtained by using the orifice plate 2 (centreline arrangement of jets) with jet diameter $d = 0.5\,cm$ are presented. Nusselt number distribution is presented as a function of non-dimensional distance along the entire length of the heated target surface and also as a function of the jet Reynolds number. As presented in the earlier chapter 4, Nusselt number distributions are shown for all the feeding channel aspect ratios studied $5 \le H/d \le 9$, the jet-to-plate distance $4 \le S/d \le 8$, and for three jet Reynolds numbers being investigated $9300 \le \mathrm{Re}_j \le 18800$. First a detail insight into the effect of jet Reynolds number onto the Nusselt number distribution, which also covers the effect of feeding channel aspect ratio on the Nusselt number. Next, the effect of the jet-to-plate distance onto the Nusselt number behavior is presented. Next, the effect of the outflow orientation on the Nusselt number distribution along the entire surface is investigated. Finally the average Nusselt number distribution is plotted as a function of the jet Reynolds number.

6.1 Effect of feeding channel aspect ratio on local Nusselt number

Figure 6.1 – 6.3, gives a detail insight into the local Nusselt number distribution presenting the effect of feeding channel aspect ratio $5 \le H/d \le 9$ on the heat transfer from the target surface. All the outflow orientations are discussed.

Figure 6.1 shows effect of feeding channel aspect ratio on the local Nusselt number distribution over the entire length of the target surface for case – 1, where the flow exits at low X/d $(X/d=0)$. The crossflow develops from large X/d to low X/d as the air exits at low X/d. The heat transferred from the target surface decreases with an decrease in feeding channel aspect ratio from H/d = 9 to 5 for all the feeding channel aspect ratios. Over the entire length of the target surface, the feeding channel aspect ratio $H/d=9$ gives the maximum heat transfer for all the jet Reynolds numbers $9300 \le \mathrm{Re}_j \le 18800$ studied. This is primarily due to the decrease in the crossflow and increase in the strength of the jets with an increase in the feeding channel ratios. Observing the effect of the feeding channel aspect ratio on the local Nusselt number distribution for all the jet Reynolds numbers studied, $H/d=9$ gives the maximum heat transfer among all the feeding channel aspect ratios studied. $H/d=7$ gives a maximum of 5% increase in the local Nusselt number compared to $H/d=5$, whereas $H/d=9$ gives 34% increase in local Nusselt number is observed compared to $H/d=7$. With an increase in the feeding channel aspect ratio the difference in the magnitude of the local Nusselt number also increases for an increase in the jet Reynolds number. Among all the Reynolds numbers studied, $\mathrm{Re}_j=18800$ gives the maximum heat transfer. A peak of local Nusselt number at $X/d=80.4$ is observed this is due to the flow entering the impingement channel at large X/d, where the effect of crossflow is minimal. At $31.2 \le X/d \le 72.2$ crossflow dominates the impingement of jets and a linearly decreasing distribution of local Nusselt number is observed towards the exit.

Figure 6.2 shows the effect of the feeding channel aspect ratio on the local Nusselt number distribution for case – 2 and for jet-to-plate distance $S/d=6$. For case – 2 the flow

exits at low X/d $(X/d=0)$, causing crossflow development towards the exit. $H/d=9$ gives the maximum heat transfer over the entire length of the target surface for all the jet Reynolds numbers studied. For all the jet Reynolds numbers studied, $H/d=7$ gives 20% more heat transfer from the target surface compared to $H/d=5$ whereas $H/d=9$ gives a maximum of 16% increase in heat transfer is observed compared to $H/d=7$. It is also observed that the magnitude of the local Nusselt number increases with an increase in the jet Reynolds number for all the feeding channel aspect ratios studied. The variation in the local Nusselt number is more sensitive with respect to a change in feeding channel aspect ratio at high jet Reynolds number whereas it is less sensitive at low jet Reynolds numbers. At $80.4 \le X/d \le 114.3$ the magnitude of local Nusselt number decreases from $X/d=80.4$ to $X/d=114.3$, this is due to the obstruction caused by the crossflow to the impinging jets.

Figure 6.3 shows the effect of feeding channel aspect ratio on the local Nusselt number distribution for case – 3 and for jet-to-plate distance $S/d=6$. For case – 3 air exits at $X/d=0$ and $X/d=114.3$, where the crossflow has a predominant effect over the heat transfer characteristics. It is observed that at $0 \le X/d \le 30$ and $80.4 \le X/d \le 114.3$ the local Nusselt number decreases towards exit, this may be due to the crossflow at the exit and thus reduces the strength of the impinging jets and the heat transferred from the target surface. The magnitude of local Nusselt number at $31.2 \le X/d \le 72.2$ is high compared to the other X/d locations this may be due to the strong impingement of jets. For an increase in feeding channel aspect ratio a corresponding increase in local Nusselt number is observed. $H/d=9$ gives the maximum values of feeding channel aspect ratio for all the jet Reynolds numbers studied. Considering the effect of feeding channel aspect ratio for all jet Reynolds

numbers on heat transfer characteristics in detail, $H/d = 9$ gives the highest heat transfer similar to case – 1 and case – 2. $H/d = 9$ gives a maximum of 21% more heat transfer compared to $H/d = 7$, further $H/d = 7$ gives a maximum of 10% more heat transfer is observed compared to $H/d = 5$. The feeding channel aspect ratios $H/d = 5$ and $H/d = 7$ gives less heat transfer due to high crossflow which dominates the strength of the impinging jets, thus thinning the boundary layer resulting in high heat transfer. Similar to case – 1 and case – 2, with respect to the effect of feeding channel aspect ratio on local Nusselt number characteristics it is observed that the local Nusselt number is sensitive to a change in feeding channel aspect ratio at high jet Reynolds numbers.

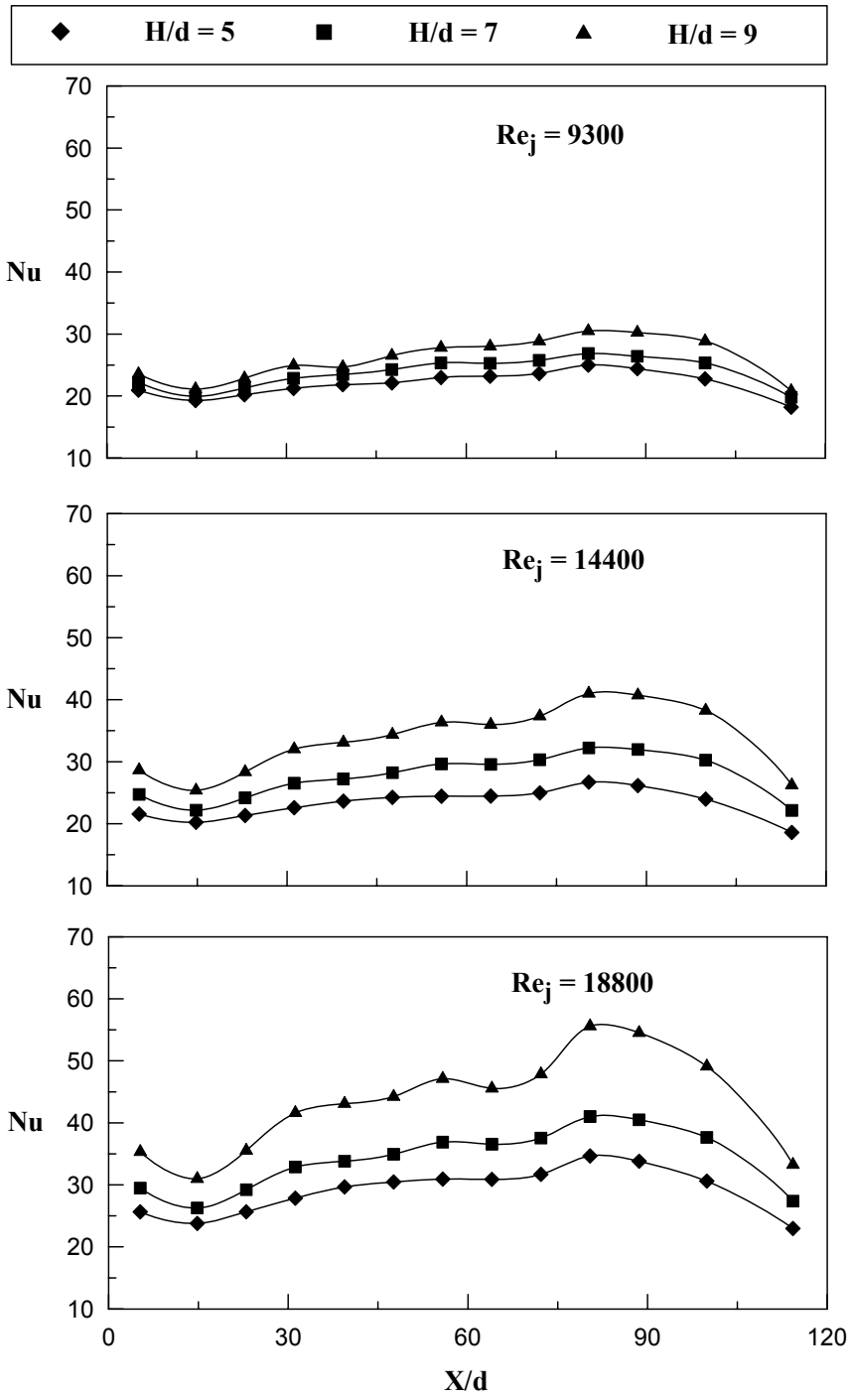

Figure 6.1 Effect of feeding channel aspect ratio $5 \le H/d \le 9$ on local Nusselt number distribution for case – 1 and jet-to-plate distance $S/d = 6$.

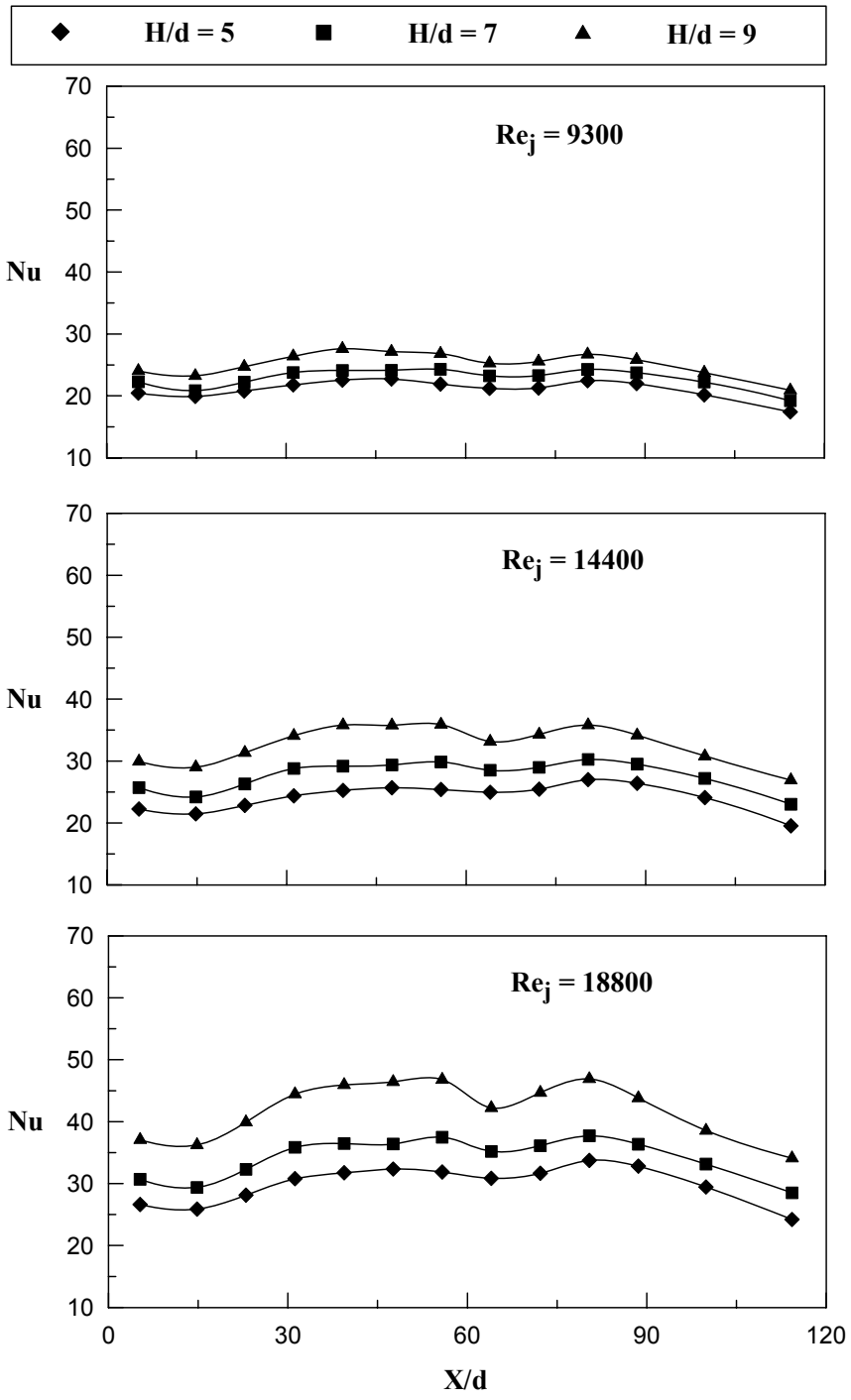

Figure 6.2 Effect of feeding channel aspect ratio $5 \le H/d \le 9$ on local Nusselt number distribution for case – 2 and jet-to-plate distance $S/d = 6$.

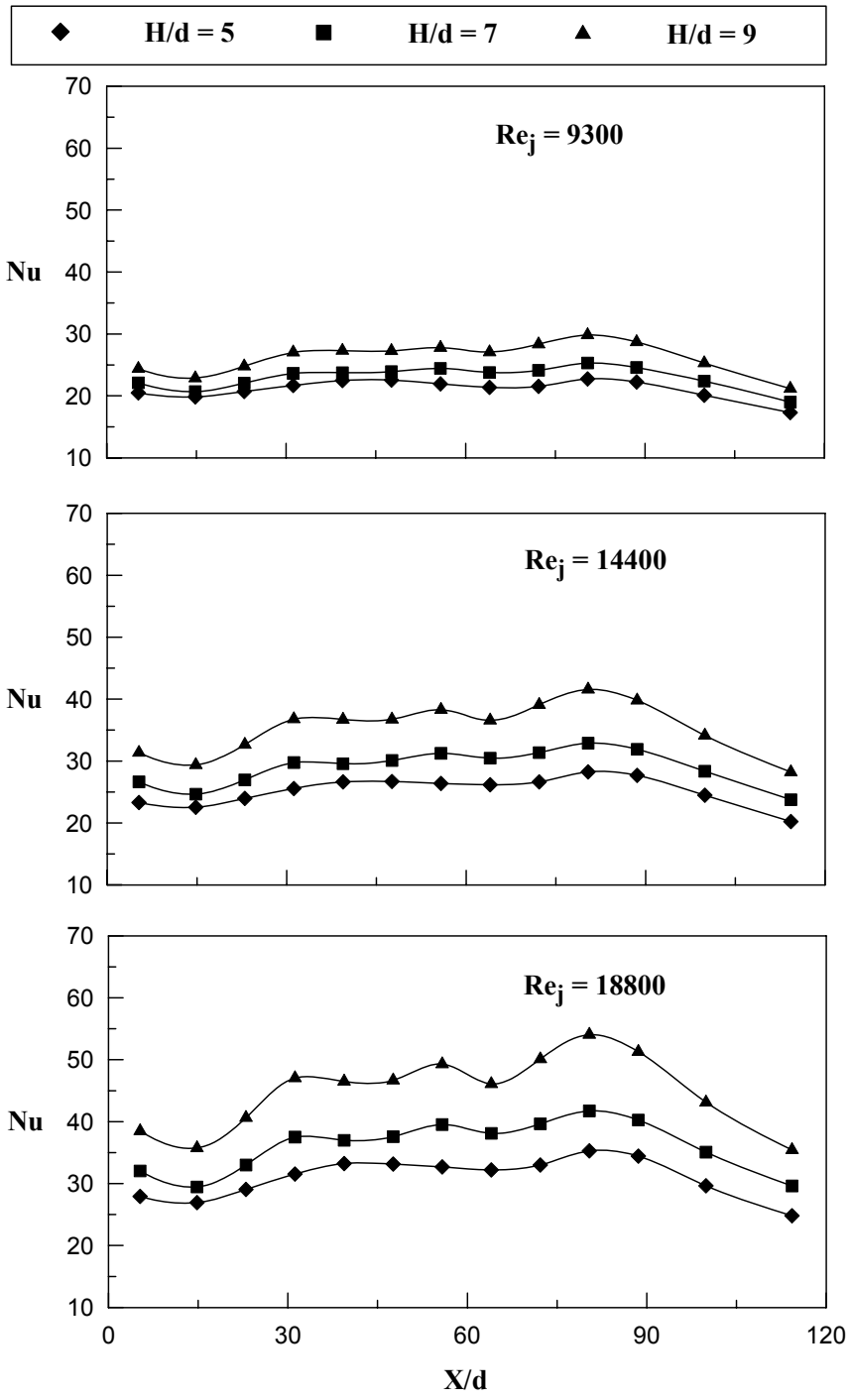

Figure 6.3 Effect of feeding channel aspect ratio $5 \le H/d \le 9$ on local Nusselt number distribution for case – 3 and jet-to-plate distance $S/d = 6$

6.2 Effect of jet Reynolds number on local Nusselt number

Figure 6.4 – 6.6 shows the local Nusselt number distribution for different jet Reynolds numbers $9300 \le \mathrm{Re}_j \le 18800$, for jet-to-plate distance $S/d = 6$, expressing the effect of the feeding channel aspect ratio on the heat transfer from the heated target surface. Among all the jet-to-plate distances studied $S/d = 6$ is considered, as it is the best case in which maximum heat is transferred from the target surface.

Figure 6.4 shows the local Nusselt number distribution plotted for case – 1, which gives a detailed insight into the effect of the feeding channel aspect ratio. Three different values of the feeding channel aspect ratio are considered in this part of the study $5 \le H/d \le 9$. The results are presented for three jet Reynolds numbers $9300 \le \mathrm{Re}_j \le 18800$. It is observed that for an increase in the jet Reynolds number there is a corresponding increase in the magnitude of local Nusselt number. High values of local Nusselt number are observed for $\mathrm{Re}_j = 18800$ compared to the other two jet Reynolds numbers. Increasing the jet Reynolds number from $\mathrm{Re}_j = 9300$ to $\mathrm{Re}_j = 14400$ a maximum of 10.7% increase in the local Nusselt number values is observed whereas for an increase from $\mathrm{Re}_j = 14400$ to $\mathrm{Re}_j = 18800$ a large increase of 40% in magnitude of local Nusselt number is observed indicating the increase in strength of jets with an increase in jet Reynolds number. For case – 1, the flow exits the impingement channel at low X/d $(X/d = 0)$. At large X/d $(X/d = 80.4)$ a peak of local Nusselt number is observed this may be due to strong impingement of the air jets and also because the effect of crossflow is minimal, which reduces the boundary layer thickness. Among all the feeding channel aspect ratios examined

$5 \le H/d \le 9$, $H/d = 5$ gives the maximum values of local Nusselt number for all the jet-to-plate distances studied. $H/d = 7$ gives a maximum of 14% increase in the local Nusselt number from the target surface compared to $H/d = 5$, whereas 35% increase in local Nusselt number is observed compared to $H/d = 9$. At $31.2 \le X/d \le 72.2$ a uniform decrease in magnitude of local Nusselt number is observed along the target surface from $X/d = 72.2$ to $X/d = 0$ for all the feeding channel aspect ratios studied, this may be due to the crossflow of the air generated towards the exit.

Figure 6.5 shows the effect of feeding channel aspect ratio on the local Nusselt number distribution for case – 2 as a function of jet Reynolds numbers $9300 \le \mathrm{Re}_j \le 18800$. For case – 2 air exits the impingement channel at $X/d = 114.3$, this leads to the development of crossflow towards the exit. Similar to the case – 1 an increase in jet Reynolds number leads to the corresponding increase in the local Nusselt number for all the feeding channel aspect ratios studied. The magnitude of local Nusselt number at $31.2 \le X/d \le 72.2$ is more compared to the other X/d locations this may be due to the strong impingement of jets at this location. Although similar distribution of local Nusselt number is observed for $H/d = 5$ and $H/d = 7$, but $H/d = 7$ gives a maximum of 12% more heat transfer from the entire target surface compared to $H/d = 5$ and $H/d = 9$ gives a maximum of 25% more heat transfer from the entire target surface compared to $H/d = 7$. The local Nusselt number is sensitive for a change in jet Reynolds number, this is observed from the difference in magnitude of local Nusselt number varying with respect to jet Reynolds number. $\mathrm{Re}_j = 18800$ gives the maximum values of local Nusselt number for all the feeding channel aspect ratios studied. Nusselt number distribution for $\mathrm{Re}_j = 9300$ and $\mathrm{Re}_j = 14400$ is close

with a maximum difference in magnitude being 30%. At $80.02 \le X/d \le 114.3$, a decrease in local Nusselt number is observed from $X/d = 80.02$ towards the exit at $X/d = 114.3$, this is due to the development of crossflow towards the exit, which obstructs the impingement of jets and thickens the boundary layer. This behavior of local Nusselt number at large X/d is observed for all the feeding channel aspect ratios studied.

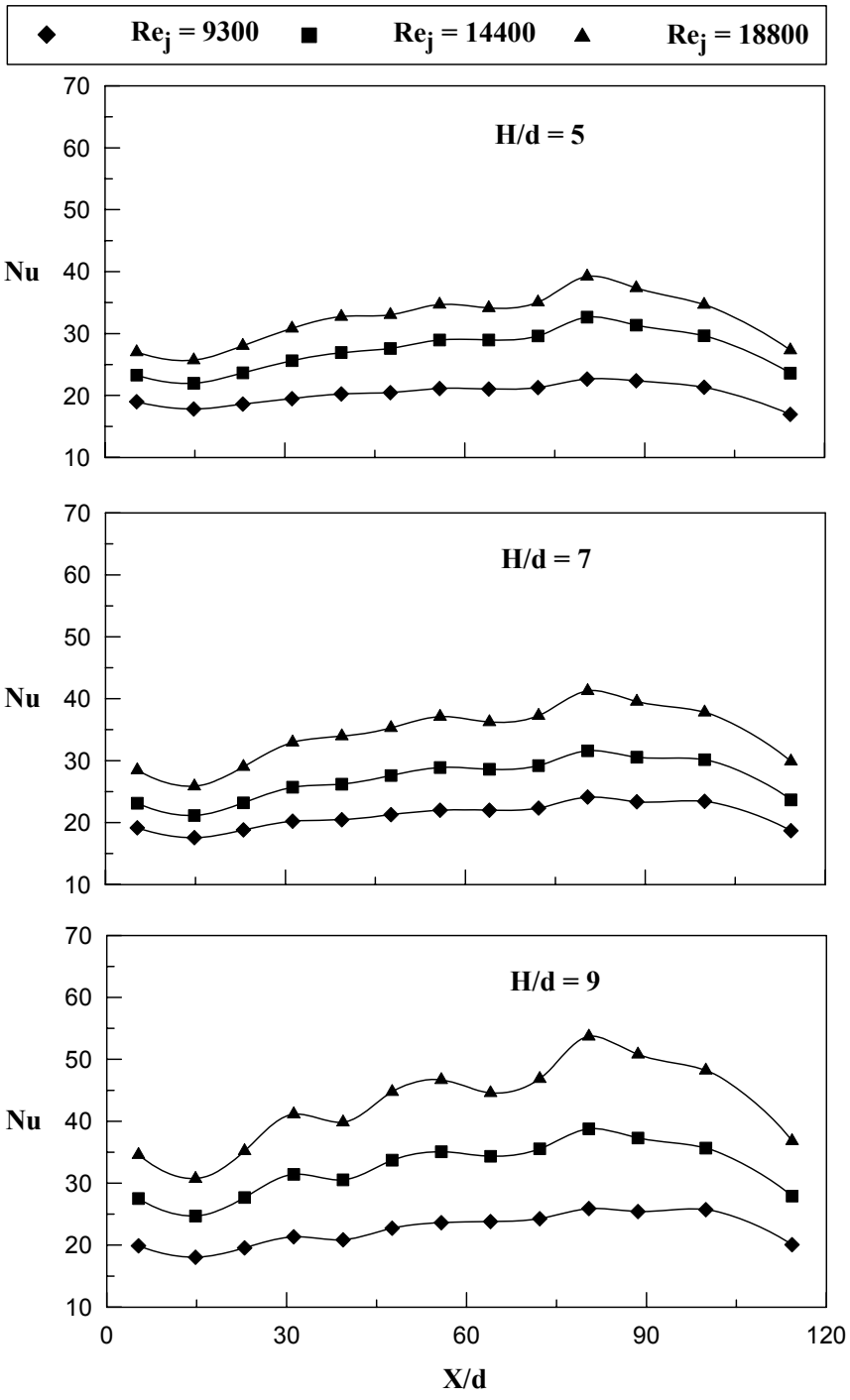

Figure 6.4 Effect of jet Reynolds number and feeding channel aspect ratio $5 \le H/d \le 9$ on local Nusselt number distribution for $S/d = 6$ and case – 1.

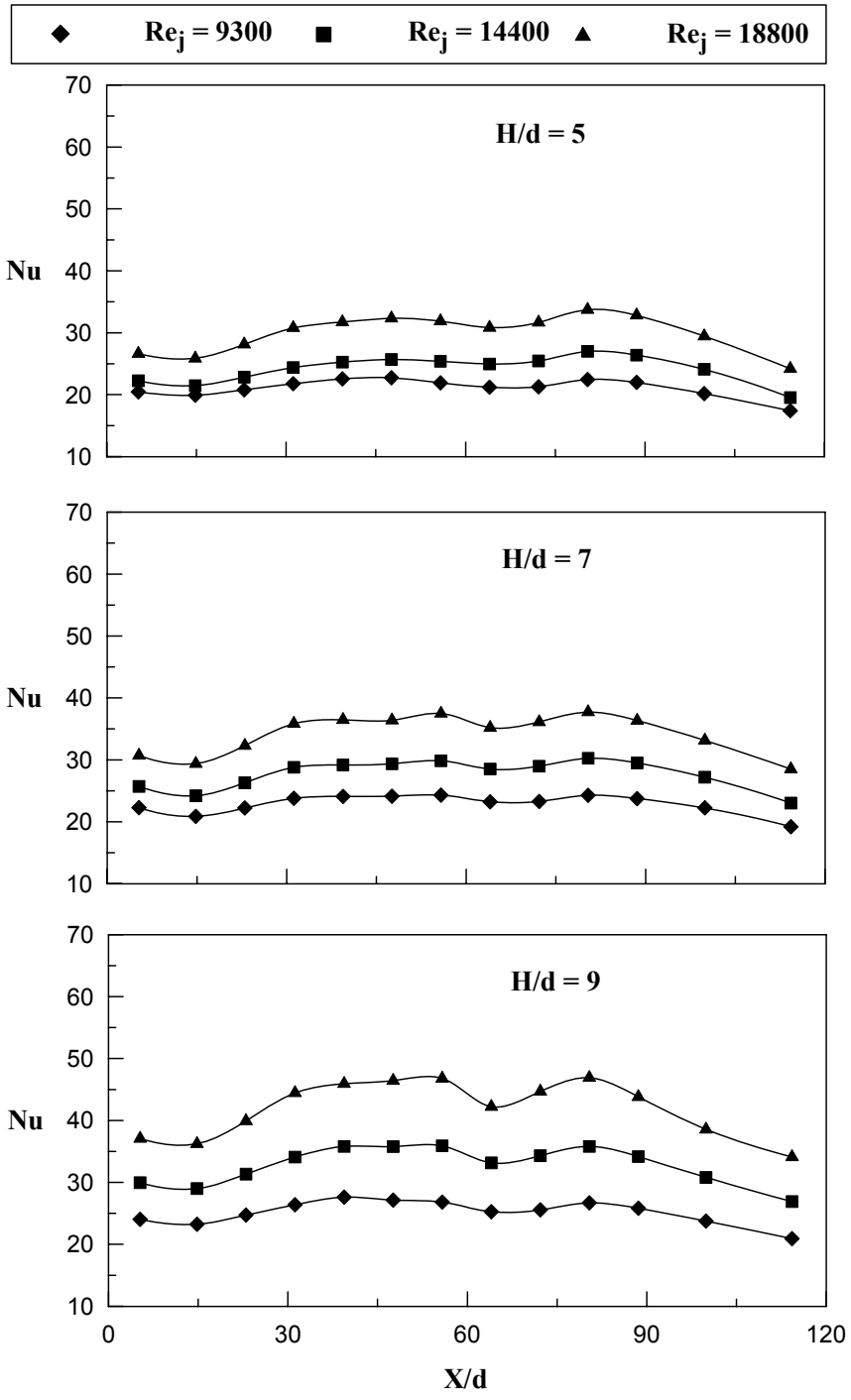

Figure 6.5 Effect of jet Reynolds number and feeding channel aspect ratio $5 \le H/d \le 9$ on local Nusselt number distribution for $S/d = 6$ and case – 2..

Figure 6.6 presents the local Nusselt number distribution for case – 3 where the air exits from both the directions at low X/d $(X/d=0)$ and large X/d $(X/d=114.3)$. It is observed that the crossflow develops at both the exit directions, which reduces the heat transferred from the target surfaces. Similar to heat transfer observed from case – 1 and case – 2, $H/d=9$ has the maximum heat transfer for case – 3. $H/d=9$ gives a maximum of 32% more heat transfer compared to $H/d=7$ and $H/d=7$ gives a maximum of 17% more heat transfer compared to $H/d=5$. The magnitude of local Nusselt number at $31.2 \le X/d \le 72.2$ is more compared to the other X/d locations this is due to the strong impingement of jets at the centre of the target surface compared to the exit locations where the crossflow dominates the impingement effect. Small peaks of local Nusselt number are observed at $X/d=80$ and $X/d=60$. At $0 \le X/d \le 30$ and $80.4 \le X/d \le 114.3$ a linearly decreasing local Nusselt number distribution is observed towards the exit this is primarily due to the crossflow obstructing the impinging jets towards the exit of impingement channel. The difference in the magnitude of local Nusselt number for an increase of jet Reynolds number from $\mathrm{Re}_j=9300$ to $\mathrm{Re}_j=14400$ is similar to the increase in magnitude from $\mathrm{Re}_j=14400$ and $\mathrm{Re}_j=18800$ for all the feeding channel aspect ratios studied. Similar to the outflow orientations 1 and 2, $\mathrm{Re}_j=18800$ gives the maximum values of local Nusselt number compared to the other jet Reynolds numbers studied.

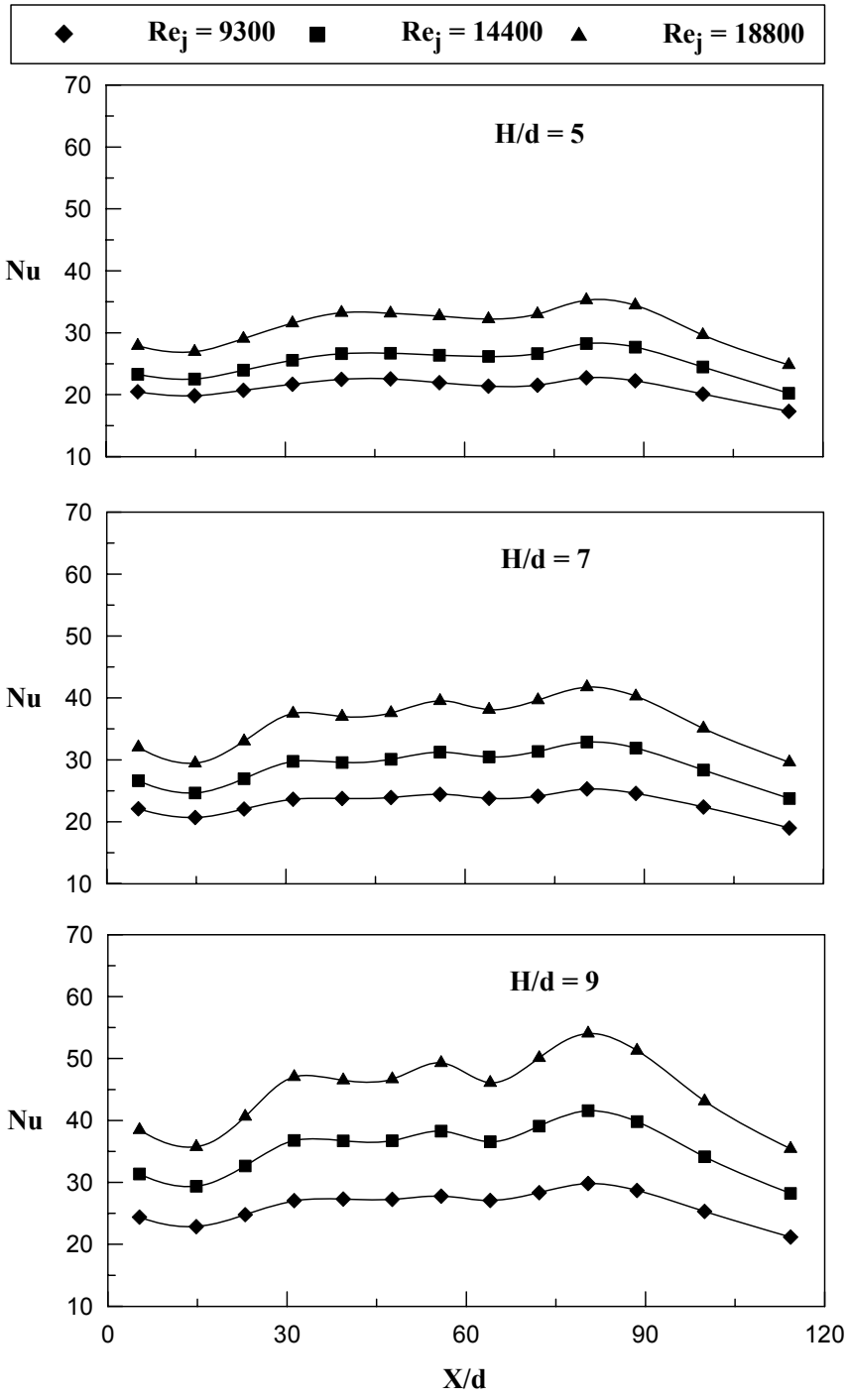

Figure 6.6 Effect of jet Reynolds number and feeding channel aspect ratio $5 \le H/d \le 9$ on local Nusselt number distribution for $S/d = 6$ and case – 3.

6.3 Effect of outflow orientation on local Nusselt number

Figure 6.7 – 6.9 shows the effect of the outflow orientation for different feeding channel aspect ratios $5 \le H/d \le 9$ on local Nusselt number. The results are presented for $S/d = 6$, due to the highest amount of heat transfer observed among all the jet-to-plate distances investigated. All the jet Reynolds numbers studied $9300 \le \mathrm{Re}_j \le 18800$ are discussed individually.

Figure 6.7 represents the effect of the outflow orientation on the local Nusselt number distribution plotted for different feeding channel aspect ratios $5 \le H/d \le 9$ for $\mathrm{Re}_j = 9300$. Among all the feeding channel aspect ratios studied very less variation in the magnitude of local Nusselt number is observed with respect to outflow orientation at $31.2 \le X/d \le 72.2$ for case – 2 and case – 3. Whereas, for case – 1 a linearly decreasing local Nusselt number distribution is observed from $X/d = 80.4$ to $X/d = 31.2$, this may be due to the crossflow getting intensified towards the exit, opposing and decreasing the strength of the impingement jets. At $80.4 \le X/d \le 114.3$ for all the feeding channel aspect ratios studied, case – 1 has the highest heat transfer due to air entering the impingement channel at this location resulting in stronger impingement reducing the boundary layer thickness. Similar to the above discussions, $H/d = 9$ has the maximum heat transfer over the entire length of the target surface. It is also observed that case – 2 has the least magnitude of local Nusselt number over the entire length of the target surface for all the feeding channel aspect ratios studied.

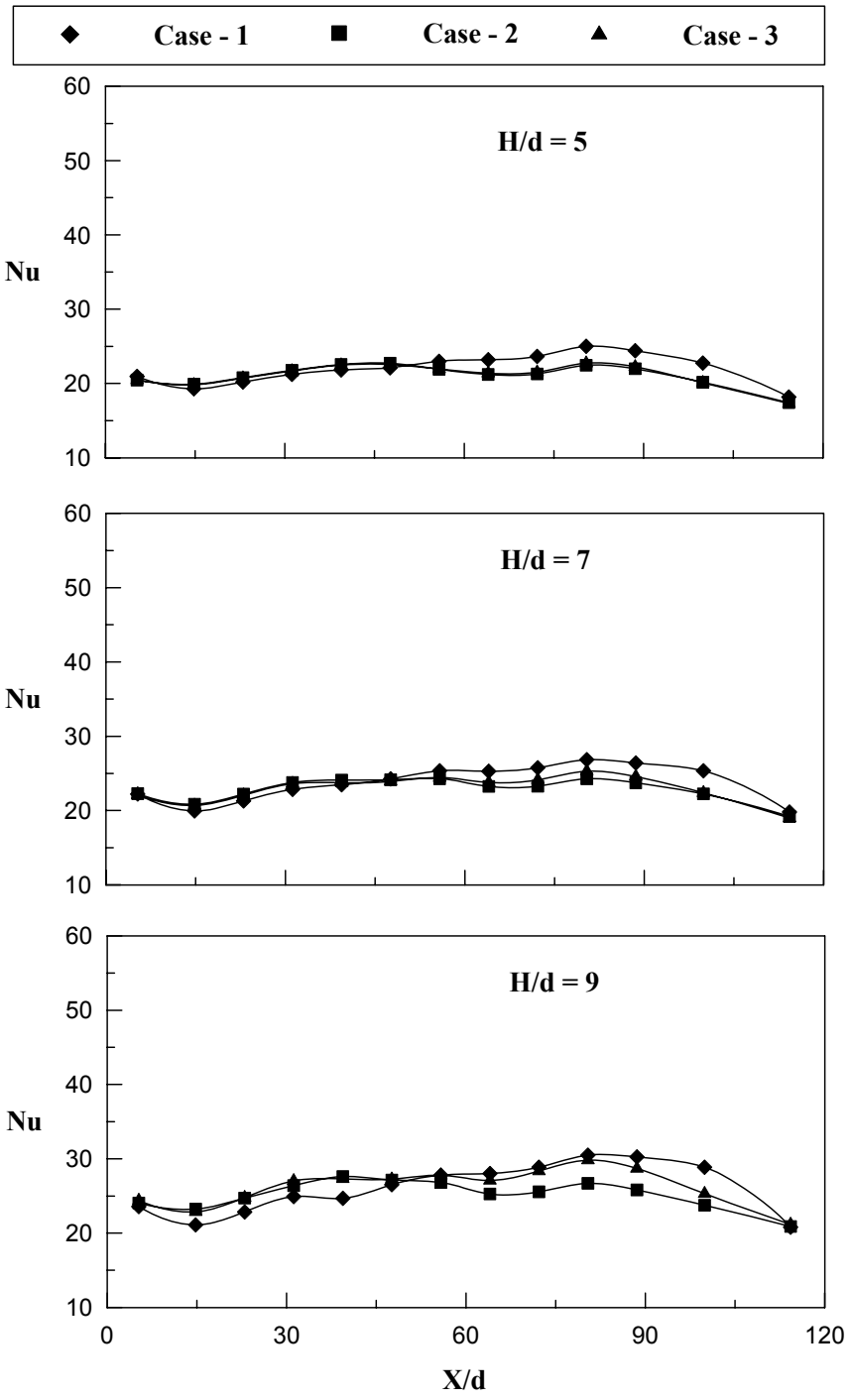

Figure 6.7 Effect of outflow orientation and feeding channel aspect ratio $5 \le H/d \le 9$ on local Nusselt number distribution for $S/d = 6$ and $\mathrm{Re}_j = 9300$.

Figure 6.8 shows the effect of feeding channel aspect ratio on the local Nusselt number distribution for different outflow orientations studied and for $\mathrm{Re}_j = 14400$. It is observed that as the jet Reynolds number increases from 9300 to 14400 a maximum of 33% increase in local Nusselt number is found similar to $\mathrm{Re}_j = 9300$, case – 1 has maximum heat transfer at $80.4 \le X/d \le 114.3$ due to the strong impingement of jets. Whereas case – 2 has the least magnitude of local Nusselt number due to the obstruction to the impinging jets caused by the crossflow. Similar to $\mathrm{Re}_j = 9300$, the local Nusselt number distribution at $31.2 \le X/d \le 72.2$ is uniform for case – 3 and case – 2 whereas a linearly decreasing local Nusselt number distribution is observed at $X/d = 23$ towards $X/d = 0$. Similar to $\mathrm{Re}_j = 9300$, $H/d = 9$ has the highest magnitude of local Nusselt number compared to the other two feeding channel aspect ratios studied. Unlike $\mathrm{Re}_j = 9300$, where the variation in the magnitude of local Nusselt number is very less, for $\mathrm{Re}_j = 14400$ the variation with respect to outflow orientation is more comparatively for all the feeding channel aspect ratios studied.

Figure 6.9 shows the effect of feeding channel aspect ratio on the local Nusselt number distribution for all the outflow orientations and for $\mathrm{Re}_j = 18800$. It is observed that very less variation in local Nusselt number values is observed at large X/d $(80.4 \le X/d \le 114.3)$ compared to $\mathrm{Re}_j = 9300$ and $\mathrm{Re}_j = 14400$ for all the outflow orientations studied. Moreover as the H/d values increase from 5 to 9 a corresponding increase in the magnitude of local Nusselt number is observed. Similar to the other to jet

Reynolds number investigated at $31.2 \le X/d \le 72.2$, case – 3 and case – 2 have the uniform distribution of local Nusselt number whereas case – 1 has a linearly decreasing local Nusselt number from $X/d = 80.4$ to $X/d = 31.2$, the reason being explained previously. Maximum heat transfer is observed for $H/d = 9$ similar to $\mathrm{Re}_j = 5000 \,\&\, 7500$ followed by $H/d = 7$ and $H/d = 5$.

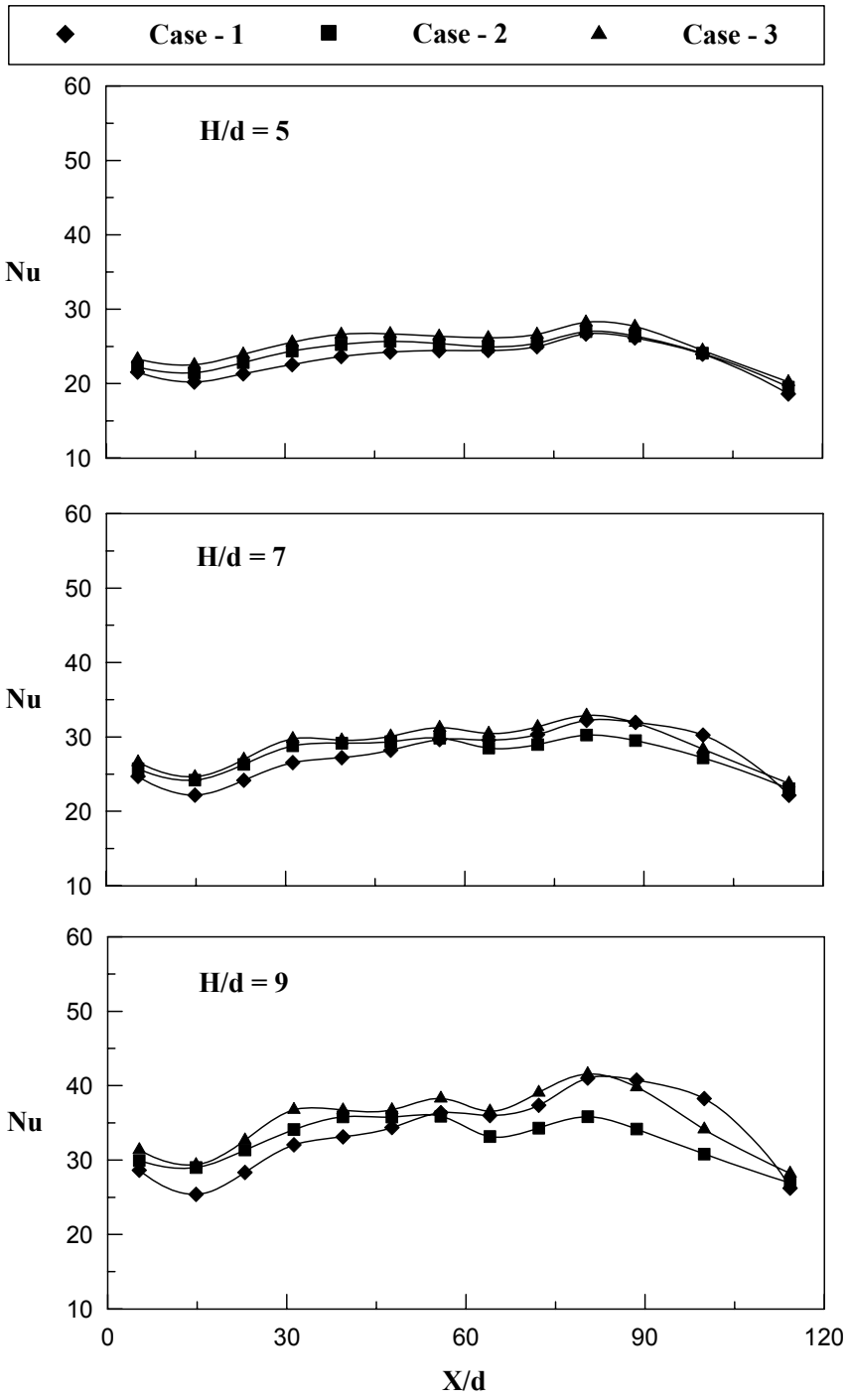

Figure 6.8 Effect of outflow orientation and feeding channel aspect ratio $5 \le H/d \le 9$ on local Nusselt number distribution for $S/d = 6$ and $\mathrm{Re}_j = 14400$.

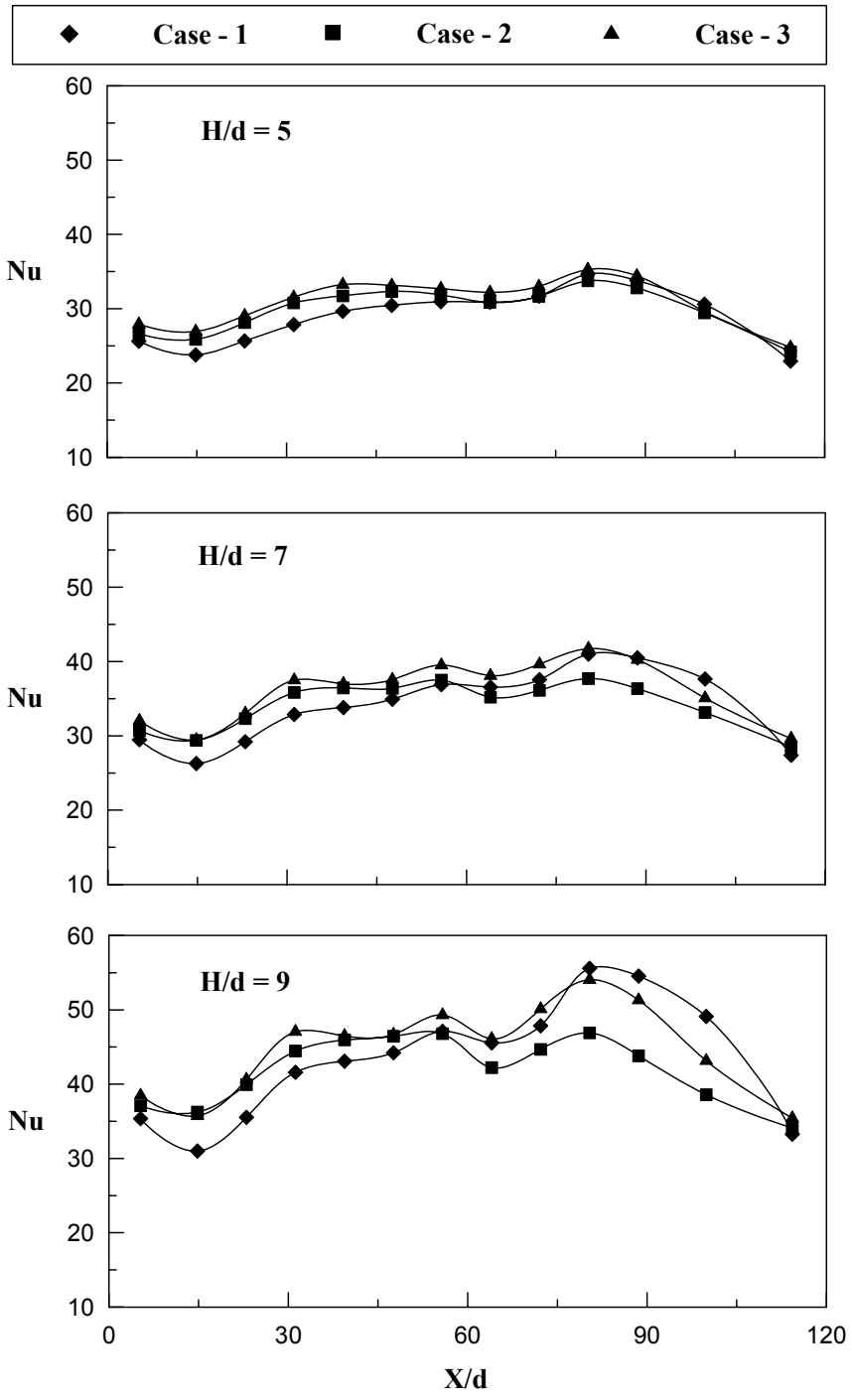

Figure 6.9 Effect of outflow orientation and feeding channel aspect ratio $5 \le H/d \le 9$ on local Nusselt number distribution for $S/d = 6$ and $\mathrm{Re}_j = 18800$.

6.4 Effect of Jet-to-plate distance on local Nusselt number

Figure 6.10 – 6.12, gives a detail insight into the local Nusselt number distribution for different jet-to-plate distances $4 \le S/d \le 8$ and $\mathrm{Re}_j = 18800$ presenting the effect of feeding channel aspect ratio $5 \le H/d \le 9$ on the heat transfer from the target surface. Jet Reynolds number $\mathrm{Re}_j = 18800$ is selected for presenting the results as this gives the maximum heat transfer among all the jet Reynolds numbers studied. All the outflow orientations are discussed.

Figure 6.10 shows effect of feeding channel aspect ratio on the local Nusselt number distribution over the entire length of the target surface for case – 1, where the flow exits at low X/d $(X/d = 0)$. The crossflow develops from large X/d to low X/d as the air exits at low X/d. The heat transferred from the target surface decreases with an increase in jet-to-plate distance from S/d = 4 to 8 for all the feeding channel aspect ratios. Over the entire length of the target surface, the jet-to-plate distance $S/d = 4$ gives the maximum heat transfer for all the feeding channel aspect ratios $5 \le H/d \le 9$ studied. Observing the effect of the feeding channel aspect ratio on the local Nusselt number distribution, $H/d = 9$ gives the maximum heat transfer among all the feeding channel aspect ratios studied. $H/d = 7$ gives a maximum of 5% increase in the local Nusselt number compared to $H/d = 5$, whereas $H/d = 9$ gives 34% increase in local Nusselt number is observed compared to $H/d = 7$. As discussed earlier in figure 6.1, a peak of local Nusselt number at $X/d = 80.4$ is observed this is due to the flow entering the impingement channel at large X/d, where the effect of crossflow is minimal. At $31.2 \le X/d \le 72.2$ crossflow dominates the

impingement of jets and a linearly decreasing distribution of local Nusselt number is observed towards the exit.

Figure 6.11 shows the effect of the feeding channel aspect ratio on the local Nusselt number distribution for case – 2 comparing with all the jet-to-plate distances studied. For case – 2 the flow exits at low X/d $(X/d=0)$, causing crossflow development towards the exit. $S/d=4$ has the maximum heat transfer from the entire length of the target surface for the feeding channel aspect ratios $H/d=5$ and $H/d=7$. For $H/d=9$, $S/d=6$ gives the maximum amount of heat transfer from the entire target surface. For case – 2, $H/d=7$ gives 20% more heat transfer from the target surface compared to $H/d=5$ whereas $H/d=9$ gives a maximum of 16% increase in heat transfer is observed compared to $H/d=7$. It is also observed that the local Nusselt number distribution is sensitive to a change in jet-to-plate distance for $S/d=4$ and $S/d=6$ for the feeding channel aspect ratio $H/d=7$, whereas some variation in the magnitude of the local Nusselt number is observed for a change in the jet-to-plate distance for other feeding channel aspect ratios studied.

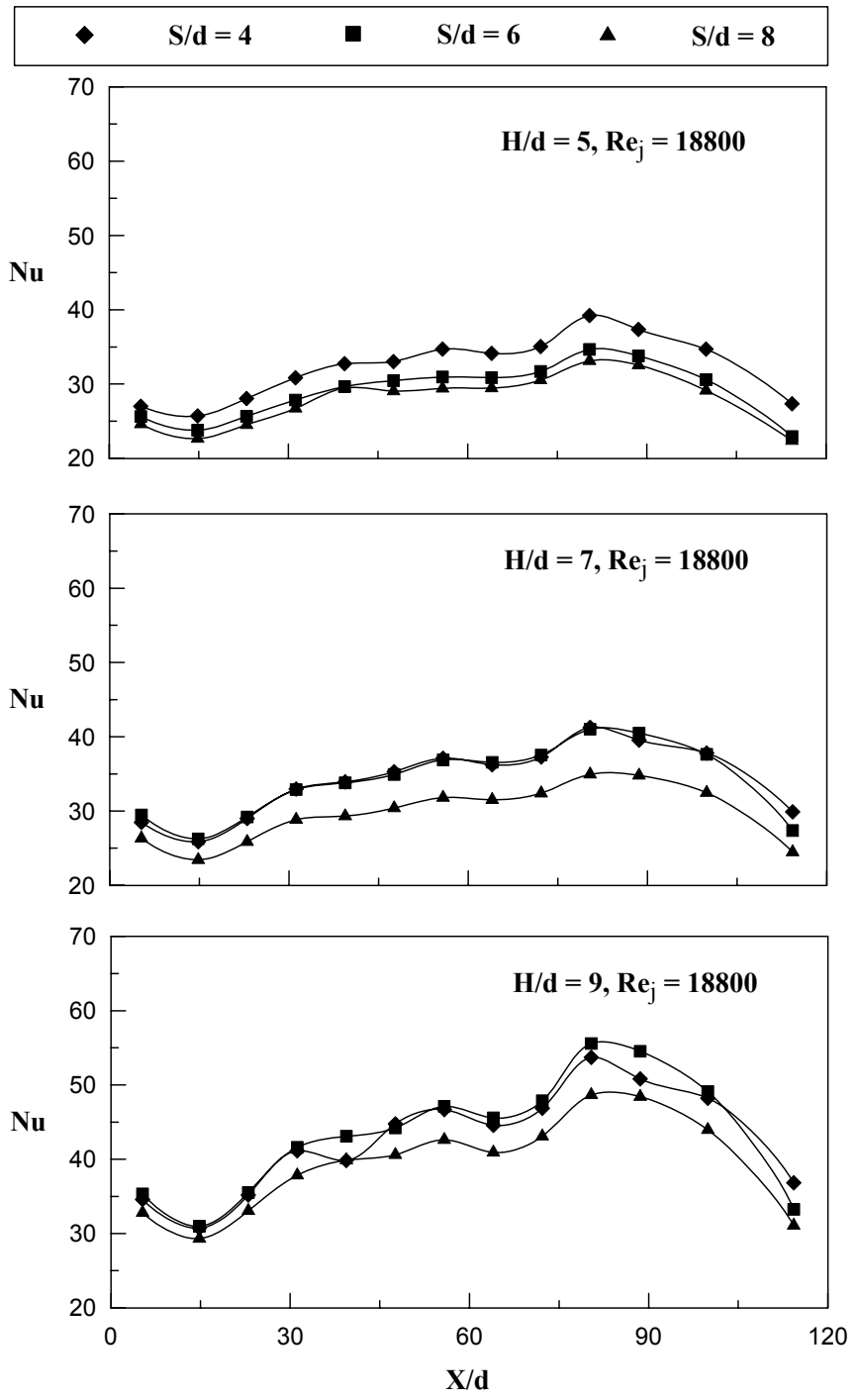

Figure 6.10 Effect of jet-to-plate distance and feeding channel aspect ratio $5 \le H/d \le 9$ on local Nusselt number distribution for $\mathrm{Re}_j = 18800$ and case – 1.

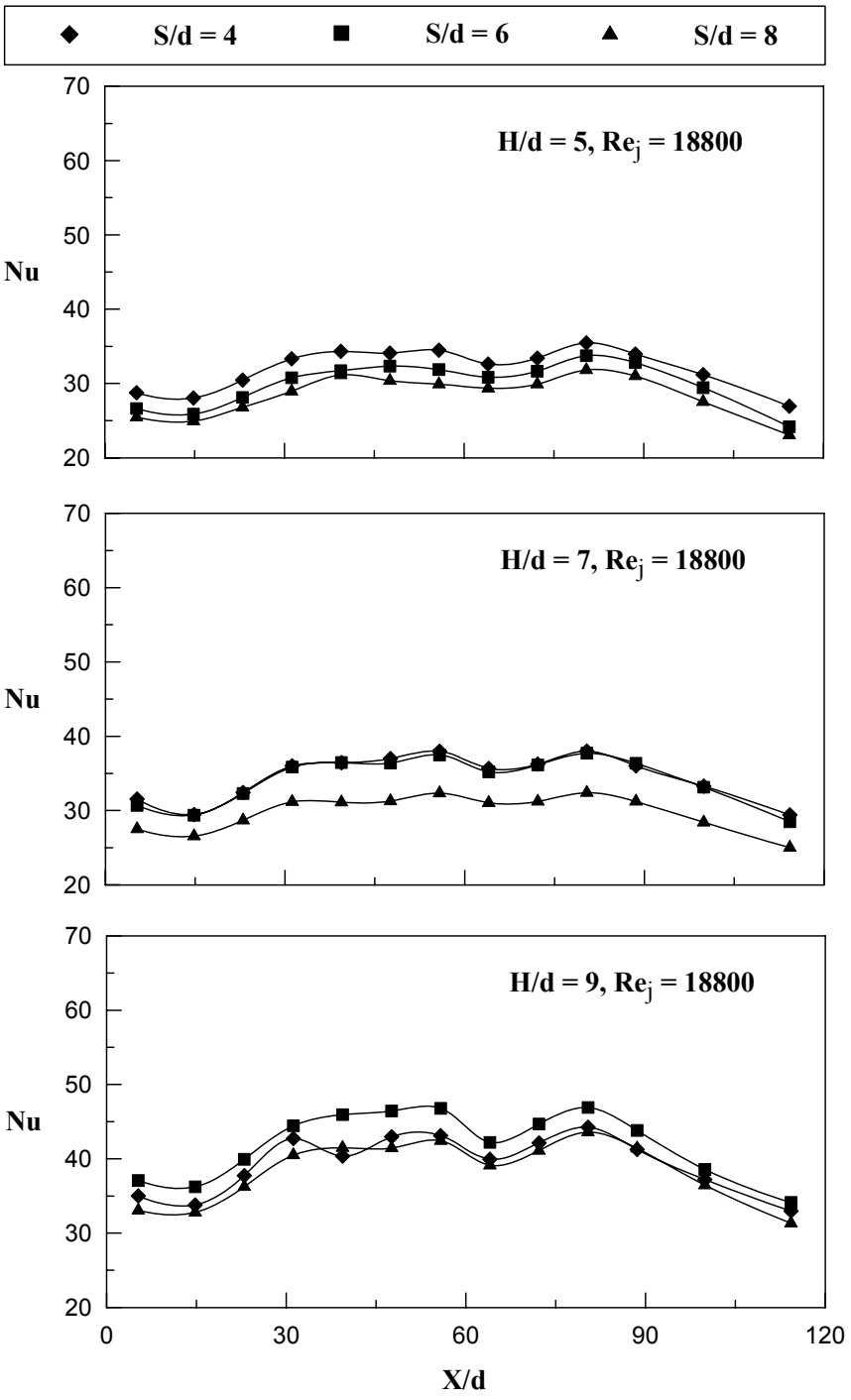

Figure 6.11 Effect of jet-to-plate distance and feeding channel aspect ratio $5 \le H/d \le 9$ on local Nusselt number distribution for $\mathrm{Re}_j = 18800$ and case – 2.

Figure 6.12 shows the effect of feeding channel aspect ratio on the local Nusselt number distribution for case – 3 and for different jet-to-plate distances $4 \le S/d \le 8$. For case – 3 air exits at $X/d = 0$ and $X/d = 114.3$, where the crossflow has a predominant effect over the heat transfer characteristics. It is observed that at $0 \le X/d \le 30$ and $80.4 \le X/d \le 114.3$ the local Nusselt number decreases towards exit, this may be due to the crossflow at the exit and thus reduces the strength of the impinging jets and the heat transferred from the target surface. The magnitude of local Nusselt number at $31.2 \le X/d \le 72.2$ is high compared to the other X/d locations this may be due to the strong impingement of jets. For an increase in jet-to-plate distance a corresponding decrease in local Nusselt number is found for $H/d = 5$ and $H/d = 7$, whereas $S/d = 6$ has maximum values of local Nusselt number for $H/d = 9$. Considering the effect of feeding channel aspect ratio on heat transfer characteristics in detail, $H/d = 9$ gives the highest heat transfer similar to case – 1 and case – 2. $H/d = 9$ gives a maximum of 31% more heat transfer compared to $H/d = 7$, further $H/d = 7$ gives a maximum of 11% more heat transfer is observed compared to $H/d = 5$. Among all the jet-to-plate distances investigated $S/d = 4$ gives the maximum heat transfer over the entire target surface for $H/d = 5$ and $H/d = 7$, this is due to the strong impingement of the jets, with less jet travel distance, which thins the boundary layer resulting in high heat transfer. With respect to the effect of jet-to-plate distance, it is observed that the variation in local Nusselt number is minimum to a change in jet-to-plate distance for all the feeding channel aspect ratios.

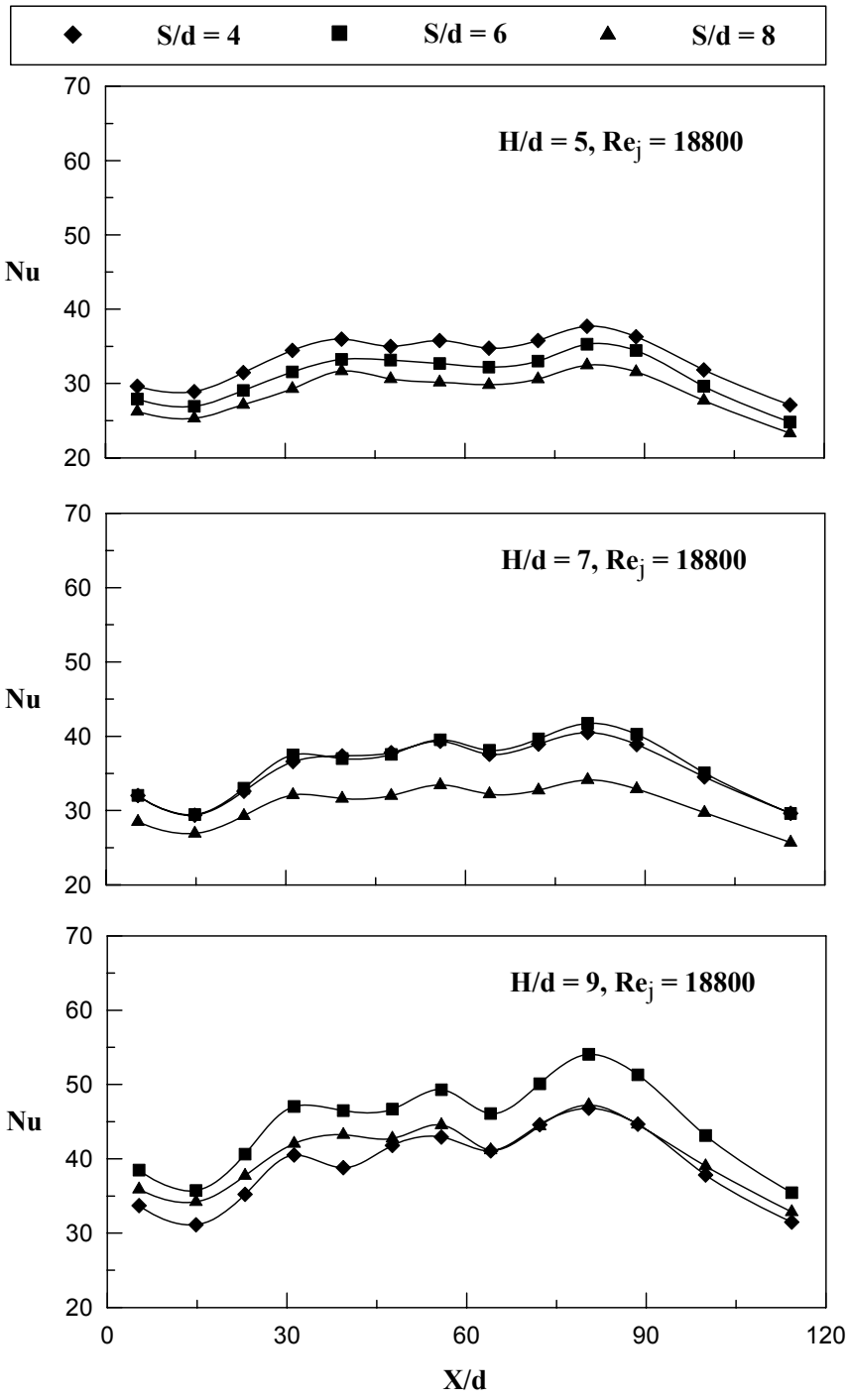

Figure 6.12 Effect of jet-to-plate distance and feeding channel aspect ratio $5 \le H/d \le 9$ on local Nusselt number distribution for $\mathrm{Re}_j = 18800$ and case – 3.

6.5 Average Nusselt Number

Figures 6.13 – 6.14 shows the average Nusselt number Nu_{avg} as a function of jet Reynolds number Re_j, plotted for all outflow orientations and the jet-to-plate distance $4 \le S/d \le 8$. The value of Nu_{avg} is an average of the detailed results on the target surface.

6.5.1 Effect of feeding channel aspect ratio

Figure 6.14 shows the effect of feeding channel aspect ratio studied $5 \le H/d \le 9$ on the averaged Nusselt number for different outflow orientation. It is observed that the averaged Nusselt number increases linearly with an increase in the jet Reynolds number, as stated in the previous discussion. Considering the effect of jet-to-plate distance, $S/d = 4$ gives the maximum values of averaged Nusselt number due to the stronger impingement of jets and $S/d = 8$ gives the least values of averaged Nusselt number as the crossflow dominates the impingement of jets. Averaged Nusselt number is sensitive for a change in jet-to-plate distance for the feeding channel aspect ratio $H/d = 5$, whereas it is less sensitive for the other two feeding channel aspect ratios as no much variation is observed with an increase in jet-to-plate distance comparatively. For $\mathrm{Re}_j = 14400$, less variation in the magnitude of Nu_{avg} is observed for a change in the jet-to-plate distance compared to the other two jet Reynolds numbers for feeding channel aspect ratios $H/d = 7$ and $H/d = 9$.

6.5.2 Effect of outflow orientation

Figure 6.13 shows the effect of the outflow orientation on averaged Nusselt number for different jet-to-plate distance. The averaged Nusselt number increases linearly with an increase in the jet Reynolds number. Among all the feeding channel aspect ratios studied $H/d = 9$ has the maximum values of the Nu_{avg}, for all the outflow orientations and for all the jet-to-plate distances studied, the reason being the strong impingement of jets with minimum effect of crossflow. $H/d = 5$ gives the least values of Nu_{avg} among all the feeding channel aspect ratios studied this may be due to crossflow getting stronger as the feeding channel aspect ratio decreases. Case – 3 has the highest magnitude of the Nu_{avg} among all the outflow orientations studied, whereas the Nu_{avg} values for case – 1 and case – 2 are close with a less variation in magnitude for all the jet Reynolds numbers. It is also observed that as the jet-to-plate distance is increased there is a corresponding decrease in the values of Nu_{avg} for all the feeding channel aspect ratios. In detail, the averaged Nusselt number distribution for $S/d = 6$ and $S/d = 8$ is almost similar for case – 2 and case –3 for feeding channel aspect ratios $H/d = 7$ and $H/d = 9$. The maximum difference in magnitude of averaged Nusselt number for case – 3 and the other two cases is 8%. For $\mathrm{Re}_j = 9300$, very less difference in magnitude of Nu_{avg} is observed with respect to all the outflow orientations whereas for the other two jet Reynolds numbers a considerable difference in magnitude of the Nu_{avg} is noticed. This may be due to the increase in the strength of the jets with an increase in the jet Reynolds number. Maximum variation in Nu_{avg} is observed for $\mathrm{Re}_j = 18800$.

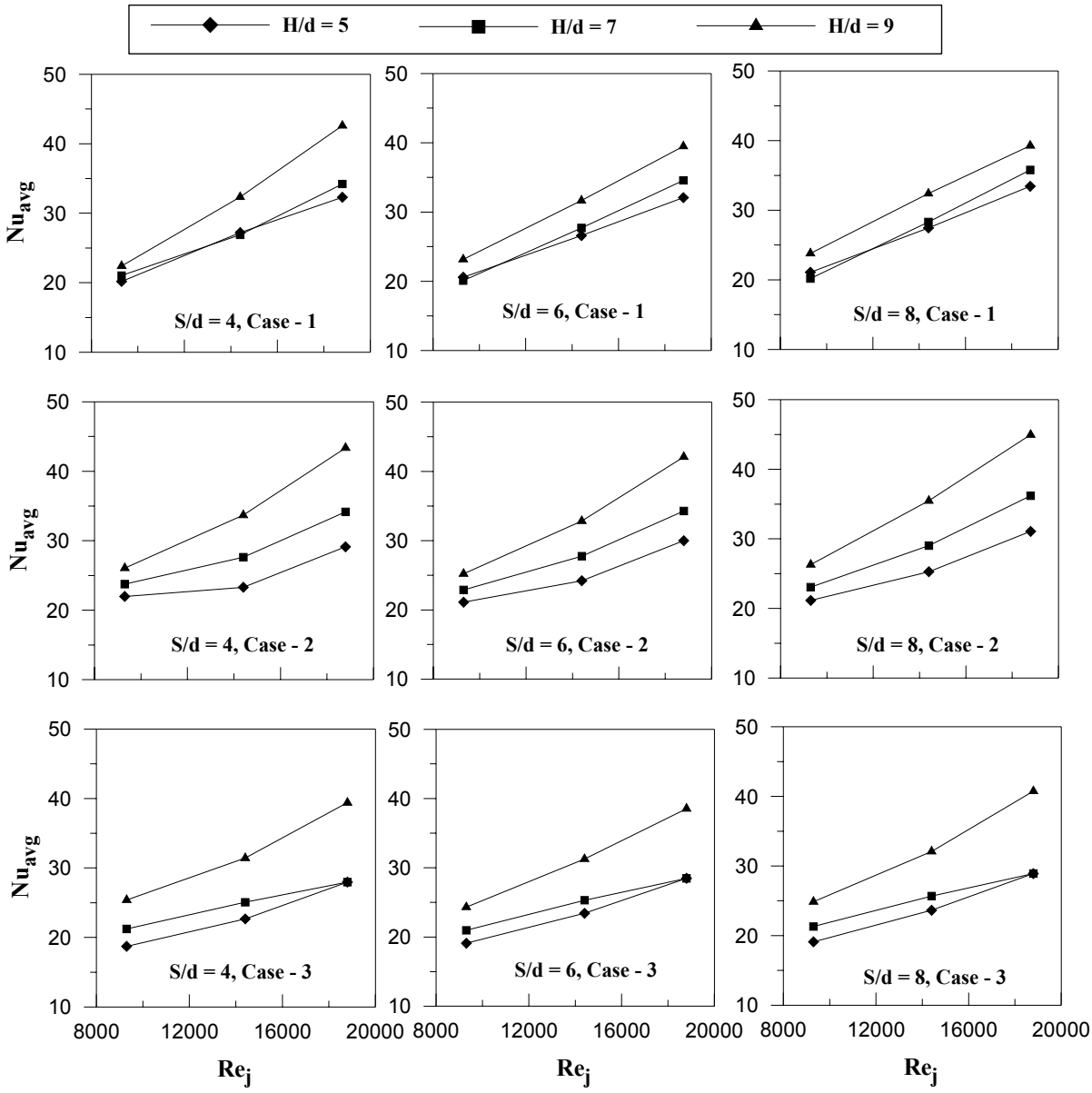

Figure 6.13 Effect of feeding channel aspect ratio $(5 \le H / d \le 9)$ and jet-to-plate distances on averaged Nusselt number for different outflow orientation.

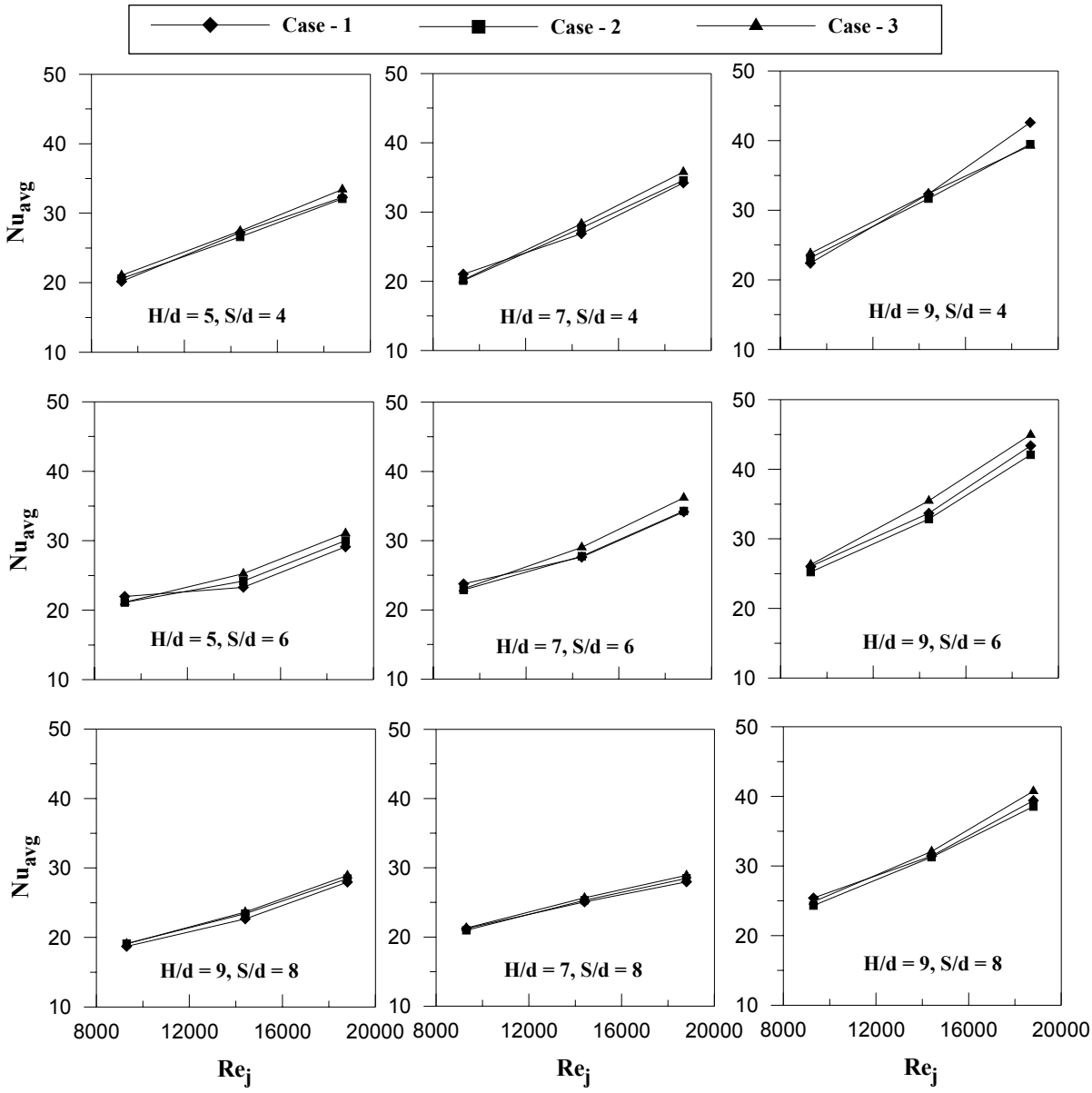

Figure 6.14 Effect of outflow orientation and feeding channel aspect ratio on averaged Nusselt number for different jet-to-plate distances $(4 \le S/d \le 8)$.

6.5.3 Correlations of Averaged Nusselt number

The results for three different outflow orientations are correlated for the jet Reynolds number Re_j and the normalized jet-to-plate distance S/d dependence as

$$Nu_{avg} = A\,(\mathrm{Re}_j)^B (S/d)^C (H/d)^D \tag{6.1}$$

The present results are correlated for all outflow orientations individually for jet Reynolds number Re_j dependence. Previous studies in the field of jet impingement have involved in developing correlations for the averaged Nusselt number as a function of the jet Reynolds number by considering many parameters. Correlations by Huang et al [21],Kercher and Tabakoff [30] and Florscheutz et al [14] are compared to the averaged Nusselt number in the present investigation. Huang et al [21] studied the outflow orientations similar to ones used in the present study. They presented results for the outflow orientation 1 and 2 correlating for Reynolds number dependence as $Nu = 0.035\,\mathrm{Re}^{0.76}$, whereas for outflow orientation 3 which has the highest magnitude of heat transferred from the target surface is correlated as $Nu = 0.082\,\mathrm{Re}^{0.727}$. Kercher and Tabakoff [30] also studied the effect of crossflow and it is similar to the case – 1 in the present study. They varied the jet hole diameter, the hole spacing x, y and the jet to target plate distance. Based on all of these geometrical parameters, they proposed a correlation of the form $Nu = \phi_1\,\phi_2\,\mathrm{Re}^m\,(z/d)^{0.91}\,\mathrm{Pr}^{1/3}$, where ϕ_1 and ϕ_2 are constants based on X/d and Y/d, respectively. Florschuetz et al [14] presented the correlations with different coefficients of inline and staggered rows. The correlation for jet

impingement with minimum crossflow is given as $Nu = 0.363(X/d)^{-0.554}(Y/d)^{-0.422}(Z/d)^{0.068}\,\mathrm{Re}_j^{-0.554}\,\mathrm{Pr}^{1/3}$.

The detailed values of the local Nusselt number are averaged over the entire length of the target surface to obtain a single averaged Nusselt number. The averaged Nusselt numbers for each outflow orientation are plotted against the jet Reynolds number. The present results are correlated for the jet Reynolds number dependence as $Nu_{avg} = 0.0399\,(\mathrm{Re}_j)^{0.794}(S/d)^{0.415}(H/d)^{2.180}$ for case 1 and 2. The correlations for Huang et al [21] for case 1 and 2 are in good comparison with the present study. Kercher and Tabakoff [30] presented the results for the outflow orientation – 1 and the results of the present study are in good comparison with the existing correlation. The case with maximum heat transfer from the target surface, outflow orientation – 3, is correlated for the jet Reynolds number dependence as $Nu_{avg} = 0.0479(\mathrm{Re}_j)^{0.785}(S/d)^{0.354}(H/d)^{4.675}$. The correlation used from Florschuetz et al [14] is for the case with minimum crossflow. Huang et al [21] also presented a separate correlation for the case with high heat transfer; this case in their study had the less crossflow effect. The results from the present study for case – 3 are lower than the existing correlations, which includes the crossflow effect. The correlation for case – 3 in the present study is in good agreement with the correlation presented by Florschuetz et al [14] and Huang et al [21]. Thus it is evident from the above discussion that the crossflow effect is more dominant on outflow orientation 1 and 2 compared to outflow orientation – 3.

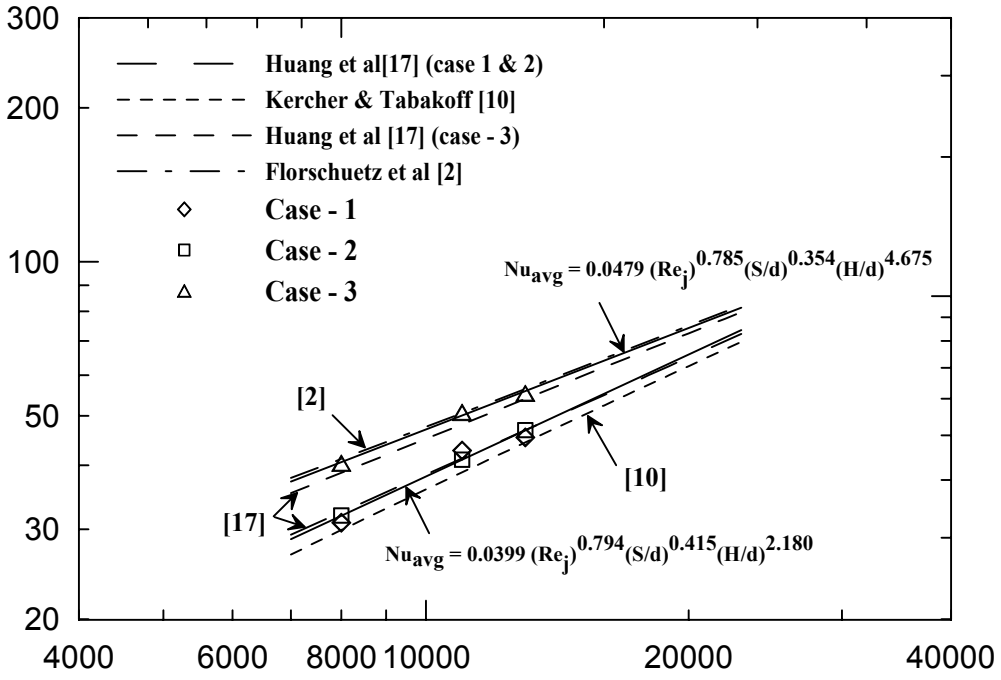

Figure 6.15 Averaged Nusselt number comparisons with the existing correlations

CHAPTER 7

ORIFICE PLATE - 3

In this chapter a detailed discussion on the results obtained by using the orifice plate 3 (staggered arrangement of jets) with jet diameter $d = 0.5\,cm$ are presented. Nusselt number distribution is presented as a function of non-dimensional distance along the entire length of the heated target surface and also as a function of the jet Reynolds number. As presented in the earlier chapters 5 and 6, Nusselt number distributions are shown for all the feeding channel aspect ratios studied $5 \le H/d \le 9$, the jet-to-plate distance $4 \le S/d \le 8$, and for three jet Reynolds numbers being investigated $9300 \le \mathrm{Re}_j \le 18800$. First a detail insight into the effect of jet Reynolds number onto the Nusselt number distribution, which also covers the effect of feeding channel aspect ratio on the Nusselt number. Next, the effect of the jet-to-plate distance onto the Nusselt number behavior is presented. Next, the effect of the outflow orientation on the Nusselt number distribution along the entire surface is investigated. Finally the average Nusselt number distribution is plotted as a function of the jet Reynolds number.

7.1 Effect of feeding channel aspect ratio on local Nusselt number

Figure 7.1 – 7.3, gives a detail insight into the local Nusselt number distribution presenting the effect of feeding channel aspect ratio $5 \le H/d \le 9$ on the heat transfer from the target surface.

All the results are presented for jet-to-plate distance $S/d = 6$ as this jet-to-plate distance gives maximum heat transfer. All the outflow orientations are discussed.

Figure 7.1 shows effect of feeding channel aspect ratio on the local Nusselt number distribution over the entire length of the target surface for case – 1, where the flow exits at low X/d $(X/d = 0)$. The crossflow develops from large X/d to low X/d as the air exits at low X/d. The heat transferred from the target surface decreases with an decrease in feeding channel aspect ratio from H/d = 9 to 5 for all the feeding channel aspect ratios. Over the entire length of the target surface, the feeding channel aspect ratio $H/d = 5$ gives the maximum heat transfer for all the jet Reynolds numbers $9300 \le \mathrm{Re}_j \le 18800$ studied. This is primarily due to the increase in the strength of the jets at low feeding channel aspect ratios. Observing the effect of the feeding channel aspect ratio on the local Nusselt number distribution for all the jet Reynolds numbers studied, $H/d = 5$ gives the maximum heat transfer among all the feeding channel aspect ratios studied. The difference in the magnitude of the local Nusselt number for all the feeding channel aspect ratios is very less for all the jet Reynolds number studied. This is observed by the curves overlapping over each other. With an increase in the feeding channel aspect ratio the difference in the magnitude of the local Nusselt number also increases for an increase in the jet Reynolds number. Among all the Reynolds numbers studied, $\mathrm{Re}_j = 18800$ gives the maximum heat transfer. As discussed earlier in figure 7.1, a peak of local Nusselt number at $X/d = 80.4$ is observed this is due to the flow entering the impingement channel at large X/d, where the effect of crossflow is minimal. At $31.2 \le X/d \le 72.2$ crossflow dominates the impingement of jets and a linearly decreasing distribution of local Nusselt number is observed towards the exit.

Figure 7.2 shows the effect of the feeding channel aspect ratio on the local Nusselt number distribution for case – 2 and for jet-to-plate distance $S/d = 6$. For case – 2 the flow exits at low X/d $(X/d = 0)$, causing crossflow development towards the exit. $H/d = 5$ gives the maximum heat transfer over the entire length of the target surface for all the jet Reynolds numbers studied. For all the jet Reynolds numbers studied, $H/d = 5$ gives a marginal increase in heat transfer from the target surface compared to $H/d = 7$ whereas $H/d = 5$ gives a maximum of 4% increase in heat transfer is observed compared to $H/d = 9$. It is also observed that the magnitude of the local Nusselt number increases with an increase in the jet Reynolds number for all the feeding channel aspect ratios studied. The variation in the local Nusselt number is more sensitive with respect to a change in feeding channel aspect ratio at high jet Reynolds number whereas it is less sensitive at low jet Reynolds numbers. At $80.4 \le X/d \le 114.3$ the magnitude of local Nusselt number decreases from $X/d = 80.4$ to $X/d = 114.3$, this is due to the obstruction caused by the crossflow to the impinging jets.

Figure 7.3 shows the effect of feeding channel aspect ratio on the local Nusselt number distribution for case – 3 and for jet-to-plate distance $S/d = 6$. For case – 3 air exits at $X/d = 0$ and $X/d = 114.3$, where the crossflow has a predominant effect over the heat transfer characteristics. It is observed that at $0 \le X/d \le 30$ and $80.4 \le X/d \le 114.3$ the local Nusselt number decreases towards exit, this may be due to the crossflow at the exit and thus reduces the strength of the impinging jets and the heat transferred from the target surface. The magnitude of local Nusselt number at $31.2 \le X/d \le 72.2$ is high compared to the other X/d locations this may be due to the strong impingement of jets. For an increase

in feeding channel aspect ratio a corresponding increase in local Nusselt number is observed. $H/d=5$ gives the maximum values of local Nusselt numbers for all the jet Reynolds numbers studied. Considering the effect of feeding channel aspect ratio for all jet Reynolds numbers on heat transfer characteristics in detail, $H/d=5$ gives the highest heat transfer similar to case – 1 and case – 2. $H/d=5$ gives a marginal increase in heat transfer compared to $H/d=7$, further $H/d=5$ gives a maximum of 5% more heat transfer compared to $H/d=9$. Similar to case – 1 and case – 2, with respect to the effect of feeding channel aspect ratio on local Nusselt number characteristics it is observed that the local Nusselt number is sensitive to a change in feeding channel aspect ratio at high jet Reynolds numbers.

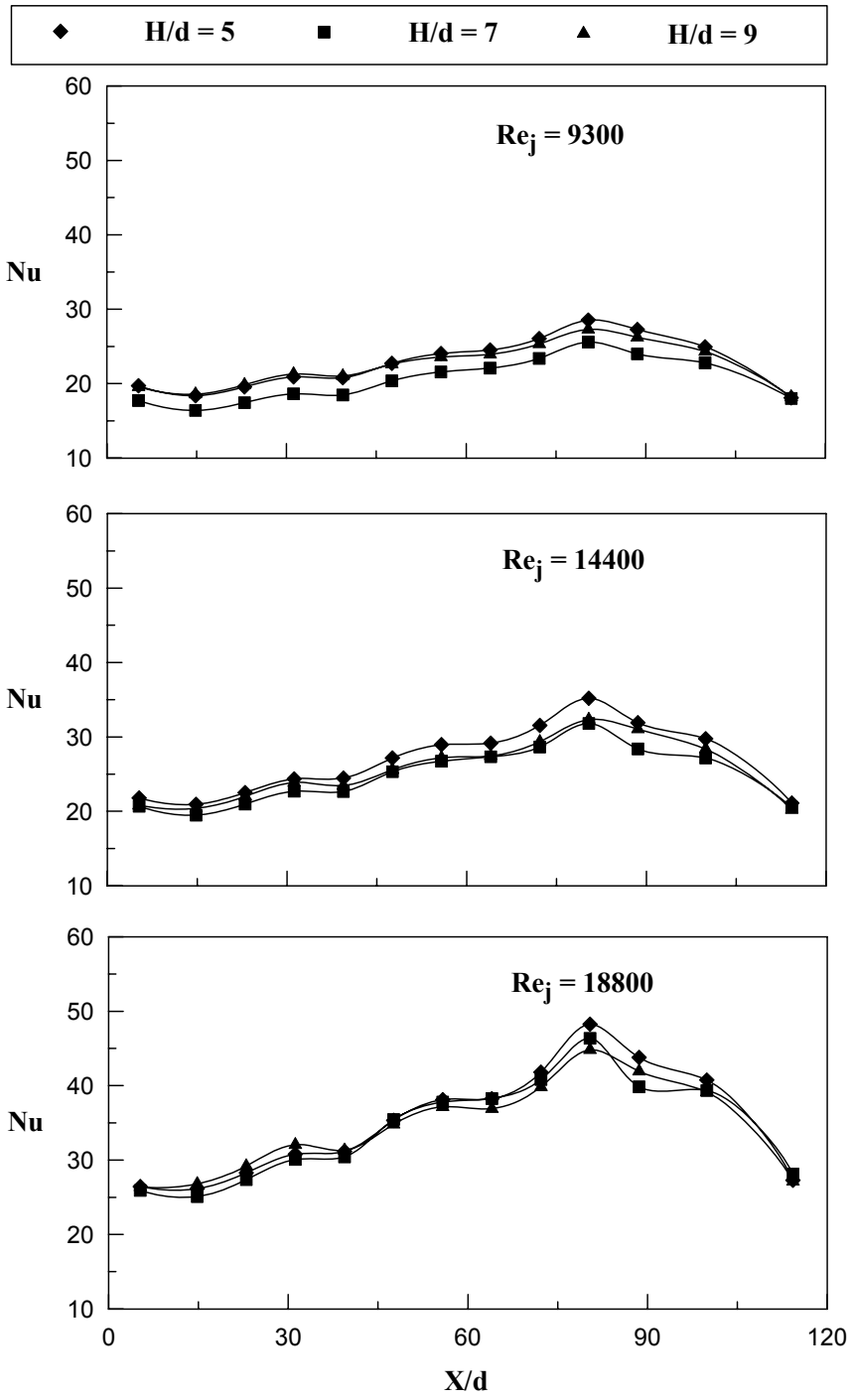

Figure 7.1 Effect of feeding channel aspect ratio $5 \le H/d \le 9$ on local Nusselt number distribution for case – 1 and jet-to-plate distance $S/d = 6$.

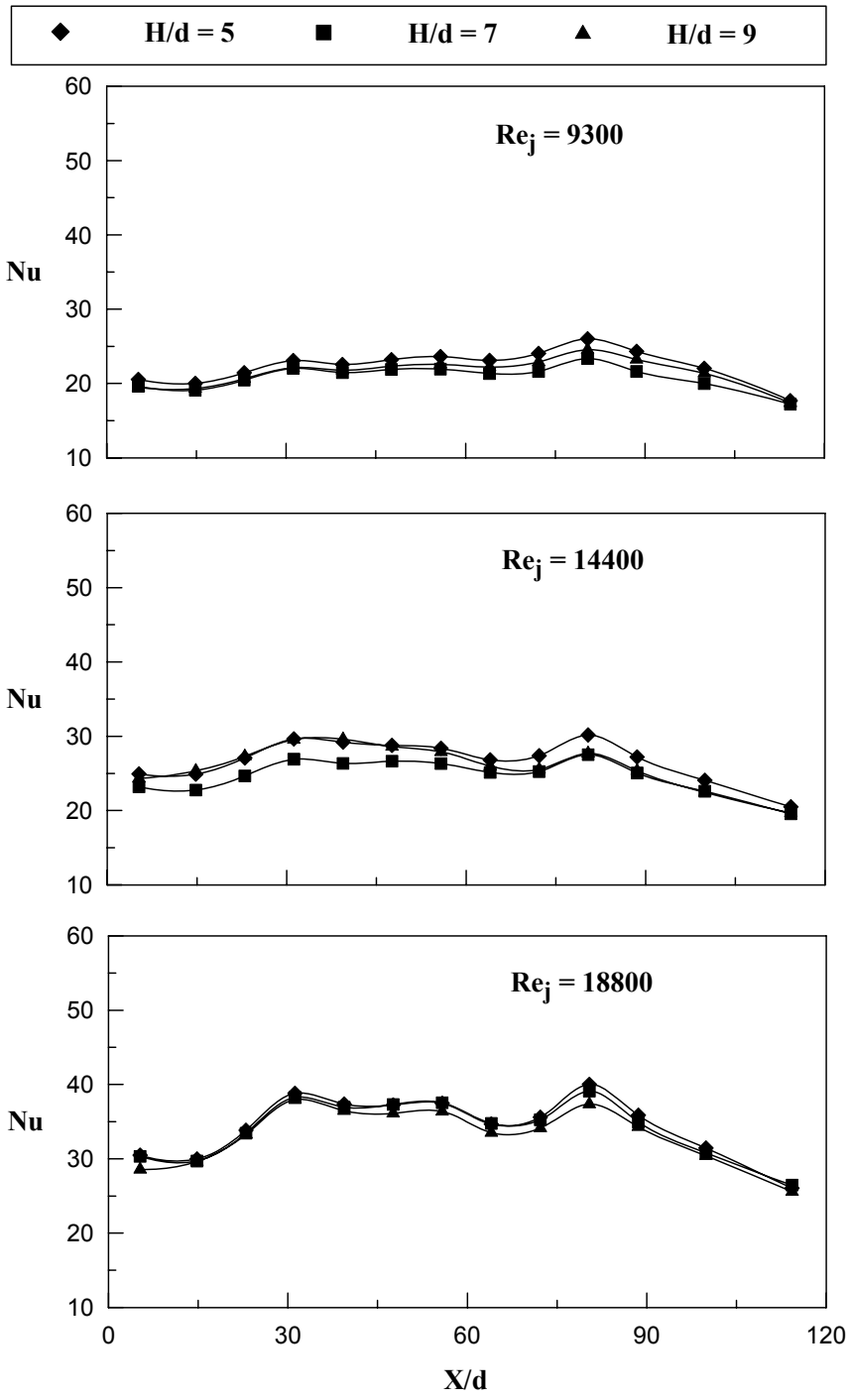

Figure 7.2 Effect of feeding channel aspect ratio $5 \le H/d \le 9$ on local Nusselt number distribution for case – 2 and jet-to-plate distance $S/d = 6$.

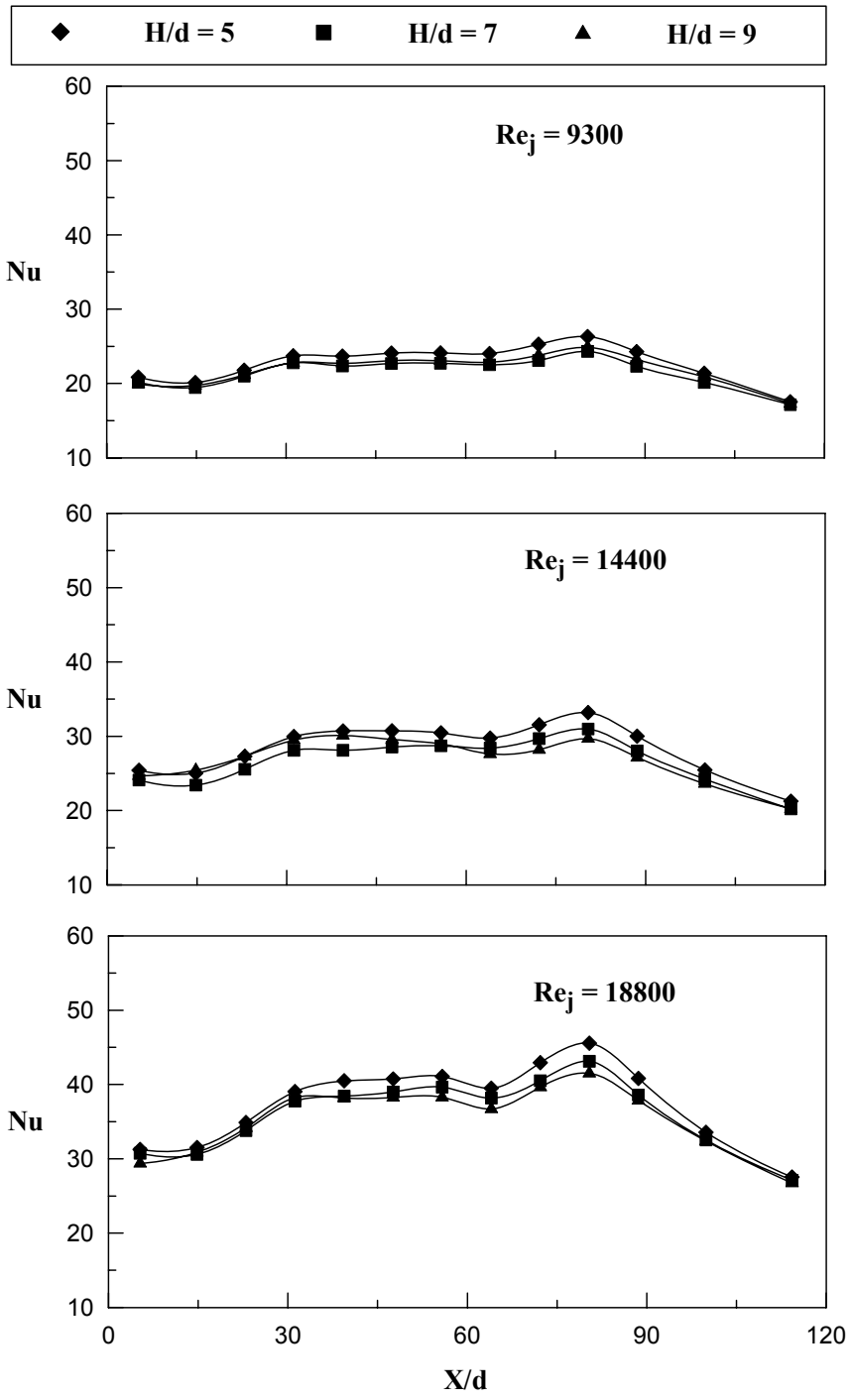

Figure 7.3 Effect of feeding channel aspect ratio $5 \le H/d \le 9$ on local Nusselt number distribution for case – 3 and jet-to-plate distance $S/d = 6$.

7.2 Effect of jet Reynolds number on local Nusselt number

Figure 7.4 – 7.6 shows the local Nusselt number distribution for different jet Reynolds numbers $9300 \le \mathrm{Re}_j \le 18800$, for jet-to-plate distance $S/d = 6$, expressing the effect of the feeding channel aspect ratio on the heat transfer from the heated target surface. Among all the jet-to-plate distances studied $S/d = 6$ is considered, as it is the best case in which maximum heat is transferred from the target surface.

Figure 7.4 shows the local Nusselt number distribution plotted for case – 1, which gives a detailed insight into the effect of the feeding channel aspect ratio. Three different values of the feeding channel aspect ratio are considered in this part of the study $5 \le H/d \le 9$. The results are presented for three jet Reynolds numbers $9300 \le \mathrm{Re}_j \le 18800$. It is observed that for an increase in the jet Reynolds number there is a corresponding increase in the magnitude of local Nusselt number. Highest values of local Nusselt number are observed for $\mathrm{Re}_j = 18800$ compared to the other two jet Reynolds numbers. Increasing the jet Reynolds number from $\mathrm{Re}_j = 9300$ to $\mathrm{Re}_j = 14400$ gives a maximum of 11% increase in the local Nusselt number values whereas for an increase from $\mathrm{Re}_j = 14400$ to $\mathrm{Re}_j = 18800$ a large increase of 42% in magnitude of local Nusselt number is observed indicating the increase in strength of jets with an increase in jet Reynolds number. For case – 1, the flow exits the impingement channel at low X/d $(X/d = 0)$. At large X/d $(X/d = 80.4)$ a peak of local Nusselt number is observed this may be due to strong impingement of the air jets and also because the effect of crossflow is minimal, which reduces the boundary layer thickness. Among all the feeding channel aspect ratios examined

$5 \le H/d \le 9$, $H/d = 5$ gives the maximum values of local Nusselt number for all the jet-to-plate distances studied. $H/d = 5$ gives a marginal increase in the local Nusselt number from the target surface compared to $H/d = 7$, whereas 7% increase in local Nusselt number is observed compared to $H/d = 9$. At $31.2 \le X/d \le 72.2$ a uniform decrease in magnitude of local Nusselt number is observed along the target surface from $X/d = 72.2$ to $X/d = 0$ for all the feeding channel aspect ratios studied, this may be due to the crossflow of the air generated towards the exit.

Figure 7.5 shows the effect of feeding channel aspect ratio on the local Nusselt number distribution for case – 2 as a function of jet Reynolds numbers $9300 \le \mathrm{Re}_j \le 18800$. For case – 2 air exits the impingement channel at $X/d = 114.3$, this leads to the development of crossflow towards the exit. Similar to the case – 1 an increase in jet Reynolds number leads to the corresponding increase in the local Nusselt number for all the feeding channel aspect ratios studied. The magnitude of local Nusselt number at $31.2 \le X/d \le 72.2$ is more compared to the other X/d locations this may be due to the strong impingement of jets at this location. Although similar distribution of local Nusselt number is observed for $H/d = 5$ and $H/d = 7$, but $H/d = 5$ gives a marginal increase in heat transfer from the entire target surface compared to $H/d = 7$ and $H/d = 5$ gives a maximum of 6% more heat transfer from the entire target surface compared to $H/d = 9$. The local Nusselt number is sensitive for a change in jet Reynolds number, this is observed from the difference in magnitude of local Nusselt number varying with respect to jet Reynolds number. $\mathrm{Re}_j = 18800$ gives the maximum values of local Nusselt number for all the feeding channel aspect ratios studied. Nusselt number distribution for $\mathrm{Re}_j = 9300$ and $\mathrm{Re}_j = 14400$ is close

with a maximum difference in magnitude being 27%. At $80.02 \le X/d \le 114.3$, a decrease in local Nusselt number is observed from $X/d = 80.02$ towards the exit at $X/d = 114.3$, this is due to the development of crossflow towards the exit, which obstructs the impingement of jets and thickens the boundary layer. This behavior of local Nusselt number at large X/d is observed for all the feeding channel aspect ratios studied.

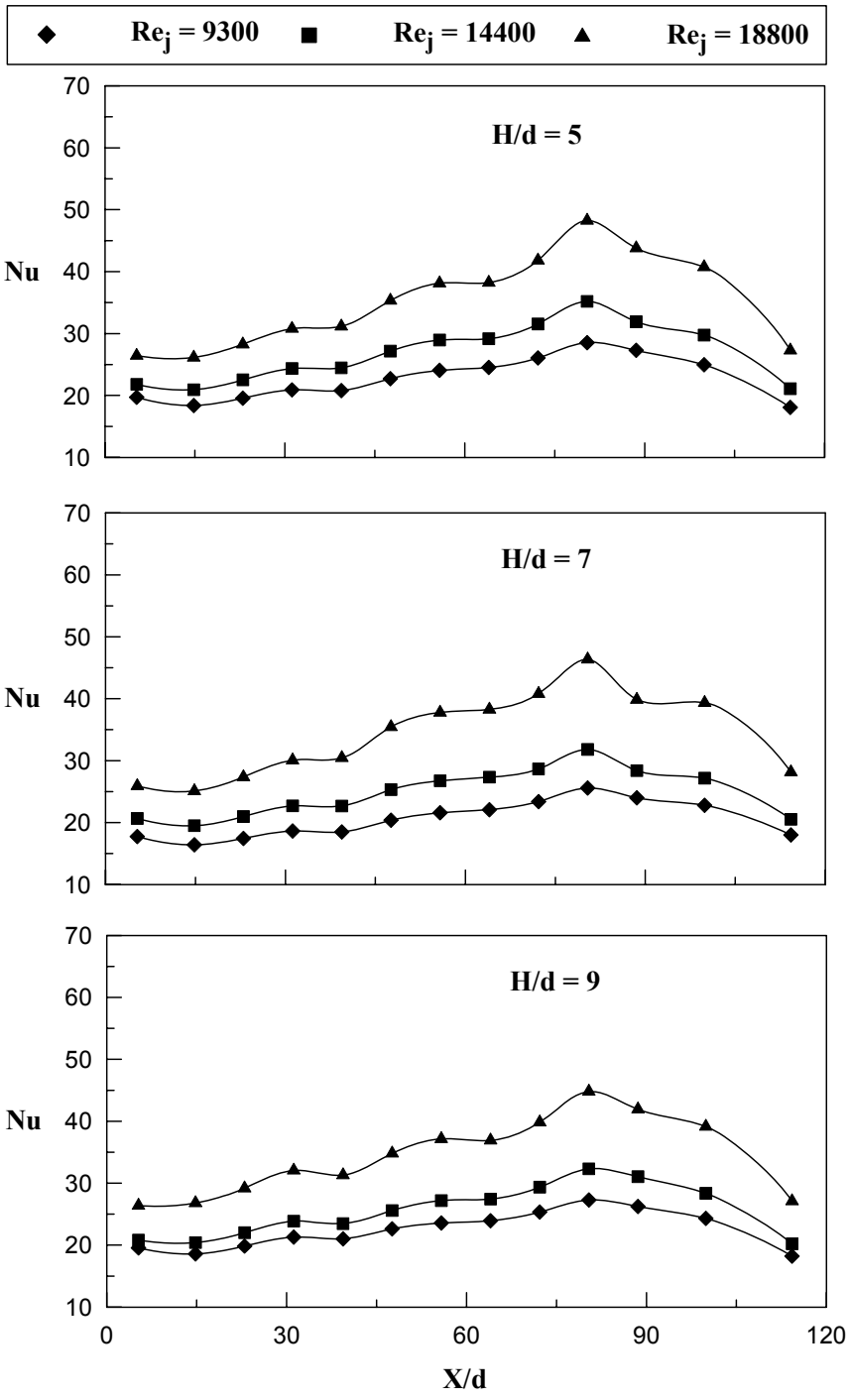

Figure 7.4 Effect of jet Reynolds number on local Nusselt number distribution for $S/d = 6$ and case – 1.

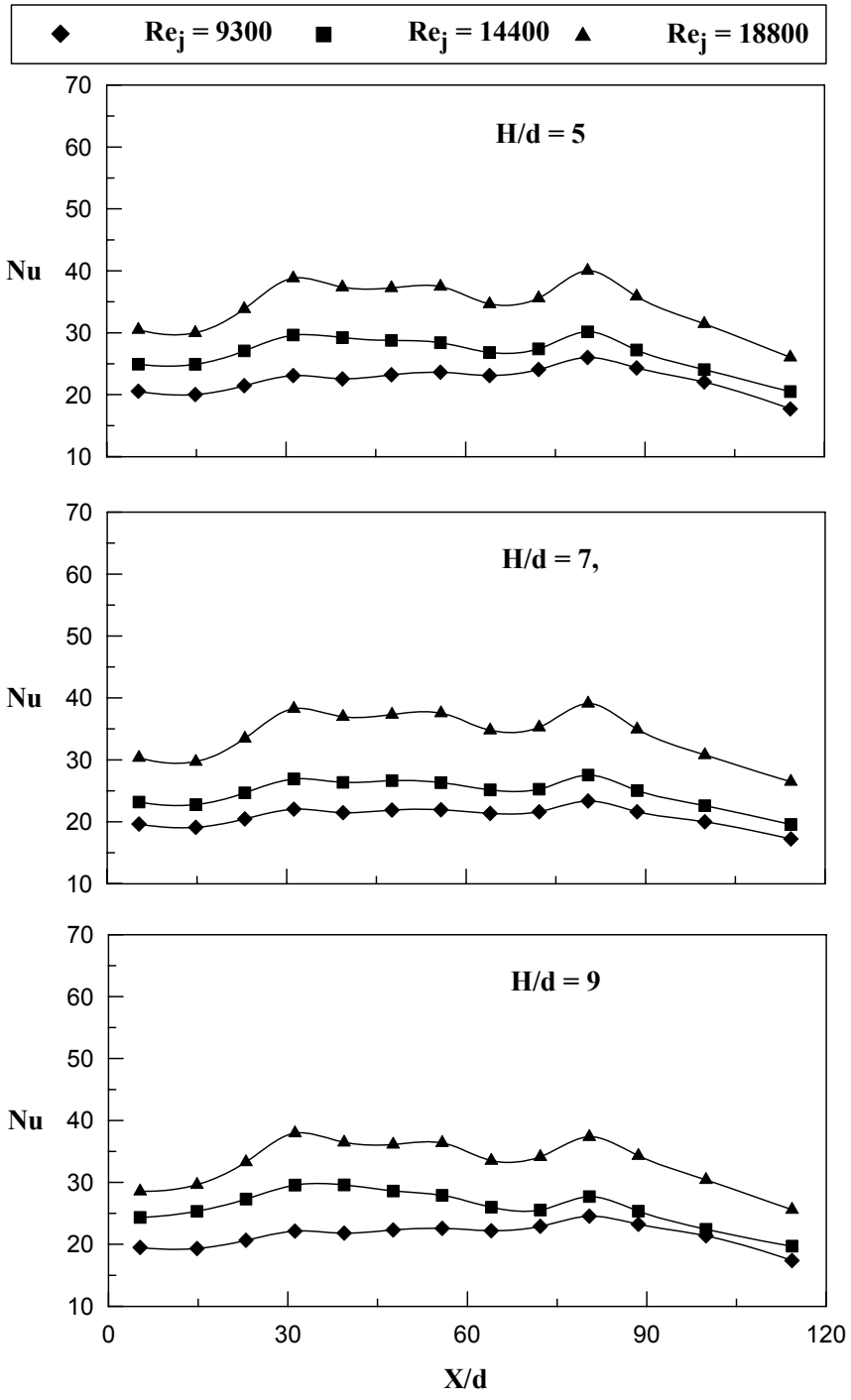

Figure 7.5 Effect of jet Reynolds number on local Nusselt number distribution for $S/d = 6$ and case – 2.

Figure 7.6 presents the local Nusselt number distribution for case – 3 where the air exits from both the directions at low X/d $(X/d=0)$ and large X/d $(X/d=114.3)$. It is observed that the crossflow develops at both the exit directions, which reduces the heat transferred from the target surfaces. Similar to heat transfer observed from case – 1 and case – 2, $H/d=5$ has the maximum heat transfer for case – 3. $H/d=5$ gives a maximum of 6.1% more heat transfer compared to $H/d=7$ and $H/d=5$ gives a maximum of 10.2% more heat transfer compared to $H/d=9$. The magnitude of local Nusselt number at $31.2 \le X/d \le 72.2$ is more compared to the other X/d locations this is due to the strong impingement of jets at the centre of the target surface compared to the exit locations where the crossflow is less dominant to the impingement effect. Small peaks of local Nusselt number are observed at $X/d=80$ and $X/d=60$ which are the result of the stronger jet impingement. At $0 \le X/d \le 30$ and $80.4 \le X/d \le 114.3$ a linearly decreasing local Nusselt number distribution is observed towards the exit this is primarily due to the crossflow obstructing the impinging jets towards the exit of impingement channel. The difference in the magnitude of local Nusselt number for an increase of jet Reynolds number from $\mathrm{Re}_j = 9300$ to $\mathrm{Re}_j = 14400$ is similar to the increase in magnitude from $\mathrm{Re}_j = 14400$ and $\mathrm{Re}_j = 18800$ for all the feeding channel aspect ratios studied. Similar to the outflow orientations 1 and 2, $\mathrm{Re}_j = 18800$ gives the maximum values of local Nusselt number compared to the other jet Reynolds numbers studied.

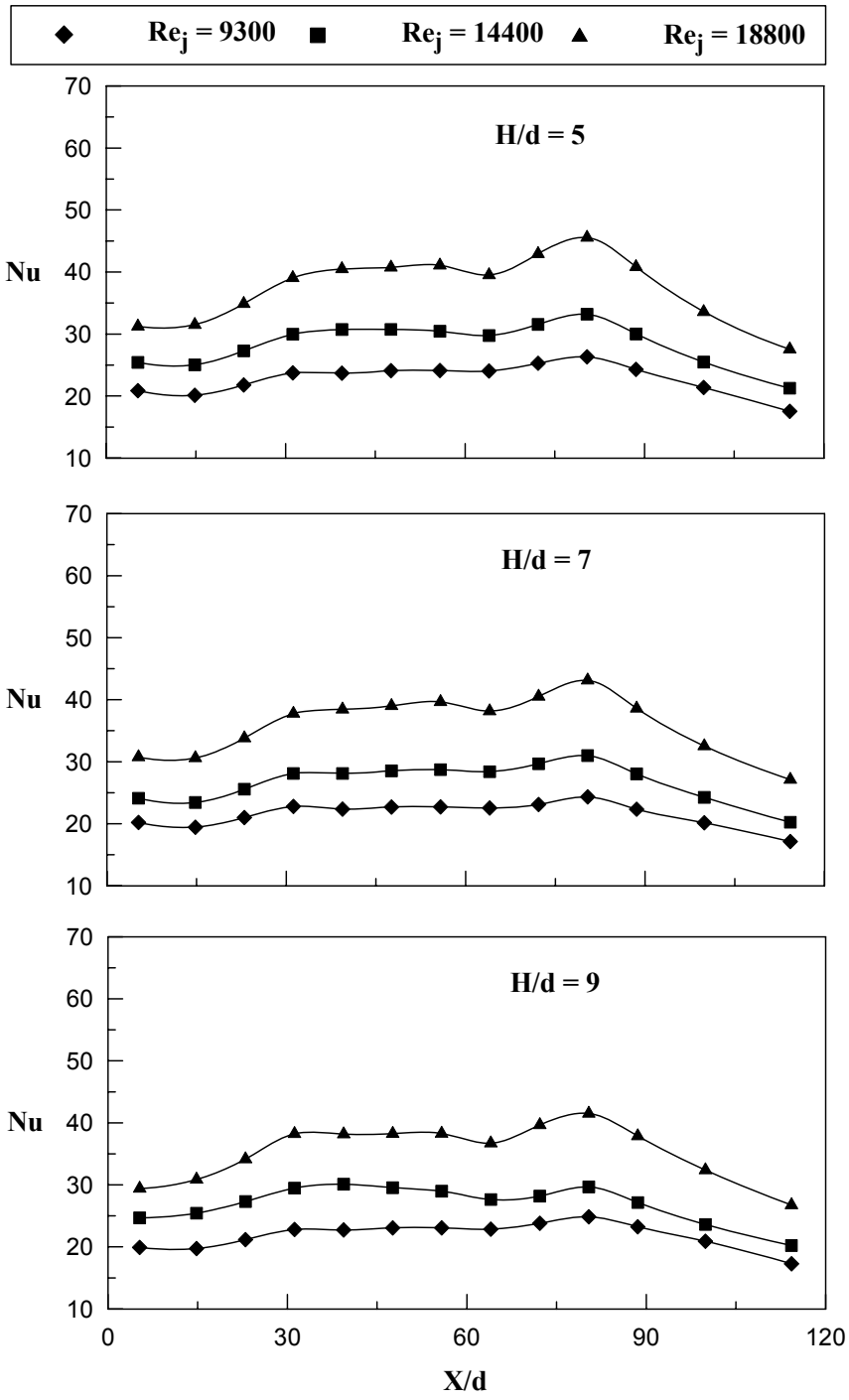

Figure 7.6 Effect of jet Reynolds number on local Nusselt number distribution for $S/d = 6$ and case – 3.

7.3 Effect of outflow orientation on local Nusselt number

Figure 7.7 – 7.9 shows the effect of the outflow orientation for different feeding channel aspect ratios $5 \le H/d \le 9$ on local Nusselt number. The results are presented for $S/d = 6$, due to the highest amount of heat transfer observed among all the jet-to-plate distances investigated. All the jet Reynolds numbers studied $9300 \le \mathrm{Re}_j \le 18800$ are discussed individually.

Figure 7.7 represents the effect of the outflow orientation on the local Nusselt number distribution plotted for different feeding channel aspect ratios $5 \le H/d \le 9$ for $\mathrm{Re}_j = 9300$. Among all the feeding channel aspect ratios studied very less variation in the magnitude of local Nusselt number is observed with respect to outflow orientation at $31.2 \le X/d \le 72.2$ for case – 2 and case – 3. Whereas, for case – 1 a linearly decreasing local Nusselt number distribution is observed from $X/d = 80.4$ to $X/d = 31.2$, this may be due to the crossflow getting intensified towards the exit, opposing and decreasing the strength of the impingement jets. At $80.4 \le X/d \le 114.3$ for all the feeding channel aspect ratios studied, case – 1 has the highest heat transfer due to air entering the impingement channel at this location resulting in stronger impingement reducing the boundary layer thickness. Similar to the above discussions, $H/d = 5$ gives the maximum heat transfer over the entire length of the target surface. It is also observed that case – 2 has the least magnitude of local Nusselt number over the entire length of the target surface for all the feeding channel aspect ratios studied.

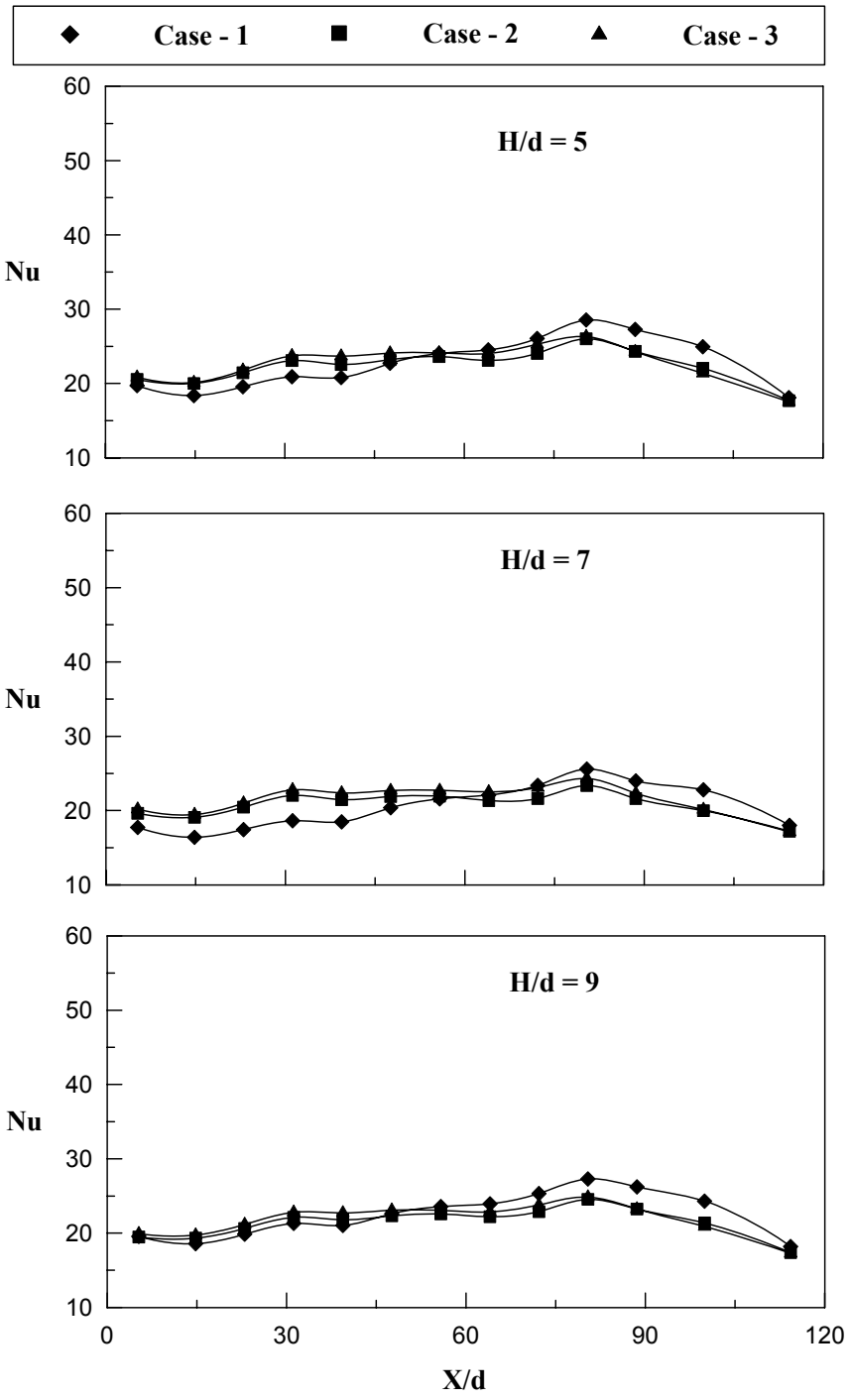

Figure 7.7 Effect of outflow orientation on local Nusselt number distribution for $S/d = 6$ and $\mathrm{Re}_j = 9300$.

Figure 7.8 shows the effect of feeding channel aspect ratio on the local Nusselt number distribution for different outflow orientations studied and for $\mathrm{Re}_j = 14400$. It is observed that as the jet Reynolds number increases from 9300 to 14400 a maximum of 23% increase in local Nusselt number is found similar to $\mathrm{Re}_j = 9300$, case – 1 has maximum heat transfer at $80.4 \le X/d \le 114.3$ due to the strong impingement of jets. Whereas case – 2 has the least magnitude of local Nusselt number due to the obstruction to the impinging jets caused by the crossflow. Similar to $\mathrm{Re}_j = 9300$, the local Nusselt number distribution at $31.2 \le X/d \le 72.2$ is uniform for case – 3 and case – 2 whereas a linearly decreasing local Nusselt number distribution is observed at $X/d = 23$ towards $X/d = 0$. Similar to $\mathrm{Re}_j = 9300$, $H/d = 5$ has the highest magnitude of local Nusselt number compared to the other two feeding channel aspect ratios studied. Unlike $\mathrm{Re}_j = 9300$, where the variation in the magnitude of local Nusselt number is very less, for $\mathrm{Re}_j = 14400$ the variation with respect to outflow orientation is more comparatively for all the feeding channel aspect ratios studied.

Figure 7.9 shows the effect of feeding channel aspect ratio on the local Nusselt number distribution for all the outflow orientations and for $\mathrm{Re}_j = 18800$. It is observed that as the jet Reynolds number increases from 14400 to 18800 a maximum of 37% increase in local Nusselt number is found similar to $\mathrm{Re}_j = 14400$. It is also observed that very less variation in local Nusselt number is observed at large X/d $(80.4 \le X/d \le 114.3)$ compared to $\mathrm{Re}_j = 9300$ and $\mathrm{Re}_j = 14400$ for all the outflow orientations studied. Moreover as the

H/d values increase from 5 to 9 a corresponding decrease in the magnitude of local Nusselt number is observed. Similar to the other two jet Reynolds number investigated at $31.2 \le X/d \le 72.2$, case $-$ 3 and case $-$ 2 have the uniform distribution of local Nusselt number whereas case $-$ 1 has a linearly decreasing local Nusselt number from $X/d = 80.4$ to $X/d = 31.2$, the reason being explained previously. Maximum heat transfer is observed for $H/d = 5$ similar to $\mathrm{Re}_j = 9300 \,\&\, 14400$ followed by $H/d = 7$ and $H/d = 9$.

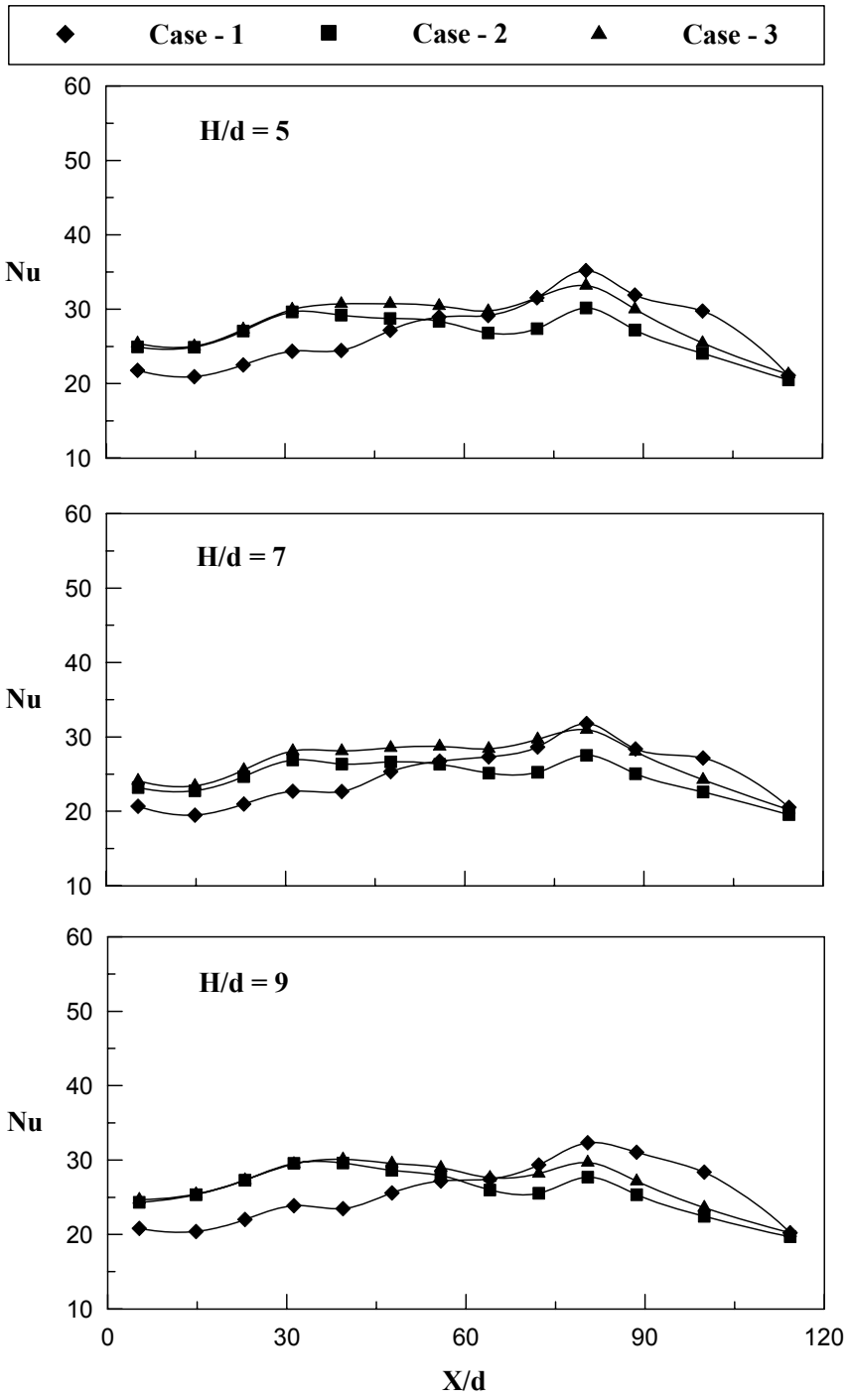

Figure 7.8 Effect of outflow orientation on local Nusselt number distribution for $S/d = 6$ and $\mathrm{Re}_j = 14400$.

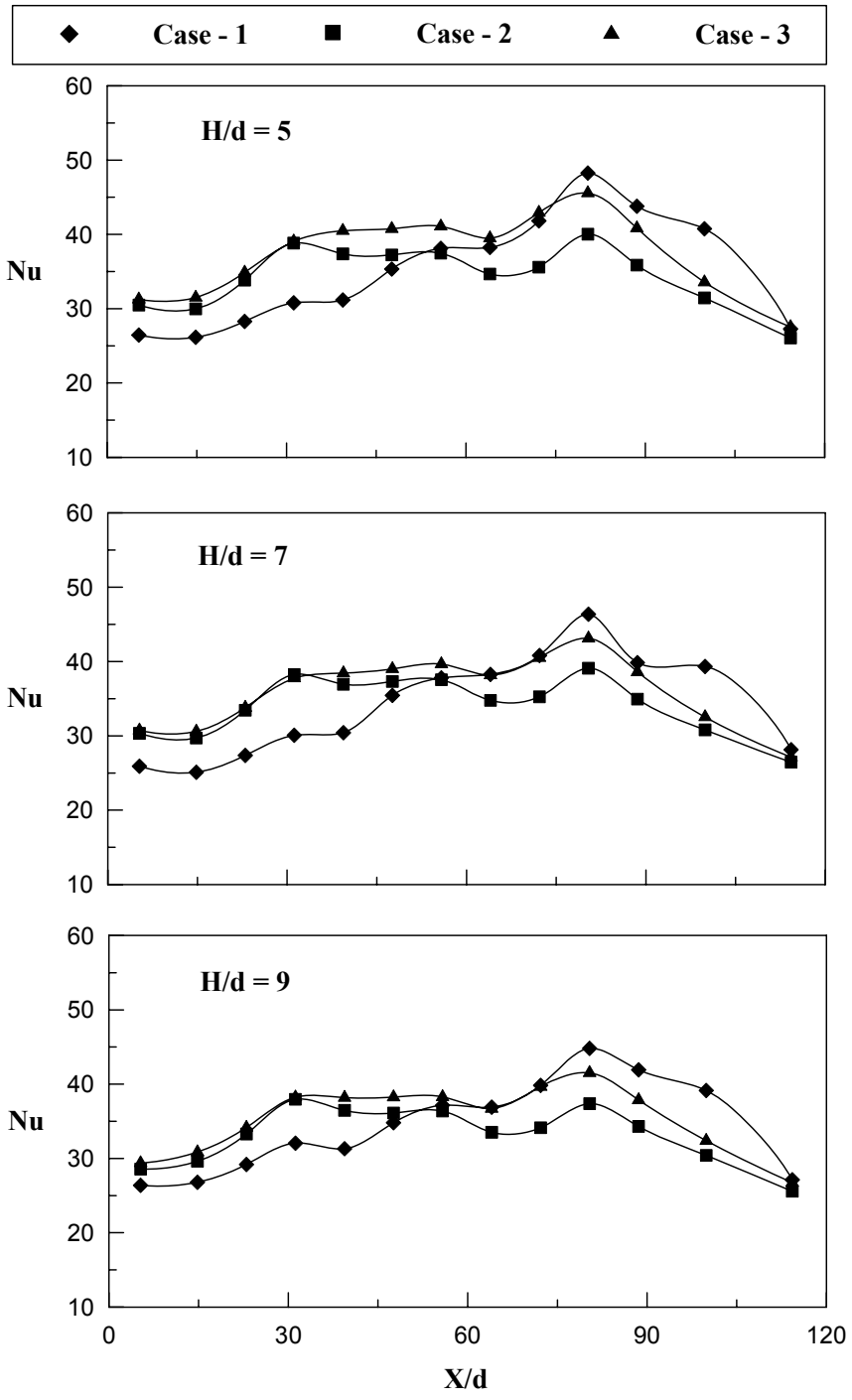

Figure 7.9 Effect of outflow orientation on local Nusselt number distribution for $S/d = 6$ and $\mathrm{Re}_j = 18800$.

7.4 Effect of jet-to-plate distance on local Nusselt number

Figure 7.10 – 7.12, gives a detail insight into the local Nusselt number distribution for different jet-to-plate distances $4 \le S/d \le 8$ and $\mathrm{Re}_j = 18800$ presenting the effect of feeding channel aspect ratio $5 \le H/d \le 9$ on the heat transfer from the target surface. Jet Reynolds number $\mathrm{Re}_j = 18800$ is selected for presenting the results as this gives the maximum heat transfer among all the jet Reynolds numbers studied. All the outflow orientations are discussed.

Figure 7.10 shows the effect of feeding channel aspect ratio on the local Nusselt number distribution over the entire length of the target surface for case – 1, where the flow exits at low X/d $(X/d = 0)$. The crossflow develops from large X/d to low X/d as the air exits at low X/d. The heat transferred from the target surface decreases with an increase in jet-to-plate distance from S/d = 4 to 8 for all the feeding channel aspect ratios. Over the entire length of the target surface, the jet-to-plate distance $S/d = 4$ gives the maximum heat transfer for all the feeding channel aspect ratios $5 \le H/d \le 9$ studied. Observing the effect of the feeding channel aspect ratio on the local Nusselt number distribution, $H/d = 5$ gives the maximum heat transfer among all the feeding channel aspect ratios studied. $H/d = 5$ gives a marginal increase in the local Nusselt number compared to $H/d = 7$, whereas $H/d = 5$ gives 6% increase in local Nusselt number is observed compared to $H/d = 9$. As discussed earlier in figure 5.1, a peak of local Nusselt number at $X/d = 80.4$ is observed this is due to the flow entering the impingement channel at large X/d, where the effect of crossflow is minimal. At $31.2 \le X/d \le 72.2$ crossflow dominates the impingement of jets and a linearly decreasing distribution of local Nusselt number is observed towards the exit.

Figure 7.11 shows the effect of the feeding channel aspect ratio on the local Nusselt number distribution for case – 2 comparing with all the jet-to-plate distances studied. For case – 2 the flow exits at low X/d $(X/d=0)$, causing crossflow development towards the exit. $S/d=4$ has the maximum heat transfer from the entire length of the target surface for the feeding channel aspect ratios $H/d=5$ and $H/d=7$. For $H/d=9$, $S/d=6$ gives the maximum amount of heat transfer from the entire target surface. For case – 2, $H/d=5$ gives 6.1% more heat transfer from the target surface compared to $H/d=7$ whereas $H/d=5$ gives a maximum of 9.2% increase in heat transfer is observed compared to $H/d=9$. It is also observed that the local Nusselt number distribution is sensitive to a change in jet-to-plate distance for $S/d=4$ and $S/d=6$ for all the feeding channel aspect ratios, whereas some variation in the magnitude of the local Nusselt number is observed for a change in the jet-to-plate distance from $S/d=6$ to $S/d=8$ for all the feeding channel aspect ratios studied.

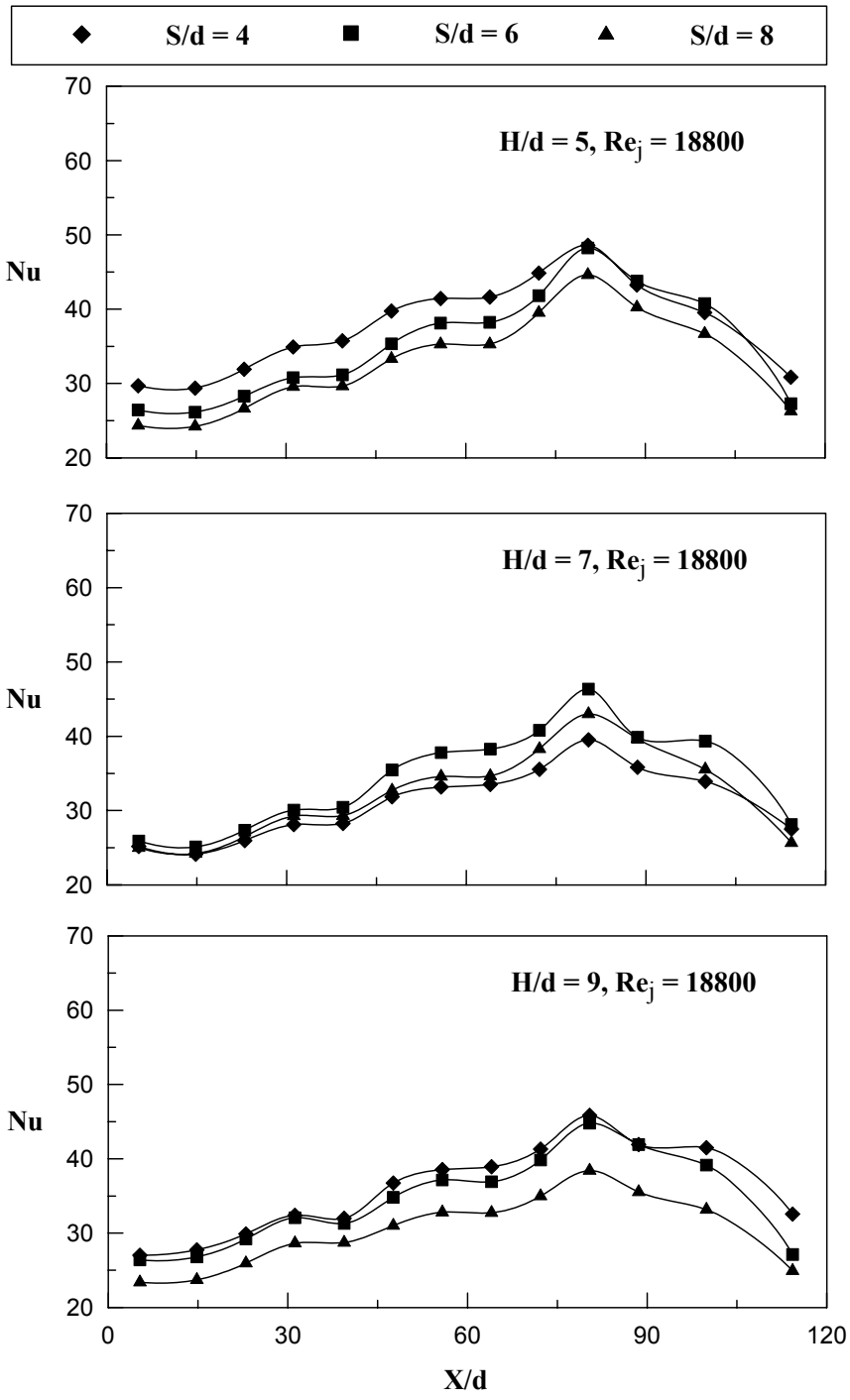

Figure 7.10 Effect of jet-to-plate distance on local Nusselt number distribution for $\mathrm{Re}_j = 18800$ and case – 1.

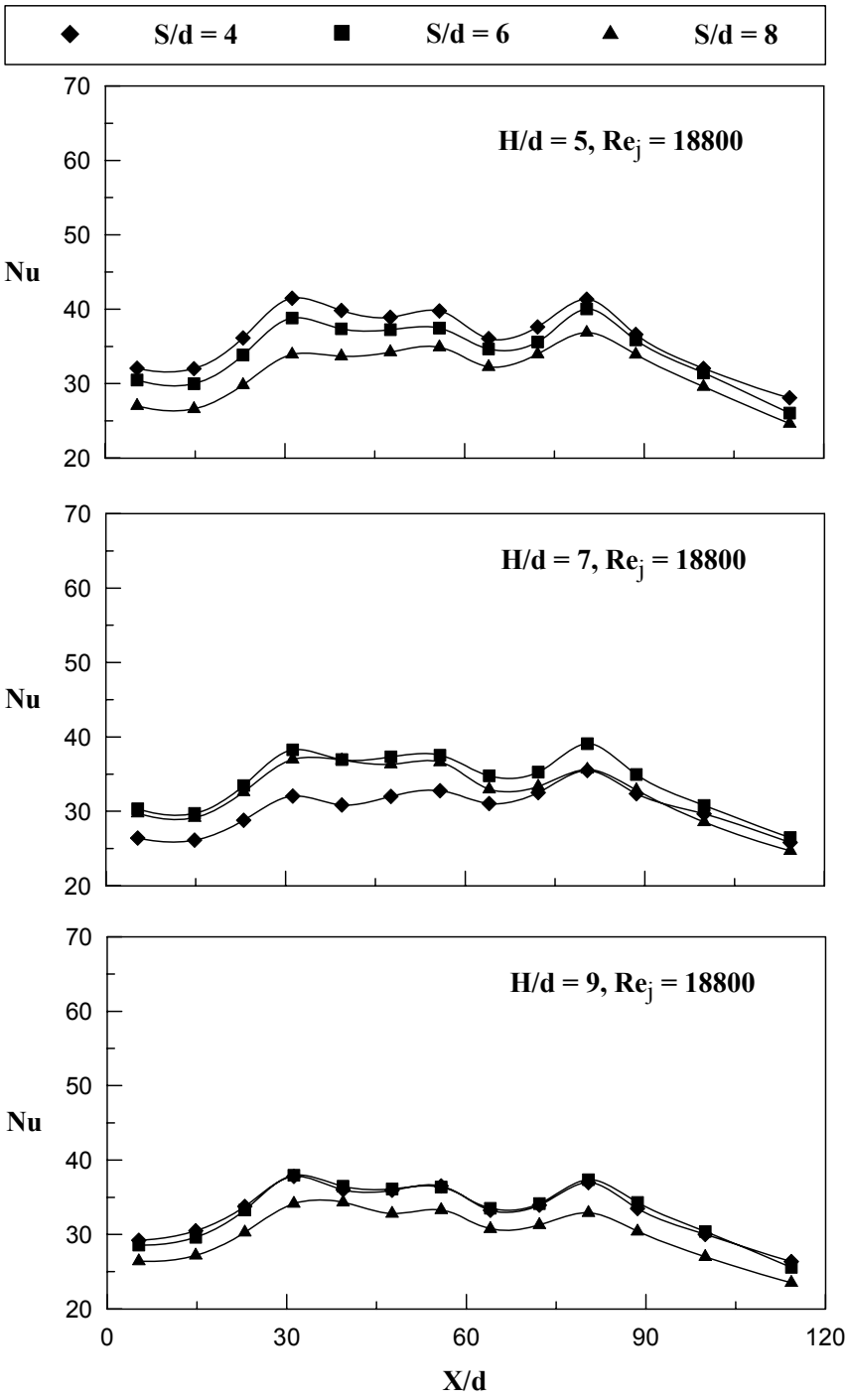

Figure 7.11 Effect of jet-to-plate distance on local Nusselt number distribution for $\mathrm{Re}_j = 18800$ and case – 2.

Figure 7.12 shows the effect of feeding channel aspect ratio on the local Nusselt number distribution for case – 3 and for three different jet-to-plate distances $4 \le S/d \le 8$. For case – 3 air exits at $X/d = 0$ and $X/d = 114.3$, where the crossflow has a predominant effect over the heat transfer characteristics. It is observed that at $0 \le X/d \le 30$ and $80.4 \le X/d \le 114.3$ the local Nusselt number decreases towards exit, this may be due to the crossflow at the exit which obstructs the jet impingement and thus reduces the strength of the impinging jets and thus the heat transferred from the target surface. The magnitude of local Nusselt number at $31.2 \le X/d \le 72.2$ is high compared to the other X/d locations this may be due to the strong impingement of jets where the effect of crossflow is minimum. For an increase in jet-to-plate distance a corresponding decrease in local Nusselt number is found for $H/d = 5$ and $H/d = 9$, whereas $S/d = 6$ has maximum values of local Nusselt number for $H/d = 7$. Considering the effect of feeding channel aspect ratio on heat transfer characteristics in detail, $H/d = 5$ gives the highest heat transfer similar to case – 1 and case – 2. $H/d = 5$ gives a maximum of 12% more heat transfer compared to $H/d = 7$, further $H/d = 5$ gives a maximum of 17% more heat transfer is observed compared to $H/d = 9$. Among all the jet-to-plate distances investigated $S/d = 4$ gives the maximum heat transfer over the entire target surface for $H/d = 5$ and $H/d = 9$, this is due to the strong impingement of the jets, with less jet travel distance, which thins the boundary layer resulting in high heat transfer. With respect to the effect of jet-to-plate distance, it is observed that the variation in local Nusselt number is less for a change in jet-to-plate distance compared to case – 1 and case – 2 for all the feeding channel aspect ratios.

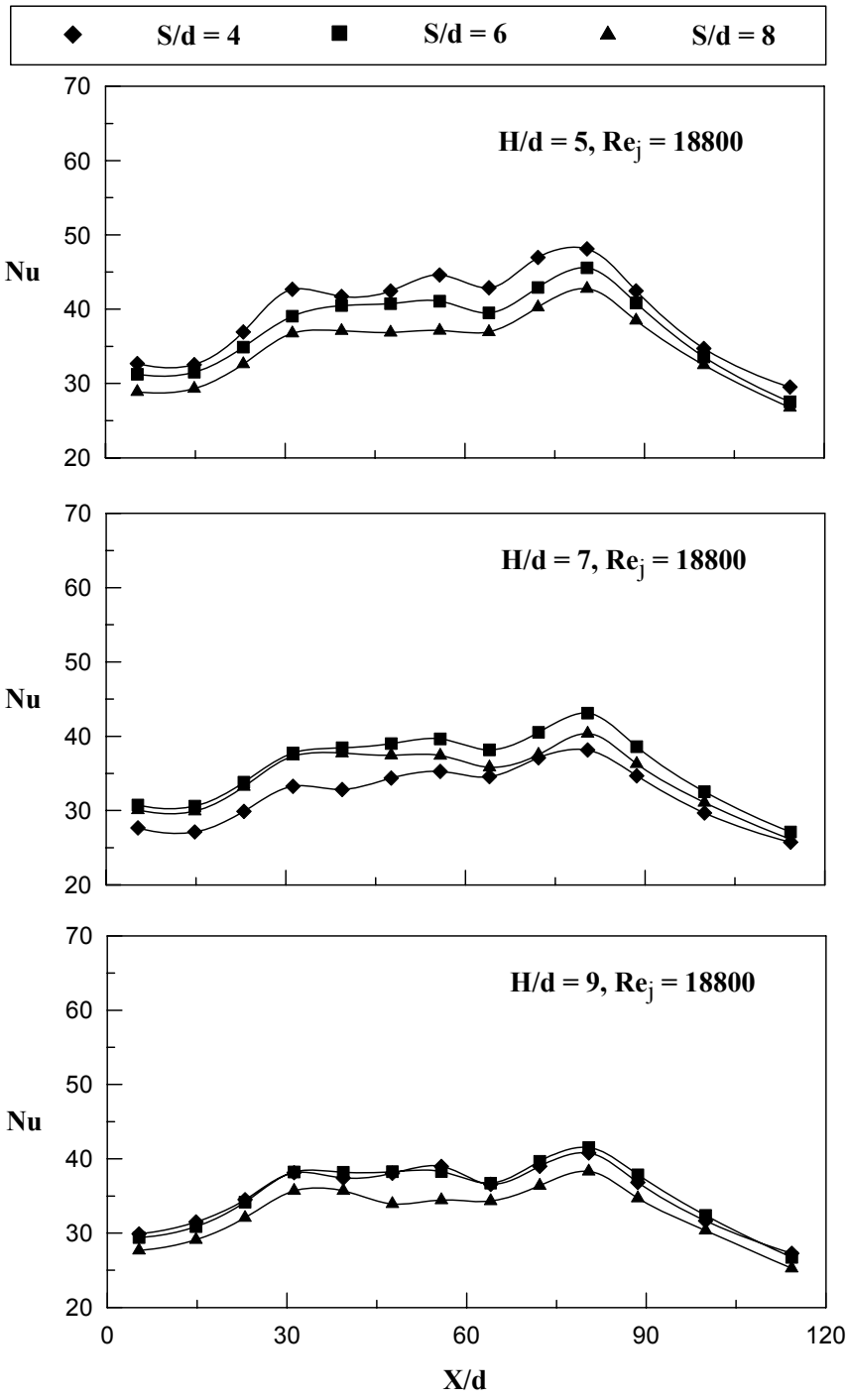

Figure 7.12 Effect of jet-to-plate distance on local Nusselt number distribution for $\mathrm{Re}_j = 18800$ and case – 3.

7.5 Average Nusselt Number

Figures 7.13 – 7.14 shows the average Nusselt number Nu_{avg} as a function of jet Reynolds number Re_j, plotted for all outflow orientations and the jet-to-plate distance $4 \le S/d \le 8$. The value of Nu_{avg} is an average of the detailed results on the target surface.

7.5.1 Effect of feeding channel aspect ratio

Figure 7.13 shows the effect of feeding channel aspect ratio $5 \le H/d \le 9$ on the averaged Nusselt number for different outflow orientation. It is observed that the averaged Nusselt number increases linearly with an increase in the jet Reynolds number, as stated in the previous discussion. Considering the effect of jet-to-plate distance, $S/d = 6$ gives the maximum values of averaged Nusselt number due to the stronger impingement of jets and $S/d = 8$ gives the least values of averaged Nusselt number as the crossflow dominates the impingement of jets. Averaged Nusselt number is less sensitive for a change in jet-to-plate distance for the feeding channel aspect ratio $H/d = 5$ as a large variation in the magnitude is observed, whereas it is less sensitive for the other two feeding channel aspect ratios as no much variation is observed with an increase in jet-to-plate distance comparatively. For $\mathrm{Re}_j = 14400$, less variation in the magnitude of Nu_{avg} is observed for a change in the jet-to-plate distance compared to the other two jet Reynolds numbers for feeding channel aspect ratios $H/d = 7$ and $H/d = 9$.

7.5.2 Effect of outflow orientation

Figure 7.14 shows the effect of the outflow orientation on averaged Nusselt number for different jet-to-plate distance. The averaged Nusselt number increases linearly with an increase in the jet Reynolds number. Among all the feeding channel aspect ratios studied $H/d = 5$ has the maximum values of the Nu_{avg}, for all the outflow orientations and for all the jet-to-plate distances studied, the reason being the strong impingement of jets with minimum effect of crossflow. $H/d = 9$ gives the least values of Nu_{avg} among all the feeding channel aspect ratios studied this may be due to less impingement effect of the jets at larger feeding channel aspect ratios. Case – 3 has the highest magnitude of the Nu_{avg} among all the outflow orientations studied, whereas the Nu_{avg} values for case – 1 and case – 2 are close with a less variation in magnitude for all the jet Reynolds numbers. It is also observed that as the jet-to-plate distance is increased there is a corresponding decrease in the values of Nu_{avg} for all the feeding channel aspect ratios. In detail, the averaged Nusselt number distribution for $S/d = 6$ and $S/d = 8$ is almost similar for case – 2 and case –3 for all the feeding channel aspect ratios. The maximum difference in magnitude of averaged Nusselt number for case – 3 and the other two cases is 7%. For $\mathrm{Re}_j = 9300$, very less difference in magnitude of Nu_{avg} is observed with respect to all the outflow orientations whereas for the other two jet Reynolds numbers a considerable difference in magnitude of the Nu_{avg} is noticed. This may be due to the increase in the strength of the jets with an increase in the jet Reynolds number. Maximum variation in Nu_{avg} is observed for $\mathrm{Re}_j = 18800$.

.

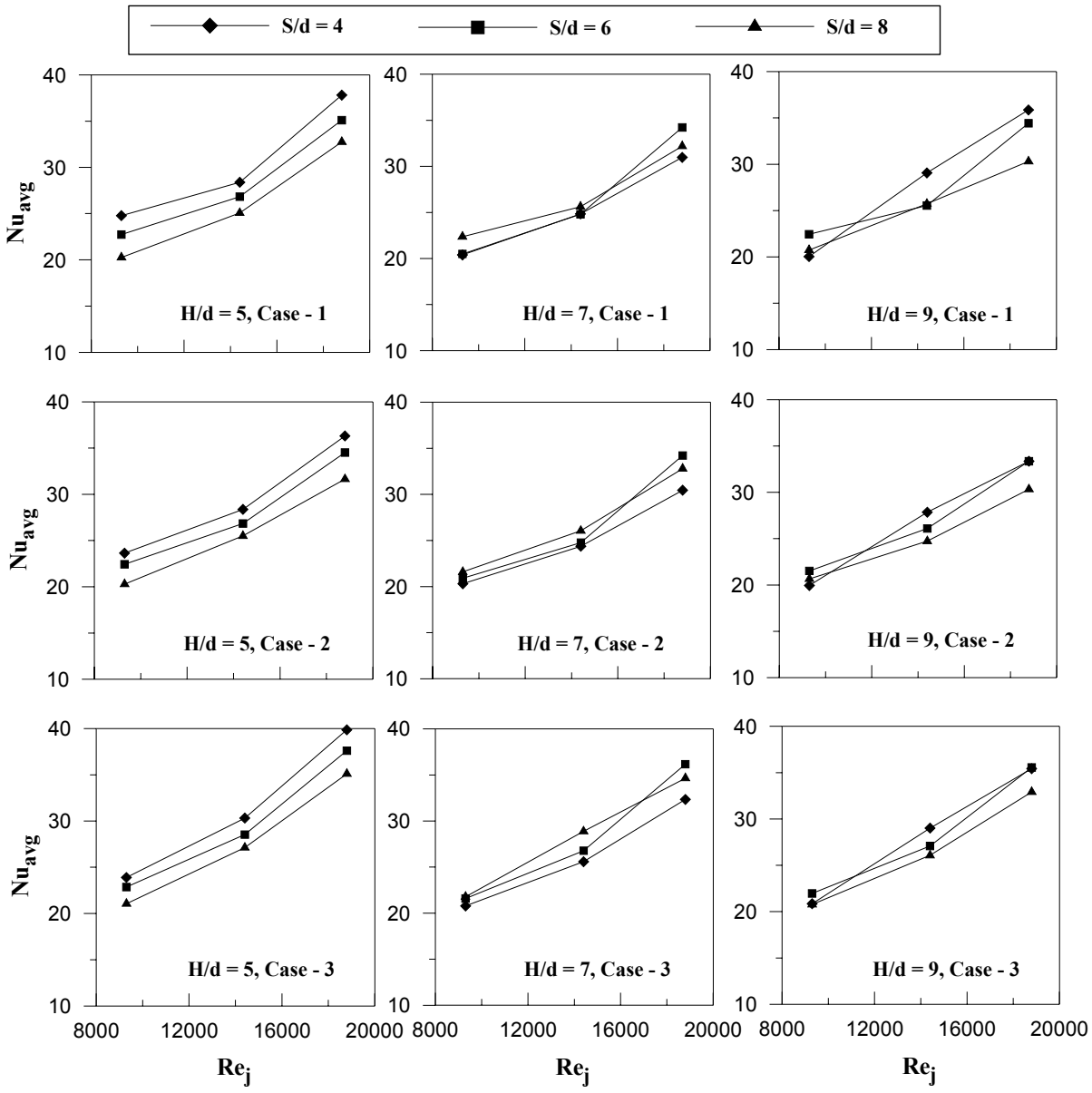

Figure 7.13 Effect of feeding channel aspect ratio $(5 \le H/d \le 9)$ and jet-to-plate distances on averaged Nusselt number for different outflow orientation.

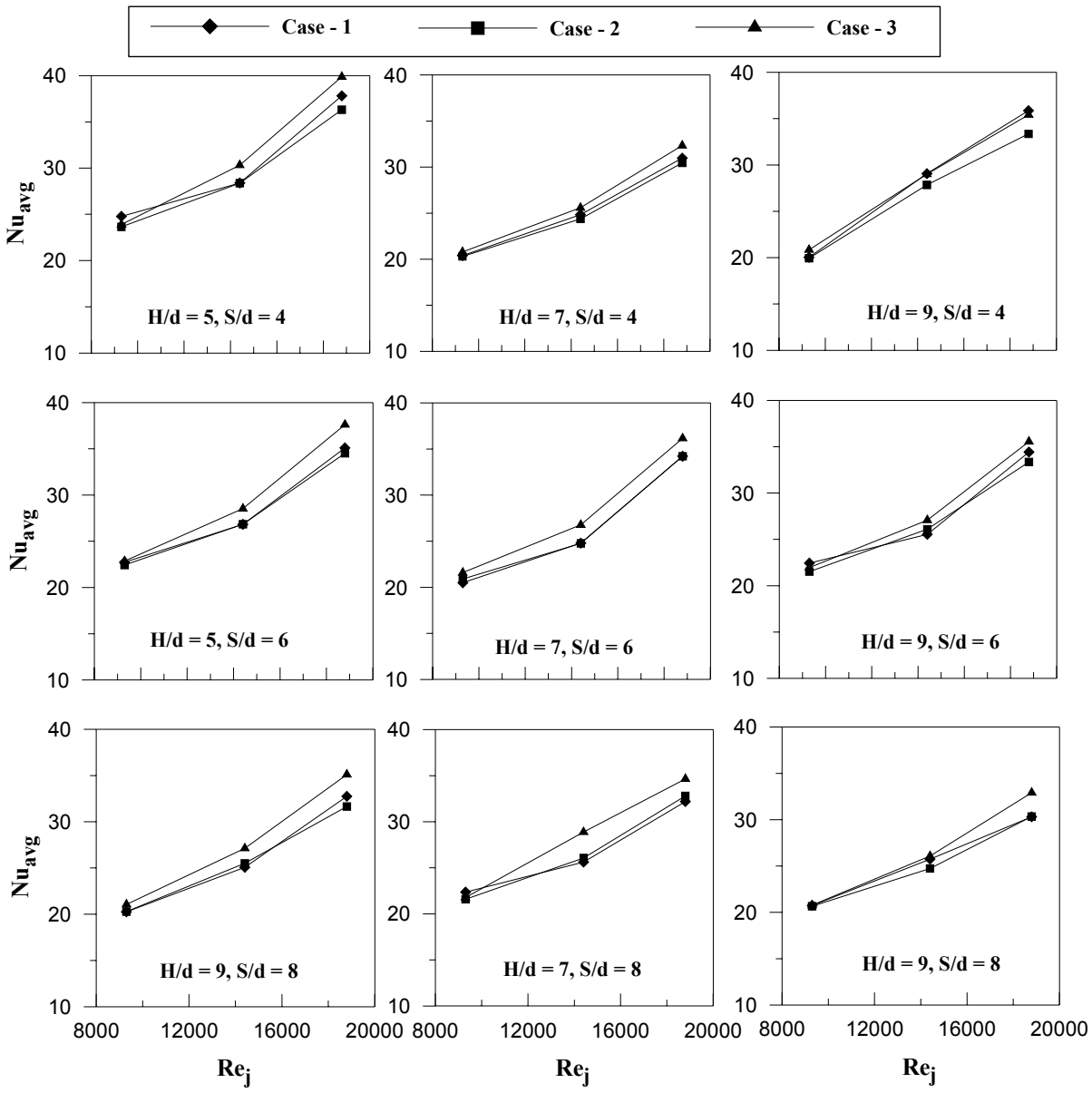

Figure 7.14 Effect of outflow orientation and feeding channel aspect ratio on averaged Nusselt number for different jet-to-plate distances $(4 \le S/d \le 8)$.

7.5.3 Correlations of averaged Nusselt number

The results for three different outflow orientations are correlated for the jet Reynolds number Re_j and the normalized jet-to-plate distance S/d dependence as

$$Nu_{avg} = A\,(\mathrm{Re}_j)^B (S/d)^C (H/d)^D \tag{7.1}$$

The present results are correlated for all outflow orientations individually for jet Reynolds number Re_j dependence. Previous studies in the field of jet impingement have involved in developing correlations for the averaged Nusselt number as a function of the jet Reynolds number by considering many parameters. Correlations by Huang et al [21],Kercher and Tabakoff [30] and Florscheutz et al [14] are compared to the averaged Nusselt number in the present investigation. Huang et al [21] studied the outflow orientations similar to ones used in the present study. They presented results for the outflow orientation 1 and 2 correlating for Reynolds number dependence as $Nu = 0.035\,\mathrm{Re}^{0.76}$, whereas for outflow orientation 3 which has the highest magnitude of heat transferred from the target surface is correlated as $Nu = 0.082\,\mathrm{Re}^{0.727}$. Kercher and Tabakoff [30] also studied the effect of crossflow and it is similar to the case – 1 in the present study. They varied the jet hole diameter, the hole spacing x, y and the jet to target plate distance. Based on all of these geometrical parameters, they proposed a correlation of the form $Nu = \phi_1\,\phi_2\,\mathrm{Re}^m\,(z/d)^{0.91}\,\mathrm{Pr}^{1/3}$, where ϕ_1 and ϕ_2 are constants based on X/d and Y/d, respectively. Florschuetz et al [14] presented the correlations with different coefficients of inline and staggered rows. The correlation for jet

impingement with minimum crossflow is given as $Nu = 0.363(X/d)^{-0.554}(Y/d)^{-0.422}(Z/d)^{0.068}\,\mathrm{Re}_j^{-0.554}\,\mathrm{Pr}^{1/3}$.

The detailed values of the local Nusselt number are averaged over the entire length of the target surface to obtain a single averaged Nusselt number. The averaged Nusselt numbers for each outflow orientation are plotted against the jet Reynolds number. The present results are correlated for the jet Reynolds number dependence as $Nu_{avg} = 0.00547\,(\mathrm{Re}_j)^{0.653}(S/d)^{0.415}(H/d)^{2.090}$ for case 1 and 2. The correlations for Huang et al [21] for case 1 and 2 are in good comparison with the present study. Kercher and Tabakoff [30] presented the results for the outflow orientation – 1 and the results of the present study are in good comparison with the existing correlation. The case with maximum heat transfer from the target surface, outflow orientation – 3, is correlated for the jet Reynolds number dependence as $Nu_{avg} = 0.000437(\mathrm{Re}_j)^{0.745}(S/d)^{0.354}(H/d)^{4.575}$. The correlation used from Florschuetz et al [14] is for the case with minimum crossflow. Huang et al [21] also presented a separate correlation for the case with high heat transfer; this case in their study had the less crossflow effect. The results from the present study for case – 3 are lower than the existing correlations, which includes the crossflow effect. The correlation for case – 3 in the present study is in good agreement with the correlation presented by Florschuetz et al [14] and Huang et al [21]. Thus it is evident from the above discussion that the crossflow effect is more dominant on outflow orientation 1 and 2 compared to outflow orientation – 3.

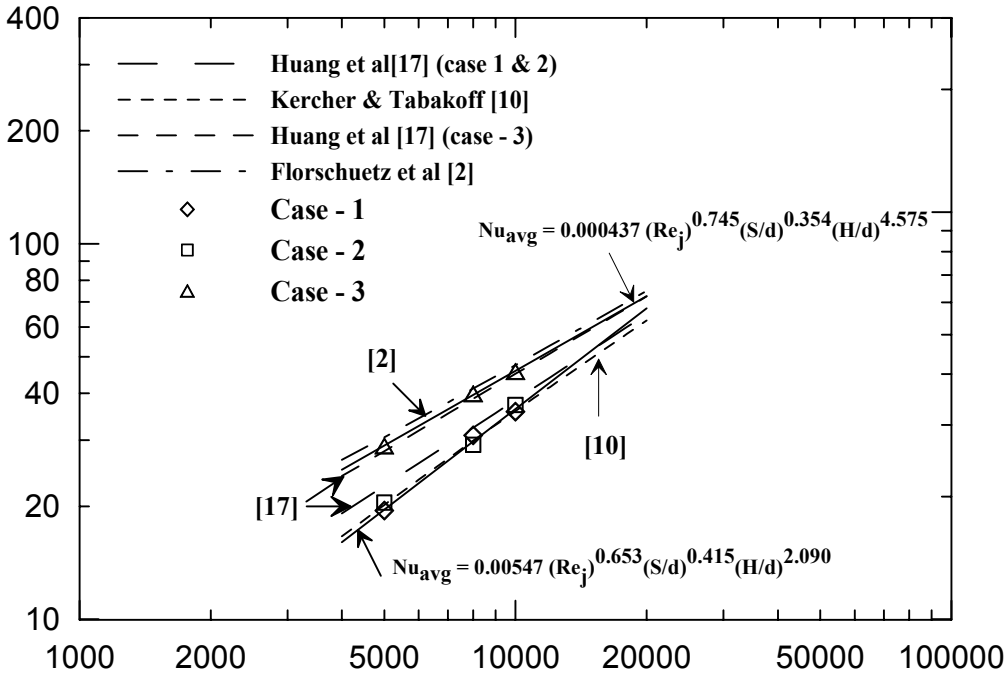

Figure 7.15 Averaged Nusselt number comparisons with the existing correlations

CHAPTER 8

ORIFICE PLATE - 4

Jet impingement heat transfer is dependent on several flow and geometrical parameters. The jet impingement Nusselt number is presented as a functional form of,

$$Nu_i = \left(\frac{h_i\, d}{k_{air}} \right) = f\left[\mathrm{Re}_j,\ \left(X/d, S/d, H/d \right), outflow\ orientation \right] \tag{8.1}$$

Where, Re_j is the flow parameter, distance along the target surface X/d, feeding channel aspect ratio H/d, and jet-to-plate distance S/d are the geometric parameters. The flow exit direction and the jet-to-plate distance are also important parameters having a significant effect on impingement heat transfer. The jet inlet condition is the direction in which the flow enters the inlet channel.

Figure 2.3 shows three outflow orientations where air comes into the feeding channel and leaves through jets made in the orifice jet plate to impinge on the heated target surface located in the impingement channel. For all the three cases air enters the feeding channel at $X/d = 114.3$. For case 1, air exits the impingement channel at low X/d $(X/d = 0)$ and therefore the crossflow develops towards the exit. For case 2, the flow exits the impingement channel at $X/d = 57.15$ and as the flow moves forward from low X/d crossflow develops at low X/d and increases towards large X/d $(X/d = 114.3)$.

For case 3, the flow exits the impingement channel at both the directions i.e., at $X/d = 0$ *and* 114.3 and the crossflow develops towards both the ends of the test section.

Tests were carried out for three different outflow orientations with Reynolds number ranging between $\left(5000 \le \mathrm{Re}_j \le 10000\right)$ by varying the jet-to-plate distance ratio (S/d) and also the feeding channel aspect ratio (H/d). Three different values of jet-to-plate distances $4 \le S/d \le 8$ and the feeding channel aspect ratio $5 \le H/d \le 9$ were considered while carrying out the experiments.

Flow orientation affects the flow inside the impingement channel and leads into different heat transfer characteristics. As air impinges on the target surface, crossflow starts developing and grows continuously towards the exit resulting into thicker boundary layer, which suppresses the jet impingement effect. In addition, crossflow causes distortion to the jet impingement in which the jet is no longer impinging normally on the target surface.

All the results presented in this paper are for $0 \le X/d \le 114.3$ over the entire span of the target plates. Where X is defined from the opposite end of the feeding channel of the test section as shown in figure 2.2. All the results presented below are being extracted using the orifice plate with tangential jets of diameter 0.5cm.

The local Nusselt number distribution for all the three outflow orientations by varying the jet-to-plate distance is presented in detail, as a function of non-dimensional location X/d on the target surface for jet Reynolds number Re_j, jet-to-plate distance S/d, and the feeding channel aspect ratio H/d in the forthcoming discussion.

8.1 Effect of feeding channel aspect ratio on local Nusselt number

Figure 8.1 – 8.3, gives a detail insight into the local Nusselt number distribution presenting the effect of feeding channel aspect ratio $5 \le H/d \le 9$ on the heat transfer from the target surface. All the results are presented for jet-to-plate distance $S/d = 6$ as this jet-to-plate distance gives maximum heat transfer. All the outflow orientations are discussed.

Figure 8.1 shows effect of feeding channel aspect ratio on the local Nusselt number distribution over the entire length of the target surface for case – 1, where the flow exits at low X/d $(X/d = 0)$. The crossflow develops from large X/d to low X/d as the air exits at low X/d. The heat transferred from the target surface decreases with an decrease in feeding channel aspect ratio from H/d = 9 to 5 for all the feeding channel aspect ratios. Over the entire length of the target surface, the feeding channel aspect ratio $H/d = 7$ gives the maximum heat transfer for all the jet Reynolds numbers $9300 \le \mathrm{Re}_j \le 18800$ studied. This is primarily due to the increase in the strength of the jets with an increase in the feeding channel ratios. Observing the effect of the feeding channel aspect ratio on the local Nusselt number distribution for all the jet Reynolds numbers studied, $H/d = 7$ gives the maximum heat transfer among all the feeding channel aspect ratios studied. $H/d = 7$ gives a margnial increase in the local Nusselt number compared to $H/d = 5$, whereas $H/d = 7$ gives a maximum of 4% increase in local Nusselt number is observed compared to $H/d = 9$ for all the jet Reynolds numbers studied. With an increase in the feeding channel aspect ratio the difference in the magnitude of the local Nusselt number also increases for an increase in the jet Reynolds number. Among all the Reynolds numbers studied, $\mathrm{Re}_j = 18800$ gives the maximum heat transfer. As discussed earlier in figure 8.1, a peak of local Nusselt number at

$X/d = 80.4$ is observed this is due to the flow entering the impingement channel at large X/d, where the effect of crossflow is minimal. At $31.2 \le X/d \le 72.2$ crossflow dominates the impingement of jets and a linearly decreasing distribution of local Nusselt number is observed towards the exit.

Figure 8.2 shows the effect of the feeding channel aspect ratio on the local Nusselt number distribution for case – 2 and for jet-to-plate distance $S/d = 6$. For case – 2 the flow exits at low X/d $(X/d = 0)$, causing crossflow development towards the exit. $H/d = 7$ gives the maximum heat transfer over the entire length of the target surface for all the jet Reynolds numbers studied. For all the jet Reynolds numbers studied, $H/d = 7$ gives a maximum of 5% more heat transfer from the target surface compared to $H/d = 5$ whereas $H/d = 7$ gives a marginal increase in heat transfer compared to $H/d = 9$. It is also observed that the magnitude of the local Nusselt number increases with an increase in the jet Reynolds number for all the feeding channel aspect ratios studied. The variation in the local Nusselt number is more sensitive with respect to a change in feeding channel aspect ratio at high jet Reynolds number whereas it is less sensitive at low jet Reynolds numbers. At $80.4 \le X/d \le 114.3$ the magnitude of local Nusselt number decreases from $X/d = 80.4$ to $X/d = 114.3$, this is due to the obstruction caused by the crossflow to the impinging jets.

Figure 8.3 shows the effect of feeding channel aspect ratio on the local Nusselt number distribution for case – 3 and for jet-to-plate distance $S/d = 6$. For case – 3 air exits at $X/d = 0$ and $X/d = 114.3$, where the crossflow has a predominant effect over the heat transfer characteristics. It is observed that at $0 \le X/d \le 30$ and $80.4 \le X/d \le 114.3$ the local Nusselt number decreases towards exit, this may be due to the crossflow at the exit and

thus reduces the strength of the impinging jets and the heat transferred from the target surface. The magnitude of local Nusselt number at $31.2 \le X/d \le 72.2$ is high compared to the other X/d locations this may be due to the strong impingement of jets. For an increase in feeding channel aspect ratio a corresponding increase in local Nusselt number is observed. $H/d = 7$ gives the maximum values of feeding channel aspect ratio for all the jet Reynolds numbers studied. Considering the effect of feeding channel aspect ratio for all jet Reynolds numbers on heat transfer characteristics in detail, $H/d = 7$ gives the highest heat transfer similar to case $-$ 1 and case $-$ 2. $H/d = 7$ gives a marginal increase in heat transfer compared to $H/d = 9$, further $H/d = 7$ gives a maximum of 3% more heat transfer is observed compared to $H/d = 5$. Similar to case $-$ 1 and case $-$ 2, with respect to the effect of feeding channel aspect ratio on local Nusselt number characteristics it is observed that the local Nusselt number is sensitive to a change in feeding channel aspect ratio at high jet Reynolds numbers.

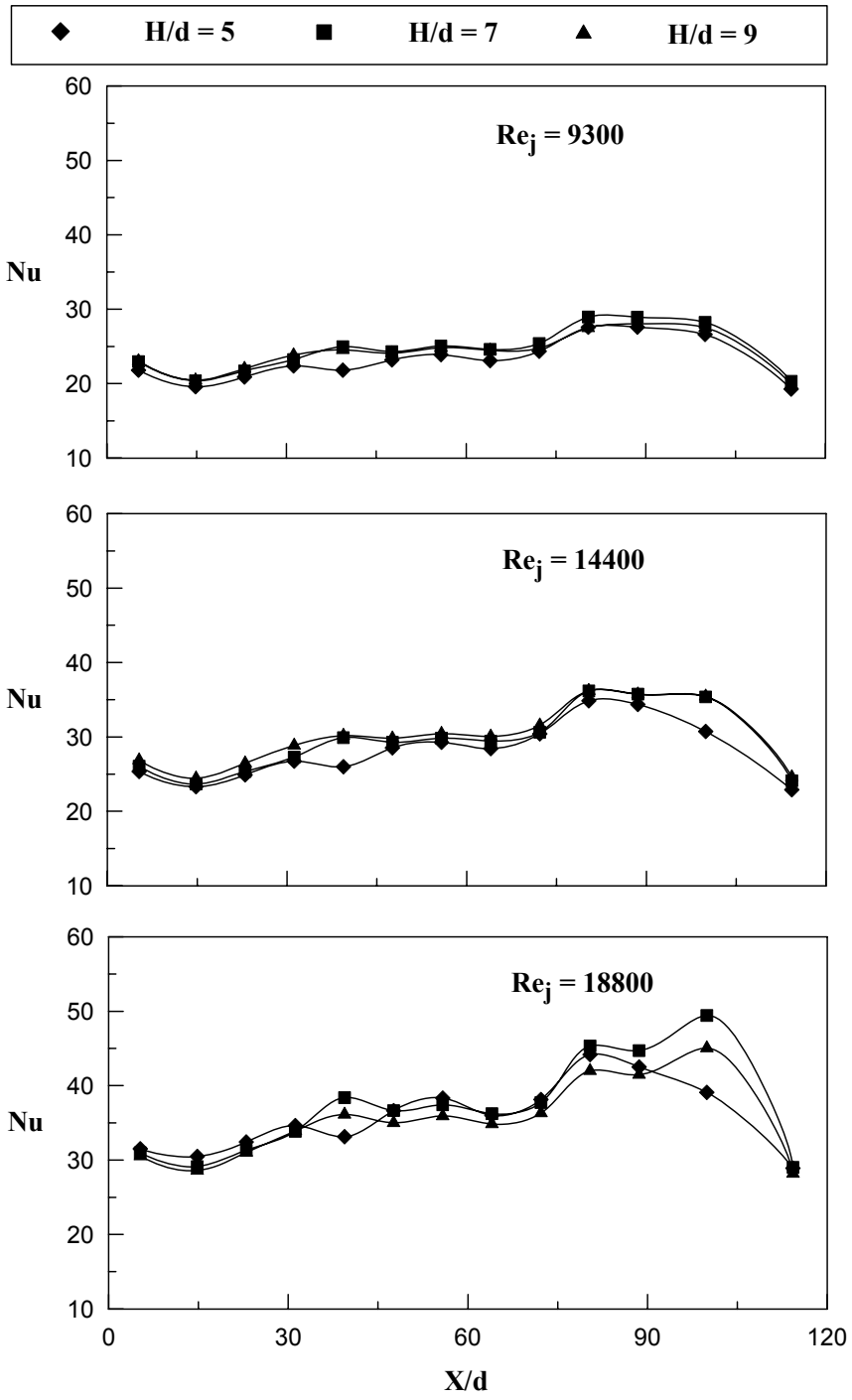

Figure 8.1 Effect of feeding channel aspect ratio $5 \le H/d \le 9$ on local Nusselt number distribution for case – 1 and jet-to-plate distance $S/d = 4$.

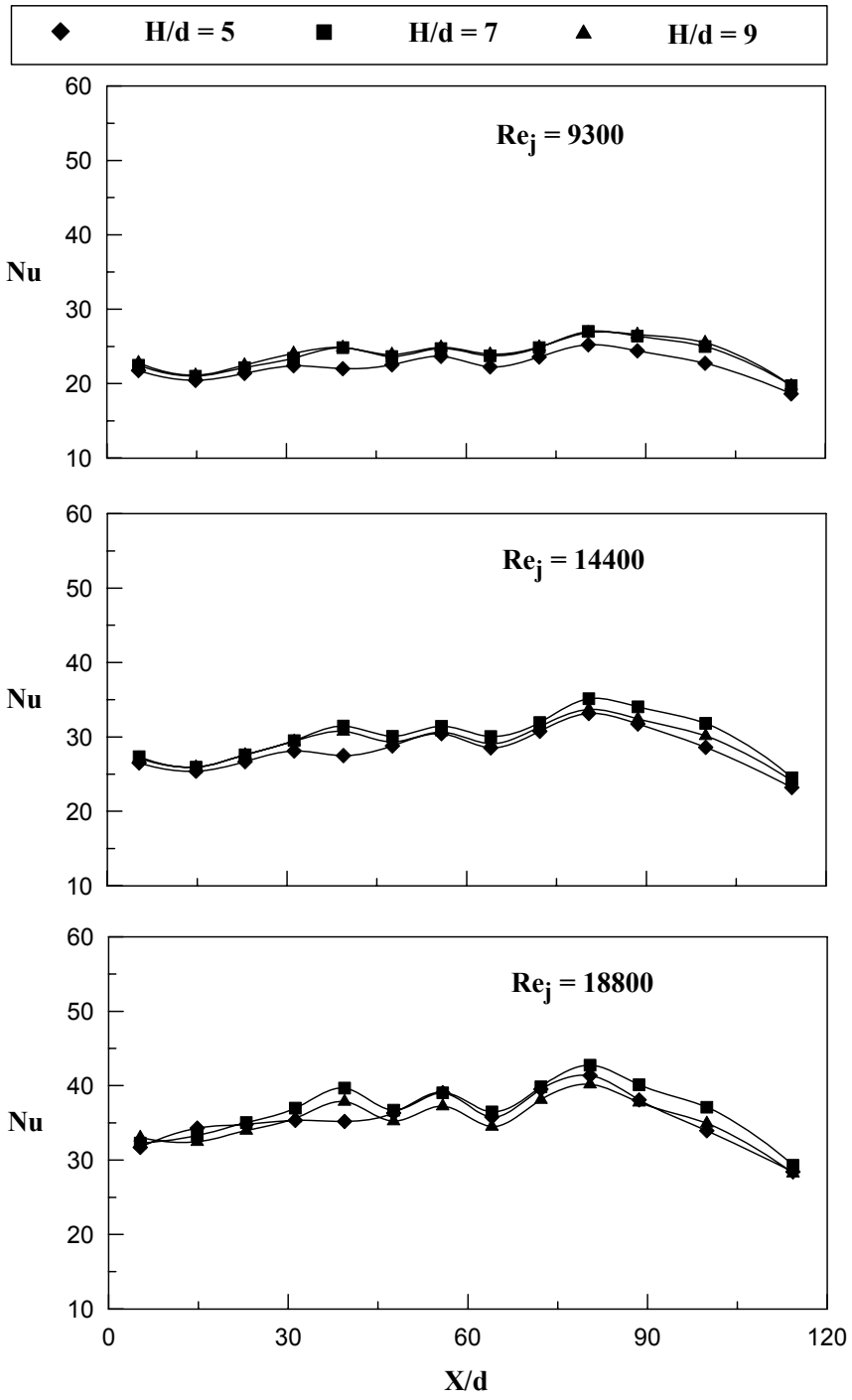

Figure 8.2 Effect of feeding channel aspect ratio $5 \le H/d \le 9$ on local Nusselt number distribution for case – 2 and jet-to-plate distance $S/d = 4$.

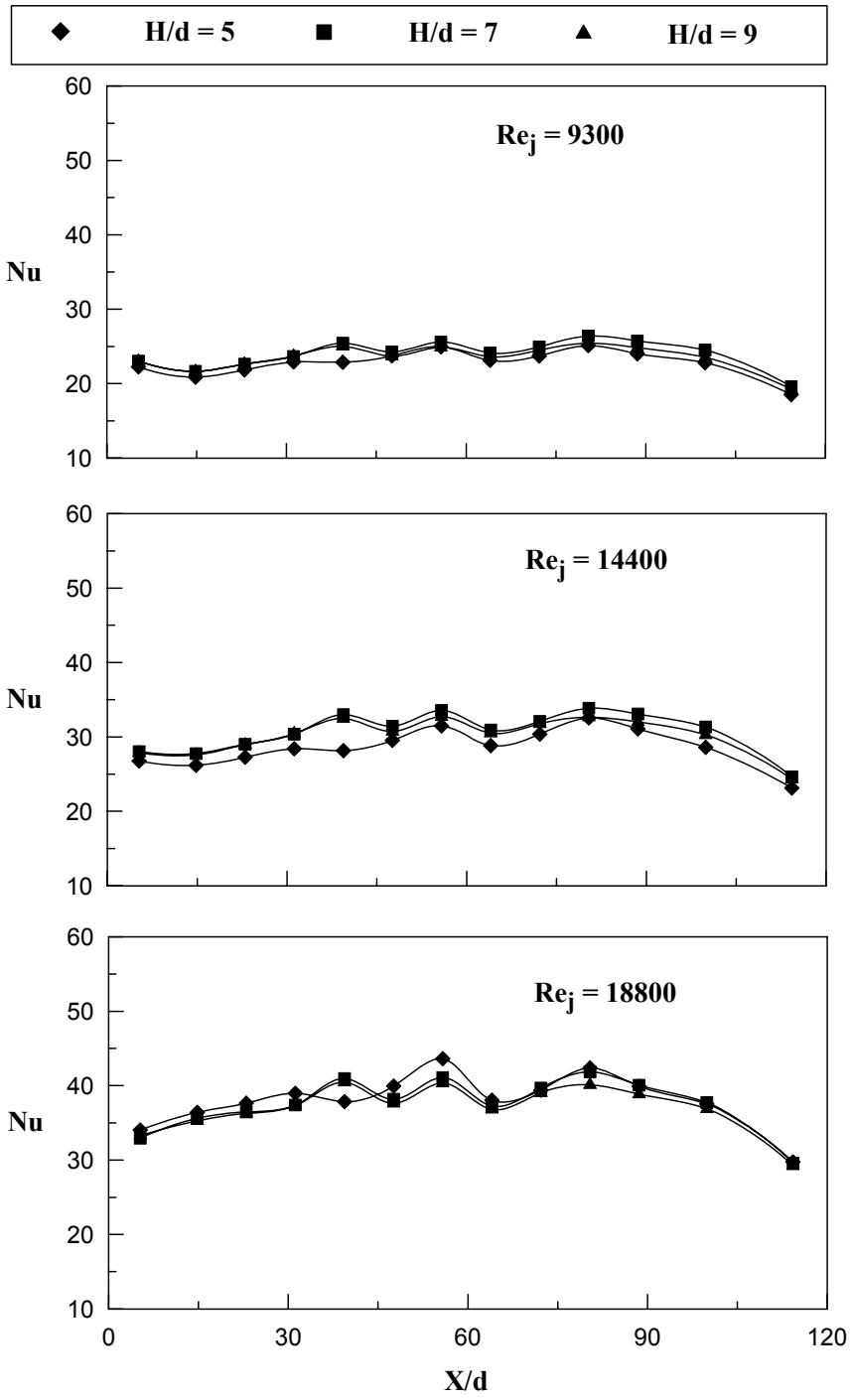

Figure 8.3 Effect of feeding channel aspect ratio $5 \le H/d \le 9$ on local Nusselt number distribution for case – 3 and jet-to-plate distance $S/d = 4$.

8.2 Effect of jet Reynolds number on local Nusselt number

Figure 8.4 - 8.6 shows the local Nusselt number distribution for different jet Reynolds numbers $9300 \le \mathrm{Re}_j \le 18800$, for jet-to-plate distance $S/d = 6$, expressing the effect of the feeding channel aspect ratio on the heat transfer from the heated target surface. Among all the jet-to-plate distances studied $S/d = 6$ is selected, as it is the best case in which maximum heat is transferred from the target surface.

Figure 8.4 shows the local Nusselt number distribution plotted for case – 1, which gives a detailed insight into the effect of the feeding channel aspect ratio. Three different values of the feeding channel aspect ratios are considered in this part of the study $5 \le H/d \le 9$. The results are presented for three jet Reynolds numbers $9300 \le \mathrm{Re}_j \le 18800$. It is observed that for an increase in the jet Reynolds number there is a corresponding increase in the magnitude of local Nusselt number. For case – 1, the flow exits the impingement channel at low X/d $(X/d = 0)$. A peak of local Nusselt number is observed at $X/d = 80.4$, this may be due to the strong impingement of jets as the air enters the impingement channel at large X/d where the effect of crossflow is minimal resulting into thinner boundary layer. Among all the feeding channel widths examined, $H/d = 7$ gives the maximum heat transfer for all the jet-to-plate distances studied. $H/d = 7$ gives a maximum of 11.8% increase in the local Nusselt number from the target surface compared to $H/d = 5$, whereas it gives a maximum of 9.7% more heat transfer compared to $H/d = 9$. At $31.2 \le X/d \le 72.2$ uniformly decreasing heat transfer is observed along the target surface for all the feeding channel aspect ratios studied, this is due to the crossflow of the air. A considerable increase in the Nusselt number is observed at large X/d $(X/d = 114.3)$ for

$\mathrm{Re}_j = 10000$, whereas for $\mathrm{Re}_j = 9300$ and $\mathrm{Re}_j = 14400$ a uniform behavior of local Nusselt number is observed this is due to the strong impingement at high velocities which leads to high heat transfer.

Figure 8.5 shows the local Nusselt number distribution for case – 2 plotted for different jet Reynolds numbers $9300 \le \mathrm{Re}_j \le 18800$ for a fixed jet-to-plate distance $S/d = 6$ and by varying the feeding channel aspect ratio $5 \le H/d \le 9$. For case – 2 air exits the impingement channel at $X/d = 114.3$ opposite to the entry flow, this leads to the development of more crossflow towards large X/d $(X/d = 114.3)$. Similar to the case – 1 an increase in jet Reynolds number leads to a corresponding increase in local Nusselt number for all the H/d values studied. At large X/d $(X/d = 114.3)$, the flow exits at this location causing greater amount of crossflow obstructing the impingement of jets at this location, thus less magnitude of local Nusselt number is observed. A uniform distribution of local Nusselt number is observed along the entire length of the heated target surface except a peak of local Nusselt number at $X/d = 80.4$ which may due to the strong impingement of jets at that location. Although similar behavior of local Nusselt number is observed for $H/d = 5$ and $H/d = 7$, but $H/d = 7$ gives a marginal increase in local Nusselt number over the entire target surface compared to $H/d = 5$, whereas a maximum of 7.36% more heat transfer is observed over the entire target surface is observed compared to $H/d = 9$. The variation in the magnitude of local Nusselt number is less for a change in jet Reynolds number for all the feeding channel aspect ratios studied, this is reflected from the similar behavior of local Nusselt number. At $80.4 \le X/d \le 114.3$, a decrease in local Nusselt number is observed from $X/d = 80.4$ towards the exit at $X/d = 114.3$, this may be due to the development of

crossflow towards the exit, which obstructs the impingement of jets and thickens the boundary layer. This behavior of local Nusselt number is observed for all the H/d values studied.

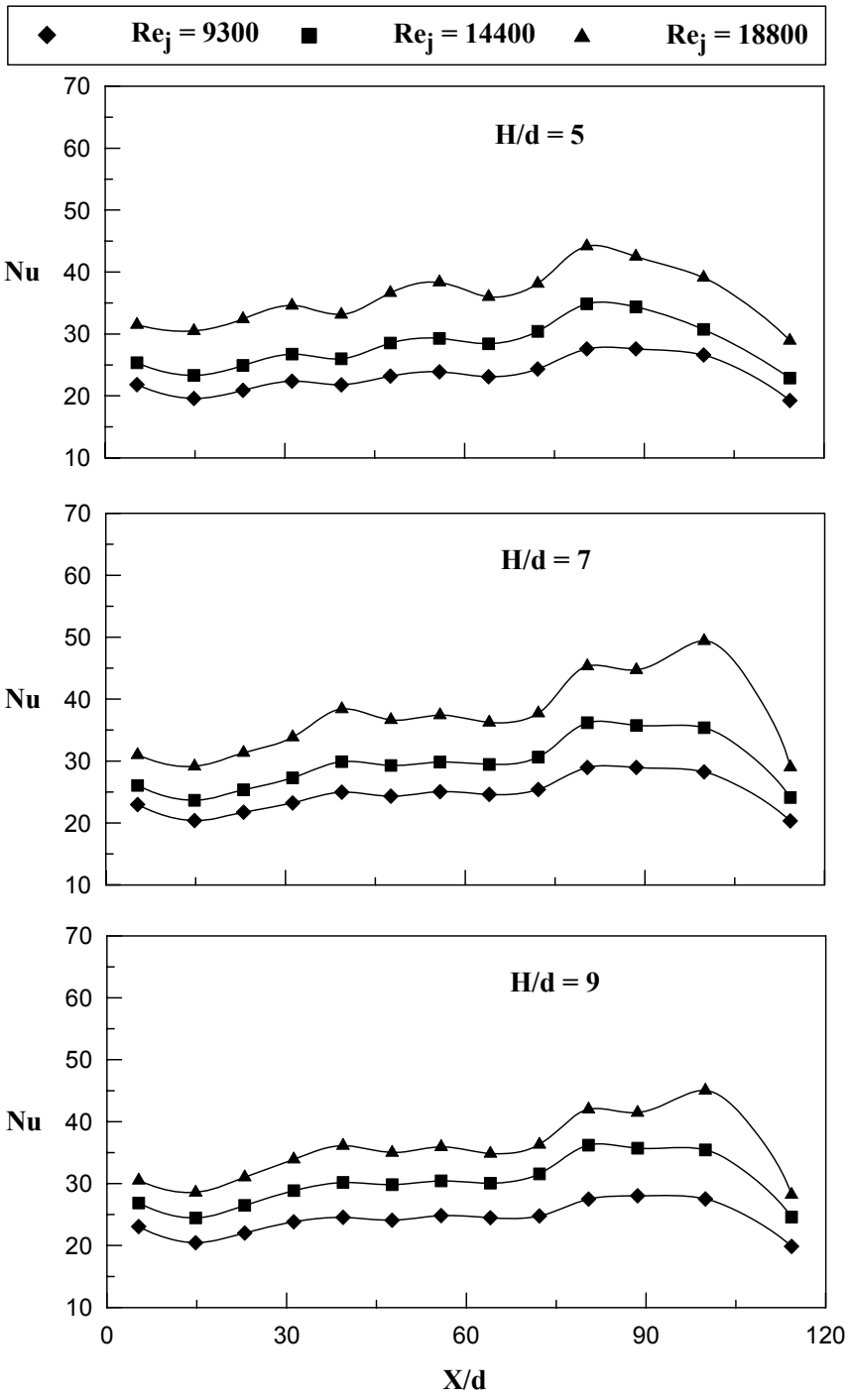

Figure 8.4 Effect of jet Reynolds number and feeding channel aspect ratio $5 \le H/d \le 9$ on local Nusselt number distribution for $S/d = 4$ and case – 1.

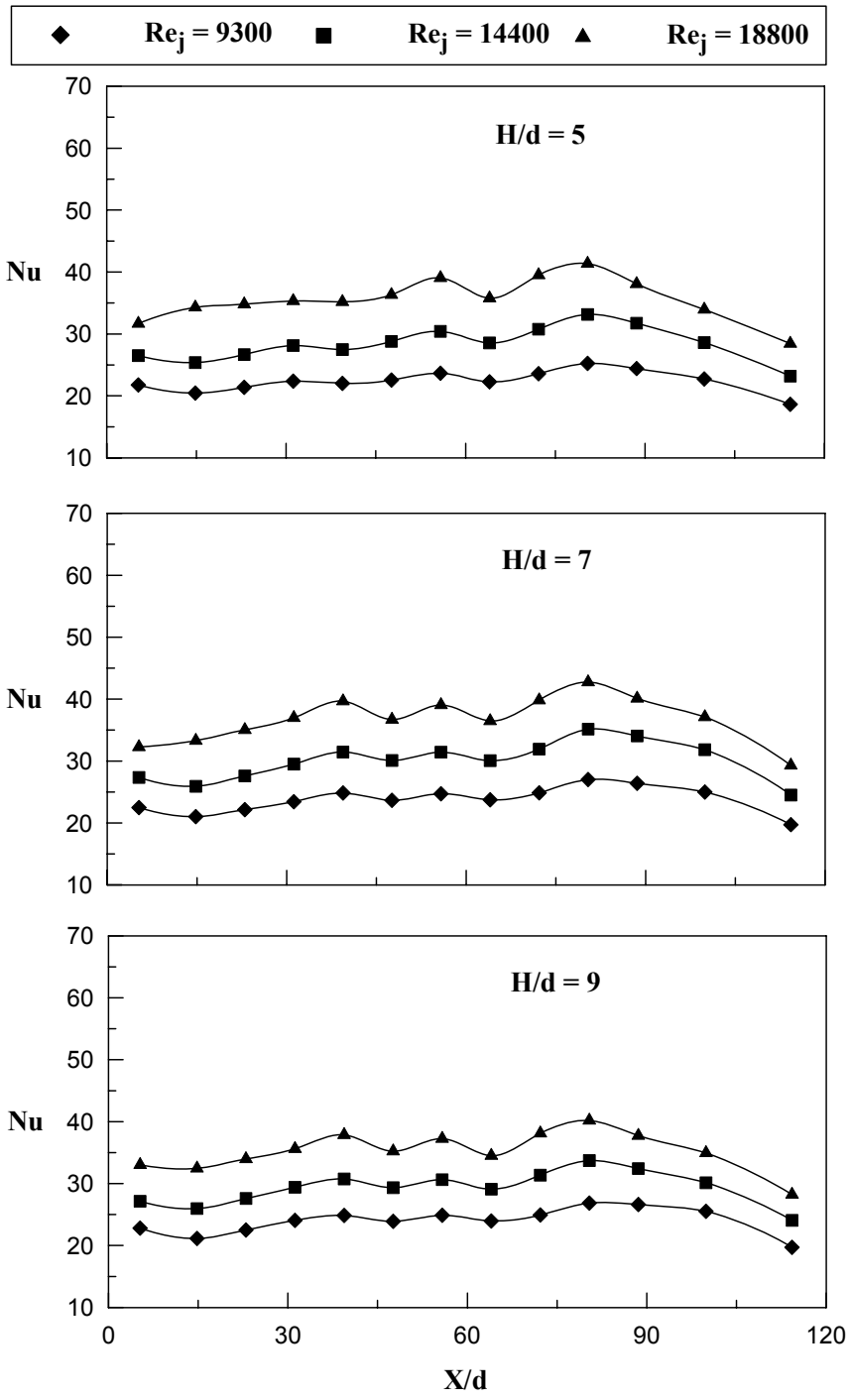

Figure 8.5 Effect of jet Reynolds number and feeding channel aspect ratio $5 \le H/d \le 9$ on local Nusselt number distribution for $S/d = 4$ and case – 2.

Figure 8.3 presents the local Nusselt number distribution for case – 3 where the air exits from both the directions at low X/d $(X/d=0)$ and large X/d $(X/d=114.3)$. It is observed that the crossflow develops at both the exit directions, which reduces the heat transferred from the target surfaces. Unlike case – 1 and case – 2, where $H/d=7$ had the maximum heat transfer, in case – 3 $H/d=5$ gives the maximum heat transfer from the target surface. $H/d=5$ gives minimum increase in heat transfer compared to $H/d=7$, whereas $H/d=5$ gives a maximum of 7.81% more heat transfer compared to $H/d=9$. The magnitude of local Nusselt number between $31.2 \le X/d \le 72.2$ and $80.4 \le X/d \le 114.3$ is almost similar for all the feeding channel aspect ratios H/d studied for case – 3, whereas for case – 1 and case – 2 completely different distribution of local Nusselt number is observed.

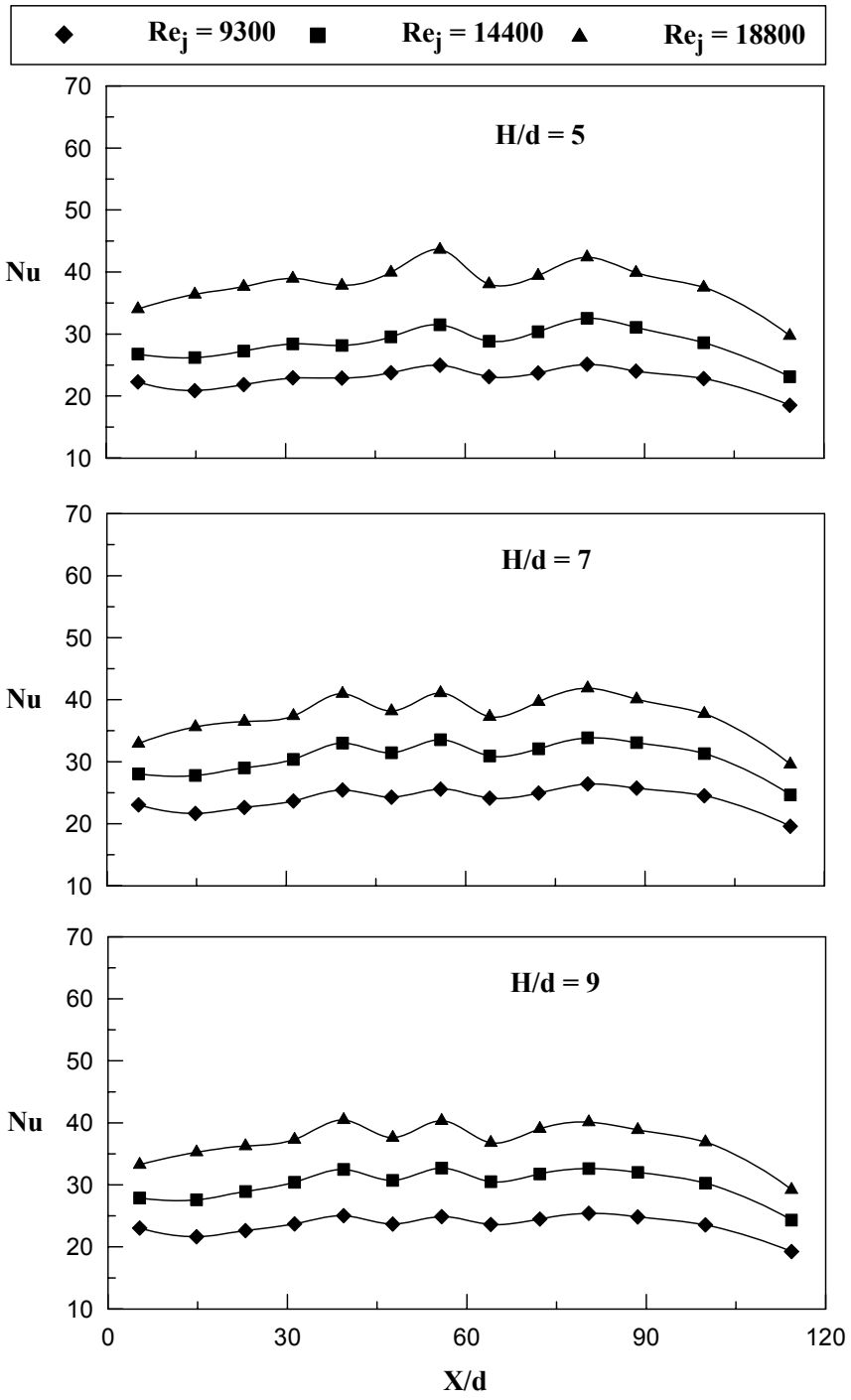

Figure 8.6 Effect of jet Reynolds number and feeding channel aspect ratio $5 \le H/d \le 9$ on local Nusselt number distribution for $S/d = 4$ and case – 3.

8.3 Effect of outflow orientation on local Nusselt number

Figure 8.7 – 8.9 shows the effect of the outflow orientation on the local Nusselt number distribution for different feeding channel aspect ratio $5 \le H/d \le 9$. The results are being presented for jet-to-plate distance $S/d = 6$, due to the highest amount of heat transfer observed with this particular jet-to-plate distance among all the jet-to-plate distances studied. All the jet Reynolds numbers studied $9300 \le \mathrm{Re}_j \le 18800$ are discussed individually.

Figure 8.7 presents the effect of the outflow orientation on the local Nusselt number distribution plotted for different feeding channel aspect ratios $5 \le H/d \le 9$ for $\mathrm{Re}_j = 5000$. Among all the H/d values studied very low variation of local Nusselt number is observed with respect to outflow orientation at low X/d $(5.3 \le X/d \le 32.2)$. It is observed that case – 3 has maximum heat transfer at $32.2 \le X/d \le 72.2$ this is due to the strong impingement in this region as the flow exits in both the directions. At $80.4 \le X/d \le 114.3$ case – 1 has the highest heat transfer due to the closed end and due to the less crossflow effect resulting in stronger impingement reducing the boundary layer thickness followed by case – 2 and case – 3 respectively. Case – 2 has the least values of local Nusselt number over the entire length of the target surface for all the feeding channel aspect ratios studied. This may be due to the air going out in the opposite direction to the air coming in which in-turn causes heavy crossflow and thus less values of local Nusselt number. Similar to the cases studied before for the effect of feeding channel aspect ratio, $H/d = 7$ has the maximum heat transfer over the entire length of the target surface.

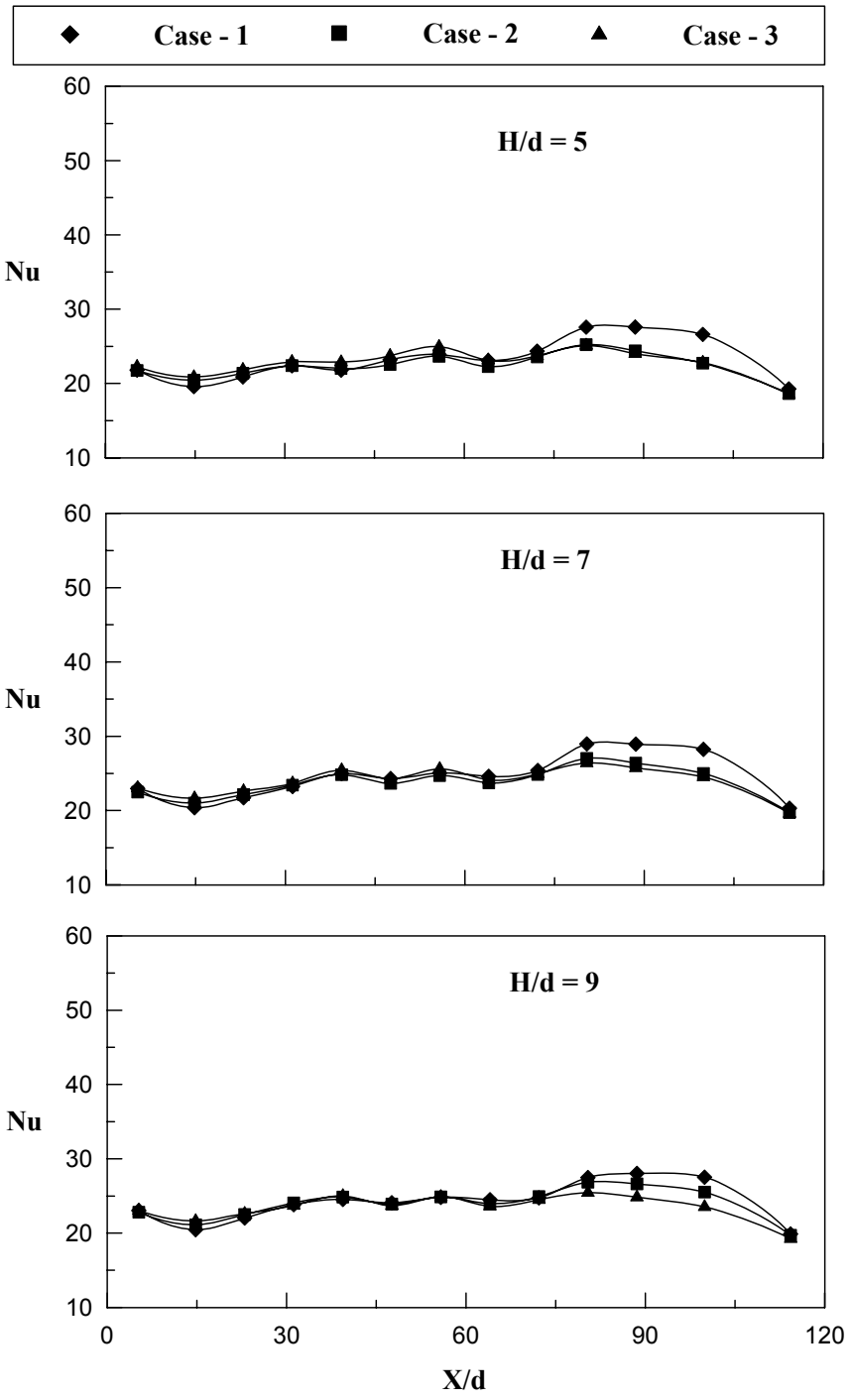

Figure 8.7 Effect of outflow orientation and feeding channel aspect ratio $5 \le H/d \le 9$ on local Nusselt number distribution for $S/d = 4$ and $\mathrm{Re}_j = 9300$.

Figure 8.8 presents the effect of the outflow orientation on the local Nusselt number distribution plotted for different feeding channel aspect ratios $5 \le H/d \le 9$ for $\mathrm{Re}_j = 14400$. It is observed that as the jet Reynolds number increases from 9300 to 14400 a maximum of 37% increase in local Nusselt number is observed. Similar to the local Nusselt number distribution for $\mathrm{Re}_j = 5000$, case – 3 has maximum heat transfer at $32.2 \le X/d \le 72.2$ due to the strong impingement of jets, whereas case – 1 and case – 2 gives less values of local Nusselt number due to the increase in the amount of the crossflow. At $80.4 \le X/d \le 114.3$ less variation in local Nusselt number is found as compared to Nusselt number distribution for $\mathrm{Re}_j = 9300$, whereas the behavior of local Nusselt number for case – 2 and case – 3 is almost similar as in both the cases air exits at large X/d $(X/d = 114.3)$ and for case – 3 air also exits at low X/d $(X/d = 0)$. Similar to $\mathrm{Re}_j = 9300$, case – 1 has the highest magnitude of local Nusselt number at $80.4 \le X/d \le 114.3$ and case – 2 has the least magnitude of local Nusselt number over the entire length of the target surface for all the feeding channel aspect ratios studied. It is also observed that the feeding channel aspect ratio $H/d = 7$ gives the maximum values of the local Nusselt numbers compared to the other H/d values.

Figure 8.9 presents the effect of the outflow orientation on the local Nusselt number distribution plotted for different feeding channel aspect ratios $5 \le H/d \le 9$ for $\mathrm{Re}_j = 18800$. It is observed that, for $\mathrm{Re}_j = 18800$, a variation in the magnitude of local Nusselt number values is observed over the entire length of the target surface for all the outflow orientations studied compared to the other two jet Reynolds numbers, $\mathrm{Re}_j = 9300$

and $\mathrm{Re}_j = 14400$ studied previously. Moreover as the H/d values increases from 5 to 9 a corresponding decrease in the magnitude of local Nusselt number is observed. Maximum heat transfer is observed for $H/d = 7$ similar to $\mathrm{Re}_j = 9300 \; and \; 14400$ where $H/d = 7$ gives the maximum values of local Nusselt number. Similar to the other two jet Reynolds number studied, at $32.2 \le X/d \le 72.2$, case – 3 has the highest magnitude of the local Nusselt number compared to case – 1 and case – 2, whereas at $80.4 \le X/d \le 114.3$ case – 1 has the highest heat transfer due to the stronger impingement of jets decreasing the boundary layer as the jets enters the impingement channel at this location thus having minimum crossflow effect. The variation in magnitude of the local Nusselt number observed at $80.4 \le X/d \le 114.3$ for $\mathrm{Re}_j = 18800$ is very high compared to the variation in the other two jet Reynolds numbers $\mathrm{Re}_j = 9300$ and $\mathrm{Re}_j = 14400$. The reason may be due to the increase in the strength of the jets with an increase in the jet velocity which causes the variation in the local Nusselt number to be less sensitive with respect to the outflow orientation.

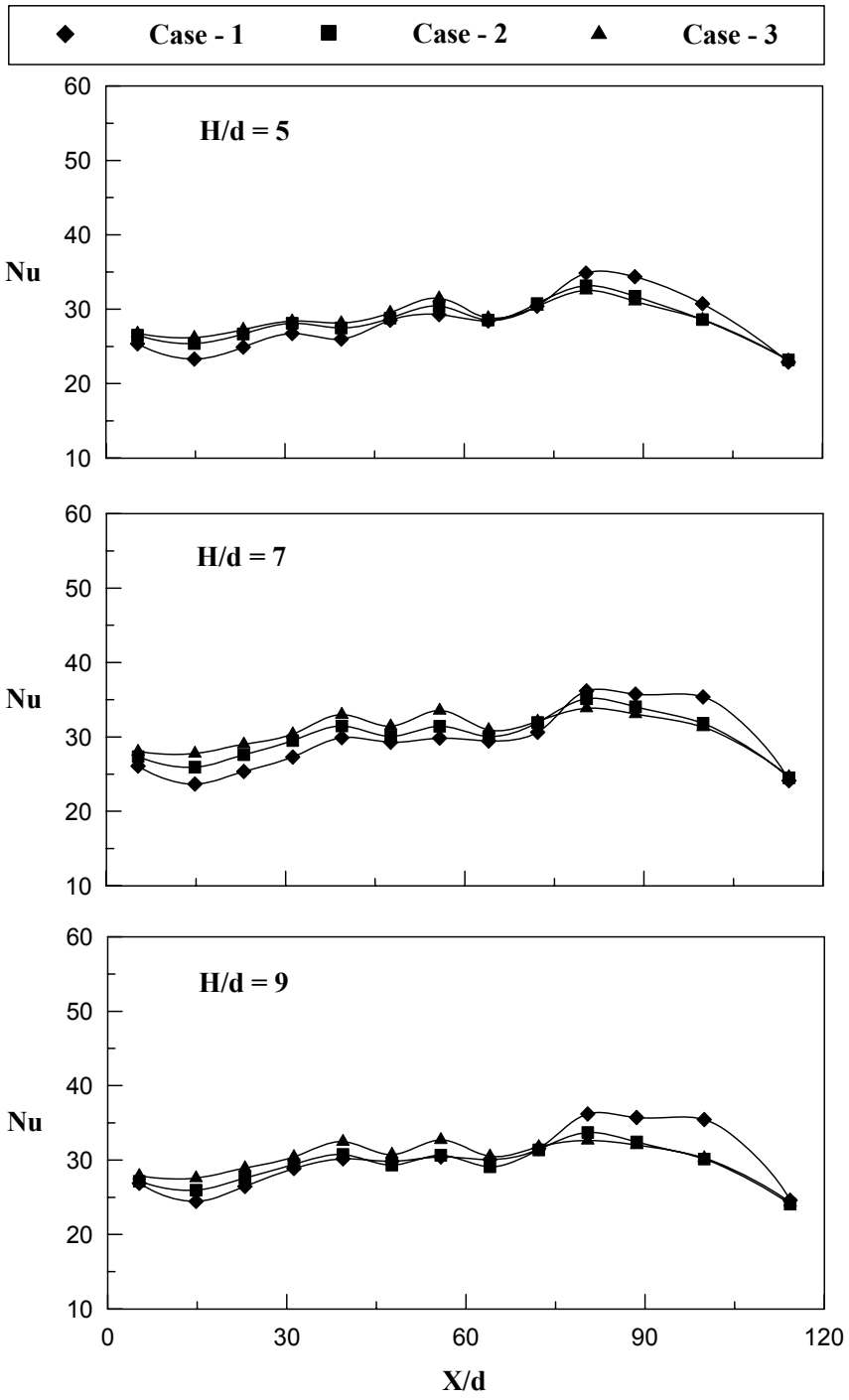

Figure 8.8 Effect of outflow orientation and feeding channel aspect ratio $5 \le H/d \le 9$ on local Nusselt number distribution for $S/d = 4$ and $\mathrm{Re}_j = 14400$.

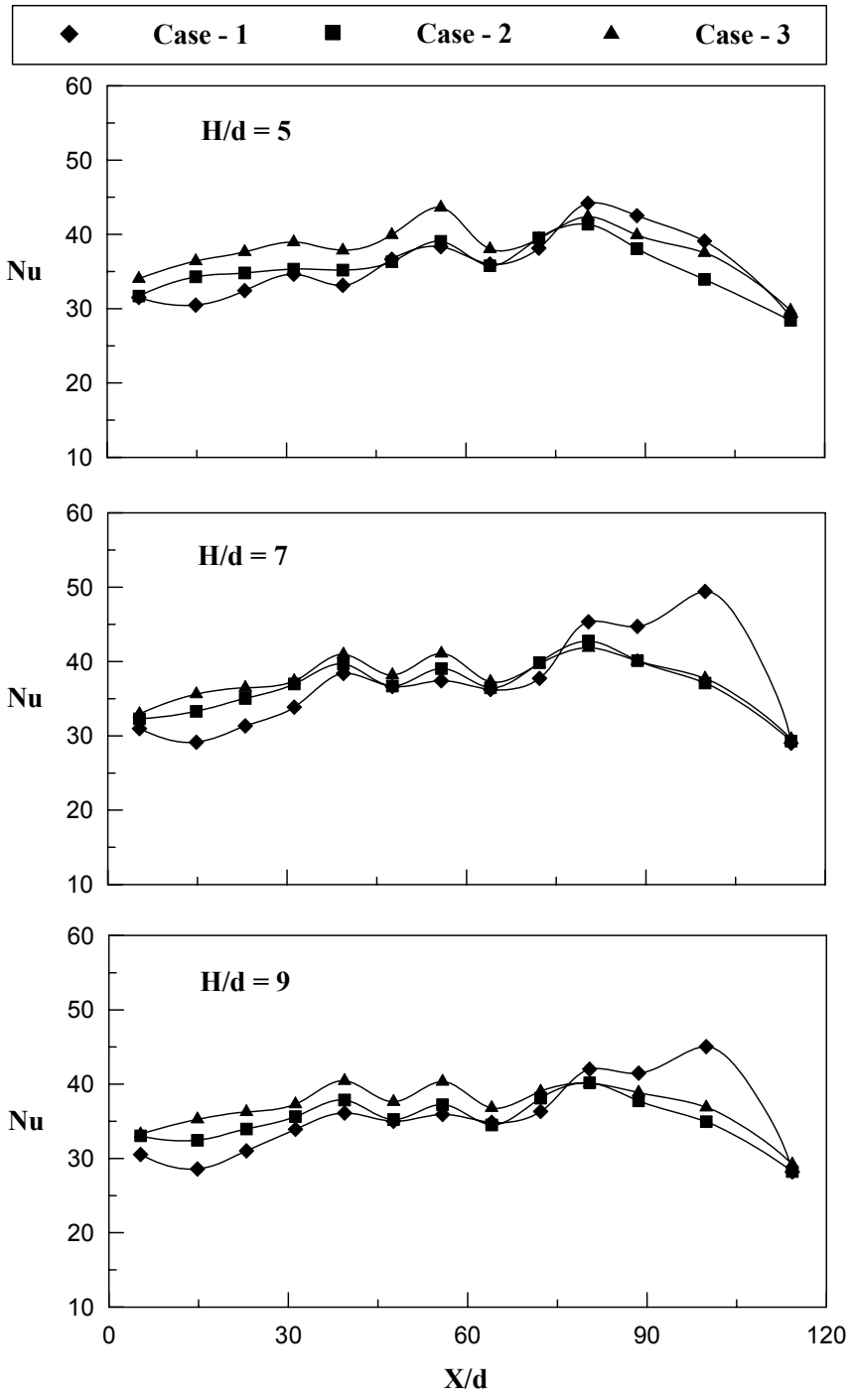

Figure 8.9 Effect of outflow orientation and feeding channel aspect ratio $5 \le H/d \le 9$ on local Nusselt number distribution for $S/d = 4$ and $\mathrm{Re}_j = 18800$.

8.4 Effect of jet-to-plate distance on local Nusselt number

Figure 8.10 –8.12, gives a detail insight into the effect of the feeding channel aspect ratio $5 \le S/d \le 9$ on the local Nusselt number distribution for different jet-to-plate distances $4 \le S/d \le 8$ with $\mathrm{Re}_j = 18800$ for all the outflow orientations on the heat transfer from the target surface. Jet Reynolds number $\mathrm{Re}_j = 18800$ is selected as this gives the maximum heat transfer among all the jet Reynolds numbers studied.

Figure 8.10 shows the local Nusselt number distribution over the entire length of the target surface for case – 1, where the flow exits at low X/d $(X/d = 0)$. The crossflow develops from large X/d $(X/d = 114.3)$ to low X/d $(X/d = 0)$ therefore a corresponding decrease in the heat transfer is observed from larger X/d to low X/d. The above phenomenon is observed for all the H/d values $5 \le H/d \le 9$. The heat transfer from the target surface decreases with an increase in jet-to-plate distance from S/d = 4 to 8, this behavior is observed for all the feeding channel aspect ratios studied. Over the entire length of the target surface, the jet-to-plate distance $S/d = 4$ gives the maximum heat transfer and $S/d = 8$ gives the least heat transfer among all the S/d values and for all the feeding channel aspect ratios studied. Observing the effect of the feeding channel aspect ratio on the local Nusselt number distribution, $H/d = 7$ gives the maximum heat transfer for the cases studied. $H/d = 7$ gives a maximum of 6% increase in local Nusselt number compared to $H/d = 5$, whereas a maximum of 11.8% more heat transfer is observed compared to $H/d = 9$. It is also observed that the magnitude of local Nusselt number at $80.4 \le X/d \le 114.3$ is more compared to that at $31.2 \le X/d \le 72.2$, this is due to the strong impingement of the jets and less crossflow effect as the flow first enters the impingement

channel at this location. At $31.2 \le X/d \le 72.2$ crossflow dominates the impingement of jets and leads to lesser magnitude of the local Nusselt number.

Figure 8.11 shows the effect of the jet-to-plate distance on the local Nusselt number distribution for case – 2 comparing different feeding channel aspect ratios $5 \le S/d \le 9$ for $\mathrm{Re}_j = 18800$. For case – 2 the flow exits at low X/d $(X/d = 0)$, which shows the development of crossflow towards low X/d. Similar to case – 1, $S/d = 4$ has the maximum heat transfer from the entire length of the target surface for all the H/d values examined $5 \le H/d \le 9$. Among all the feeding channel aspect ratios studied, $H/d = 7$ gives the maximum amount of heat transfer from the entire target surface. Although the Nusselt number distribution for $H/d = 5\ and\ 7$ is similar $H/d = 7$ has a marginal increase in heat transfer from the target surface compared to $H/d = 5$ whereas a maximum of 9.1% increase in heat transfer is observed compared to $H/d = 9$. It is observed that the local Nusselt number distribution for $H/d = 9$ is less sensitive for a change in the jet-to-plate distance as the magnitude of local Nusselt number is similar with a very less difference in magnitude. For the feeding channel aspect ratios $H/d = 5$ and $H/d = 7$, the change in jet-to-plate distance has considerable variation on the local Nusselt number distribution compared to $H/d = 9$. The maximum variation in the magnitude of the local Nusselt number for $H/d = 5\,and\,7$ with respect to the jet-to-plate distance is 5%.

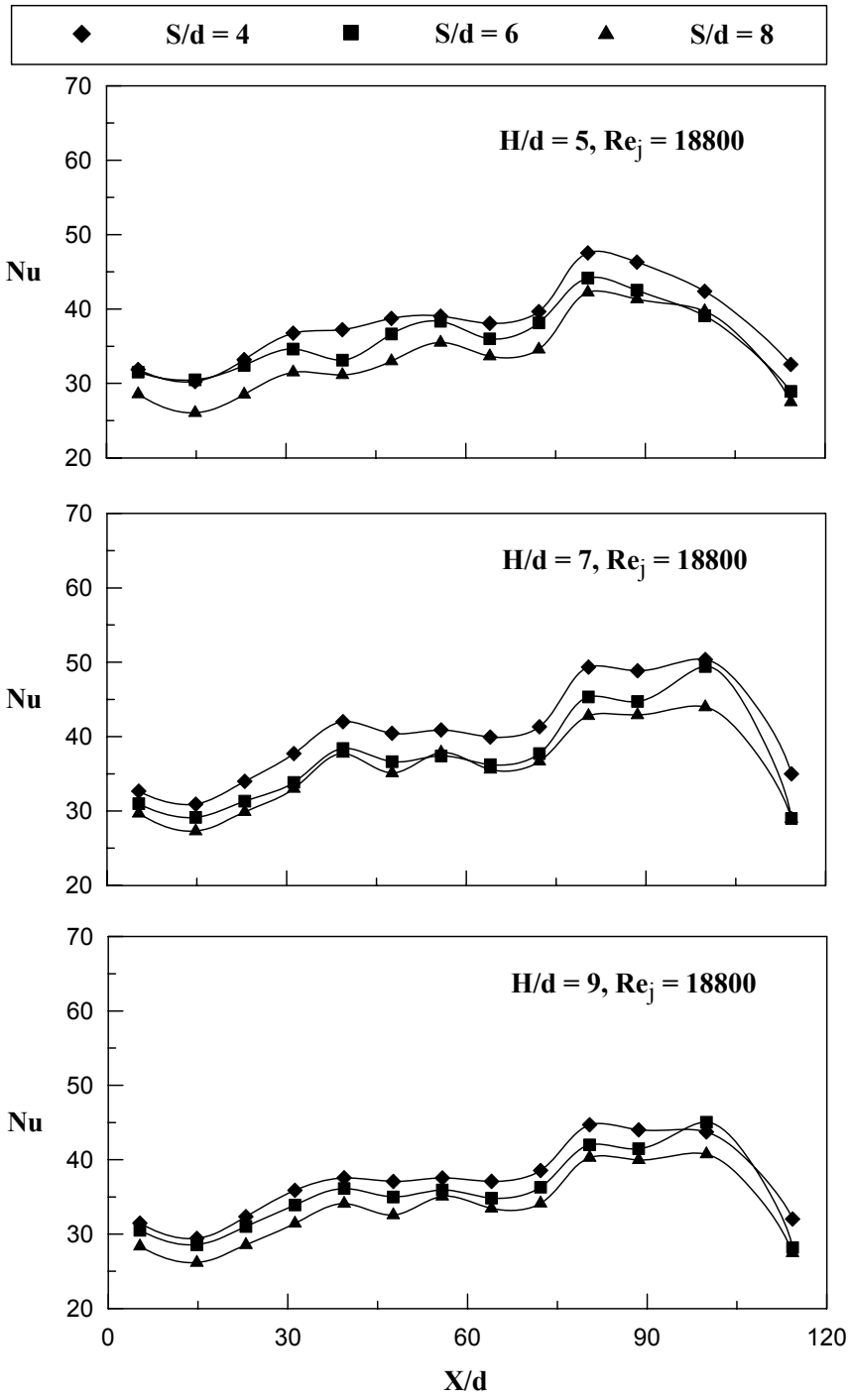

Figure 8.10 Effect of jet-to-plate distance and feeding channel aspect ratio $5 \le H/d \le 9$ on local Nusselt number distribution for $\mathrm{Re}_j = 18800$ and case – 1.

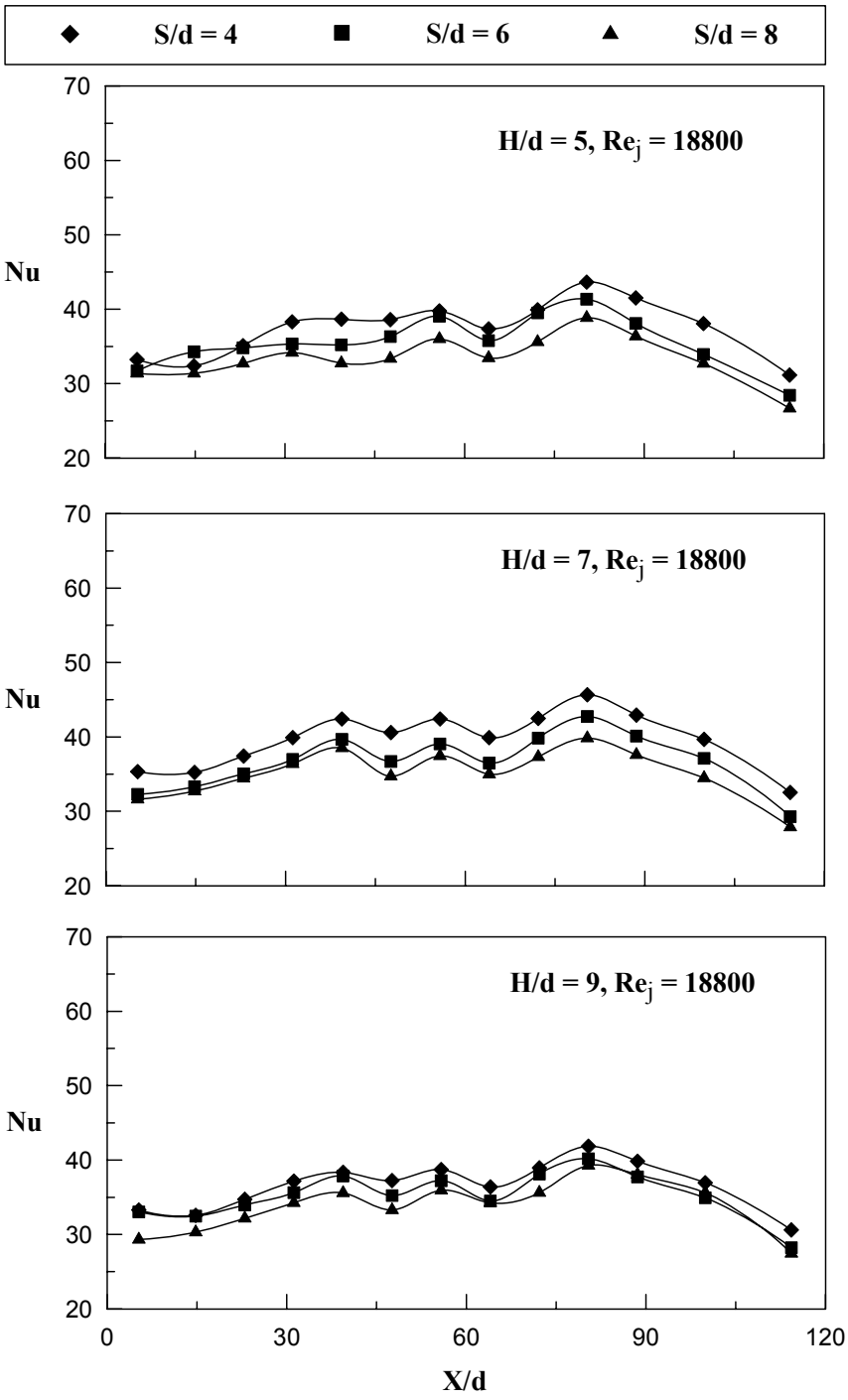

Figure 8.11 Effect of jet-to-plate distance and feeding channel aspect ratio $5 \le H/d \le 9$ on local Nusselt number distribution for $\mathrm{Re}_j = 18800$ and case – 2.

Figure 8.12 shows the effect of the jet-to-plate distance on the local Nusselt number distribution for case – 3 comparing different feeding channel aspect ratios $5 \le S/d \le 9$ for $\mathrm{Re}_j = 18800$. For case – 3 air exits at $X/d = 0$ and $X/d = 114.3$, where the crossflow has a predominant effect over the heat transfer characteristics. It is observed that at $80.4 \le X/d \le 114.3$ the local Nusselt number decreases towards exit i.e. at large X/d $(X/d = 114.3)$ for all the H/d values examined $5 \le H/d \le 9$. The heat transfer at $32.2 \le X/d \le 72.2$ has less magnitude of local Nusselt number this may be due to the effect of the crossflow dominating the strength of the impinging jets. For an increase in jet-to-plate distance a corresponding decrease in local Nusselt number is observed. Investigating the effect of feeding channel aspect ratio, $H/d = 7$ gives the highest heat transfer similar to case – 1 and case – 2. $H/d = 9$ gives very less values of local Nusselt number compared to $H/d = 5$, further a maximum of 11% more heat transfer is observed compared to $H/d = 7$. Among all the jet-to-plate distances investigated $S/d = 4$ gives the maximum heat transfer over the entire length of the target surface, this is due to the strong impingement of the jets, with less travel distance, which thins the boundary layer resulting in high values of local Nusselt number. Whereas $S/d = 8$ gives the minimum values of the local Nusselt number over the entire length of the target surface similar to the other two outflow orientations discussed earlier.

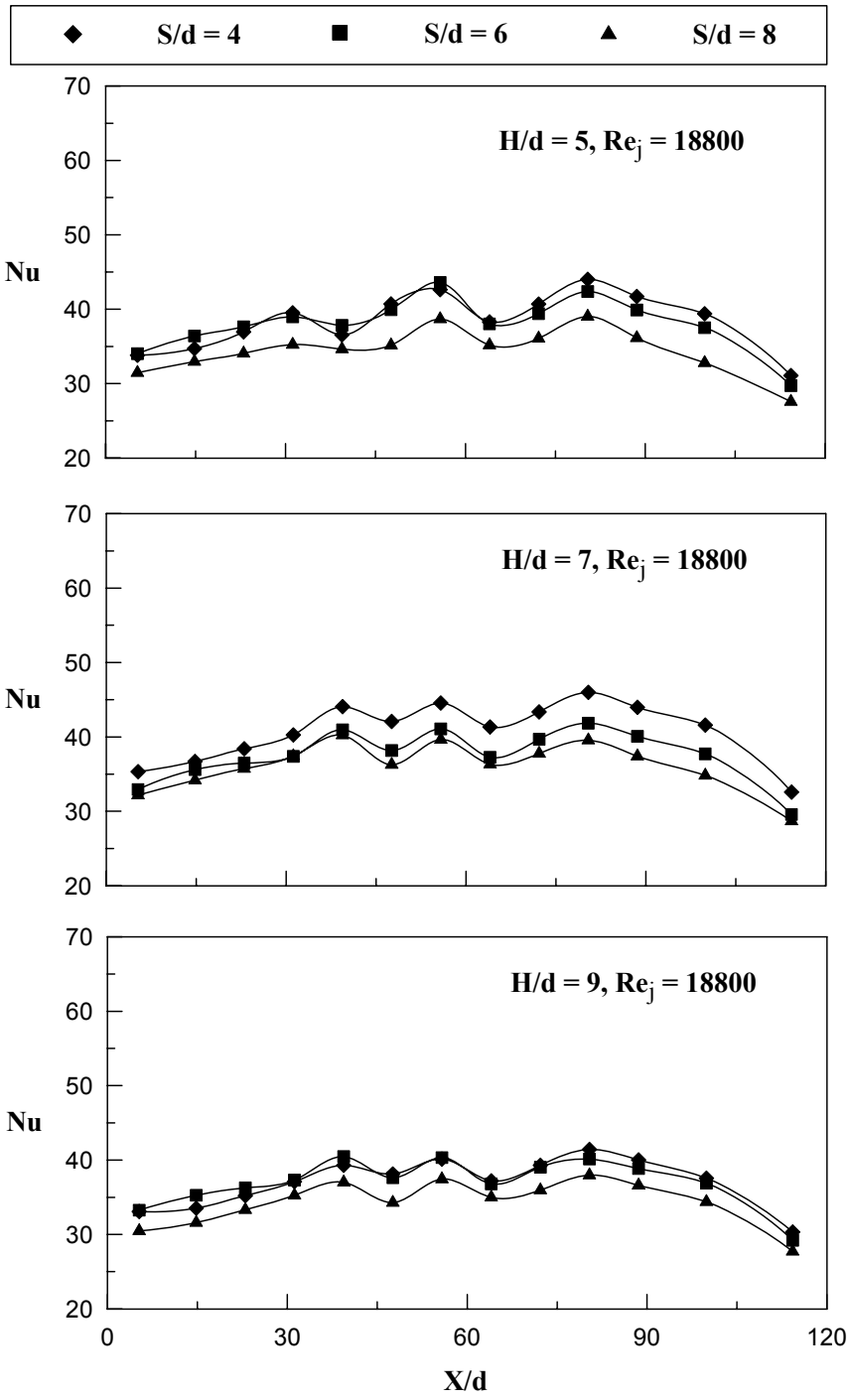

Figure 8.12 Effect of jet-to-plate distance and feeding channel aspect ratio $5 \le H/d \le 9$ on local Nusselt number distribution for $\mathrm{Re}_j = 18800$ and case – 3.

8.5 Average Nusselt Number

Figures 8.13 - 8.14 shows the average Nusselt number Nu_{avg} as a function of jet Reynolds number Re_j, considering all the outflow orientations, the feeding channel aspect ratio $5 \le H/d \le 9$ and the jet-to-plate distances $4 \le S/d \le 8$. The value of Nu_{avg} is an average of the detailed results on the entire target plate surface. The detailed results from the present study are averaged over the entire target plate to produce a single averaged Nusselt number.

8.5.1 Effect of feeding channel aspect ratio

Figure 8.13 shows the feeding channel aspect ratio $(5 \le H/d \le 9)$ for averaged Nusselt number as a function of the jet Reynolds number for all the outflow orientations studied. The averaged Nusselt numbers are shown for all the jet-to-plate distances $(4 \le S/d \le 8)$ and for all the outflow orientations. The averaged Nusselt number increases linearly with an increase in the jet Reynolds number. Among all the jet-to-plate distances studied the jet-to-plate distance $S/d = 4$ has the highest values of the averaged Nusselt number indicating the optimum jet-to-plate distance. The magnitude of averaged Nusselt number is almost the same for the remaining two jet-to-plate distances 4 and 8 with a maximum variation of 6%. It is also observed that as the feeding channel aspect ratio H/d increases from 5 to 7 there is a corresponding increase in the magnitude of the average Nusselt number and with an increase of H/d from 7 to 9 there is a corresponding decrease in the magnitude of averaged Nusselt number, indicating decrease in the strength of the

impinging jets with an increase in the feeding channel aspect ratios. For $\mathrm{Re}_j = 18800$, the difference in the magnitude of the average Nusselt number is quite large compared to the other two jet Reynolds numbers studied. The jet Reynolds number $\mathrm{Re}_j = 9300$, is less sensitive to the jet-to-plate distance as there in no much variation observed from the magnitude of the averaged Nusselt number. Large variation in the averaged Nusselt number is observed at less value of the feeding channel aspect ratios $H/d = 5$ and $H/d = 7$ with respect to the jet-to-plate distances, whereas the feeding channel aspect ratio $H/d = 9$ is less sensitive to a change in the jet-to-plate distance as very less variation is observed in the averaged Nusselt number. Case – 1 and case – 3 have the maximum values of averaged Nusselt number compared to case – 2 as the flow exit in opposite direction compared to the flow entry, which causes crossflow obstructing the impingement of jets.

8.5.2 Effect of outflow orientation

Figure 8.14 shows the averaged Nusselt number distribution as a function of jet Reynolds number. The effect of feeding channel aspect ratio $(5 \le H/d \le 9)$ and the effect of the jet-to-plate distance $(4 \le S/d \le 8)$ are shown in detail. It is observed that as the feeding channel aspect ratio is decreased from 9 to 7 there is a corresponding increase in the values of averaged Nusselt numbers, whereas a further decrease in the feeding channel aspect ratio from 7 to 5 leads to a decrease in the average Nusselt number this may be due to the disturbance caused to the impinging jet with an increase in the crossflow at low feeding channel aspect ratios. This indicates that $H/d = 7$ gives the maximum values of heat

transfer among all the feeding channel aspect ratios studied. Moreover it is also observed that an increase in the jet-to-plate distance (S/d) leads to a corresponding decrease in the average Nusselt number values. Among all the outflow orientations studied, case – 3, the case where the flow exits in both the directions $X/d = 0$ and $X/d = 114.3$ has the high amount of heat transferred from the target surface, where as case – 2 has the least amount of heat transferred from the target surface for all the feeding channel aspect ratios examined, this may be because of the flow exit in opposite direction as to that of the entry in the impingement channel. Outflow orientation – 2 has the least amount of heat transferred from the target surface, this may also be due to the obstruction caused to the flow of jets at large X/d due to the crossflow of the air at the exit of the impingement channel.

The feeding channel aspect ratio $H/d = 9$ gives a very less variation in the averaged Nusselt number with respect to the outflow orientations at all the jet Reynolds numbers, where as for $H/d = 5$ *and* 7 a considerable variation in the magnitude of averaged Nusselt number is observed for outflow orientation – 3 with respect to the other two outflow orientations. The jet Reynolds number $\mathrm{Re}_j = 9300$, is less sensitive to the outflow orientation as there in no much variation observed in the magnitude of the average Nusselt number at this present location.

Among all the feeding channel aspect ratios studied $H/d = 7$ gives the highest values of averaged Nusselt number indicating high heat transfer from the target surface for all the jet-to-plate distances studied, whereas $H/d = 9$ gives the least amount of heat transfer. The feeding channel aspect ratio $H/d = 5$ gives the less values of averaged Nusselt number compared to $H/d = 7$ because of the disturbance caused to the boundary layer due to the

effect of the crossflow becoming more severe at very less H/d values, a maximum difference of 4% is observed in the magnitude of the averaged Nusselt number.

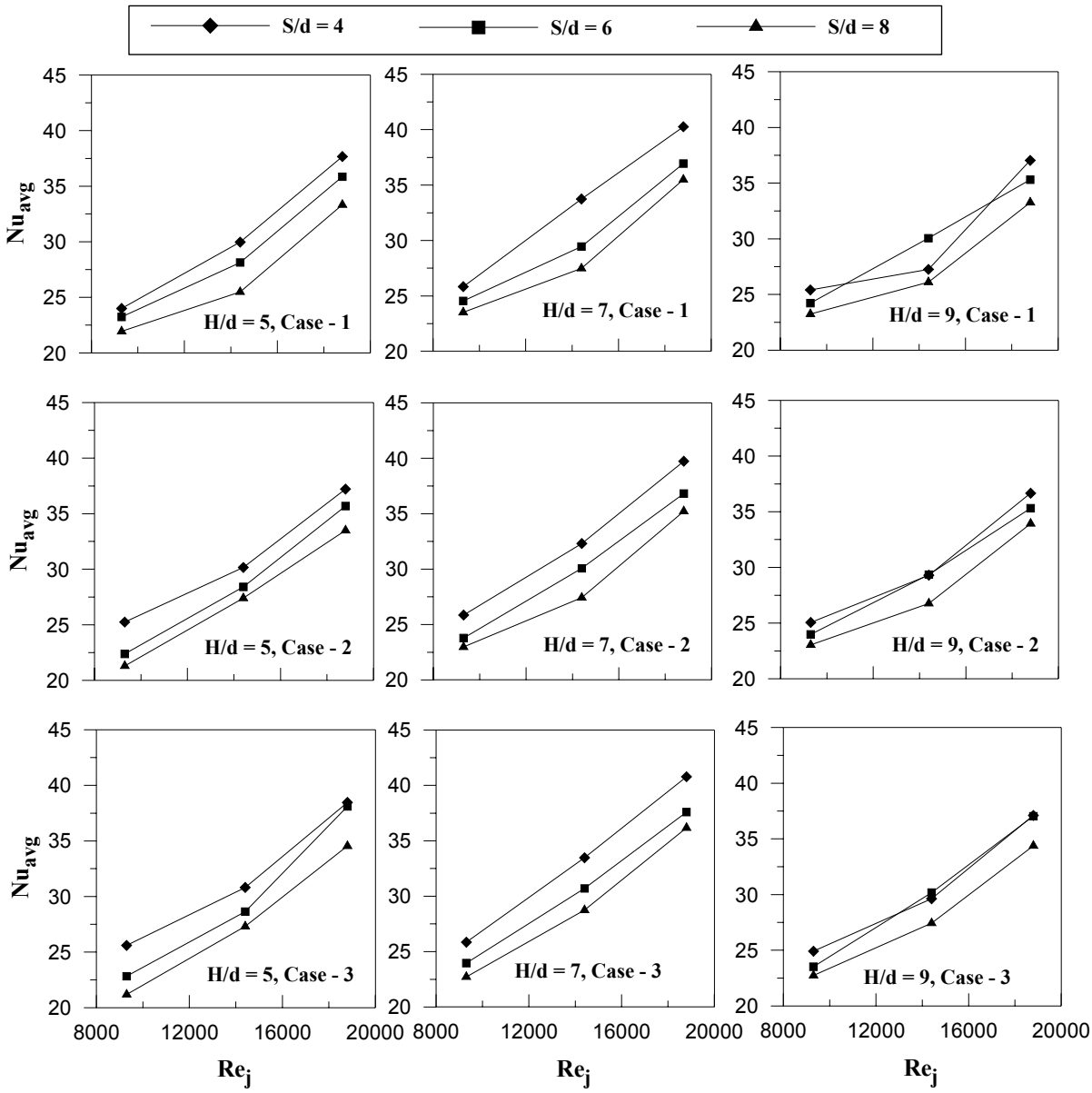

Figure 8.13 Effect of feeding channel aspect ratio $(5 \le H/d \le 9)$ and jet-to-plate distances on averaged Nusselt number for different outflow orientation.

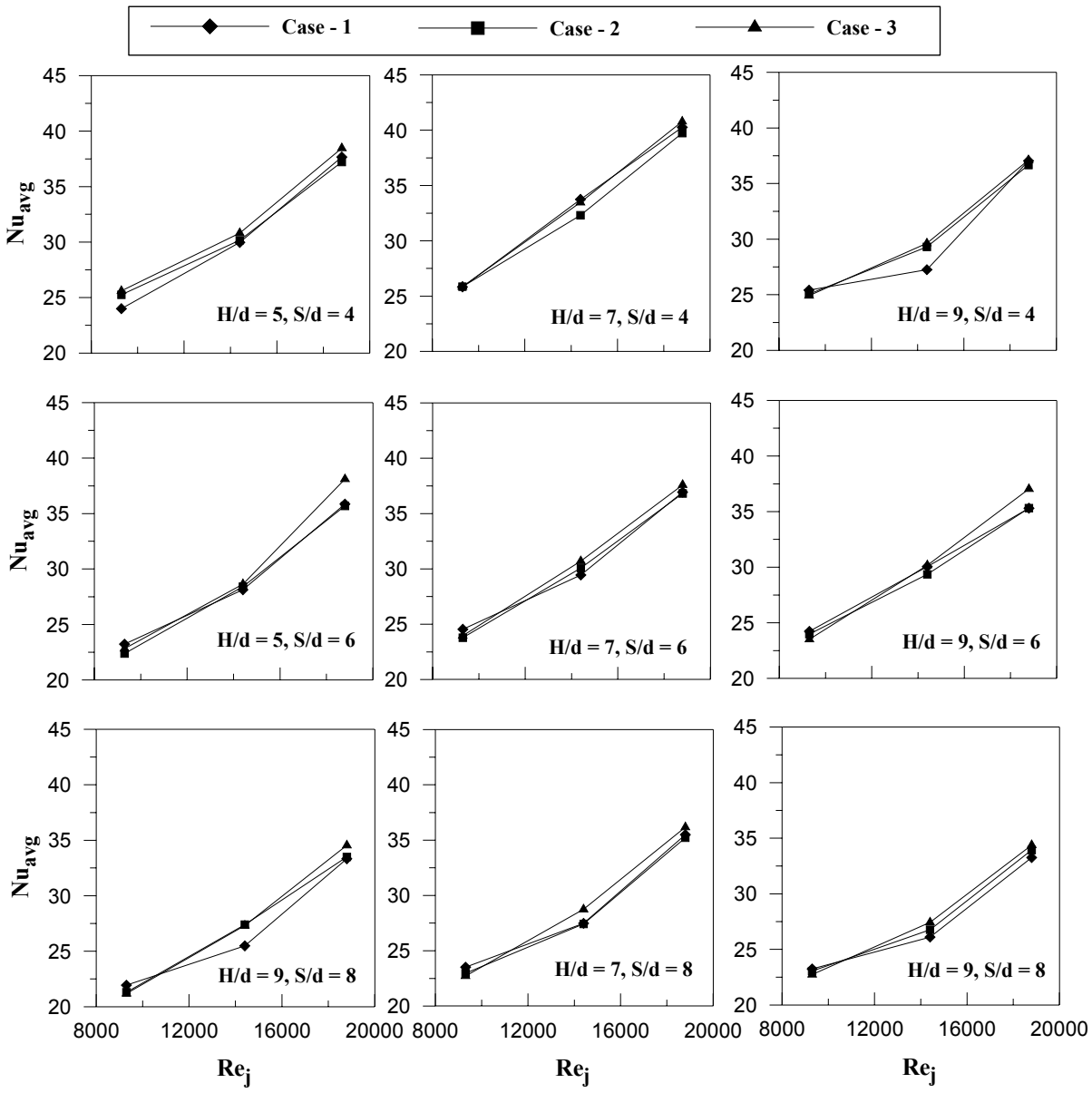

Figure 8.14 Effect of outflow orientation and feeding channel aspect ratio on averaged Nusselt number for different jet-to-plate distances $(4 \le S/d \le 8)$.

8.4.3 Correlations of averaged Nusselt number

The results for three different outflow orientations are correlated for the jet Reynolds number Re_j and the normalized jet-to-plate distance S/d dependence as

$$Nu_{avg} = A\,(\mathrm{Re}_j)^B (S/d)^C (H/d)^D \tag{8.2}$$

The present results are correlated for all outflow orientations individually for jet Reynolds number Re_j dependence. Previous studies in the field of jet impingement have involved in developing correlations for the averaged Nusselt number as a function of the jet Reynolds number by considering many parameters. Correlations by Huang et al [21],Kercher and Tabakoff [30] and Florscheutz et al [14] are compared to the averaged Nusselt number in the present investigation. Huang et al [21] studied the outflow orientations similar to ones used in the present study. They presented results for the outflow orientation 1 and 2 correlating for Reynolds number dependence as $Nu = 0.035\,\mathrm{Re}^{0.76}$, whereas for outflow orientation 3 which has the highest magnitude of heat transferred from the target surface is correlated as $Nu = 0.082\,\mathrm{Re}^{0.727}$. Kercher and Tabakoff [30] also studied the effect of crossflow and it is similar to the case – 1 in the present study. They varied the jet hole diameter, the hole spacing x, y and the jet to target plate distance. Based on all of these geometrical parameters, they proposed a correlation of the form $Nu = \phi_1\,\phi_2\,\mathrm{Re}^m\,(z/d)^{0.91}\,\mathrm{Pr}^{1/3}$, where ϕ_1 and ϕ_2 are constants based on X/d and Y/d, respectively. Florschuetz et al [14] presented the correlations with different coefficients of inline and staggered rows. The correlation for jet

impingement with minimum crossflow is given as $Nu = 0.363(X/d)^{-0.554}(Y/d)^{-0.422}(Z/d)^{0.068}\,\mathrm{Re}_j^{-0.554}\,\mathrm{Pr}^{1/3}$.

The detailed values of the local Nusselt number are averaged over the entire length of the target surface to obtain an single averaged Nusselt number. The averaged Nusselt numbers for each outflow orientation are plotted against the jet Reynolds number. The present results are correlated for the jet Reynolds number dependence as $Nu_{avg} = 0.000869\,(\mathrm{Re}_j)^{0.674}(S/d)^{0.611}(H/d)^{2.815}$ for case 1 and 2. The correlations for Huang et al [21] for case 1 and 2 are in good comparison with the present study. Kercher and Tabakoff [30] presented the results for the outflow orientation – 1 and the results of the present study are in good comparison with the existing correlation. The case with maximum heat transfer from the target surface, outflow orientation – 3, is correlated for the jet Reynolds number dependence as $Nu_{avg} = 0.000437(\mathrm{Re}_j)^{0.745}(S/d)^{0.354}(H/d)^{4.575}$. The correlation used from Florschuetz et al [14] is for the case with minimum crossflow. Huang et al [21] also presented a separate correlation for the case with high heat transfer; this case in their study had the less crossflow effect. The results from the present study for case – 3 are lower than the existing correlations, which includes the crossflow effect. The correlation for case – 3 in the present study is in good agreement with the correlation presented by Florschuetz et al [14] and Huang et al [21]. Thus it is evident from the above discussion that the crossflow effect is more dominant on outflow orientation 1 and 2 compared to outflow orientation – 3.

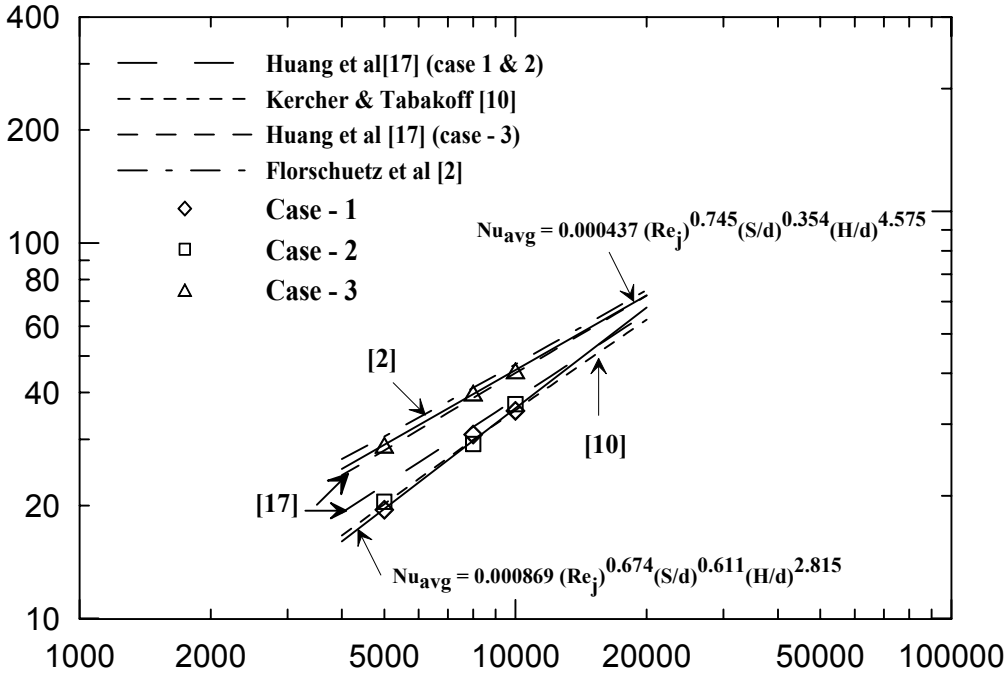

Figure 8.15 Averaged Nusselt number comparisons with the existing correlations

CHAPTER 9

CONCLUSIONS

In this chapter a detailed conclusion about the heat transfer characteristics obtained by using different orifice plates in the current experimental investigation is presented. The effect of feeding channel aspect ratio, outflow orientation, jet-to-plate distance and the orifice jet size and pattern on the heat transfer in a rectangular duct with an array of equally spaced jets is studied using the jet impingement technique.

8.1 Orifice plate – 1

The effect of outflow orientation and the feeding channel aspect ratio $2.5 \le H/d \le 4.5$ on local Nusselt number using jet impingement technique (single array of tangential jets), for a jet Reynolds numbers $5000 \le \mathrm{Re}_j \le 10000$ is investigated. The conclusions are as follows.

1. The Nusselt number is significantly affected by the outflow orientation, based upon the average Nusselt number calculation, under the same jet Reynolds number, outflow orientation – 3 gives the maximum heat transfer over the entire target surface among all the outflow orientations studied, whereas outflow orientation – 2 has the least values of averaged Nusselt number.

2. The feeding channel aspect ratio also significantly affects the heat transfer characteristics all along the target surface. $H/d = 2.5$ gives the highest heat transfer among all the feeding channel aspect ratios investigated. This may be due to the impinging jets dominating the crossflow effect to give the higher magnitude of Nusselt number.
3. Correlations of average Nusselt numbers in the present rectangular duct with single array of impinging jets have been developed in terms of the jet Reynolds number for three different outflow orientations individually.

8.2 Orifice plate 1 & 2

The effect of outflow orientation on local Nusselt number using jet impingement technique (single array of jets), for a jet Reynolds numbers $(5000 \le \mathrm{Re}_j \le 10000)$, the feeding channel aspect ratio $(2.5cm \le H \le 4.5cm)$ and also by varying the orifice jet diameter $d = 0.5\ and\ 1cm$ is investigated. The conclusions are as follows.

1. The Nusselt number distribution is significantly affected by the outflow orientation, based upon the average Nusselt number calculation, under the same jet Reynolds number for $d = 0.5cm$, case – 3 gives the maximum heat transfer over the entire target surface among all the outflow orientations studied, whereas case – 2 has the least values of average Nusselt number.

2. Under the same Reynolds number for $d = 1cm$, case – 3gives the maximum heat transfer among all the outflow orientations studied, whereas case – 1has the least values of average Nusselt number.
3. The feeding channel aspect ratio significantly affects the heat transfer coefficient. It is also observed that the feeding channel aspect ratio $H/d = 2.5$ provides the maximum heat transfer for both the orifice jet sizes.
4. Correlations of averaged Nusselt numbers in the present rectangular duct with single array of impinging jets have been developed in terms of the jet Reynolds number for three different outflow orientations individually.

8.3 Orifice plate – 2

The effect of outflow orientation on local Nusselt number using jet impingement technique (single array of jets), for a jet Reynolds numbers $(9300 \le \mathrm{Re}_j \le 18800)$, jet-to-plate distance $(4 \le S/d \le 8)$, the feeding channel aspect ratio $(5 \le H/d \le 9)$ and with orifice jet diameter $d = 0.5\ cm$ is investigated. The conclusions are as follows.

1. The Nusselt number is significantly affected by the outflow orientation, based upon the average Nusselt number calculation, under the same jet Reynolds number for $d = 0.5cm$, case – 3 gives the maximum heat transfer over the entire target surface among all the outflow orientations studied, whereas case – 2 has the least values of average Nusselt number.

2. The jet-to-plate distance S/d also significantly affects the Nusselt number. It is also observed that the case for jet-to-plate distance $S/d = 6$ provides the maximum heat transfer, this is because at less S/d values the crossflow dominates and at high S/d values the less jet strength results in lesser magnitude of Nusselt number.
3. The feeding channel aspect ratio H/d also significantly affects the Nusselt number. It is also observed that the case for jet-to-plate distance $H/d = 9$ provides the maximum heat transfer. The crossflow dominates the strength of the impinging jets at low H/d values resulting in lesser magnitude of Nusselt numbers. Increasing the H/d values results in stronger impinging jets overcoming the crossflow effect and thus higher magnitudes of Nusselt number.
4. Correlations of average Nusselt numbers in the present rectangular duct with single array of impinging jets have been developed in terms of the jet Reynolds number for three different outflow orientations individually.

8.4 Orifice plate – 3

The effect of outflow orientation and the feeding channel aspect ratio $5 \le H/d \le 9$ on local Nusselt number using jet impingement technique (single array of staggered jets), for a jet Reynolds numbers $(9300 \le \mathrm{Re}_j \le 18800)$, jet-to-plate distance $4 \le S/d \le 8$ is investigated. The conclusions are as follows.

5. The Nusselt number is significantly affected by the outflow orientation, based upon the average Nusselt number calculation, under the same jet Reynolds number for $d = 0.5cm$, case -3 gives the maximum heat transfer over the entire target surface

among all the outflow orientations studied, whereas case – 2 has the least values of average Nusselt number.

6. The jet-to-plate distance S/d also significantly affects the Nusselt number. It is also observed that the case for jet-to-plate distance $S/d = 6$ provides the maximum heat transfer, this is because at less S/d values the crossflow dominates and at high S/d values the less jet strength results in lesser magnitude of Nusselt number.
7. The feeding channel aspect ratio H/d also significantly affects the heat transfer coefficient. It is also observed that the case for jet-to-plate distance $H/d = 5$ provides the maximum heat transfer. The crossflow dominates the strength of the impinging jets at low H/d values resulting in lesser magnitude of Nusselt numbers. Increasing the H/d values results in stronger impinging jets overcoming the crossflow effect and thus higher magnitudes of Nusselt number.
1. Correlations of average Nusselt numbers in the present rectangular duct with single array of impinging jets have been developed in terms of the jet Reynolds number for three different outflow orientations individually.

8.5 Orifice plate – 4

The effect of outflow orientation and the feeding channel aspect ratio $5 \le H/d \le 9$ on local Nusselt number using jet impingement technique (single array of tangential jets), for a jet Reynolds numbers $(9300 \le \mathrm{Re}_j \le 18800)$, jet-to-plate distance $4 \le S/d \le 8$ is investigated. The conclusions are as follows.

2. The Nusselt number is significantly affected by the outflow orientation, based upon the average Nusselt number calculation, under the same jet Reynolds number,

outflow orientation 3 gives the maximum heat transfer over the entire target surface among all the outflow orientations studied, whereas outflow orientation 2 has the least values of average Nusselt number.

3. The feeding channel also significantly affects the heat transfer characteristics all along the target surface. $H/d = 7$ gives the highest heat transfer among all the feeding channel aspect ratios investigated.
4. The jet-to-plate distance S/d also significantly affects the heat transfer coefficient. It is also observed that the case for jet-to-plate distance $S/d = 4$ provides the maximum heat transfer for both the orifice jet sizes, whereas $S/d = 8$ gives the least heat transfer over the heated target surface.
5. Correlations of average Nusselt numbers in the present rectangular duct with single array of impinging jets have been developed in terms of the jet Reynolds number for three different outflow orientations individually.

APPENDIX A

SAMPLE CALCUATIONS OF LOCAL NUSSELT NUMBER

All the independent parameters like the temperature of the copper plates, mass flow rate of air, voltage supplied to the heater, resistance by the heater, inlet temperature of the air coming into the test section are measured using the Data Acquisition system.

The magnitude of the local Nusselt number is evaluated using the equations 2.4 to 2.17 shown in chapter 2. All the experiments for the local Nusselt number evaluation are carried out for the constant heat flux condition, thus the voltage supplied to the heater is kept constant through all the experiments.

Sample calculation

The present set of calculations are presented for orifice plate – 2, Case – 2 with $\mathrm{Re}_j = 9300$, $S/d = 4$ and $H/d = 9$, for orifice plate – 1.

Parameters	Values
Voltage supplied to heater	77.66 V
Resistance of the heater	60.05 Ω
Inlet Temperature	21°C
Thickness of wood	0.03 m
Thermal conductivity of wood	0.087 W/m^{2}K
Thermal conductivity of air	0.0257 W/m^{2}K

The temperature of the copper plates T_s, is the average of the two readings of temperature taken for each copper plate.

X/d	Plate no	T_s (^oC)	Area of plates (m^2)	Q_{total} (W)	Q_{cond} (W)	Q_{rad} (W)	Q_{actual} (W)	h (W/m^2K)	Nu
2.65	1	61.26	0.00223	9.38	0.21	0.0014	9.16	102.26	19.90
7.4	2	65.27	0.00168	7.08	0.18	0.0014	6.90	92.73	18.04
11.5	3	61.93	0.00168	7.08	0.16	0.0011	6.91	100.53	19.56
15.6	4	58.60	0.00168	7.08	0.15	0.0009	6.93	109.71	21.34
19.7	5	59.44	0.00168	7.08	0.15	0.0009	6.93	107.23	20.86
23.8	6	56.37	0.00168	7.08	0.14	0.0008	6.94	116.80	22.72
27.9	7	55.04	0.00168	7.08	0.13	0.0007	6.95	121.50	23.64
32	8	54.81	0.00168	7.08	0.13	0.0007	6.95	122.34	23.80
36.1	9	54.16	0.00168	7.08	0.13	0.0006	6.95	124.80	24.28
40.2	10	52.14	0.00168	7.08	0.12	0.0005	6.96	133.09	25.89
44.3	11	52.68	0.00168	7.08	0.12	0.0006	6.96	130.74	25.43
49.95	12	52.32	0.00168	7.08	0.12	0.0006	6.96	132.31	25.74
57.15	13	60.95	0.00315	13.27	0.30	0.0019	12.97	103.07	20.05

BIBLIOGRAPHY

1. Arjocu, S. C. and Liburdy, J. A. (1999). "Near surface characterization of an impinging elliptic jet array". *Trans. ASME - J. Fluids Eng*., 121:384–390.
2. Barata, J. M. M. (1996). "Fountain flows produced by multiple impinging jets in a crossflow". *AIAA Journal*, 34 (12) 2523–2530.
3. Baughn, J. W., Anderson, M. R., Mayhew, J. E., and Wolf, J. D. (1999). "Hysteresis of thermo chromic liquid crystal temperature measurement based on hue". *Trans. ASME - J. Heat Transfer*, 121 (4) 1067–1072.
4. Baughn, J. W. and Shimizu, S. (1989). "Heat transfer measurements from a surface with uniform heat flux and an impinging jet". *Trans. ASME - J. Heat Transfer*, 111:1096–1098.
5. Chang Haipang, Zhang Dalin, Huan Taipang, "Impingement Heat Transfer From Rib Roughened surface Within Arrays of Circular Jets. The effect of relative position o fjet hole to the ribs" ASME *Journal of Heat transfer*, 97-GT-331 June 2- June 5, 1997.
6. Chupp, R. E., Helms, H. E., McFadden, P. W., and Brown, T. R., 1969, "evaluation of Internal Heat-transfer coefficients for impingement-cooled turbine airfoils," *J. Aircraft*, 6, pp. 203-208.
7. Coleman, H. W. and Steele, W. G., 1999, *"Experimental and Uncertainty Analysis for Engineers," Wiley*, New York.

8. Colucci, D. W. and Viskanta, R. (1996). “Effect of nozzle geometry on local convective heat transfer to a confined impinging air jet”. *Exp. Thermal Fluid Sci*., (13) pp. 71–80.
9. Cooper, D., Jackson, D. C., Launder, B. E., and Liao, G. X. (1993). “Impinging jet studies for turbulence model assessment — I Flow-field experiments”. *Int. J. Heat Mass Transfer*, 36 (10) pp. 2675–2684.
10. Dittus, F. W., and Boelter, L. M. K., University of California at Berkeley, *Publications in Engineering*, Vol. 2, p. 443.
11. Ekkad, S. V. and Han, J. C., 1997, “Detailed Heat transfer distributions in two-pass square channels with ribs turbulators,” *International Journal of Heat & Mass Transfer*, Vol. 40, pp.2525-2537.
12. Ekkad, S. V., Huang, Y., and Han, J.C., “Impingement Heat transfer on a Target Plate with Film Cooling Holes,” *Journal of Thermophysics and Heat transfer,*Vol. 13, No. 4, Oct 1999, pp.522-528.
13. Florschuetz, L. W., Truman, C. R., and Metzger, D. E., “Stream-wise flow and heat transfer distributions for jet impingement with cross flow.” *Journal of Heat transfer*, Vol 103, No. 2, 1981, pp. 337-342.
14. Florschuetz, L. W., Metzger, D. E., Su, C. C., Isoda, Y., and Tseng, H. H., “Heat transfer Characteristics for Jet Array Impingement with Initial Cross flow,” *Journal of Heat Transfer*, Vol. 106, No. 1, 1984, pp.34-41.

15. Gardon, R. and Cobonpue, J. (1962). “Heat transfer between a flat plate and jets of air impinging on it. In International Developments in Heat Transfer”, pages 454–460, *New York. ASME*.

16. Goldstein R. J. and A. I. Behbahani, 1982 “Impingement of a circular jet with and without cross flow,” International Journal of Heat and Mass transfer, Vol. 25, No. 9, pp. 1377-1382.

17. Han, J. C., Chanra, P. R., and Lau. S. C., 1988, “Local Heat/Mass Transfer Distributions around sharp 180^{o} turns in Two-pass smooth and Rib-roughened channels,” *ASME Journal of Heat transfer*, Vol. 110, pp 91-98.

18. Han, J. C., and Zhang, P., 1991, “Effect of Rib-Angle Direction on Local Mass Transfer Distribution in a Three-Pass Rib-Roughened Channel,” ASME Journal of Turbomachinery, 113, pp. 123-130.

19. Han, J. C., and Zhang, Y. M. and Lee, C. P., 1991, “Augmented Heat transfer in Square channel with parallel, crossed, and V-shaped Angled ribs,” ASME Journal of Heat transfer, 113, pp. 590-596.

20. Hollworth B. R., L. Dagan, “Arrays of Impinging Jets with spent fluid removal through vent holes on the Target surface.” *Journal of Engineering for power.* Vol 102, Oct 1980, pp. 994-999.

21. Huang, Y., Ekkad, S. V., and Han, J. C., 1998, “Detailed Heat transfer Distributions Under an Array of Orthogonal impinging Jets,” AIAA. *J. Thermo physics*. Heat Transfer, 12, pp. 73-79.

22. Huber, A.M., and Viskanta, R., "Effect of Jet-Jet Spacing on convective Heat transfer to confined, Impinging Arrays of Axisymmetric Air jets," *International Journal of Heat and Mass transfer*, Vol. 37, No. 10, 1994a, pp.2859-2869.

23. Huber, A. M., and Viskanta, R., "Comparison of convective Heat transfer to perimeter and center jet in a confined, Impinging Array of Axisymmetric Air Jets," *International Journal of Heat and Mass Transfer*, Vol. 37, No.10, 1994b, pp.3025-3030.

24. Huber, A. M. and Viskanta, R. (1994c). "Impingement heat transfer with a single rosette Nozzle". *Exp. Thermal Fluid Sci*., (9) pp. 320–329.

25. Hwang, J. J., and Chang, B. Y., 2000, "Effect of Outflow Orientation on Heat transfer and Pressure drop in an Triangular Duct with an Array of Tangential Jets," *J. of Heat Transfer* ASME, Vol. 122, pp. 669-678.

26. Hwang, J. J., Shih, N. C., Cheng, C. S., Shih, K. T., and Tsai, Y. P., "Jet Spacing Effect on Impinged Heat transfer ina Triangular duct with a Tangential Jet-Array", *International Journal of Transport Phenomena,* Vol. 5, 2003, pp.65-74.

27. Ichimiya, K. (1994). "Heat transfer and flow characteristics of a single circular impinging jet considered on heat conduction in a heated section". *In Int. Symp. Turb., Heat Mass Transfe*r, volume 1, pages 2.2.1–2.2.6, Lisbon.

28. Incropera, F. P., and De-Witt, P. D., "Fundamentals of Heat transfer", John Wiley & Sons, New York, 1981.

29. Kataoka, K. (1990). "Impingement heat transfer augmentation due to large scale eddies". *In Heat Transfer 1990, volume 1 of Proc. 9th Int. Heat Transfer Conf.*, pages 255–273.

30. Kercher, D. M., and Tabakoff, W., "Heat transfer by a square array of round ai rjets impinging perpendicular to a flat surface including the effect of spent air," *Journal of Engineering for power,* Vol. 92, No. 1,1970, pp. 73-82.

31. Kline, S. J., and McClintock, F, A., "Describing Uncertainities in Single-Sample experiments," *Mech Engg. (ASME)*, Vol 75, pp. 3-8.

32. Lee, J. and Lee, S.-J. (2000). "The effect of nozzle configuration on stagnation region heat transfer enhancement of axisymmetric jet impingement". *Int. J. Heat Mass Transfer*, 43:3497–3509.

33. Livingood, J. N. B. and Hrycak, P. (1973). "Impingement heat transfer from turbulent air stream jets to flat plates – a literature survey". NASA TM X-2778, NASA.

34. Matsumoto, R., Ishihara, I., Yabe, T., Ikeda, K., Kikkawa, S., and Senda, M. (1999). "Impingement heat transfer within arrays of circular jets including the effect of crossflow" (AJTE99-6386). *In Proc. 5th ASME/JSME Joint Thermal Eng. Conf.*, pages 1–8.

35. Metzger, D. E., and Bunker, R. S., "Local Heat transfer in internally cooled Turbine Airfoil Leading Edge Regions: Part I – Impingement cooling without film coolant Extraction," *Journal of Turbo machinery*, Vol.112, No. 3, 1990, pp. 451-458.

36. Metzger, D. E., Florschuetz, L. W., Takeuchi, D. I., Behee, R. D., and Berry, R. A. (1979). "Heat transfer characteristics for inline and staggered arrays of circular jets with crossflow of spent air". *Trans. ASME - J. Heat Transfer*, 101:526–531.

37. Obot, N. T. and Trabold, T. A. (1987). "Impingement heat transfer within arrays of circular jets: Part 1 – effects of minimum, intermediate, and complete crossflow for small and large spacings". *Trans. ASME - J. Heat Transfer*, 109:872–879.

38. Popiel, C. O. and Boguslawski, L. (1986). "Mass or heat transfer in impinging single, round jets emitted by a bell-shaped nozzle and sharp-ended orifice. In Heat Transfer" 1986, volume 3 of Proc. *8th Int. Heat Transfer Conf*., pages 1187–1192.

39. Pramanick, A., Ekkad, S. V., and Yang, H., "Flow predictions in a two-pass channel with heat transfer enhancement by impingement and swirl", ISHMT-ASME, *Heat and Mass transfer Conference,* Calcutta, India, 2001.

40. Taslim M. E. and T. Li, "Measurements of Heat transfer coefficients in Rib roughened trailing edge cavities with crossover jets." AMSE 98-GT-435.1998.

41. Todd S. Griffith, Luai Al-Hadrami, and Je-Chin Han, 2002, "Heat Transfer in rotating rectangular cooling channels (AR=4) with angled ribs," *Journal of Heat Transfer*, Vol. 124, pp. 617-625.

42. Trabold, T. and A Obot, N., "Impingement Heat Transfer Within Arrays of Circular Jets. Part I: Effects of Minimum, Intermediate, and complete cross flow for small and large spacings," *Journal of Heat transfer*, Vol. 109, No. 4, 1987, pp.872-879.

43. Viskanta, R. (1993). "Heat transfer to impinging isothermal gas and flame jets". *Exp. Thermal Fluid Sci.*, 6:111–134.

44. Yule, A. J. (1978). “Large-scale structure in the mixing layer of a round jet”. *J. Fluid Mech.*, 89 (3) pp. 413–432.

45. Taylor B.N. and Kuyatt C. E., “Guidelines for Evaluating and Expressing the Uncertainty of NIST Measurement Results”, *National Institute of Standards and Technology* Technical Note 1297, 1994

46. Fred Thomas, W., “An Experimental study of the effects of rotation on convective heat transfer in smooth and pin fin ducts of narrow cross-section”, PhD dissertation, Rensselaer Polytechnic Institute, New York, 1999.

47. Figliola R. S., and Beasely, D. E., “Theory and Design of Mechanical measurements”, 2000, 3rd Edition, Wiley Publishing house.

VITAE

- Born in Hyderbad, India on October 12, 1981.
- Pursued B. Tech in Mechanical Engineering in 2002 from Jawaharlal Nehru Technological University, Hyderabad, India.
- Pursued M.S. in Mechanical Engineering (Thermofluids and Heat Transfer) in 2005 from King Fahd University of Petroleum and Minerals, Dhahran, Saudi Arabia.
- Email: khaleelahmed_ny@yahoo.com

PUBLICATIONS

- **Effect of Outflow orientation on heat transfer in a rectangular channel with a single array of impinging jets**, *Luai M. Al-Hadhrami*, and *Khaleel Ahmed. M.,* Proceedings of 6th World Conference on Experimental Heat transfer, Fluid Mechanics and Thermodynamics, 5 – b – 16, Japan.
- **Effect of orifice jet size and outflow orientation on heat transfer in a rectangular channel with a single array of impingement jets**, *Khaleel Ahmed. M., and Luai M. Al-Hadhrami*. International symposium of Transport Phenomenon - 16, Prague, Czech Republic.